THE UNIVERSITY OF CHICAGO

REVEALING THE ATMOSPHERES OF HIGHLY IRRADIATED EXOPLANETS: FROM ULTRA-HOT JUPITERS TO VENUS ANALOGUES

A DISSERTATION SUBMITTED TO
THE FACULTY OF THE DIVISION OF THE PHYSICAL SCIENCES
IN CANDIDACY FOR THE DEGREE OF
DOCTOR OF PHILOSOPHY

DEPARTMENT OF GEOPHYSICAL SCIENCES

BY
MEGAN LESSER MANSFIELD

CHICAGO, ILLINOIS
JUNE 2021

"Don't you see the starlight, starlight?

Don't you dream impossible things?"

– Taylor Swift

TABLE OF CONTENTS

LIST OF FIGURES

LIST OF TABLES

ACKNOWLEDGMENTS

First and foremost, thank you to Jacob for your mentoring, guidance, and sharing your enthusiasm of rock climbing, without which grad school would be much more boring (and stuck at ground level). Thanks also to Edwin, Leslie, and Fred for your support, scientific insight, and sitting through all those long committee meetings.

Thank you to my family - especially Mom, Dad, Sarah, Elizabeth, Pierce, Uncle Jeff and Uncle Jack, Grammy and Poppy - for your love and encouragement, and for excitedly listening as I attempt to explain my space rocks to you. I hope you never get tired of my long-winded explanations. Thanks also to Josh, my doppelgänger rave crab, for your love and for all the cute cat posts you show me to help me through proposal season.

Thank you to Orion and Luna. You're the best cats, even when you wake me up at 5 am asking for breakfast.

Thank you to the whole Bean group - Adina, Andreas, Julian, David, Ben, and Madison - for interesting science discussions. Thank you to the Double Cat Space Squid Squad (Megan B, Adina, and Sasha) for being the best friends a grad student could ask for. And thanks to the lunch crew - Anne, Nigel, Andy, Kellie, Sam, Claire, and Cara - for random conversations, letting me test my DM skills on you all, and stretching my brain every day with our attempts to do the NY Times Crossword.

Thank you to NASA for financial support through a FINESST grant.

I gratefully acknowledge that, throughout my PhD, I have lived and worked on the original homelands and traditional territory of the Kiikaapoi (Kickapoo), Peoria, Kaskaskia, Potawatomi, Ojibwe, Miami, and Očhéthi Šakówiŋ (Sioux) people. I also acknowledge my use of telescopes situated on Mauna Kea, in the traditional territory of the Kanaka ʻŌiwi (Hawaiian) people, and on Cerro Pachon, in the traditional territory of the Diaguita people.

Finally, thank you so much to my high school physics teacher, Sara Karbeling. Your enthusiasm and encouragement are what set me on this path, and look where I ended up!

ABSTRACT

Spectroscopy of transiting exoplanets has revealed a wealth of information about their atmospheric compositions and thermal structures. In particular, studies of highly irradiated exoplanets at temperatures much higher than those found in our solar system have provided detailed information on planetary chemistry and physics because of the high level of precision which can be obtained from such observations.

In this dissertation I use a variety of observation and modeling techniques to study the atmospheres of highly irradiated transiting exoplanets and learn about their physics and chemistry. In the first part of my thesis I present a detailed study of ultra-hot Jupiters, planets with equilibrium temperatures above 2000 K. I present *Hubble Space Telescope* (*HST*) secondary eclipse observations of the ultra-hot Jupiter HAT-P-7b, which shows a featureless emission spectrum. This spectrum, in combination with similar observations of other ultra-hot Jupiters, led to the realization that the ultra-hot Jupiters are a distinct class of planets with spectra heavily impacted by molecular dissociation. I next present a *Spitzer Space Telescope* phase curve of KELT-9b, the hottest known exoplanet, which shows the impacts of extreme molecular dissociation at the highest temperatures. KELT-9b is so hot that molecular hydrogen dissociates and significantly impacts the heat transport throughout its atmosphere. Finally, I expand these initial investigations to a population study of all hot Jupiter emission spectra observed with *HST* to investigate the impact of molecular dissociation across a wider range of temperatures.

In the second part of my thesis I investigate the physics and chemistry of the highly irradiated exo-Neptune HAT-P-11b. I present a discovery of helium in the *HST* transmission spectrum of HAT-P-11b. This discovery was only the second time helium was detected using *HST*, and it allows us to probe atmospheric escape at the uppermost levels of the atmosphere and study the history of atmospheric loss on the planet.

In the coming years we will have the opportunity to study exoplanet atmospheres in even more detail using the *James Webb Space Telescope* (*JWST*). In the final section of my thesis

I present modeling tools I have developed which will be key to interpreting future *JWST* exoplanet observations. I first present a data reduction and analysis pipeline that can be used to interpret *JWST* eclipse mapping observations of hot Jupiters, which will give us the ability to resolve the daysides of these planets in latitude, longitude, and altitude. I next turn to smaller planets and present a model of inferred albedos for hot, rocky planets which can be used to determine whether such planets have atmospheres, a key prerequisite for the presence of life.

CHAPTER 1

INTRODUCTION

The main goals of exoplanet atmosphere spectroscopy are to determine exoplanets' compositions and thermal structures in order to further our understanding of planetary formation, physics, and chemistry. The study of extrasolar planets offers an opportunity to investigate planetary origins and climate in a broader context than studies of our solar system. We now know of over 4000 exoplanets orbiting thousands of stars[1], and we can use this large sample of planets to learn more about planet formation processes in a statistical sense (see Figure 1.1). The exoplanet population also offers a much greater diversity of planets than what is available in our own solar system. For example, hot Jupiters, which orbit very close to their host stars, and mini-Neptunes/super-Earths, planets intermediate in size between the Earth and Neptune, are absent from our Solar System, but exoplanet discovery missions such as Kepler have discovered thousands of these planets [28].

Spectroscopic observations of transiting planets provide the best path toward fulfilling the full promise of exoplanets for astrophysics and planetary science because of the detailed information they reveal about exoplanet atmospheres. There are three main types of spectroscopic observations which reveal complementary information about the planet being observed (Figure 1.2). Primary transits occur when the planet passes in front of the star. When this happens, some of the star's light is transmitted through the planet's atmosphere. The planet will appear larger at wavelengths where the atmosphere is more opaque, so primary transits can reveal the molecular composition of the atmosphere on the planet's limbs. Composition determinations for these planets are important because they provide records of their formation and migration [e.g., 312, 187]. In particular, the core accretion model of planet formation predicts a trend of decreasing atmospheric metallicity with increasing planet mass for giant planets [84]. Additionally, measuring the carbon-to-oxygen (C/O) ratio provides information on the environment in which a planet forms, its relative accretion

1. from `https://exoplanetarchive.ipac.caltech.edu`

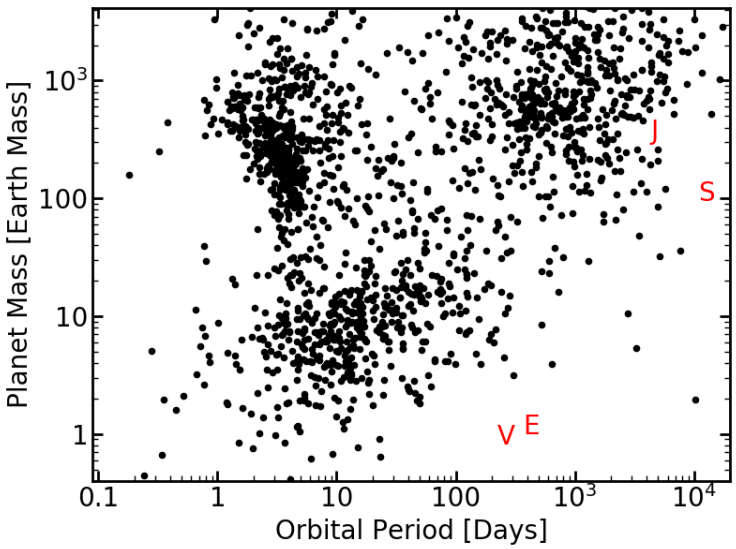

Figure 1.1: Orbital period versus planet mass for all confirmed exoplanets with masses less than 13 Jupiter masses and orbital periods less than 20,000 days. Red letters indicate the positions of the Earth (E), Venus (v), Jupiter (J), and Saturn (S). The known exoplanets are much more abundant and span different parts of this parameter space than the solar system planets. Data from `https://exoplanetarchive.ipac.caltech.edu`.

of gases and solids, the size of solid bodies it accretes, and how the planet migrated to its current location [e.g., 222, 186, 213, 3, 69].

During secondary eclipses, the planet's thermal emission is blocked from view as it passes behind the star. Spectroscopic observations of secondary eclipses show the planet's emission at a variety of pressure levels in the atmosphere, so they can be used to determine both the composition and the thermal structure of the atmosphere on the planet's dayside. Secondary eclipse observations therefore provide information on an exoplanet's climate and which molecules dominate its energy balance [e.g., 268, 34, 83].

Finally, thermal phase curves measure the planet's emission throughout a full orbit. Close-in planets like hot Jupiters are generally assumed to be synchronously rotating, in which case a phase curve shows the thermal emission as a function of longitude on the planet. This can reveal information about which physical processes dominate heat transport from the dayside, which always faces the star, to the nightside, which permanently faces away from the star [e.g., 268, 243, 47, 115, 230, 22, 155].

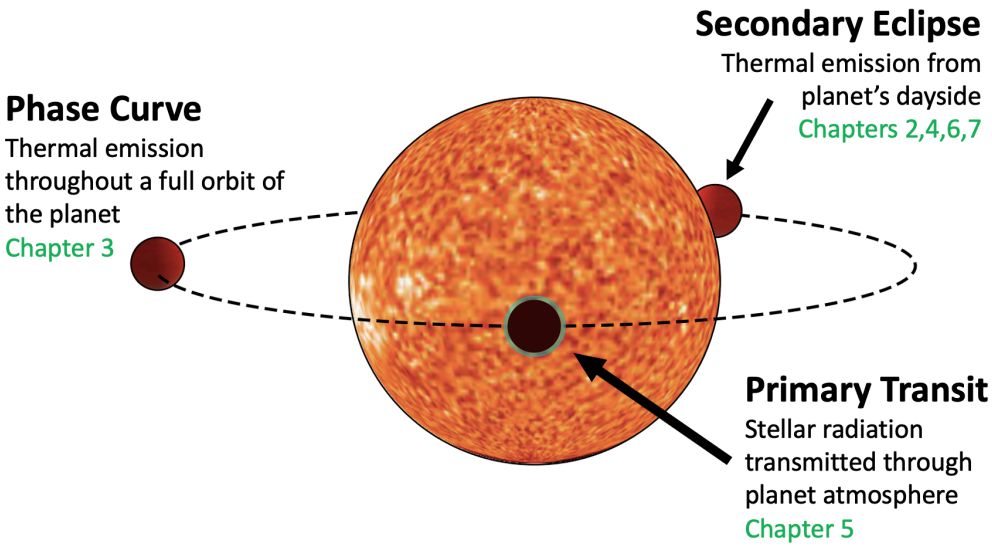

Figure 1.2: Illustration of the three main types of transiting exoplanet observations. Primary transits are when the planet passes in front of the star and show the star's radiation transmitted through the planet's atmosphere. Secondary eclipses show the planet's thermal emission disappearing as it passes behind the star. Phase curves, in which the planet is observed throughout a full orbit, show the thermal emission of the planet as a function of longitude. Green text indicates chapters which discuss each of these techniques. Figure courtesy of Kevin Stevenson.

In this thesis, I will present observations of highly irradiated exoplanets aimed at addressing three large, open questions in exoplanet atmosphere spectroscopy. In Part I, I present a series of observations which reveal the thermal structures and heat transport of ultra-hot Jupiters, the hottest known exoplanets. In Chapter 2, I present an *HST* secondary eclipse spectrum of HAT-P-7b, an ultra-hot Jupiter with a dayside temperature of ≈ 2700 K. The spectrum appears featureless, with a noticeable lack of the water absorption features that earlier theories predicted would be observed. This result, along with similar results for other hot Jupiters [6, 163, 233], led to the realization that the ultra-hot Jupiters are a unique class of planets strongly influenced by high-temperature chemical effects such as molecular dissociation and H^- opacity. This chapter is based on Mansfield et al. [197].

In Chapter 3, I present a *Spitzer* phase curve of the hottest known ultra-hot Jupiter, KELT-9b. The phase curve shows a reduced day-night temperature difference which matches predictions from models including the effects of H_2 molecular dissociation and recombination.

Because KELT-9b is so hot, H_2 dissociation is widespread enough to have an observable impact on the rate of heat transfer from the dayside to the nightside. This chapter is based on Mansfield et al. [200].

In Chapter 4, I expand these individual studies to a population study of all 20 hot Jupiters that have been observed with *HST* between $1.1-1.7$ μm. In this study we developed a metric to quantify the strength of water absorption/emission features in *HST* secondary eclipse spectra and compared the full set of observations to 1D model predictions. The broad trends in observed water feature strength with temperature match the model predictions. However, the individual data sets show scatter around the mean trend which can best be explained by variations in atmospheric metallicity and C/O ratio among the observed population of planets. This result matches expectations from planet formation models, which predict variation in atmospheric abundances [e.g., 213, 3, 187].

In Part II, I present observations of atmospheric escape on the highly irradiated exo-Neptune HAT-P-11b. Photoevaporation is theorized to sculpt the radius distribution of close-in exoplanets [177, 225, 226, 91, 308], but hydrogen Lyα observations to measure this atmospheric escape have been limited to planets with high-velocity gas escape because of interstellar absorption [e.g., 313]. The helium absorption triplet at 10833 Å has recently been proposed as an alternative way to probe the escaping atmospheres of highly irradiated exoplanets [264, 223]. I present a detection of helium escape in the atmosphere of HAT-P-11b, which was only the second space-based detection of this feature [276]. Our data are best fit by hydrodynamic escape models with atmospheric escape rates of $\dot{M} \approx 10^9$ – $10^{11}\,\mathrm{g\,s^{-1}}$. We also confirm the independent detection of helium in HAT-P-11b by the CARMENES instrument, making this the first exoplanet with consistent detections of the same signature of photoevaporation from both ground- and space-based facilities. This chapter is based on Mansfield et al. [198].

One of the biggest advances in exoplanet observations will be enabled by *JWST*, which will launch in October 2021. In Part III, I present modeling tools I have developed which can

be used to interpret exoplanet observations. In Chapter 6, I present the Eigenspectra method, a data reduction and analysis pipeline for spectroscopic eclipse mapping observations of hot Jupiters. Spectroscopic eclipse mapping is the only method which can resolve the daysides of hot Jupiters in latitude, longitude, and altitude simultaneously [321, 246]. However, eclipse mapping observations do not provide perfect proxies for each spatial dimension, so one must carefully account for inherent degeneracies and uncertainties when reconstructing a global brightness map. The Eigenmapping method provides a framework for avoiding these degeneracies while constructing spectroscopic eclipse maps, while also ensuring that the derived spectra have the highest precision possible and retain as much information as possible about spectral variations across the surface of the planet. This chapter is based on Mansfield et al. [199]

In Chapter 7, I turn to models of highly irradiated rocky planet observations with *JWST*. The launch of *JWST* will give us the capability to look in detail at the atmospheres of rocky planets orbiting M dwarf stars. However, it is still unknown whether such planets can retain atmospheres over long timescales, or whether the high-energy irradiation from their stars will strip their atmospheres [177, 225, 226, 248, 90, 308]. I present a method of detecting atmospheres on terrestrial exoplanets using the albedo inferred from secondary eclipse photometry with the *JWST* Mid-Infrared Instrument (MIRI). We find that a high inferred albedo can be unambiguously interpreted as evidence of an atmosphere on planets with equilibrium temperatures of $T_{eq} = 300 - 880$ K. This method is complementary to the eclipse photometry method of Koll et al. [152] because it provides a way to detect tenuous atmospheres which are too thin to transport significant heat but thick enough to host high-albedo clouds. The presence of an atmosphere is a key prerequisite for the development of life, so this method, combined with that of Koll et al. [152], will be a first step toward determining the habitability of rocky planets observed with *JWST*. This chapter is based on Mansfield et al. [196].

Finally, I conclude in Chapter 8 by discussing remaining open questions in the field of

highly irradiated exoplanets and opportunities to advance our understanding of these unique bodies in the coming years.

Part I

Revealing the Atmospheres of Ultra-Hot Jupiters

As described above, secondary eclipse and phase curve observations can reveal information on the thermal structures of exoplanet atmospheres. The observed secondary eclipse depth of an exoplanet is given by

$$\frac{F_p}{F_*} = \frac{B_\lambda(T_p)}{B_\lambda(T_*)} \left(\frac{R_p}{R_*}\right)^2, \tag{1.1}$$

where B_λ is the Planck function (here the star and planet have both been approximated as blackbodies), T_p is the planet's dayside temperature, T_* is the stellar effective temperature, and R_p and R_* are the planet and stellar radius, respectively. From this equation, it can be seen that the planets which are most amenable to secondary eclipse observations will be those that are relatively hot and relatively large compared to their host stars. Ultra-hot Jupiters, which have dayside temperatures above 2000 K [233], are therefore the optimal targets for thermal emission observations in secondary eclipse.

Fortney et al. [83] predicted that the thermal emission spectra of hot Jupiters would be divided into two categories (see Figure 1.3). They predicted that planets with equilibrium temperatures below $\approx$ 2000 K would have uninverted temperature-pressure (T-P) profiles, which would produce absorption features in their secondary eclipse spectra. However, planets with hotter equilibrium temperatures would be hot enough that TiO and VO could exist in vapor form in the upper regions of their atmospheres which are probed by emission spectroscopy [125]. These molecules would absorb incoming starlight at short wavelengths and heat the upper atmosphere, similar to how ozone heats Earth's stratosphere. This extra heating would create thermal inversions in the T-P profiles of these planets, which would result in emission features in the secondary eclipse spectra.

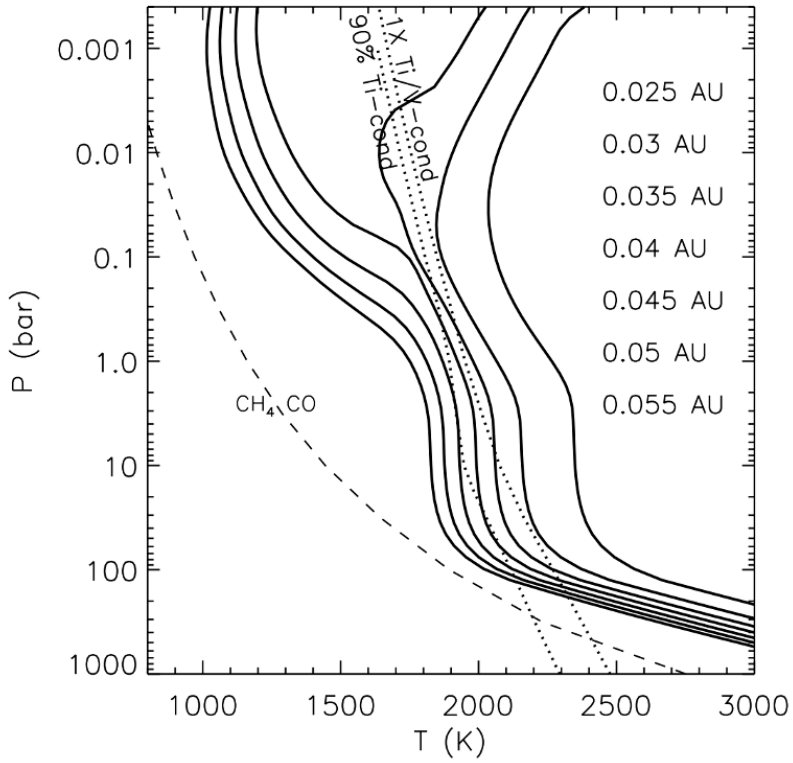

Figure 1.3: Modeled T-P profiles for a hot Jupiter at varying distances from the Sun. The planet at 0.055 AU (leftmost line) and the planet at 0.025 AU (rightmost line) have the lowest and highest temperatures at all pressures, respectively. The dotted lines show temperatures below which 90% of Ti and V will have condensed out. Planets below the dotted lines show uninverted T-P profiles. Those at higher temperatures show thermal inversions at pressures of $\approx 0.1 - 0.001$ bar because of the existence of vapor TiO/VO at these altitudes. Figure from Fortney et al. [83].

CHAPTER 2

AN *HST*/WFC3 THERMAL EMISSION SPECTRUM OF HAT-P-7B

In order to investigate whether the predictions of Fortney et al. [83] accurately describe hot Jupiter atmospheres, we observed the secondary eclipse of the hot Jupiter HAT-P-7b with the *HST* Wide Field Camera 3 (WFC3) instrument between $1.1 - 1.7$ μm[1]. This bandpass is primarily sensitive to water vapor in exoplanet atmospheres, and the largest molecular feature in this wavelength range is a water vapor absorption band centered at about 1.4 μm. Over the last decade, a large sample of exoplanets have been observed using *HST*/WFC3 to understand their atmospheric water abundances [e.g., 270, 305], and it has become an important tool in understanding exoplanet atmospheres.

HAT-P-7b is a hot Jupiter with an intermediate dayside equilibrium temperature of 2600 K (assuming zero albedo and dayside only recirculation). HAT-P-7b was previously observed with *Spitzer* and found to have a thermal inversion [44, 323]. However, because *Spitzer* can only observe exoplanet spectra in a few broadband regions, there are degeneracies with the molecular abundances that make it difficult to determine the exact thermal structure with these data alone [188, 173]. Spectroscopy in general, and WFC3 measurements in particular, can remove these degeneracies by resolving molecular bands. We describe our *HST* observations of HAT-P-7b in Section 2.1. In Section 2.2, we describe our data analysis and results, and we summarize our findings in Section 2.3.

1. This chapter is based on Mansfield et al. [197], which was coauthored by Jacob L. Bean, Michael R. Line, Vivien Parmentier, Laura Kreidberg, Jean-Michel Désert, Jonathan J. Fortney, Kevin B. Stevenson, Jacob Arcangeli, and Diana Dragomir. M. Mansfield reduced and analyzed the data presented in this chapter, created the two-parameter eclipse model described in Section 2.2.3, and led the data-model comparison. J. L. Bean is PI of the *HST* program GO-14792 which obtained the observations of HAT-P-7b. M. R. Line created the 1D models described in Section 2.2.2. V. Parmentier created the 3D models described in Section 2.2.1. L. Kreidberg assisted in data reduction. All other authors are co-Is on *HST* program GO-14792.

2.1 Observations

We observed secondary eclipses of HAT-P-7b on 23 December 2016 and 4 January 2017 using the *HST* WFC3 IR detector as part of program GO-14792. We used the G141 grism to observe the emission spectrum of HAT-P-7b between 1.1-1.7 μm. Each of the two visits consisted of five consecutive *HST* orbits, in which HAT-P-7 was visible for approximately 50 minutes per orbit and occulted by the Earth for the remainder of each orbit. At the beginning of each orbit, we took a direct image of the target with the F126N narrow-band filter for wavelength calibration.

The observations were taken in spatial scan mode with the 256×256 subarray using the SPARS10, NSAMP=16 readout pattern, resulting in a total exposure time of 103.129 s. We used a scan rate of 0.08 arcsec/second, which produced spectra extending approximately 80 pixels in the spatial direction and with peak pixel counts of about 35,000 electrons per pixel. We used bi-directional scans to maximize the duty cycle, which yielded 21 exposures per orbit and a duty cycle of 64%. An example spatial scan is shown in Figure 2.1. Although the spectrum of a background star overlaps with that of HAT-P-7 in the full image, our data reduction used the individual ramp samples, in which the two stars are well separated.

We reduced the *HST* data using the data reduction pipeline described in Kreidberg et al. [161]. All observation times were converted to $\mathrm{BJD_{TDB}}$ [64]. We used an optimal extraction procedure instead of aperture extraction to extract the data [122]. We tested several different aperture sizes to determine one that captured the full spectrum without capturing large areas of background. We masked cosmic rays so that optimal extraction could fit the point spread function of the data without being influenced by cosmic rays. A typical frame had one cosmic ray masked out. To subtract the background out of each frame, we visually inspected the images to find a clear background spot on the detector and subtracted the median of this background area from each pixel in the aperture. To determine the uncertainties on the measurements we added the photon noise, read noise, and median absolute deviation of the background in quadrature.

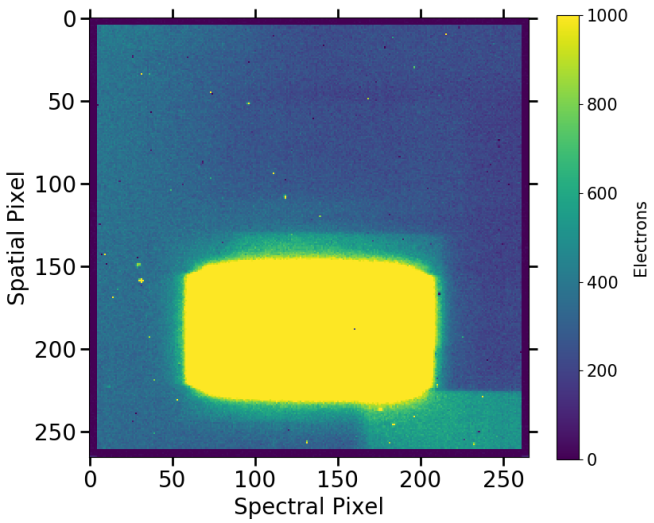

Figure 2.1: An example spatial scan. The spectrum of HAT-P-7 overlaps with a background star in the full image here, but our data reduction used the individual ramp samples, in which the two stars are well separated.

Following standard procedure for *HST* WFC3 eclipse observations, we discarded the first orbit of each visit. We also discarded the first exposure from each orbit in the first visit and the first two exposures from each orbit in the second visit to improve the quality of the fit. The spectra were binned into 14 channels with a width of 9 pixels per channel, giving a resolution of $R = 30 - 44$. We also created a broadband white light curve by summing the spectra over the entire wavelength range.

We fit both the white light curve and the spectroscopic light curves with a model that combined a secondary eclipse model [158] and a systematics model based on Berta et al. [24]. For the white light curve, the free parameters in the secondary eclipse model were the mid-eclipse time T_{sec} and the planet-to-star flux ratio F_p/F_s. The orbital period, ratio of the semi-major axis to the stellar radius, inclination, planet-to-star radius ratio, and eccentricity were fixed to the values determined by Wong et al. [323], which were $P = 2.2047372$ days, $a/R_s = 4.03$, $i = 82.2°$, $R_p/R_s = 0.07809$, and $e = 0.0016$, respectively.

We fit the instrument systematics with an equation of the form

$$M(t) = E(t)(cs + vt_{vis})(1 - e^{-r_1 t_{orb} - r_2}) \tag{2.1}$$

where $M(t)$ is the modeled flux, $E(t)$ is the eclipse model, c is a normalization constant, s is a scaling factor to correct for an offset in normalization between scan directions [205], v is a visit-long linear slope, t_{vis} is the time since the beginning of the visit, r_1 is the amplitude of an orbit-long exponential ramp, r_2 is the time constant of the orbit-long ramp, and t_{orb} is the time since the beginning of the orbit. T_{sec}, f_p/f_s, r_1, and r_2 were fixed to the same values for both visits, while c, v, and s varied between visits. The fit to the white light curve thus contained a total of 10 free parameters.

Previous studies of *HST* WFC3 data have shown that adding a quadratic term to the visit-long trend in the model of the instrument systematics provides a better fit, primarily for very bright stars [279, 175]. We tested adding a quadratic term to the visit-long trend, but found Bayesian Information Criterion (BIC) values that were higher by about 8 on average for the quadratic model compared to the linear model, indicating that the linear model is preferred for this data set.

We estimated the parameters with a Markov Chain Monte Carlo (MCMC) fit using the `emcee` package for Python [82]. The best-fit white light curve, which is shown in Figure 2.2, had $\chi^2_\nu = 2.24$ and an average residual of 90 ppm. The value of T_{sec} determined from the fit to the white light curve was $2457757.68242 \pm 0.00097$ $\mathrm{BJD_{TDB}}$. The spectroscopic light curves were fit with the same model as the white light curve, with the exception that T_{sec} was fixed to the best-fit value from the fit to the white light curve. An example pairs plot for the MCMC fit to the 1.234 - 1.271 μm light curve is shown in Figure 2.3. The spectroscopic light curves achieved photon-limited precision, with χ^2_ν values between $0.89 - 1.25$. The final secondary eclipse spectrum, along with *Spitzer* data from Wong et al. [323], is shown in Figure 2.4, and the planet-to-star flux ratio for each bandpass is listed in Table 2.1.

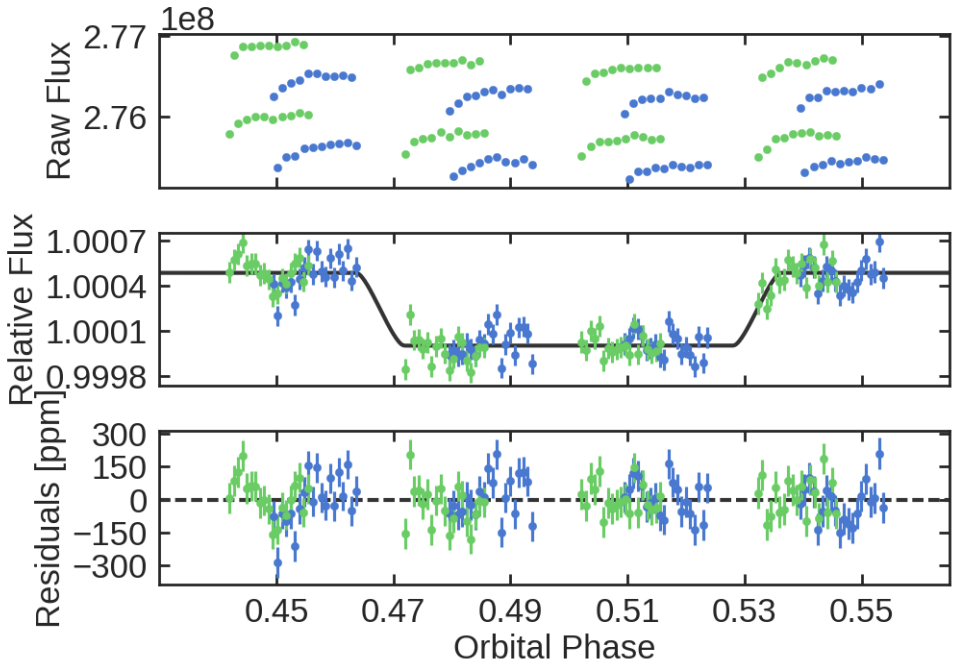

Figure 2.2: Raw flux of the secondary eclipse of HAT-P-7b (upper panel), best fit broadband white light curve (middle panel), and residuals to the fit (lower panel). Blue points are from the eclipse on 23 December 2016, and green points are from 4 January 2017. The offsets between the two sets of green and blue points in the upper panel are due to the difference between the forward and reverse scans. The fit has $\chi^2_\nu = 2.24$ and an average residual of 90 ppm.

Table 2.1: Secondary eclipse spectrum of HAT-P-7b.

Wavelength Range (μm)	f_p/f_s (%)
1.120 - 1.158	0.0334 ± 0.0037
1.158 - 1.196	0.0413 ± 0.0038
1.196 - 1.234	0.0404 ± 0.0037
1.234 - 1.271	0.0501 ± 0.0037
1.271 - 1.309	0.0503 ± 0.0038
1.309 - 1.347	0.0498 ± 0.0037
1.347 - 1.385	0.0530 ± 0.0037
1.385 - 1.423	0.0510 ± 0.0037
1.423 - 1.461	0.0547 ± 0.0039
1.461 - 1.499	0.0621 ± 0.0041
1.499 - 1.536	0.0607 ± 0.0042
1.536 - 1.574	0.0593 ± 0.0044
1.574 - 1.612	0.0594 ± 0.0046
1.612 - 1.650	0.0593 ± 0.0045

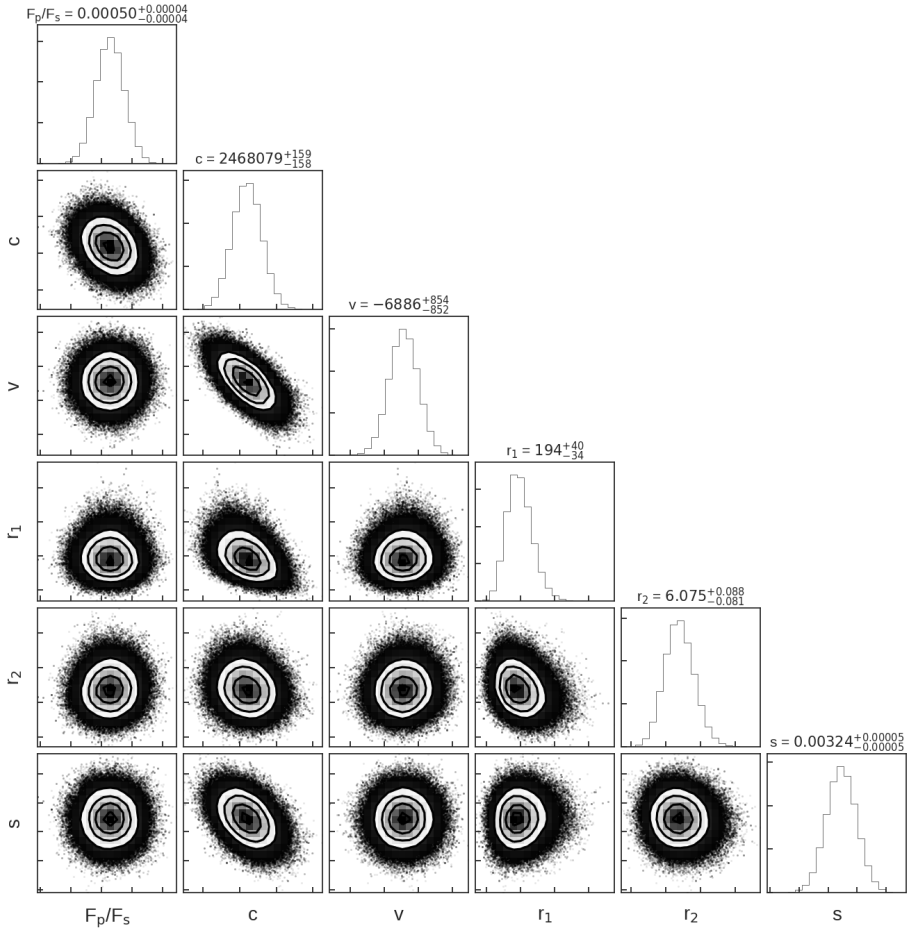

Figure 2.3: Pairs plot showing the distributions of fit parameters for the MCMC fit to the $1.234-1.271$ μm light curve. The off-diagonal panels show marginalized posterior probability for pairs of parameters, with 1, 2, and 3σ intervals indicated with black contours. The grey shading is darker for higher probability density. The panels on the diagonal show marginalized posterior probability distributions for each parameter, and the dashed lines indicate the median values and 68% confidence intervals. The planet-to-star flux ratio is not strongly correlated with any of the other fit parameters. For parameters that are allowed to vary between visits (c, v, and s), the distributions are for the eclipse observed on 23 December 2016.

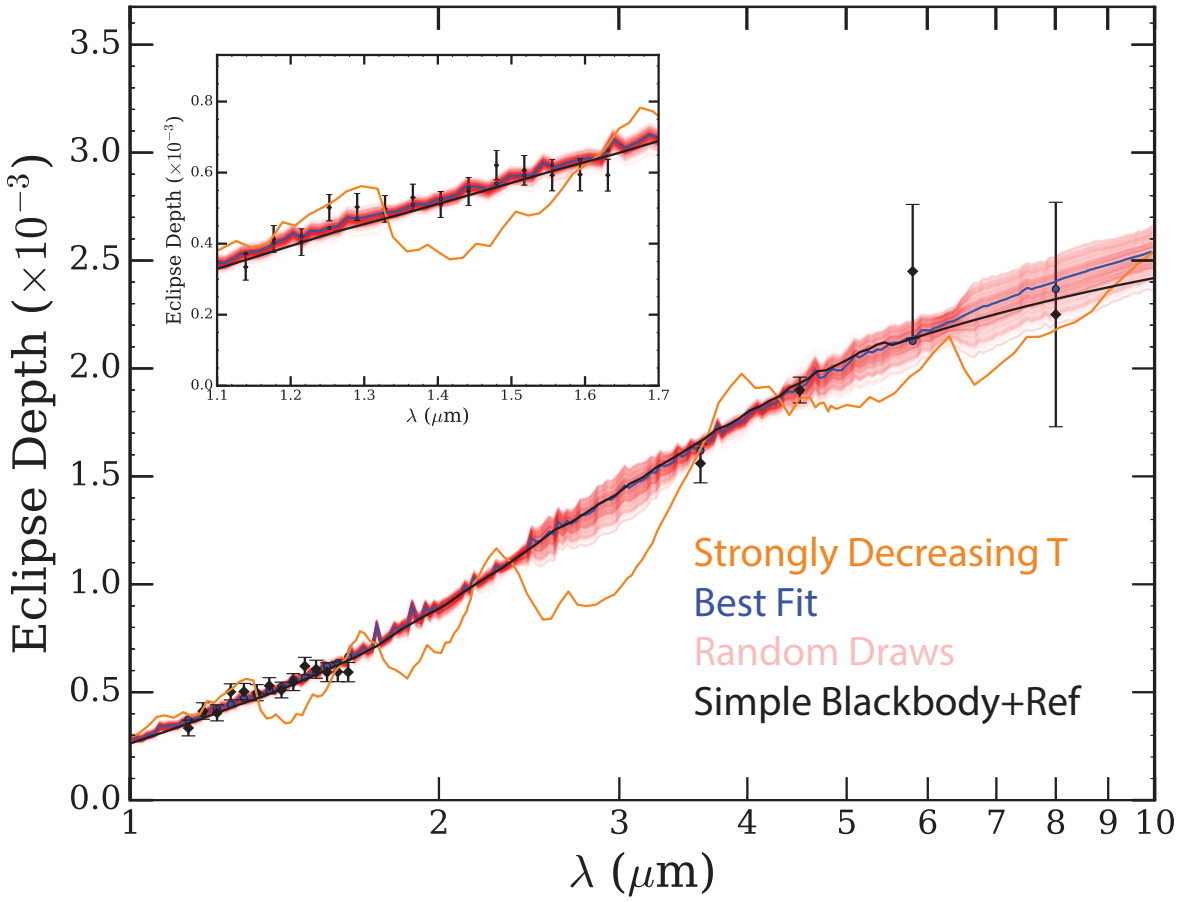

Figure 2.4: Secondary eclipse spectrum of HAT-P-7b with a suite of theoretical models. Black points with 1σ error bars represent observations by WFC3 reported in this paper and by *Spitzer* reported in Wong et al. [323]. The insert shows the WFC3 data from 1.1-1.7 μm. The dark blue line represents the best-fitting 1D atmospheric model, as described in Section 2.2.2, and the surrounding red lines show 500 spectra randomly drawn from the posterior. Blue points outlined in black show the best-fitting 1D model binned to the data resolution. The black line shows a fit to a simple model of thermal and reflected light, as described in Section 2.2.3. The orange line shows a model atmosphere with a monotonically decreasing temperature-pressure profile that provides a reasonable match to the *Spitzer* data, calculated using the methods of Fortney et al. [83].

2.2 Analysis

The spectrum of HAT-P-7b is shaped like a blackbody and clearly rejects a model with a monotonically decreasing temperature with altitude, as can be seen in Figure 2.4. This could be due to a lack of near-infrared opacity sources like water in the atmosphere, an isothermal atmospheric structure, or a previously unrecognized grey opacity obscuring absorption or emission features. To understand why we see this blackbody-like spectrum, we used three different modeling approaches: a 3D GCM, 1D self-consistent forward models, and a simple model of blackbody thermal emission plus reflected stellar light. The data are well-fit by a blackbody model, so we use these models with varying amounts of complexity to explore the planetary physics and chemistry and put the blackbody-like spectrum in context, rather than using fit quality metrics to search for a single best-fit model.

2.2.1 Fit to 3D GCM

We first performed 3D GCM calculations to help interpret the spectrum and guide how we approached fitting the data with parameterized models. To model the three-dimensonal structure of HAT-P-7b, we used the SPARC/MITgcm clobal circulation model [267]. Our setup is similar to the one used in Parmentier et al. [231] but with planetary and stellar parameters chosen to match the HAT-P-7 system. The atmospheric opacities and mean molecular weight used in the calculations correspond to a solar composition atmosphere, a solar composition atmosphere depleted in TiO and VO, or a solar composition atmosphere with the abundance of every element apart from hydrogen and helium increased or decreased by the same amount. We assume local chemical equilibrium. Atmospheric drag of various possible origins (ohmic dissipation, hydrodynamic instabilities, etc.) is modeled as a Rayleigh drag present throughout the whole model and acting with a drag timescale τ_{Drag}. The model was run for 300 Earth days and all quantities were averaged over the last 100 days. Figure 2.5 shows the planet-to-star flux ratio and T-P profile at the substellar point for each 3D

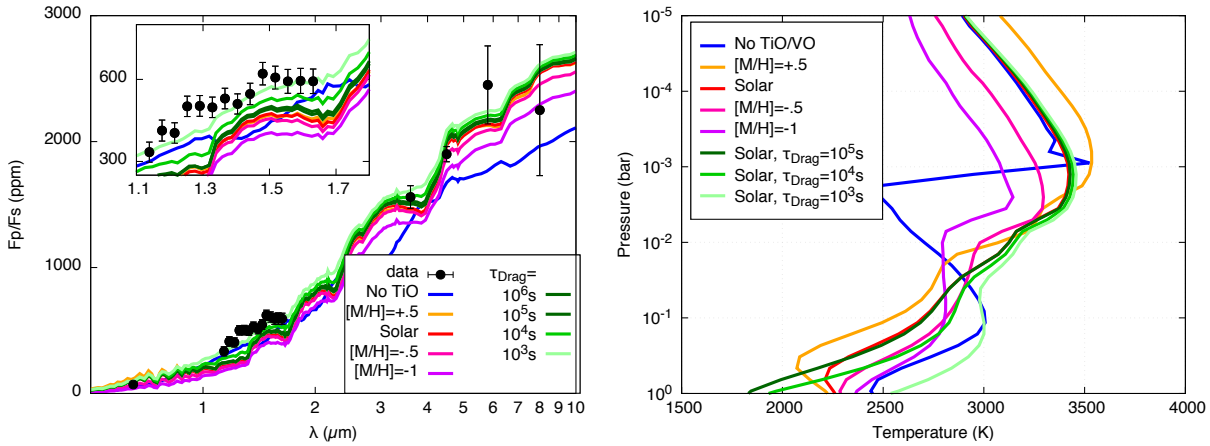

Figure 2.5: Planet-to-star flux ratio as a function of wavelength (left) and dayside temperature-pressure profiles (right) for each 3D GCM run. The red, blue, orange, pink, and magenta lines show models with solar composition, without TiO and VO, and with metallicities of +0.5, −0.5, and −1.0, respectively. The dark to light green lines show atmospheres with solar composition and decreasing drag timescales.

model.

The best fitting 3D models contain both TiO/VO and H^- opacities, and have a thermal inversion due to absorption by TiO/VO in the upper atmosphere. Models with lower metallicities have a deeper photosphere leading to more efficient heat redistribution and thus lower fluxes in the WFC3 bandpass. The low-metallicity models would therefore require even more drag than in the solar metallicity case to match the observations. Although we include H^- opacity, it does not contribute significantly to the atmospheric opacity. However, water dissociation has a large impact on the observed spectrum. Water dissociation limits the range of pressures probed, which limits our observations to the part of the atmosphere near the tropopause and produces a blackbody-like spectrum. If water were not dissociating in the upper atmosphere, our observations would probe a region of the atmosphere which extended above the tropopause and we would see emission features.

Models containing TiO/VO with varying drag timescales produce similar quality fits to the *Spitzer* data points, but the WFC3 points can only be fit well with a short drag timescale of $\tau_{\rm Drag} = 10^3$ s. Models with less drag (i.e. more redistribution) do not produce hot enough daysides to match the WFC3 data. Preliminary calculations of $\tau_{\rm Drag}$, which scales with the

square of the planetary magnetic field, suggest that such a small $\tau_{\rm Drag}$ is not unrealistic for such hot planets [235]. However, the models with TiO/VO opacities also appear to have small emission features, which do not match the blackbody-like shape of the WFC3 data. One other possible explanation for the warmer dayside is nightside clouds, which would increase the greenhouse effect without increasing the planetary albedo [282, 140, 231, 283]. Nightside clouds on HAT-P-7b were also suggested by Armstrong et al. [7] as an explanation for time variability in the brightness offset of its phase curve. It remains to be seen whether Lorentz forces or nightside clouds are the real explanation for why the nominal GCM underpredicts the WFC3 data.

2.2.2 Fit to 1D grid models

We also retrieve compositional and thermal information by fitting the spectrum with a grid of self-consistent 1D models. We choose this self-consistent grid-based approach as spectra with little to no spectral features tend to drive classic retrievals [e.g., 173] towards unphysical regions of parameter space.

The 1D models self-consistently solve for the radiative-convective-thermochemical equillbirium atmosphere solution. For the radiative transfer, we use the Toon et al. [299] two stream source function technique to solve for planetary thermal fluxes at each atmospheric level. Incident stellar flux at the top of the atmosphere [from a PHOENIX model – 128] is treated as a simple exponential attenuation at an average cosine incident angle of $1/\sqrt{3}$. The Newton-Raphson iteration technique is used to determine the layer temperatures that ensure zero net flux divergence across each model layer. Opacities for H_2O, CH_4, CO, CO_2, NH_3, HCN, C_2H_2, H_2S, Na, K, TiO, VO, FeH, H_2-H_2/He CIA [182], and H^- bound-free and free-free [133, 21] are treated within the "on-the-fly" correlated-k framework [e.g., 166, 5]. H_2 and He Rayleigh scattering are added in as a continuum absorber. Molecular abundances are computed using the NASA CEA Gibbs free energy minimization code [101] given the Lodders et al. [176] elemental abundances.

We reduce our parameterization of the 1D atmospheres to 3 parameters: day-night redistribution (f), which scales the incident stellar flux, a metallicity, [M/H], which scales the Lodders et al. [176] elemental abundances in the CEA routine, and a carbon-to-oxygen ratio (C/O). A grid of 1D models are computed along this 3-vector parameter set with the f ranging between 1 and 4 in steps of 0.25, [M/H] from -1.5 to 2.5 dex in steps of 0.5 dex, and C/O between 0.1 and 2 on a non-uniform grid that more finely samples C/O values near 1 [e.g., 212]. The grid spacing is chosen to be fine enough that interpolation errors are negligible, and the grid range is chosen to be broad enough to capture a physically sensible range of values. In all of these models we assume that the relative abundances of all elements except C and O remain constant.

To fit the 3-parameter model grid spectra (at an R=100) to the data, we use the `emcee` package [82] combined with the Python `griddata` N-dimensional interpolation routine. Only *HST* and *Spitzer* data were used in the fit. The best-fitting spectrum is shown in Figure 2.4. We include uniform prior ranges on f, [M/H], and log(C/O) between $1.75 - 2.66$, $-1.5 - 2.5$, and $-1.0 - 0.3$, respectively. We explored values of $f > 2.66$ but decided to exclude them due to energy balance arguments that values larger than 2.66 violate energy conservation [e.g., 47].

Like the 3D GCM, the 1D grid models show a thermal inversion due to TiO/VO absorption heating the upper atmosphere. Figure 2.6 shows the T-P profile for the best-fitting grid model in bold red, with 1σ errors representing the spread in the self-consistent T-P profiles that fall within the posterior shown by the red shaded area. Thin red and blue lines show the contribution functions for *Spitzer* and WFC3 data points, respectively, with dark blue lines showing data in the water band from 1.33-1.48 μm. The contribution functions suggest that the data are primarily probing a region of the atmosphere near the tropopause where the temperature profile switches from non-inverted to inverted.

The dashed lines on Figure 2.6 show the thermo-chemical equilibrium mixing ratios for a set of important absorbing molecules, computed along the self-consistent T-P profile for

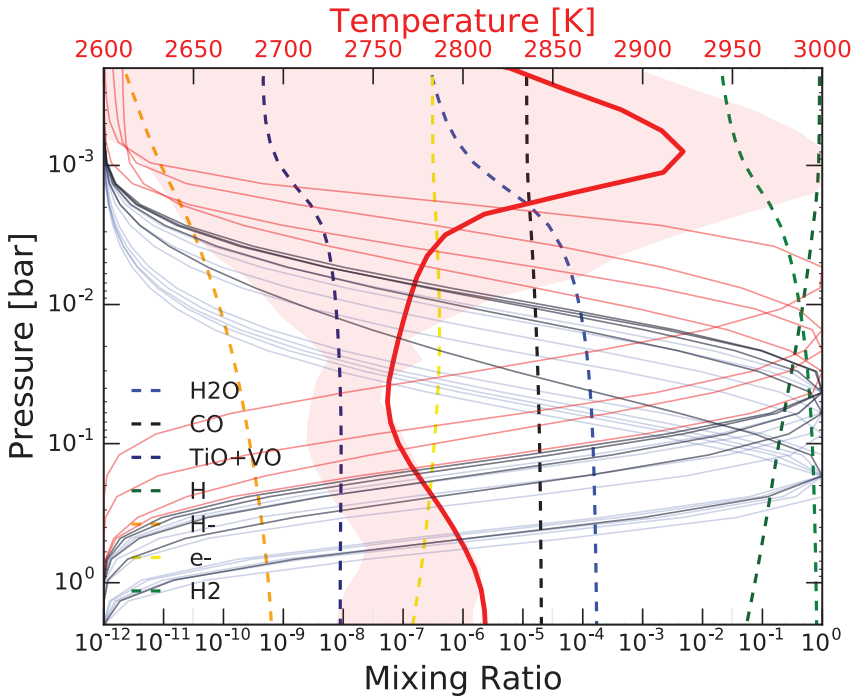

Figure 2.6: Temperature-pressure profile for the best-fit 1D interpolated spectrum (bold red line) and 1σ error (red shaded area). Temperatures are shown on the top x-axis. The model has a thermal inversion. Thin, solid lines indicate the contribution functions for data points in the *Spitzer* bandpass (red), and the WFC3 bandpass (blue), with darker blue lines showing points inside the water band from 1.33-1.48 μm. The measurements probe between about 0.2 bar and 2 mbar, where the T-P profile changes temperature gradually. The dashed curves show thermo-chemical equilibrium mixing ratios for important absorbing molecules, computed along the self-consistent T-P profile shown in bold red. Mixing ratios are shown on the bottom x-axis.

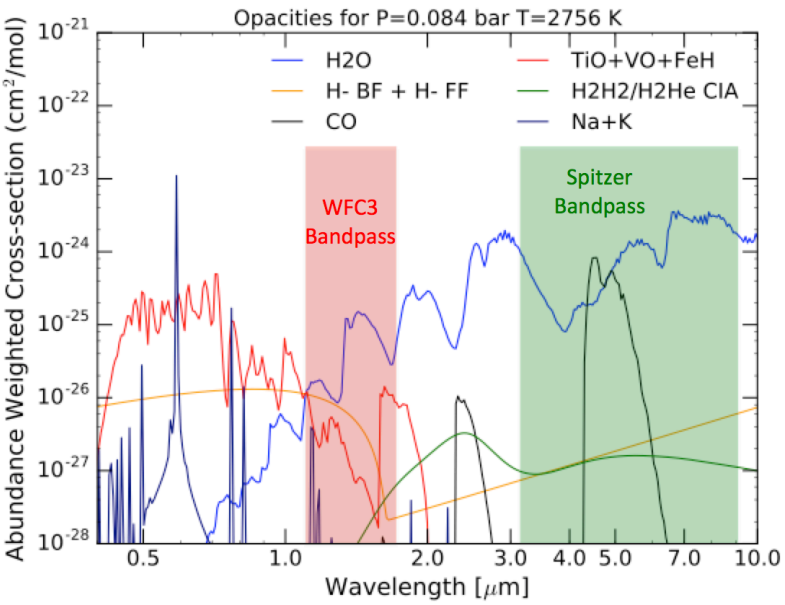

Figure 2.7: Opacities of molecular water (blue), H^- bound-free and free-free (H^- BF+FF, orange), CO (black), TiO+VO+FeH (red), Na+K (dark blue), and hydrogen/hydrogen and hydrogen/helium collision-induced absorption (CIA, green) at a pressure of 0.084 bar in the best-fitting 1D model. The red shaded area indicates the WFC3 bandpass, and the green shaded area indicates the *Spitzer* bandpass.

the best fit. The water abundance begins to decrease rapidly around 2 mbar because water begins to dissociate in the hot upper atmosphere. This suggests that the WFC3 and *Spitzer* observations probe the part of the atmosphere just below the tropopause because water dissociation limits the pressure range observed in that bandpass. If there were no water dissociation in the atmosphere, the *Spitzer* observations would extend up to higher pressures in the atmosphere and we would observe an emission feature. However, water is still an important source of molecular opacity in the WFC3 bandpass, as shown in Figure 2.7. This figure shows opacities at a pressure of 0.084 bar, near the part of the atmosphere sampled by the WFC3 bandpass outside the water band. The opacity from molecular water dominates over all other opacities at this pressure, including H^- opacity, in contrast to what is found for WASP-18b in Arcangeli et al. [6].

Figure 2.8 shows a pairs plot for the 1D grid model fits. The key ingredient of this retrieval is the assumption of radiative-convective-thermochemical equilibrium. The factor

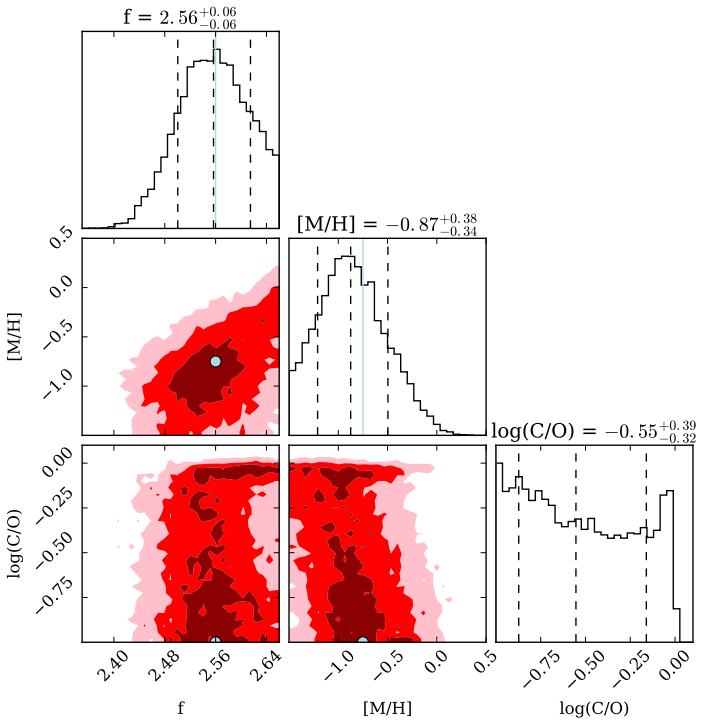

Figure 2.8: Pairs plot for the 1D grid models, showing the heat redistribution (f), metallicity, and C/O ratio. The off-diagonal panels show marginalized posterior probability for pairs of parameters, with 1, 2, and 3σ intervals indicated with dark red, red, and light red shading. The panels on the diagonal show marginalized posterior probability distributions for each parameter, and the dashed lines indicate the median values and 68% confidence intervals. Blue lines and points indicate values for the best-fit interpolated spectrum.

f measures heat redistribution, where $f = 1$ indicates full redistribution, $f = 2$ indicates redistribution over the dayside only, $f = 2.66$ corresponds to zero heat redistribution and is the maximum possible value [47]. The best-fitting model has $f = 2.56 \pm 0.06$, indicating that HAT-P-7b has relatively weak heat redistribution. This high value of f likely suggests that the thermal emission we observe is being dominated by a localized "hot spot" on the planetary dayside.

Although f is highly correlated with the metallicity, the grid models produce a strong constraint on f. Changing the metallicity affects the value of f because it changes the observed T-P profile. At higher metallicities, the abundances of TiO/VO and H_2O are both higher, but the abundances of TiO/VO increase faster than the abundance of H_2O. The

higher TiO/VO abundances warm the upper atmosphere due to increased optical absorption, but the deeper atmosphere probed by WFC3 is cooler in order to maintain radiative equilibrium, as shown in Figure 2.9. The cooling of the deeper atmosphere is then compensated for by increasing f, which warms the dayside by redistributing less of the heat to the nightside. This tradeoff can not continue indefinitely, however, because at very high metallicities the spectrum will begin to show emission features due to a stronger thermal inversion (Figure 2.9). Similarly, at very low metallicities the spectrum will begin to show absorption features due to a monotonically decreasing T-P profile. These changes in the metallicity are degenerate with changes in the relative abundances of Ti and O, but our model assumes that the ratio of Ti to O remains constant as the metallicity changes.

The models can also constrain the C/O because a higher C/O would decrease the abundances of TiO and VO in the atmosphere, which would weaken the thermal inversion. Therefore, the 1D models constrain the C/O < 1 at 99% confidence. This continues the trend of planets with C/O < 1, with no planets having high C/O values [23]. Decreasing the C/O, however, does not impact the spectrum shape or T-P profile because the TiO/VO opacity is only weakly dependent in this part of parameter space. Figure 2.8 demonstrates that the grid models only produce an upper limit on the C/O.

2.2.3 Simple Two-Parameter Eclipse Model

Although the previous models only considered thermal emission from the planet, it has been suggested that reflected starlight may contribute significantly to the flux observed by *HST* at near-infrared wavelengths [260, 141]. Reflected light can dominate over thermal emission in the near infrared for hot Jupiters with high albedos. Keating & Cowan [141] found that reflected light may contribute significantly to the planetary flux at secondary eclipse for WASP-43b in the WFC3 bandpass. In order to determine whether reflected light is important in the WFC3 bandpass for HAT-P-7b, we performed a simple fit to a model of the combined reflected light and thermal emission for a planet whose emission can be

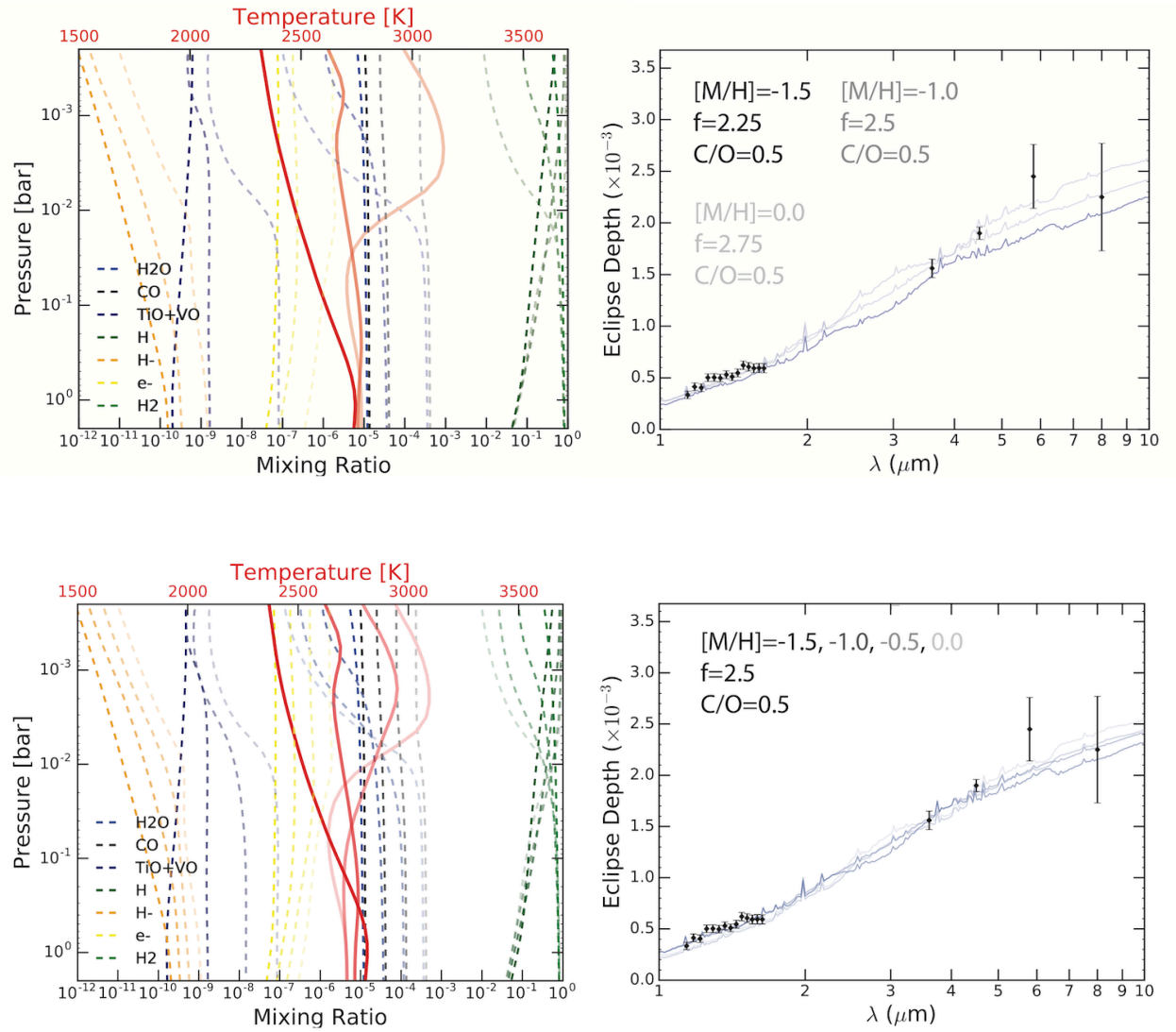

Figure 2.9: Changes in the emission spectra and T-P profiles of the 1D models as a function of the metallicity ([M/H]) and heat redistribution (f). All of the T-P profiles and mixing ratios in the left panels are set up in the same manner as in Figure 2.6, with the shades of each line corresponding to the dark, middle, and light spectra shown in the right panels. The top panels show that increasing both [M/H] and f simultaneously produces the same temperature in the lower atmosphere. The bottom panels show how at higher [M/H] the inversion gets stronger and emission features begin to appear. The emission features are most apparent at high metallicities between $2 - 4$ μm.

described as a blackbody and that has a constant geometric albedo across all wavelengths. For such a planet, the flux from the planet can be described by

$$\frac{F_p}{F_s} = A_g \left(\frac{R_p}{a}\right)^2 + \frac{B_\lambda(T_d)}{F_{s,ph}} \left(\frac{R_p}{R_s}\right)^2 \tag{2.2}$$

where $\frac{F_p}{F_s}$ is the planet-to-star flux ratio, A_g is the geometric albedo, R_p is the planet radius, R_s is the stellar radius, a is the distance between the planet and star, $B_\lambda(T_d)$ is the blackbody flux at the planetary dayside temperature T_d, and $F_{s,ph}$ is the stellar flux in each bandpass [141]. $F_{s,ph}$ was determined by interpolating between Phoenix models [128] using the Python package `pysynphot` to obtain a model with $T = 6441\,\mathrm{K}$, $\log(g) = 4.02\,\mathrm{cm\ s^{-2}}$, and $[\mathrm{Fe/H}] = 0.15$, which are the stellar parameters for HAT-P-7 [300]. For this model, $B_\lambda(T_d)$ and $F_{s,ph}$ were both integrated over the bandpasses of the data.

We fit this model to a combined data set including our WFC3 data and the *Spitzer* and *Kepler* data from Wong et al. [323] using the `emcee` Python package [82]. The free parameters in this fit were the geometric albedo A_g and the planetary dayside temperature T_d. This fit is shown by the green line in Figure 2.4. We found HAT-P-7b to have a geometric albedo of $A_g = 0.077 \pm 0.006$ and a dayside temperature of $T_d = 2654 \pm 17\,\mathrm{K}$. The albedo and dayside temperature are correlated, but well constrained by the combined data set because the infrared data, and the *Spitzer* data in particular, are primarily sensitive to the temperature, while the *Kepler* data add sensitivity to the reflected light. This estimate of the albedo is fairly consistent with previous estimates of HAT-P-7b's albedo [44, 216, 323].

Because the geometric albedo is a function of wavelength, it could be different in the *Kepler* and WFC3 bandpasses. To ensure that fitting with a single geometric albedo was valid, we also performed a fit to the WFC3 and *Spitzer* data including only thermal emission. This fit had a best-fit temperature of $T_d = 2692 \pm 14\,\mathrm{K}$. We found through an F test that including an albedo parameter does not significantly improve the fit at these wavelengths longer than 1 μm. Therefore, the WFC3 and *Spitzer* data can be fit well by a single-

temperature blackbody, and the albedo is constrained primarily by the planet-to-star flux in the *Kepler* bandpass. Contrary to what Keating & Cowan [141] found for WASP-43b, the contribution of reflected light in the WFC3 bandpass is insignificant for HAT-P-7b.

Although we found that HAT-P-7b has a low albedo, Sudarsky et al. [285] suggest that very hot giant planets with effective temperatures over 1500 K should have high albedos, as they should have silicate clouds forming high in their atmospheres. For example, $MgSiO_3$ should condense at a pressure of about 0.3 bar [285]. However, both our 3D and 1D models of HAT-P-7b predict the presence of TiO/VO high in its atmosphere, at pressures around 0.1-0.001 bar. The presence of such strong optical absorbers above the hypothesized silicate cloud deck could explain the low albedo that we observe.

Assuming that the planetary Bond albedo is equal to its geometric albedo, we can use the simple thermal and reflected light fit to calculate the heat redistribution across the surface of the planet. The heat redistribution is given by the equation

$$T_d = T_0(1 - A_B)^{1/4} \left(\frac{2}{3} - \frac{5}{12}\epsilon\right)^{1/4} \tag{2.3}$$

where $T_0 = T_s\sqrt{\frac{R_s}{a}}$ is the irradiation temperature, T_s is the stellar temperature, A_B is the Bond albedo, and ϵ is the redistribution efficiency [260]. ϵ is the inverse of the parameter f used in our 1D modeling, so smaller values of ϵ indicate less efficient heat redistribution. Using this equation, we find that the redistribution is $\epsilon = 0.38 \pm 0.11$, which indicates that HAT-P-7b has very inefficient heat redistribution.

2.3 Discussion

1D grid modeling of the spectrum of HAT-P-7b suggests that the atmosphere contains a thermal inversion, and constrains the metallicity ($[M/H] = -0.87^{+0.38}_{-0.34}$) and carbon-to-oxygen ratio ($C/O < 1$ at 99% confidence). The new self-consistent 1D model developed in this paper, which assumes thermochemical and radiative-convective equilibrium, allows measure-

ment of the atmospheric metallicity even though no molecular features are directly observed because of the effect of metallicity on the strength of the inversion. Figure 2.10 shows the atmospheric metallicity as a function of planet mass for solar system planets [325, 80, 139, 277] and exoplanets. The exoplanet measurements plotted in Figure 2.10 are based on either water abundances (red points) or the new self-consistent modeling developed in this paper (blue points). The exoplanet data plotted in this figure, and their sources, are listed in Table 2.2. The inferred metallicity of HAT-P-7b is well below the metallicity predicted by the trend in Figure 2.10. The low metallicity of HAT-P-7b could just be due to the expected intrinsic scatter around this trend [84]. Alternatively, Madhusudhan et al. [186] predicted that sub-solar oxygen and carbon abundances could indicate a planet that formed farther away from its star and then underwent disk-free migration. They also predicted that planets which formed in this manner would have super-solar C/O ratios. Our upper limit on the C/O for HAT-P-7b does not definitively reveal whether its C/O ratio is super- or sub-solar, so more observations will be necessary to determine whether this theory can explain its low metallicity. This new modeling has the potential to reveal the compositions of other planets with blackbody-like spectra, such as WASP-12b [287].

The 1D modeling also strongly constrains the dayside temperature because the atmosphere is almost isothermal over the bandpass observed by *HST* and *Spitzer*, and shows that HAT-P-7b has very poor heat redistribution. This agrees with a simple model of combined emitted and reflected light, which also shows that HAT-P-7b has a high dayside temperature, weak heat redistribution, and a low albedo. This is also in agreement with previous *Spitzer* phase curves of HAT-P-7b, which showed that the planet had a hot dayside with $T = 2667 \pm 57\,\mathrm{K}$, a very low albedo, and weak heat redistribution [323]. The weak heat redistribution predicted by these models fits the general trend that has been observed that planets at higher irradiation temperatures have less efficient heat redistribution, and therefore warmer daysides [260].

Although the 1D modeling indicates that HAT-P-7b has a thermal inversion due to

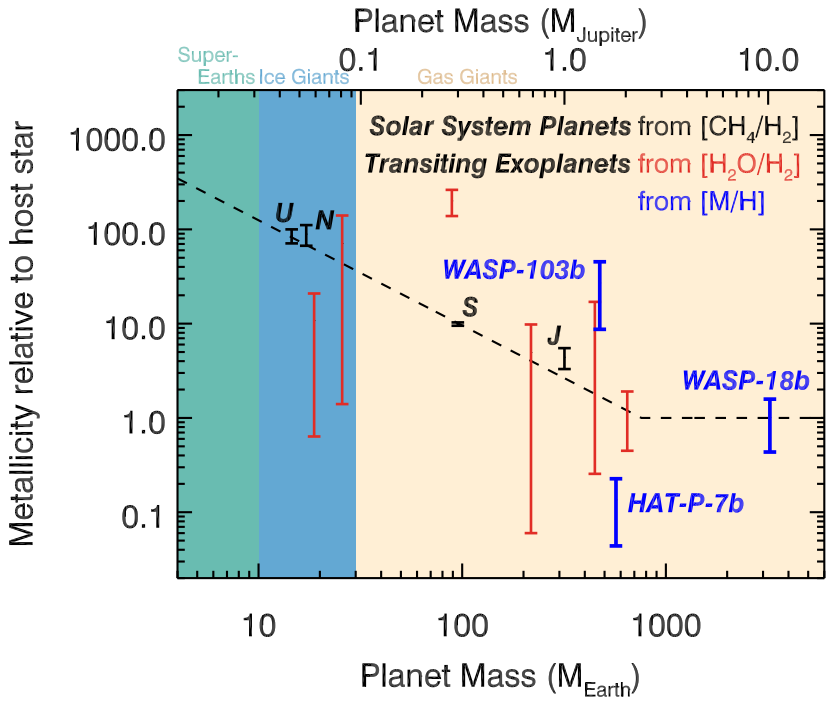

Figure 2.10: Trend in atmospheric metallicity vs. mass for solar system planets [black points, 325, 80, 139, 277] and exoplanets with visible water features (red points, see Table 2.2). Blue points show results for planets without clear molecular detections, for which the metallicities have been determined using the new self-consistent modeling developed in this paper and in Arcangeli et al. [6]. The black dotted line is a fit to the values for the solar system planets, but plateauing at 1 once the planet metallicity equals the stellar metallicity.

Table 2.2: Exoplanet mass and metallicity data plotted in Figure 2.10

Name	Planet Mass (M_{jup})	Source	Planet Metallicity ($\times$ solar, 1σ range)	Source	Stellar Metallicity ([M/H] or [Fe/H])	Source
HAT-P-7b[a]	1.78	Pál et al. [227]	$0.06 - 0.3$	this work	0.15 ± 0.08	Torres et al. [300]
HAT-P-11b[b]	0.081	Bakos et al. [9]	$3.0 - 300$	Fraine et al. [85]	0.33 ± 0.07	Torres et al. [300]
HAT-P-26b[b]	0.059	Hartman et al. [111]	$0.8 - 26.3$	Wakeford et al. [316]	0.10 ± 0.08	Torres et al. [300]
HD 209458b	0.69	Torres et al. [301]	$0.06 - 9.8$[b] $0.1 - 1.0$[c]	Line et al. [175] Brogi et al. [30]	0.00 ± 0.05	Torres et al. [301]
WASP-12b[b]	1.41	Hebb et al. [113]	$0.3 - 20.0$	Kreidberg et al. [162]	0.07 ± 0.07	Torres et al. [300]
WASP-18b[a]	10.2	Triaud et al. [303]	$0.6 - 2.0$	Arcangeli et al. [6]	0.11 ± 0.07	Torres et al. [300]
WASP-39b[b]	0.28	Faedi et al. [74]	$105 - 199$	Wakeford et al. [317]	-0.12 ± 0.10	Faedi et al. [74]
WASP-43b	2.03	Gillon et al. [97]	$0.4 - 1.7$[b] $0.3 - 1.7$[d]	Stevenson et al. [283]	-0.05 ± 0.17	Hellier et al. [114]
WASP-103b[a]	1.49	Gillon et al. [98]	$10 - 53$	Kreidberg et al. [163]	0.06 ± 0.13	Gillon et al. [98]

[a]From self-consistent modeling
[b]From H_2O detection
[c]From low-resolution + high-resolution spectroscopy
[d]From CO + CO_2

absorption by TiO/VO, this inversion is not definitively observed because the data can be well-fit by a blackbody with $T = 2692 \pm 14\,\mathrm{K}$. The best-fitting 1D model suggests that the atmosphere does contain a thermal inversion, and that the WFC3 and *Spitzer* data sample a part of the atmosphere near the tropopause where the T-P profile switches from non-inverted to inverted. In this region, the contribution functions are wide relative to the scale of the changes in the T-P profile, so the observations all appear to probe regions of similar temperatures and produce a featureless spectrum. However, this case can not be distinguished from a completely isothermal atmosphere. Even our model does not return a perfectly isothermal atmosphere, and it is possible that there are spectral features in the WFC3 bandpass below our level of precision. The WFC3 spectrum of WASP-18b, which has a signal-to-noise nearly four times that of our spectrum, shows some subtle emission features, and so a higher-precision spectrum of HAT-P-7b may reveal a similar structure [6].

The 1D modeling also indicates that the blackbody-like spectrum of HAT-P-7b is produced because we are probing a range of pressures in the atmosphere, all of which have similar temperatures, and not just because only one pressure level is probed at all wavelengths. However, water dissociation in the upper atmosphere does limit the range of pressures probed. Other similar hot planets, like WASP-18b and WASP-103b, display muted spectral features in the WFC3 bandpass because of water dissociation and H^- opacity [6, 163, 233].

We also modeled the spectrum of HAT-P-7b with a 3D GCM. However, the GCM is unable to precisely reproduce the observed spectrum. Both the solar composition and the low-metallicity GCMs are colder on the dayside than the data suggest, which could be due to increased Lorentz forces causing more drag in the atmosphere or nightside clouds warming the planet. Additionally, the modeled spectra appear to have small emission features, which do not match the observed blackbody-like spectrum. In order to understand the cause of this discrepancy between the 3D GCM and the data for very hot planets like HAT-P-7b, more spectroscopic data are required over wider wavelength ranges and a larger parameter space exploration of parameters such as metallicity and Ti/O ratio in the GCM is needed.

Overall, the large dayside temperature of HAT-P-7b is extremely puzzling as the very low heat redistribution it implies cannot be reproduced by current GCMs. More observations and theoretical work are needed to understand what causes such a poor energy redistribution. Additionally, because our observations did not reveal any spectral features, further observations will be necessary to confirm the low value of the planet's metallicity. The *James Webb Space Telescope* (*JWST*) will have the ability to spectroscopically observe thermal emission of transiting planets over a large wavelength range. Spectroscopic observations of thermal emission with *JWST* at the wavelengths covered by *Spitzer*, where the GCM models for HAT-P-7b show the largest differences from each other, could resolve the discrepancy between the GCM and the observations. High-resolution spectroscopy [274] could also aid in understanding the thermal structure of HAT-P-7b by directly detecting the TiO responsible for the thermal inversion, as Nugroho et al. [221] did for WASP-33b. Additionally, phase curves taken using *JWST* or the *Atmospheric Remote-sensing Exoplanet Large-survey* [*ARIEL*, 298] could determine if nightside clouds are responsible for heating the dayside to temperatures above those predicted by the GCM.

CHAPTER 3

EVIDENCE FOR H_2 DISSOCIATION AND RECOMBINATION HEAT TRANSPORT IN THE ATMOSPHERE OF KELT-9B

As described in the previous chapter, the atmospheres of ultra-hot Jupiters are expected to undergo molecular dissociation, which can significantly influence heat transport throughout their atmospheres [233]. In particular, H_2 dissociates into hydrogen atoms on their daysides and recombines near the terminator [22, 155, 230]. This process is predicted to distribute significant energy in a manner similar to latent cooling from water evaporation, with heat deposited in the regions where H recombines into H_2 [22]. Such heat redistribution should lead to smaller phase curve amplitudes [22, 155]. H_2 dissociation also provides a source of hydrogen atoms for the production of H^-, which is an important opacity source for ultra-hot Jupiters [6].

In order to test predictions for energy transport in ultra-hot Jupiters, we present a phase curve of the transiting planet KELT-9b observed with the *Spitzer Space Telescope* at 4.5 μm[1]. KELT-9b is the hottest known planet, with a dayside temperature of $\sim$ 4500 K [94]. This ultra-hot planet has been shown previously to contain neutral and ionized metals [120, 121], and it is predicted to be heavily influenced by H_2 dissociation/recombination [22, 155, 146, 178]. It is also predicted to be too hot for clouds to form, even on the nightside, which simplifies potential interpretations of its phase curve [146]. We describe our observations and data reduction process in Section 3.1. We compare our observations to a set of general

1. This chapter is based on Mansfield et al. [200], which was coauthored by Jacob L. Bean, Kevin B. Stevenson, Thaddeus D. Komacek, Taylor J. Bell, Xianyu Tan, Matej Malik, Thomas G. Beatty, Ian Wong, Nicolas B. Cowan, Lisa Dang, Jean-Michel Désert, Jonathan J. Fortney, B. Scott Gaudi, Dylan Keating, Eliza M.-R. Kempton, Laura Kreidberg, Michael R. Line, Vivien Parmentier, Keivan G. Stassun, Mark R. Swain, and Robert T. Zellem. M. Mansfield reduced and analyzed the data presented in this chapter and led the data-model comparison. J. L. Bean is PI of the *Spitzer* program 14059 which obtained the observations of KELT-9b. K. B. Stevenson assisted in data reduction. T. D. Komacek and X. Tan created the 3D GCMs described in Section 3.2. T. J. Bell created the energy balance model described in Section 3.3. M. Malik created the 1D models used in Figure 3.7. T. G. Beatty and D. Keating performed independent data reductions to test the dependence of the results on the reduction method. I. Wong identified the periodic stellar signal discussed in Section 3.1. All other authors are co-Is on *Spitzer* program 14059

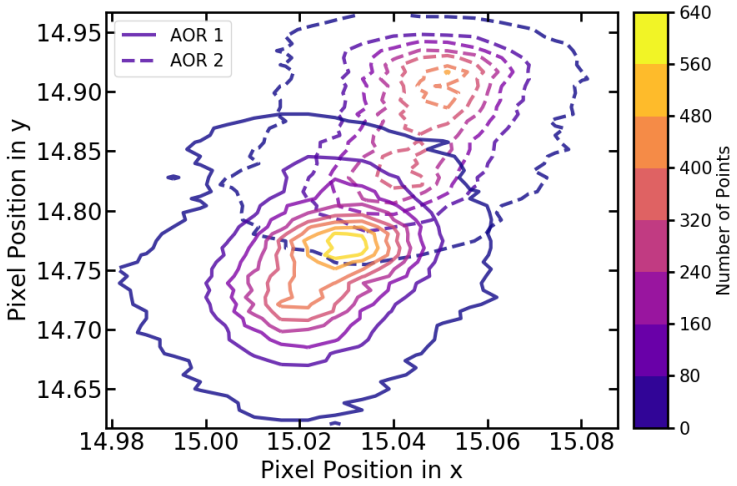

Figure 3.1: Contour plots showing the pointing in each of the two AORs. AOR 1 is in solid contours and AOR 2 is in dashed contours. The two pointings overlap significantly, allowing construction of an accurate pixel sensitivity map spanning the entire observation period.

circulation models (GCMs) in Section 3.2 and energy balance models in Section 3.3. We discuss our results in Section 3.4.

3.1 Observations and Data Reduction

We observed a single phase curve of KELT-9b with the InfraRed Array Camera (IRAC) at 4.5 μm on October 22-24, 2018 as part of a Cycle 14 large program (program ID: 14059). We used the subarray mode with 0.4-second frame times. Before beginning science observations, we performed a standard 30-minute pre-observation using the PCRS peak-up to mitigate spacecraft drift. Science observations were divided into two contiguous astronomical observation requests (AORs), which lasted for 22.3 and 18.6 hr, respectively. The two AORs had significant overlap in pointing, as shown in Figure 3.1, and this observation had the most stable pointing overall of the nine phase curves observed to date in program 14059. A total of 371,392 frames were observed. We chose not to analyze the 30-minute pre-observation because it fell on a region of the detector that has little overlap with the two science AORs.

We reduced the data using the Photometry for Orbits, Eclipses, and Transits (POET) pipeline [37, 281, 52]. We tested a range of fixed and variable aperture sizes [169] and found

the smallest scatter was achieved with a fixed circular aperture with a radius of 2.5 pixels. We binned sets of 4 images together for the data reduction because we found that this is the smallest bin size that produces a strong constraint on the Point Response Function Full Width at Half-Maximum (PRF FWHM). We modeled position-dependent systematics using Bilinearly Interpolated Subpixel Sensitivity (BLISS) mapping with a step size of 0.006 pixels [281]. The BLISS map is shown in Figure 3.2. We also decorrelated against the PRF FWHM, as this has been recently shown to improve the fit quality [210]. We tested models with linear, quadratic, and cubic dependences on the PRF FWHM in both the x and y directions, as well as a model without this dependency, and found that a linear model in both directions provides the preferred solution as determined by the Bayesian Information Criterion (BIC)[2]. Additionally, we modeled a long-term linear trend over the entire phase curve. We tested a quadratic long-term trend and found that the linear trend is favored, with a ΔBIC= 8. Figure 3.3 shows the trends over time of the parameters we decorrelate against.

We modeled the phase-dependent emission of KELT-9b using a two-term sinusoid of the form

$$F_p = A_1 \cos\left[\frac{2\pi(t-t_1)}{p}\right] + A_2 \cos\left[\frac{4\pi(t-t_2)}{p}\right], \tag{3.1}$$

where t is time, $p = 1.4811$ d is the orbital period, and A_1, A_2, t_1, and t_2 are free parameters. The second sinusoid allows a fit to an asymmetric phase curve and has been used to model several other phase curves [e.g., 148, 283]. We tested models using one or three sinusoids, but found a model with two sinusoids is preferred with a ΔBIC= 8 compared to a one-term model and a ΔBIC= 21 compared to a three-term model. This test gives us additional confidence in our analysis because third-order harmonics should not exist on a static map [48] We additionally tested for the presence of ellipsoidal variations by fixing the offset t_2 to a time chosen such that the sinusoid has maxima at quadrature and minima at transit

2. The usefulness of the BIC is limited in this case because BLISS mapping involves several free parameters that are not counted, but the ΔBIC can still be used to differentiate between models with different numbers of parameters.

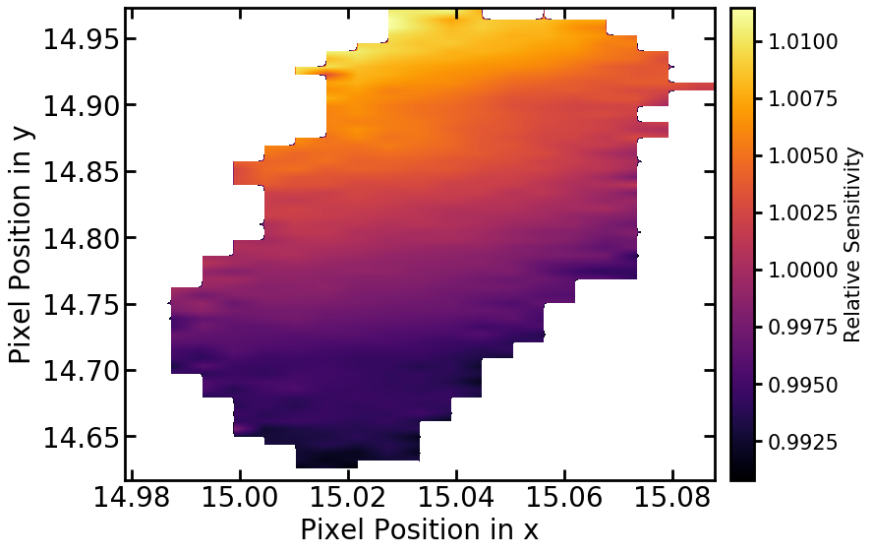

Figure 3.2: BLISS map illustrating the position-dependent pixel sensitivity. Yellow (purple) colors indicate regions of the pixel that are more (less) sensitive. Sensitivity drops with distance from the pixel center at (15.0,15.0), as expected.

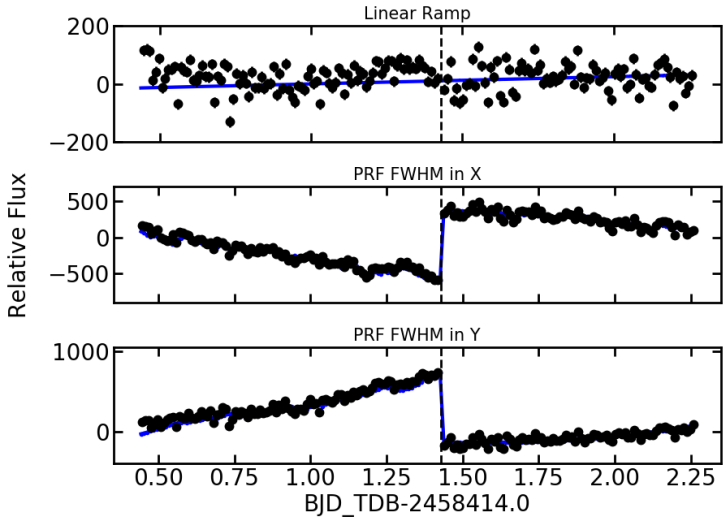

Figure 3.3: Trends over time of the main parameters we decorrelate against: a long-term linear ramp (top) and the PRF FWHM in the x (middle) and y (bottom) directions. Blue lines show the best-fit models, and black points show the data. The data were binned into sets of 4 frames for the analysis, but for clarity the data here and in the other figures in this chapter are shown binned into 180 bins of 2037 frames each ($\approx$ 15 min/bin). The vertical dashed line indicates the break between the two AORs, where a slight change in telescope pointing causes a jump in the PRF FWHM.

and eclipse [269]. We found no evidence for ellipsoidal variations above the noise level of the observations, and so left t_2 as a free parameter in the final fit. We fit the transit and eclipses using the model of Mandel & Agol [194], and used a linear model of stellar limb darkening during the transit.

Wong et al. [324] found an additional periodicity in *TESS* phase curves of KELT-9b with a period of ≈ 7.6 hr and semi-amplitude of 117 ppm, which they attribute to stellar pulsations. We confirm the presence of this periodicity through a periodogram analysis of the residuals to our fit. We therefore include a model for this periodicity in our analysis using the equation

$$F_* = 1 + \alpha \sin\left[\frac{2\pi(t - T_0)}{\Pi}\right] + \beta \cos\left[\frac{2\pi(t - T_0)}{\Pi}\right], \tag{3.2}$$

where T_0 is the transit midpoint and α, β, and Π are free parameters. We find that including these pulsations has an almost negligible influence on our fitted phase curve parameters, which is not surprising because the planet's thermal emission at these infrared wavelengths is more than ten times larger than the stellar pulsation signal. Nevertheless, we retrieve a period and amplitude for the signal consistent with that of Wong et al. [324], and including it in our model removes some of the correlated noise present in the raw phase curve.

We estimated the parameters using a Differential Evolution Markov Chain Monte Carlo (MCMC) fit [293] with uniform priors for all parameters. Figure 3.4 shows a pairs plot from the MCMC fit and Table 3.1 lists the values of all fitted parameters. The data exhibit time-correlated noise, so we followed the red noise correction procedure of Diamond-Lowe et al. [57] and included this effect in our uncertainty estimates using the wavelet analysis described by Carter & Winn [39]. We initially fit for the γ parameter described in Carter & Winn [39], and then in the final MCMC fixed it to the best-fit value of $\gamma = 0.58$.

The detrended phase curve is shown in Figure 3.5. The RMS of the residuals when binning the data into 180 points (≈ 15 min/bin) is 118 ppm, and the photon noise is 60 ppm.

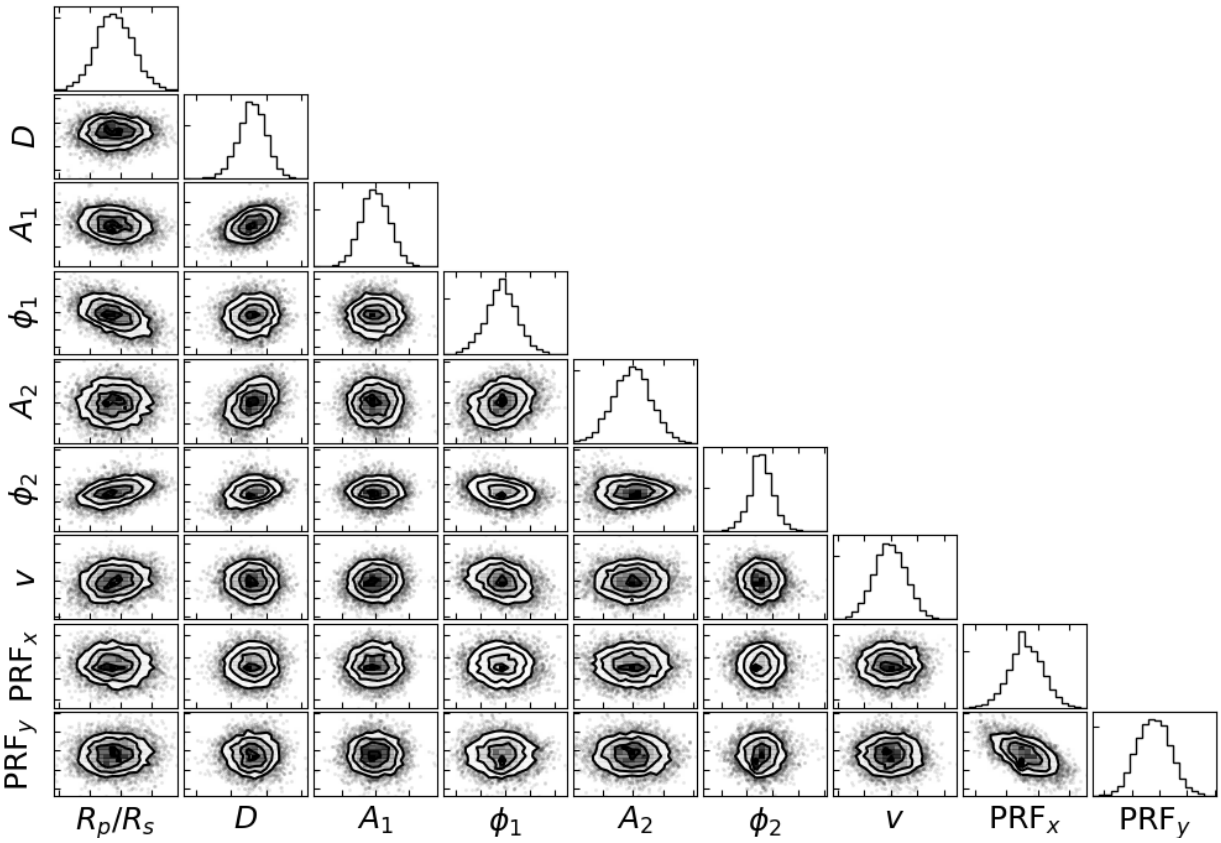

Figure 3.4: Pairs plot showing the key parameters we fit for in the phase curve of KELT-9b. Parameter abbreviations are defined in Table 3.1 and Equation 3.1.

Fitted Parameters	**Value**
Transit Midpoint [$\mathrm{BJD_{TDB}}$]	2458415.36261(16)
R_p/R_s	0.08004(41)
Linear Limb Darkening, u_1	0.203(23)
Eclipse 1 Midpoint [$\mathrm{BJD_{TDB}}$]	2458414.62237(32)
Eclipse 2 Midpoint [$\mathrm{BJD_{TDB}}$]	2458416.10367(37)
Eclipse Duration, T_{14} [days]	0.16255(47)
Eclipse Depth, D [%]	0.3131(62)
A_1 [ppm]	975(32)
t_1 [$\mathrm{BJD_{TDB}}$]	2458414.5544(90)
A_2 [ppm]	89(22)
t_2 [$\mathrm{BJD_{TDB}}$]	2458414.555(33)
α [ppm]	0(7)
β [ppm]	$-140(20)$
Π [hr]	7.56(0.13)
Linear Ramp, v [ppm/day]	157(36)
Linear Fit to x PRF FWHM, PRF_x	$-0.1143(43)$
Linear Fit to y PRF FWHM, PRF_y	0.0451(51)
Derived Parameters	**Value**
Phase Curve Amplitude, A	0.609 ± 0.020
Phase Offset [°]	$18.7^{+2.1}_{-2.3}$
Dayside Brightness Temperature, T_{day} [K]	4566^{+140}_{-136}
Hottest Hemisphere Brightness Temperature [K]	4636^{+145}_{-138}
Nightside Brightness Temperature, T_{night} [K]	2556^{+101}_{-97}
Day-Night Temperature Contrast, A_T	$0.440^{+0.017}_{-0.016}$

Table 3.1: Best-fit values and errors on all free parameters in the final fit and physical parameters derived from the fit. Numbers in parentheses give 1σ uncertainties on the least significant digits. Errors on derived temperatures incorporate the error in the stellar temperatures.

Table 3.1 lists several parameters derived from the phase curve, including the dayside and nightside brightness temperatures (4566^{+140}_{-136} K and 2556^{+101}_{-97} K, respectively), which were derived using PHOENIX models for the star [128]. The error on our derived temperatures incorporates the relatively large error on the stellar effective temperature of KELT-9 [$T_{\rm eff} = 10170 \pm 450$ K, 94]. The dayside temperature we observe at 4.5 μm is consistent with the temperature of 4600 ± 150 K observed in the z' band [94], which is expected from some 1D models of KELT-9b's atmosphere given the measurement uncertainties [192]. We also derived a day-night temperature contrast of

$$A_T = \frac{T_{\rm day} - T_{\rm night}}{T_{\rm day}} = 0.440^{+0.017}_{-0.016}, \tag{3.3}$$

an amplitude of

$$A = \frac{F_{max} - F_{min}}{F_{max}} = 0.609 \pm 0.020, \tag{3.4}$$

and a phase offset of $18.7^{+2.1}_{-2.3}{}^{\circ}$.

To ensure the robustness of our results, we tested analyzing the two AORs separately and analyzing a phase curve with the bump in the data at $\mathrm{BJD_{TDB}} \approx 2458415.8$ d masked out, and in all cases derived phase offsets and amplitudes that were consistent to within 1σ. These data were also analyzed independently by T. Beatty and D. Keating to test for dependence on the data reduction method. The resulting amplitudes and phase offsets agreed within 1.5σ. A combined analysis of these data with a *Spitzer* 3.6 μm phase curve of KELT-9b will be presented in a future paper (T. Beatty et al. in prep.).

3.2 Comparison to General Circulation Models

We used the GCM of Tan & Komacek [289] to compare the phase curve to numerical predictions. This GCM includes the effects of cooling due to dissociation of molecular hydrogen and heating from recombination of atomic hydrogen, along with changes in the specific heat and specific gas constant due to H_2 dissociation/recombination. The dynamical core of the

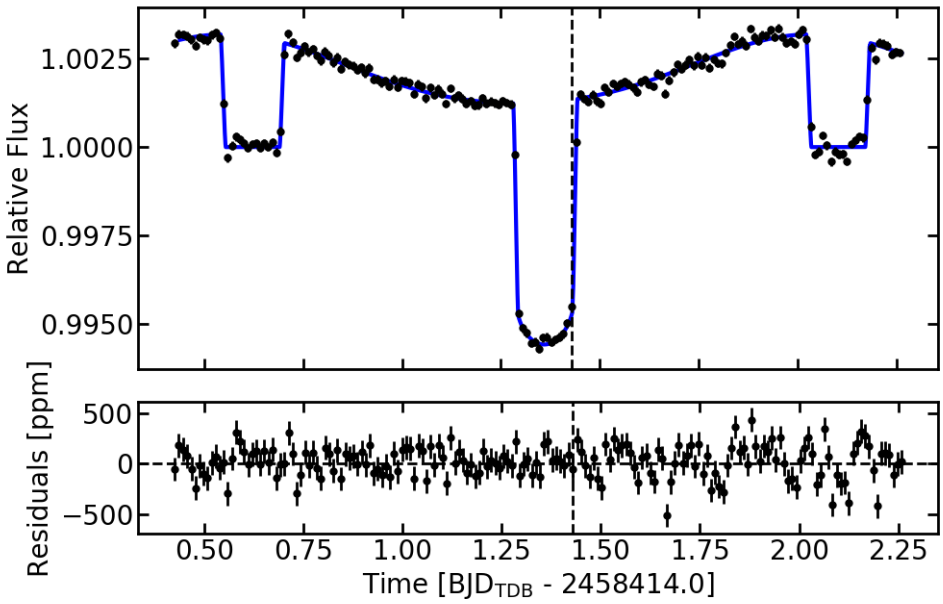

Figure 3.5: Phase curve of KELT-9b (black points) and best-fit model (blue line). The dashed vertical line shows the break between the two AORs. The lower panel shows residuals to the model fit. The RMS of the residuals at this binning is 118 ppm, and the photon noise is 60 ppm.

MITgcm solves the primitive equations of motion on a cubed-sphere grid [2]. We used a double-grey approximation, with one visible and one infrared band in the radiative transfer calculation [153], the opacity of which depends on pressure alone[3]. This opacity profile is the same as used in [289]. We use this simplified opacity profile for our idealized model because relevant opacities have not been calculated exactly at the temperature of KELT-9b [87] and our GCM setup is unable to fully capture dayside-to-nightside opacity differences. We used 192 grid points in longitude and 96 in latitude, with 50 vertical levels evenly spaced in log-pressure from 1 mbar to 100 bars. We chose a model top of 1 mbar because the pressure-dependent double-grey opacity scheme used in the GCM does not apply at low pressures [244]. We fix the stellar $T_{\rm eff}$, a/R_*, and R_p/R_* to the values from Gaudi et al. [94].

3. The thermal opacity profile is $\log_{10}\kappa_{\rm th} = 0.0498(\log_{10}p)^2 - 0.1329\log_{10}p - 2.9457$ and the visible opacity profile is $\log_{10}\kappa_{\rm v} = 0.0478(\log_{10}p)^2 - 0.1366\log_{10}p - 3.2095$, with opacity in units of $\mathrm{m^2kg^{-1}}$ and pressure is in units of Pa.

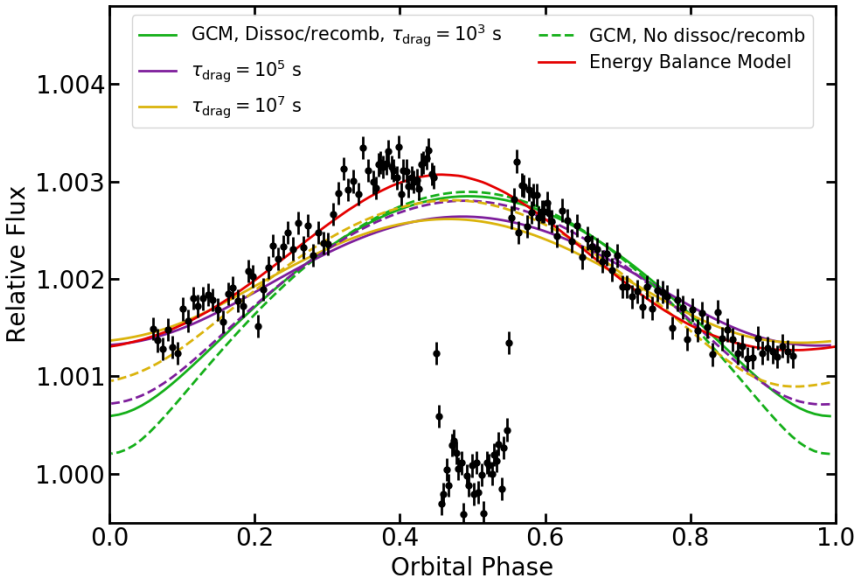

Figure 3.6: Phase-folded phase curve of KELT-9b (black data points). The transit at phases of 0 and 1 is omitted to better show the phase variation. Green, purple, and gold lines show GCMs with drag timescales of 10^3, 10^5, and 10^7 seconds, respectively (Section 3.2). Solid and dashed lines indicate GCMs with and without the effects of H_2 dissociation and recombination, respectively. The red line shows the EBM including the effects of H_2 dissociation and recombination (Section 3.3).

We performed multiple GCM experiments with varying frictional drag to crudely represent magnetic effects [235, 245, 249] and/or large-scale turbulence [329, 88]. We used a Rayleigh drag that is linear in wind speed, $f_{\rm drag} = -\mathbf{u}/\tau_{\rm drag}$, where $\mathbf{u}$ is velocity and $\tau_{\rm drag}$ is the frictional drag timescale. We considered a broad range of frictional drag timescales $\tau_{\rm drag} = 10^3, 10^5, 10^7$ s, to represent the unknown dipolar magnetic field strength [326] and/or length-scale of instabilities [151]. Frictional drag begins to strongly affect the circulation for $\tau_{\rm drag} \lesssim 10^5$ s [153], while $\tau_{\rm drag} = 10^7$ s represents very weak drag. For each assumed drag timescale, we ran GCM experiments both including and not including the effects of H_2 dissociation, resulting in six separate GCM experiments. Our simulations with weak drag have an eastward equatorial jet, while our simulations with strong drag have day-to-night flow at photospheric levels. We compare the simulated phase curves to the observations in Figure 3.6.

We compare our observations to the models using the derived amplitude listed in Ta-

ble 3.1. The observed low amplitude $A = 0.609 \pm 0.020$ indicates significant heat redistribution from the hot dayside. Overall, we find that simulations including the impact of H_2 dissociation/recombination and with relatively weak drag provide a better match to the phase curve amplitude, while those without H_2 dissociation/recombination and/or with strong drag predict too-large amplitudes and too-cold nightsides.

Recent work has suggested that, in many cases, differences in opacity on the day- and nightsides of hot Jupiters may lead to different pressures being probed through the phase curve in the 4.5 μm bandpass [58]. This can complicate an otherwise straightforward determination of the amount of heat transport in the atmosphere, because the observed day-night temperature contrast may be partially due to the changing photospheric pressure. To determine the impact this could have on our measurements, we modeled the dayside and nightside emission using the 1D radiative transfer code HELIOS [192]. We used dayside and nightside temperature-pressure (T-P) profiles from the GCM run with $\tau_{\rm drag} = 10^7$ and including the effects of H_2 dissociation/recombination. Figure 3.7 shows the contribution functions for the *Spitzer* bandpass using these T-P profiles. We found that the 4.5 μm photosphere was at a pressure of ≈ 10 mbar on both the dayside and the nightside. Since the dayside and nightside 4.5 μm photospheres are at approximately the same pressure, the temperature difference we observe is primarily due to horizontal heat transport.

We also observe a large phase offset of $18.7^{+2.1}_{-2.3}{}^\circ$. While the GCM experiments including H_2 dissociation and recombination are able to explain the small amplitude of the phase curve, none of the simulations predict the large offset we observe. The simulations predict an offset of no more than 5°, which is inconsistent with our observations at $> 5\sigma$ confidence.

3.3 Comparison to Energy Balance Models

As a second test of the impact of H_2 dissociation and recombination on the phase curve of KELT-9b, we compare our findings to the open source `Bell_EBM`[4] energy balance model

4. `https://github.com/taylorbell57/Bell_EBM`

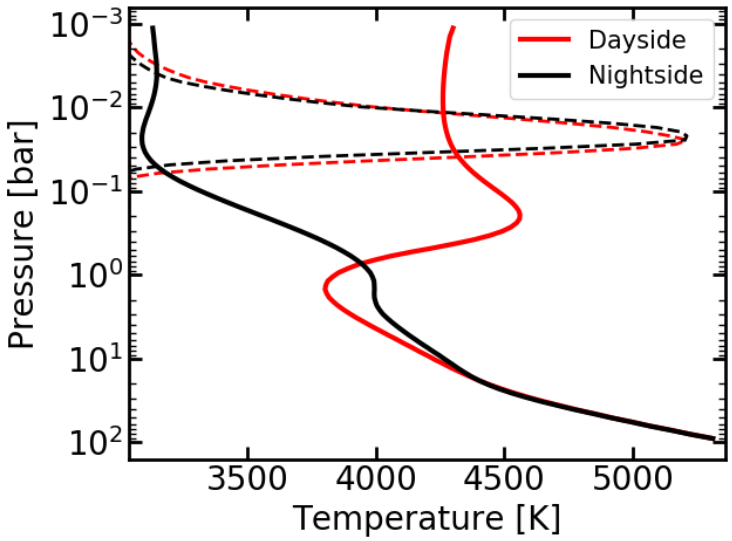

Figure 3.7: Temperature-pressure profiles from the GCM run with $\tau_{\rm drag} = 10^7$ and including the effects of H_2 dissociation. The dayside and nightside averaged profiles are shown in red and black, respectively. Dashed lines show contribution functions for the center of the *Spitzer* 4.5 μm bandpass from 1D modeling using HELIOS [192]. The photosphere is at $\sim$ 10 mbar on both the day- and nightsides.

[EBM, 22]. We use this analytic model in addition to the GCM because it allows us to perform a fit to the data and retrieve parameters that can be compared for models with and without H_2 dissociation/recombination. The EBM was fit to the phase curve using the MCMC package `emcee` [82]. In order to allow convergence in a reasonable time frame, we fixed the 4.5 μm reference pressure to $P_0 = 0.1$ bar and fixed the stellar $T_{\rm eff}$, a/R_*, and R_p/R_* to the values from Gaudi et al. [94]. We use $P_0 = 0.1$ bar because it is the approximate depth at which heat is deposited and re-radiated and because longer convergence times at lower pressures mean that it is unfeasible to run even a simplified EBM fit at lower pressures. We fit for the wind speed in the planet's rotating reference frame (v_{wind}) and the planet's Bond albedo (A_B). To convert the planet's temperature map into a light curve, we used a 4.5 μm stellar brightness temperature of 8287 K found using a PHOENIX stellar model with $T_{\rm eff} = 10200$ K [128].

Our initial fits showed that the EBM was generally able to recover the phase offset and amplitude of the phase curve, but the fitted phase curve was too sharply peaked which re-

sulted in an overall poor fit. To improve the fit, we considered another model including a deep redistribution term that redistributes some fraction of the absorbed stellar flux uniformly around the planet. This term mimics the deeper layers (below ∼10 bars) of GCMs which are nearly longitudinally isothermal as the radiative timescale increases rapidly with depth [e.g., 267, 244]. This parameter allowed the EBM to fit the data well with a reduced chi-squared of 1.4 for a model with ≈ 21 % of the absorbed flux redistributed uniformly. The best-fit EBM is shown in Figure 3.6.

The model including the effects of H_2 dissociation and recombination gives a $v_{\rm wind}$ of 6.1 $\mathrm{km\,s^{-1}}$, which is on the same order of magnitude as expected for typical ultra-hot Jupiters and is similar to the ≈ 5 km wind speed in our GCM [151] . Meanwhile, neglecting the effects of H_2 dissociation/recombination requires an unphysically high wind speed of 67 $\mathrm{km\,s^{-1}}$ to explain the observed heat redistribution, which is further evidence of the impact of H_2 chemistry on the planet's circulation. The model also gives an albedo of 0.195 ± 0.010, which is similar to derived Bond albedos for other ultra-hot Jupiters [261, 331, 163].

3.4 Discussion

The most striking result from the KELT-9b phase curve is the small amplitude, which shows the influence of H_2 dissociation/recombination on this planet. Recent work accounting for H_2 dissociation/recombination has demonstrated that the cooling and heating from these processes can transport significant heat, leading to reduced phase curve amplitudes on the hottest ultra-hot Jupiters [22, 155]. When H_2 dissociation is not taken into account, hotter planets are expected to have less heat transport because of their shorter radiative timescales [e.g., 268, 47]. Assuming a solar composition gas and using our model photospheric pressure of $P \approx 10$ mbar, we estimate that KELT-9b has an extremely short radiative timescale of $\tau_{rad} \approx 30$ s [268]. With that short radiative timescale, and ignoring the effects of H_2 dissociation/recombination and frictional drag, the theory of [154] and [332] predicts a normalized dayside-to-nightside temperature contrast of 0.999, much greater than the observed value of

$0.440^{+0.017}_{-0.016}$. Note that including the effects of frictional drag would only act to increase the dayside-to-nightside temperature contrast [153].

This result extends the interpretation of the phase curves of WASP-33b and WASP-103b, two ultra-hot Jupiters which were previously shown to have warm nightsides [331, 163]. These two planets, which both have dayside brightness temperatures around 3000 K, were hypothesized to be impacted by H_2 dissociation/recombination [22, 155]. The extreme irradiation of KELT-9b enhances the impact of H_2 dissociation on the phase curve and provides stronger evidence for this process on ultra-hot Jupiters.

The reduced phase curve amplitude is well fit by both GCMs and the analytic EBM when the effects of H_2 dissociation/recombination are included. We find that relatively weak $\tau_{\rm drag} \geq 10^5$ s is required to match the nightside flux, but strong drag better explains the hot dayside. Additionally, none of the GCMs reproduce the large offset we observe. The large offset could be due to MHD effects that are not currently accounted for in the GCM used in this work. Future work investigating how magnetic effects influence both the phase curve offset and amplitude [e.g., 249, 250, 118] could shed light on the remaining discrepancies between the Spitzer observations and GCMs.

CHAPTER 4

A HOT JUPITER SPECTRAL SEQUENCE WITH EVIDENCE FOR COMPOSITIONAL DIVERSITY

In Chapters 2 and 3, our observations of HAT-P-7b and KELT-9b demonstrated how ultra-hot Jupiter secondary eclipse spectra and phase curves are affected by molecular dissociation in their atmospheres. The combined influences of molecular dissociation and H^- opacity provide good explanations for several other featureless *HST* secondary eclipse spectra of ultra-hot Jupiters (e,g., WASP-18b, 6; WASP-103b, 163). However, the population of ultra-hot Jupiters shows a diversity of secondary eclipse spectra which cannot be explained by molecular dissociation and H^- opacity alone. For example, WASP-121b, which has a dayside temperature of $T_{day} \approx 2650$ K, is nearly the same temperature as HAT-P-7b and yet shows subtle emission features in its secondary eclipse spectrum [211]. Kepler-13Ab, which is one of the hottest known ultra-hot Jupiters at $T_{day} \approx 3300$ K, shows signs of water absorption features [16].

In order to better understand this diversity of hot Jupiter secondary eclipse spectra, we conducted a population study of all 20 hot Jupiters which have been observed in secondary eclipse using the *HST*/WFC3 instrument between $1.1 - 1.7$ μm[1]. Similar population-level studies have been done for brown dwarfs [195] and transmission spectra of hot Jupiters [270], but there has been no unified, population-level study of the thermal emission spectra of hot Jupiters.

1. This chapter is based on a paper currently in review by Megan Mansfield, Michael R. Line, Jacob L. Bean, Jonathan J. Fortney, Vivien Parmentier, Lindsey Wiser, Eliza M.-R. Kempton, Ehsan Gharib-Nezhad, David K. Sing, Mercedes López-Morales, Claire Baxter, Jean-Michel Désert, Mark R. Swain, and Gael M. Roudier. M. Mansfield reduced and analyzed the new data presented in this chapter and led the data-model comparison. M. Mansfield is also the PI of the *HST* program GO-16168, which obtained the observations of WASP-77Ab presented in this chapter. M. R. Line created the 1D exoplanet model grids presented in Section 4.2, while the brown dwarf model grids were created by L. Wiser. E. Gharib-Nezhad generated opacities and absorption cross-sections for the 1D models. D. K. Sing and M. López-Morales are co-PIs of the *HST* program GO-14767 which obtained the observations of HAT-P-41b, KELT-7b, WASP-74b, WASP-76b, WASP-79b, and WASP-121b presented in this chapter. All other authors contributed to the interpretation of the results.

Manjavacas et al. [195] presented the spectra of 10 of the hot Jupiters in this study but did not examine in detail the physical causes for the observed spectral features. Melville et al. [209] similarly examined the spectra of 10 hot Jupiters but only analyzed them in the context of models with fixed temperature-pressure (T-P) profiles, with no feedback between the T-P profile and the chemistry. Here we expand on these studies by doubling the sample of hot Jupiter secondary eclipse spectra and comparing the spectra to a grid of models with fully consistent T-P profiles to understand in detail what drives their feature strengths. Because our models combine a set of basic self-consistent assumptions which are expected to hold true for hot Jupiters (e.g., energy balance in the atmosphere and thermochemical equilibrium [178]) with a complete set of relevant opacities, we can use them to create self-consistent predictions for hot Jupiter spectra, which can then be compared to the observed data.

There have also been several population-level studies of photometric observations taken by *Spitzer* during secondary eclipse [18, 302, 138, 335, 142, 17, 12, 93, 61]. However, because these studies focused on broadband photometry, they were only able to generally constrain hot Jupiter compositions. This study expands on those works by uniformly analyzing all *HST* thermal emission spectra and performing a more comprehensive analysis of their compositional diversity.

In Section 4.1 we describe our data reduction methods for new reductions of seven hot Jupiter spectra, as well as a reanalysis of one spectrum from the literature. In Section 4.2, we describe a grid of 1D radiative-convective-thermochemical equilibrium models we constructed to compare to the observed spectra. In Section 4.3, we combine our seven new data reductions and one reanalysis with twelve results from the literature to form a complete sample of all 20 planets observed in secondary eclipse with *HST*/WFC3+G141 between $1.1 - 1.7$ μm. Finally, we present our conclusions in Section 4.4.

Planet	*HST* Program #	Date(s) of Observation	Sampling Sequence	Exposure Time [s]	Exposures per Orbit
HAT-P-41b	14767(1) - Sing et al. [271]	10/09/16	SPARS10, NSAMP=12	81.089	19
KELT-7b	14767(1) - Sing et al. [271]	08/18/17	SPARS10, NSAMP=4	22.317	37
Kepler-13Ab	13308(2) - Zhao [333]	04/28/14, 10/13/14	SPARS10, NSAMP=3	7.624	101
WASP-74b	14767(1) - Sing et al. [271]	05/02/17	SPARS25, NSAMP=4	69.617	19
WASP-76b	14767(1) - Sing et al. [271]	11/03/16	SPARS10, NSAMP=15	103.129	19
WASP-77Ab	16168(2) - Mansfield et al. [201]	11/07/20, 12/19/20	SPARS25, NSAMP=6	89.662	18
WASP-79b	14767(1) - Sing et al. [271]	11/15/16	SPARS25, NSAMP=7	138.381	13
WASP-121b	14767(1) - Sing et al. [271], 15134(4) - Evans [73]	11/10/16-11/11/16, 03/12/18-03/13/18, 03/14/18, 02/03/19, 02/04/19	SPARS10, NSAMP=15	103.129	16

Table 4.1: Observing details for the eight planets for which new data reductions were described in Section 4.1. Numbers in parentheses next to the *HST* program number indicate the number of eclipses observed in that program. Note that the spectrum of Kepler-13Ab was observed in stare mode, while all other observations were taken in spatial scanning mode.

4.1 Data Reduction of New Secondary Eclipse Observations

We reduced and analyzed *HST*/WFC3+G141 spectra of seven planets. At the time this study was begun, these were all of the remaining secondary eclipse data sets in the *HST* archive that had not been published yet. Since we began this project, results for three planets have been published [65, 89, 211, 238]. In all of these cases, our reductions produced spectra consistent with the published results. Table 4.1 lists the details of these observations, which included single eclipses of HAT-P-41b, KELT-7b, WASP-74b, WASP-76b, and WASP-79b; two eclipses of WASP-77Ab; and five eclipses of WASP-121b.

We reduced the data using the same data reduction pipeline as was used in Chapter 2 to reduce the secondary eclipse of HAT-P-7b [161]. We used an optimal extraction procedure [122] and masked cosmic rays. To subtract the background out of each frame, we visually inspected the images to find a clear background spot on the detector and subtracted the median of this background area. The uncertainties on the measurements were determined

by adding in quadrature the photon noise, read noise, and median absolute deviation of the background.

Following standard procedure for *HST*/WFC3 eclipse observations, we discarded the first orbit of each visit. The spectra of each planet, with the exception of WASP-77Ab, were binned into 14 channels at a resolution $R \approx 30 - 40$. The observations of WASP-77Ab showed a higher signal-to-noise which allowed for finer binning, so we binned that spectrum into 19 channels with a resolution $R \approx 40 - 60$. We also created a broadband white light curve for each planet by summing the spectra over the entire wavelength range.

We fit both the white light curves and spectroscopic light curves with a model in the form

$$M(t) = E(t)(cs + vt_{vis})(1 - e^{-r_1 t_{orb} - r_2}), \tag{4.1}$$

where M(t) is the modeled flux, E(t) is an eclipse model found using `batman` [158], and the rest of the equation is a systematics model based on Berta et al. [24]. In this systematics model, c is a normalization constant, s is a scaling factor to account for an offset in normalization between scan directions, v is a visit-long linear trend, t_{vis} is the time since the beginning of the visit, r_1 and r_2 are the amplitude and time constant of an orbit-long exponential ramp, respectively, and t_{orb} is the time since the beginning of the orbit. For the white light curves, the free parameters in the eclipse model were the mid-eclipse time T_0 and the planet-to-star flux ratio F_p/F_s. For the spectroscopic light curves, the mid-eclipse time T_0 was fixed to the best-fit value from the white light curve and the only free parameter in the eclipse model was the planet-to-star flux ratio F_p/F_s.

The single eclipses observed for most of these planets had poor coverage of ingress and egress, so they could not constrain parameters such as the secondary eclipse time to the level of precision provided by previous observations. Therefore, following best practices from previous studies [e.g., 197, 219, 65, 89, 238], all other eclipse parameters were fixed to the literature values listed in Table 4.2. For the systematics model, c, v, and s were allowed to vary between visits, while r_1 and r_2 were fixed to the same values for all visits. Four of

the data sets (for HAT-P-41b, WASP-74b, WASP-79b, and WASP-121b) only used forward scanning instead of bi-directional scanning, so for these observations we fixed $s = 1$. The first secondary eclipse observation for WASP-121b occurred two years before the other four observations and showed significant differences in the ramp shape, so we allowed this first eclipse to be fit with different values of r_1 and r_2 than the other four visits.

Planet	Period [days]	a/r_*	Inclination [°]	r_p/r_*
HAT-P-41b	2.694050 [278]	5.45 [278]	87.70 [278]	0.1028 [134]
KELT-7b	2.734770 [278]	5.50 [278]	83.76 [278]	0.0888 [238]
Kepler-13Ab	1.763588 [16]	4.29 [16]	86.04 [16]	0.0874 [16]
WASP-74b	2.137750 [278]	4.86 [278]	79.81 [278]	0.0980 [278]
WASP-76b	1.809882 [89]	4.08 [89]	88.50 [89]	0.1087 [89]
WASP-77Ab	1.360030 [278]	5.43 [278]	89.40 [278]	0.13012 [306]
WASP-79b	3.662380 [278]	7.03 [278]	85.40 [278]	0.1049 [278]
WASP-121b	1.274926 [54]	3.75 [54]	87.60 [54]	0.1245 [54]

Table 4.2: Literature values for fixed eclipse parameters in the light curve models for the eight data reductions described in Section 4.1.

The data sets for WASP-76b and WASP-79b showed additional correlated noise after applying this systematic model, so for these two data sets we tested adding an additional quadratic term to the visit-long trend. While adding this additional term was able to correct for the correlated noise, it introduced strong degeneracies between the fit parameters and the planet-to-star flux ratio. In order to avoid these degeneracies, we fit for only a linear visit-long trend in our final fit and used the divide-white method to correct for the additional noise [161].

We estimated the parameters with a Markov Chain Monte Carlo (MCMC) fit using the `emcee` package for Python [82]. The final secondary eclipse spectra for all of the planets are shown in Figure 4.1, and the planet-to-star flux ratio in each wavelength bin is listed in Tables 4.3 and 4.4. The white light curves had reduced chi-squared values between $1.9 < \chi^2_\nu < 15.2$. The spectroscopic light curves generally achieved photon-limited precision, with $\approx$ 90 % of the light curves having reduced chi-squared values between $0.7 < \chi^2_\nu < 2.0$. However, occasional individual spectroscopic light curves had higher reduced chi-squared values between $2.0 < \chi^2_\nu < 3.4$. Therefore, before fitting each spectroscopic light curve we

Wavelength [μm]	HAT-P-41b	KELT-7b	Kepler-13Ab	WASP-74b	WASP-76b	WASP-79b	WASP-121b
$1.120 - 1.159$	207 ± 157	284 ± 51	580 ± 106	288 ± 67	424 ± 44	12 ± 33	914 ± 32
$1.159 - 1.197$	461 ± 140	328 ± 45	698 ± 103	357 ± 54	589 ± 33	58 ± 60	956 ± 32
$1.197 - 1.236$	622 ± 91	328 ± 49	666 ± 102	304 ± 57	614 ± 37	297 ± 54	1009 ± 33
$1.236 - 1.274$	545 ± 95	318 ± 54	866 ± 103	310 ± 55	533 ± 35	298 ± 64	1001 ± 29
$1.274 - 1.313$	452 ± 84	368 ± 48	992 ± 106	429 ± 48	645 ± 35	155 ± 49	996 ± 30
$1.313 - 1.351$	503 ± 79	321 ± 50	932 ± 106	401 ± 50	723 ± 33	272 ± 54	1079 ± 32
$1.351 - 1.390$	590 ± 81	371 ± 54	821 ± 107	407 ± 67	804 ± 33	92 ± 50	1206 ± 30
$1.390 - 1.429$	515 ± 82	415 ± 51	879 ± 112	346 ± 50	739 ± 36	186 ± 52	1309 ± 31
$1.429 - 1.467$	561 ± 84	411 ± 53	857 ± 114	486 ± 59	980 ± 37	116 ± 53	1266 ± 31
$1.467 - 1.506$	501 ± 87	445 ± 55	895 ± 118	428 ± 51	1027 ± 35	130 ± 58	1362 ± 32
$1.506 - 1.544$	666 ± 89	424 ± 56	1133 ± 124	428 ± 53	993 ± 37	242 ± 57	1311 ± 36
$1.544 - 1.583$	613 ± 96	439 ± 56	977 ± 128	560 ± 56	1273 ± 40	185 ± 59	1370 ± 36
$1.583 - 1.621$	687 ± 96	447 ± 64	1363 ± 131	633 ± 71	970 ± 45	333 ± 70	1352 ± 39
$1.621 - 1.660$	733 ± 106	392 ± 61	967 ± 140	527 ± 61	909 ± 47	168 ± 72	1322 ± 40

Table 4.3: Secondary eclipse spectra for seven of the eight planets for which new data reductions were performed in this work. The spectrum of WASP-77Ab, which had a higher signal-to-noise and could therefore be binned at a finer wavelength resolution, is given in Table 4.4. All eclipse depths are in units of ppm.

re-scaled the uncertainties by a constant factor such that each light curve had $\chi^2_\nu = 1$ to give more conservative error estimates.

4.1.1 Correction for Companion Stars to WASP-76 and WASP-77A

WASP-76 has a companion star whose spectrum is blended with that of the primary star in the WFC3 data. We corrected for the presence of this companion star using the following equation:

$$F_{corr} = F_{obs}\left(1 + \frac{F_B}{F_A}\right), \tag{4.2}$$

where F_{corr} is the corrected planet-to-star flux ratio in a given bandpass, F_{obs} is the observed flux ratio in that bandpass including the companion star contamination, F_B is the flux of the companion star in that bandpass, and F_A is the flux of the primary star in that bandpass. We used ATLAS models [41] with temperatures of 6250 K and 4824 K to represent the primary star and the companion star, respectively [275].

WASP-77A also has a companion star, WASP-77B, which has a projected distance large enough that their spectra do not overlap in stare mode. However, the spectra of these two

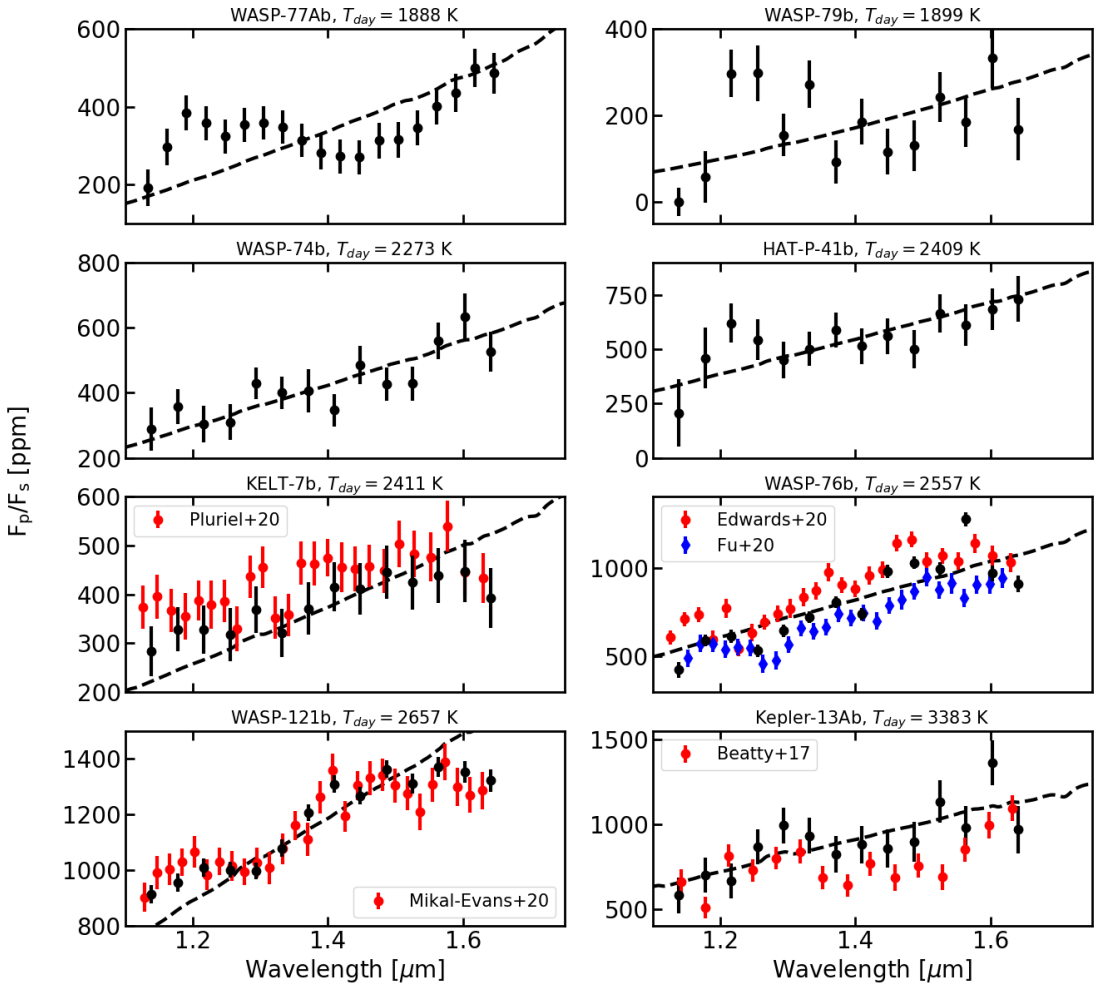

Figure 4.1: *HST*/WFC3 secondary eclipse spectra for the eight data reductions presented in this paper (black points). Black dashed lines indicate best-fit blackbody spectra, and temperatures above each plot give the corresponding dayside temperature T_{day}. Red and blue points show previous data reductions from the literature [16, 65, 89, 211, 238], which all show good agreement with the results presented here.

Wavelength [μm]	WASP-77Ab
$1.120 - 1.148$	192 ± 47
$1.148 - 1.177$	297 ± 46
$1.177 - 1.205$	384 ± 45
$1.205 - 1.234$	359 ± 44
$1.234 - 1.262$	324 ± 43
$1.262 - 1.291$	354 ± 43
$1.291 - 1.319$	359 ± 42
$1.319 - 1.347$	348 ± 42
$1.347 - 1.376$	313 ± 43
$1.376 - 1.404$	283 ± 43
$1.404 - 1.433$	273 ± 44
$1.433 - 1.461$	271 ± 44
$1.461 - 1.489$	313 ± 45
$1.489 - 1.518$	315 ± 46
$1.518 - 1.546$	346 ± 45
$1.546 - 1.575$	402 ± 47
$1.575 - 1.603$	436 ± 48
$1.603 - 1.632$	499 ± 49
$1.632 - 1.660$	486 ± 51

Table 4.4: Secondary eclipse spectrum of WASP-77Ab. All eclipse depths are in units of ppm.

stars overlap during spatial scans. In order to correct for this overlap, we observed a single stare mode exposure with an exposure time of 0.556 s at the beginning of each of the two visits. For each visit, we used the optimal extraction method described above [122] to extract the stare mode spectra of WASP-77A and WASP-77B. We then corrected the observed flux for the presence of the companion star using the equation

$$F_{*,corr} = F_{*,obs} \left(\frac{F_A}{F_A + F_B} \right), \tag{4.3}$$

where $F_{*,corr}$ is the corrected flux in units of electrons, $F_{*,obs}$ is the observed flux in units of electrons, and F_A and F_B are the observed fluxes of the primary and companion star in that bandpass, respectively.

4.1.2 Reanalysis of Kepler-13Ab

In addition to the seven new data reductions described above, we performed a reanalysis of the emission spectrum of Kepler-13Ab. The details for the two observed secondary eclipses of

Kepler-13Ab are listed in Table 4.1. These data were also reduced using the data reduction pipeline described in Kreidberg et al. [161], and we again discarded the first orbit of each visit. We additionally discarded 14 of the 1008 observed spectra because they showed anomalously low fluxes in the broadband white light curve compared to the rest of the spectra. The spectrum was binned into 14 channels at a resolution of $R \approx 30 - 40$.

The spectrum of Kepler-13Ab was observed in stare mode. Stare mode observations commonly show one or more of three types of systematics: a visit-long trend, an L-shaped hook trend over an individual orbit, and thermal breathing [315]. We tested including all of these components in our fit and found that only a visit-long trend was necessary to explain the systematics. Therefore, we fit both the white light curve and the spectroscopic light curves with a model in the form

$$M(t) = E(t)(c + vt_{vis}). \tag{4.4}$$

Following our method for the other data sets, the free parameters in the white light curve fit were c, v, T_0, and F_p/F_s. For the spectroscopic light curves, the free parameters were c, v, and F_p/F_s, and T_0 was fixed to the best-fit value from the white light curve. All other eclipse parameters were fixed to the literature values listed in Table 4.2. The parameters c and v were allowed to vary between visits.

We estimated the parameters with a Markov Chain Monte Carlo (MCMC) fit using the `emcee` package for Python [82]. The final secondary eclipse spectrum for Kepler-13Ab is shown in Figure 4.1, and the planet-to-star flux ratio in each wavelength bin is listed in Table 4.3. The white light curve had a reduced chi-squared of $\chi^2_\nu = 1.33$. The spectroscopic light curves generally achieved photon-limited precision and had reduced chi-squared values between $\chi^2_\nu = 0.94 - 1.08$.

4.2 A 1D Grid of Radiative-Convective-Thermochemical Equilibrium Models

We created a new grid of self-consistent, 1D hot Jupiter models to compare their emission spectra to the population of observed planets. These models were generated using the Sc-CHIMERA code, validated against established brown dwarf models [256] and analytic models [237], assuming cloud-free, radiative-convective-thermochemical equilibrium atmospheres. The models' assumption of chemical equilibrium is likely a good approximation for the highly irradiated planets that make up the majority of our observed population [146]. A two stream source function technique [299] is employed to solve for the planetary thermal fluxes at each atmospheric level (under the hemispheric mean approximation). We modeled the stellar flux via a standard two stream approximation (for both direct and diffuse fluxes, under the quadrature approximation) assuming cosine incident angle of 0.5, utilizing the PHOENIX models for the stellar spectra [128]. A Newton-Raphson iteration [206] is used to determine the temperature at each model layer which ensures zero net flux divergence. We include absorption cross-sections from 0.1 - 100 μm (where available) for H_2O, CO, CO_2, CH_4, NH_3, H_2S, PH_3, HCN, C_2H_2, TiO, VO, SiO, FeH, CaH, MgH, CrH, AlH, Na, K, Fe, Mg, Ca, C, Si, Ti, O, Fe^+, Mg^+, Ti^+, Ca^+, C^+, H_2, H_2-H_2/He CIA, [182, 292, 165, 96], H^- bound-free and free-free [21, 133], and H_2/He Rayleigh scattering, and additional UV opacities for CO, SiO, and H_2[165]. Pre-computed cross-sections were converted into correlated-k coefficients at a spectral resolution of 250 using a 10 point double Gauss quadrature (with half covering the top 5% of the correlated-k cumulative distribution function) with mixed-gas optical depths computed using the random-overlap resort-rebin framework [e.g., 166, 5]. Thermochemical equilibrium molecular abundances were computed using the NASA CEA Gibbs free energy minimization code [101] combined with elemental rain-out due to condensate formation (all major Si, Fe, Mg, Ca, Al, Na, and K bearing condensates are included) given the Lodders et al. [176] elemental abundances.

We parameterized the model atmospheres with a set of five parameters: the stellar effective temperature (T_{eff}), the planetary gravity (g), the planetary metallicity ($\left[\frac{\mathrm{M}}{\mathrm{H}}\right]$), the planetary carbon-to-oxygen ratio ($\frac{\mathrm{C}}{\mathrm{O}}$), and the planetary internal temperature (T_{int}). Figure 4.2 shows the T-P profiles and resultant secondary eclipse spectra for our fiducial model, which uses system parameters for a standard hot Jupiter ($T_{\mathrm{eff}} = 5300$ K, $g = 10$ m/s^2, $\left[\frac{\mathrm{M}}{\mathrm{H}}\right] = 0.0$, $\frac{\mathrm{C}}{\mathrm{O}} = 0.55$, and $T_{\mathrm{int}} = 150$ K). Models at different irradiation temperatures were created by re-scaling the incident stellar spectrum (the PHOENIX model for a given stellar effective temperature) by the ratio of the desired irradiation temperature to the bolometric temperature of a planet at 0.05 AU around a 1 solar radius star. We created hot Jupiter models with irradiation temperatures between $500 - 3600$ K, with step sizes of $50 - 200$ K.

Following Lothringer & Barman [179], we calculate the absorption mean opacity κ_J and the Planck mean opacity κ_B at a pressure of 10^{-2} bar as a function of equilibrium temperature for our fiducial models. The absorption mean opacity at a given pressure P is given by

$$\kappa_J(P) = \frac{\int_0^\infty \kappa_\lambda(T,P) J_\lambda(P)\, d\lambda}{\int_0^\infty J_\lambda(P)\, d\lambda}, \tag{4.5}$$

where κ_λ is the monochromatic true absorption coefficient, J_λ is the mean intensity at a given wavelength, and T is the local temperature in the planet's atmosphere. The Planck mean opacity is given by

$$\kappa_B(P) = \frac{\int_0^\infty \kappa_\lambda(T,P) B_\lambda(T)\, d\lambda}{\int_0^\infty B_\lambda(T)\, d\lambda}, \tag{4.6}$$

where $B_\lambda(T)$ is the Planck function. The absorption mean opacity represents the efficiency with which the atmosphere can absorb photons, while the Planck mean opacity represents the efficiency with which the atmosphere can emit photons [179]. Therefore, the ratio κ_J/κ_B, which is also shown in Figure 4.2 describes the relative efficiency of stellar absorption vs. thermal re-radiation. A ratio $\kappa_J/\kappa_B > 1$ generally indicates the presence of a thermal inversion in the T-P profile. The hot Jupiters in this study can generally be thought of as emitting most of their radiation at near-infrared wavelengths, whereas incoming starlight

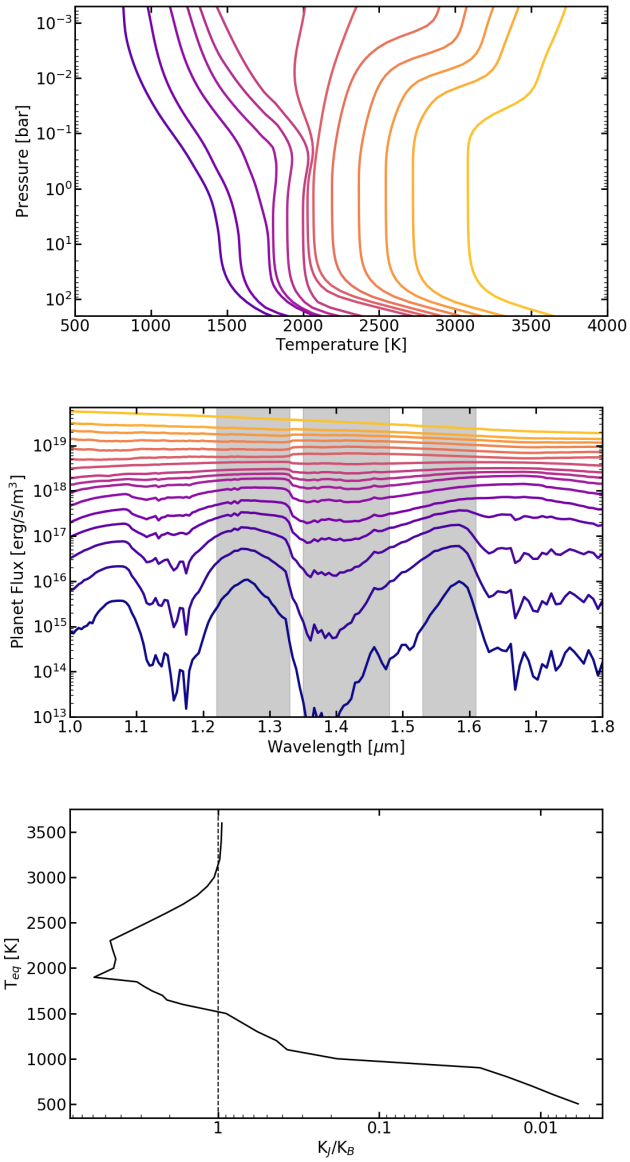

Figure 4.2: Temperature-pressure (T-P) profiles (top) and resulting dayside planet fluxes (middle) for the fiducial model grid, which covers approximately the same range of temperatures as spanned by the observations. Blue and yellow lines show models with the coolest and warmest irradiation temperatures, respectively. For clarity, only every other model in the grid is shown here. Grey shaded bands indicate the "out-of-band" and "in-band" regions used to calculate the water feature strength (S_{H_2O}) described in Section 4.3. The bottom panel shows the ratio of the absorption mean opacity (κ_J) to the Planck mean opacity (κ_B) as a function of equilibrium temperature (T_{eq}) in these models at a pressure of 10^{-2} bar, assuming zero albedo and full redistribution. This ratio describes the relative efficiency of heating vs. cooling in the models [179], and a ratio of $\kappa_J/\kappa_B > 1$ generally indicates the presence of a thermal inversion in the T-P profile. This panel is plotted with temperature on the y-axis for ease of comparison to Figure 4.5.

from their host stars peaks at visible wavelengths. Therefore, increasing the amount of molecules such as TiO that are optically active at visible wavelengths will increase κ_J, and increasing the amount of molecules such as H_2O that are optically active at near-infrared wavelengths will increase κ_B.

We also created subset grids as a function of irradiation temperature where a single parameter dimension was varied while all other parameters were held fixed to their fiducial model values (no cross-variance). We examined models with a stellar $T_{\rm eff}$ = 3300 K, 4300 K, 6300 K, 7200 K, and 8200 K; g = 1 m/s^2 and 100 m/s^2; $\left[\frac{\rm M}{\rm H}\right] = -1.5$ and 1.5; and $\frac{\rm C}{\rm O} = 0.01$ and 0.85. For models with different metallicities, elemental abundance ratios were held constant while the overall metallicity was re-scaled relative to H. We also created a model grid where the internal temperature varies with the planetary irradiation temperature following Equation 3 in Thorngren et al. [295].

Opacity from gaseous TiO/VO is theorized to be a driving force behind the transition between uninverted hot Jupiter atmospheres with monotonically decreasing T-P profiles and atmospheres containing thermal inversions [83]. Some previous observations of hot Jupiters have suggested that vapor TiO/VO may not be present in high-temperature atmospheres if it is condensed in cooler parts of the atmosphere [e.g., 16]. This process, known as cold-trapping, effectively works to remove TiO/VO from places in the atmosphere where vaporized TiO/VO would be expected to be present in equilibrium. In order to study the impact of potential cold-trapping, we created models where the TiO and VO opacities are artificially set to zero until a given temperature threshold. We tested models where TiO/VO opacity is zeroed out for temperatures below 2000 K, 2500 K, and 3000 K.

Recent studies have suggested clouds may have an impact on the strength of molecular absorption features observed in thermal emission [e.g., 142, 290]. To test the impact the presence of clouds would have on the trends in our models, we created two cloudy models. We used the cloud model of Ackerman & Marley [1], as implemented by Mai & Line [189]. Both models had a constant vertical mixing strength of 10^8 cm^2/s using the Zahnle et al.

[330] timescale prescription. We tested models with sedimentation efficiencies of $f_{sed} = 0.1$ and 1.0.

Our hot Jupiter models predict three primary spectral regimes. At the lowest dayside temperatures ($T_{\rm day} < 2100$ K for the fiducial model), the models exhibit absorption features due to monotonically decreasing temperature profiles. At intermediate temperatures (2100 K $< T_{\rm day} <$ 3000 K for the fiducial model), the modeled thermal structures exhibit a rising temperature with increasing altitude (decreasing pressure) due to the gas-phase onset of TiO and VO which push $K_J/K_B > 1$, in turn causing emission features. At the highest temperatures ($T_{\rm day} > 3000$ K for the fiducial model), the models still show strong thermal inversions (becoming stronger primarily due to the dissociation of water, an efficient coolant) but the resulting secondary eclipse spectra are relatively featureless because of a combination of high-temperature effects such as molecular dissociation and the onset of H^- opacity, which cause all the WFC3+G141 wavelengths to probe the same altitude/pressure level, hence brightness temperature [233, 178, 6, 163, 197]. The exact temperatures of the transitions between these regimes, as well as the strength of absorption and emission features present in the models, depend on the parameters of each set of models.

In order to demonstrate the difference between models of hot Jupiter atmospheres (which are primarily irradiated from above by their host stars) and brown dwarf atmospheres (which are primarily heated from below by the brown dwarf's interior), we created a separate model grid of cloud-free brown dwarf models using the same Sc-CHIMERA code setup. We parameterized the brown dwarf model atmospheres with a set of four parameters: the brown dwarf effective temperature ($T_{eff,bd}$), the brown dwarf gravity (g), the brown dwarf metallicity ($\left[\frac{\rm M}{\rm H}\right]$), and the brown dwarf carbon-to-oxygen ratio ($\frac{\rm C}{\rm O}$). These models thus used an identical set of parameters to the hot Jupiter models, with the exception of irradiation from within the brown dwarf instead of from an exterior star. The fiducial brown dwarf models had $g = 1000$ m/s^2, $\left[\frac{\rm M}{\rm H}\right] = 0.0$, and $\frac{\rm C}{\rm O} = 0.55$. We created models with brown dwarf effetive temperatures between $1000 - 2800$ K with a step size of 200 K. We also created grids with

Planet	*HST* Program #	Number of Eclipses	Observation Mode	Literature Reference
CoRoT-2b	12181 [55]	3	Stare Mode	Wilkins et al. [320]
HAT-P-7b	14792 [14]	2	Spatial Scan	Mansfield et al. [197]
HAT-P-32Ab	14767 [271]	1	Spatial Scan	Nikolov et al. [219]
HD 189733b	12881 [204]	1	Spatial Scan	Crouzet et al. [51]
HD 209458b	13467 [13]	5	Spatial Scan	Line et al. [175]
TrES-3b	12181 [55]	1	Stare Mode	Ranjan et al. [242]
WASP-4b	12181 [55]	1	Stare Mode	Ranjan et al. [242]
WASP-12b	12230 [286]	1	Stare Mode	Stevenson et al. [279]
WASP-18b	13467 [13]	5	Spatial Scan	Arcangeli et al. [6]
WASP-33b	12495 [56]	2	Spatial Scan	Haynes et al. [112]
WASP-43b	13467 [13]	5	Spatial Scan	Kreidberg et al. [160]
WASP-103b	13660 [334], 14050 [159]	4	Spatial Scan	Kreidberg et al. [163]

Table 4.5: References and *HST* program numbers for the twelve planets whose spectra were taken from the literature.

metallicities of $\left[\frac{\mathrm{M}}{\mathrm{H}}\right] = -1.0$ and 1.0. Additionally, while a gravity of $g = 1000$ m/s^2 is typical for a brown dwarf, we created grids with $g = 100$ m/s^2 and $g = 10$ m/s^2 for direct comparison to lower-gravity hot Jupiters.

4.3 Comparison of Observed Spectra to 1D Models

We combined the eight new data reductions and analyses with twelve results from the literature to form a complete sample of planets observed with *HST*/WFC3+G141 in the wavelength region from $1.1 - 1.7$ μm. Table 4.5 contains detailed information on each of the twelve literature results we considered. The planets in this study have observed dayside temperatures in the *HST*/WFC3+G141 bandpass between $1450 - 3500$ K and radii between $0.9 - 2.0$ Jupiter radii. The full set of 20 spectra are shown in Figure 4.3.

For both the models and the population of 20 observed hot Jupiters, we examined the degree of absorption or emission observed in the water feature at 1.4 μm, the primary feature in the *HST*/WFC3+G141 bandpass. We quantified their deviation from a blackbody using an *HST* water feature strength metric, which is illustrated in Figure 4.4. For each data set, we first fit a blackbody to the two "out-of-band" regions of the spectrum, which have wavelengths of $1.22 - 1.33$ μm and $1.53 - 1.61$ μm and are defined based on where the models in Figure 4.2

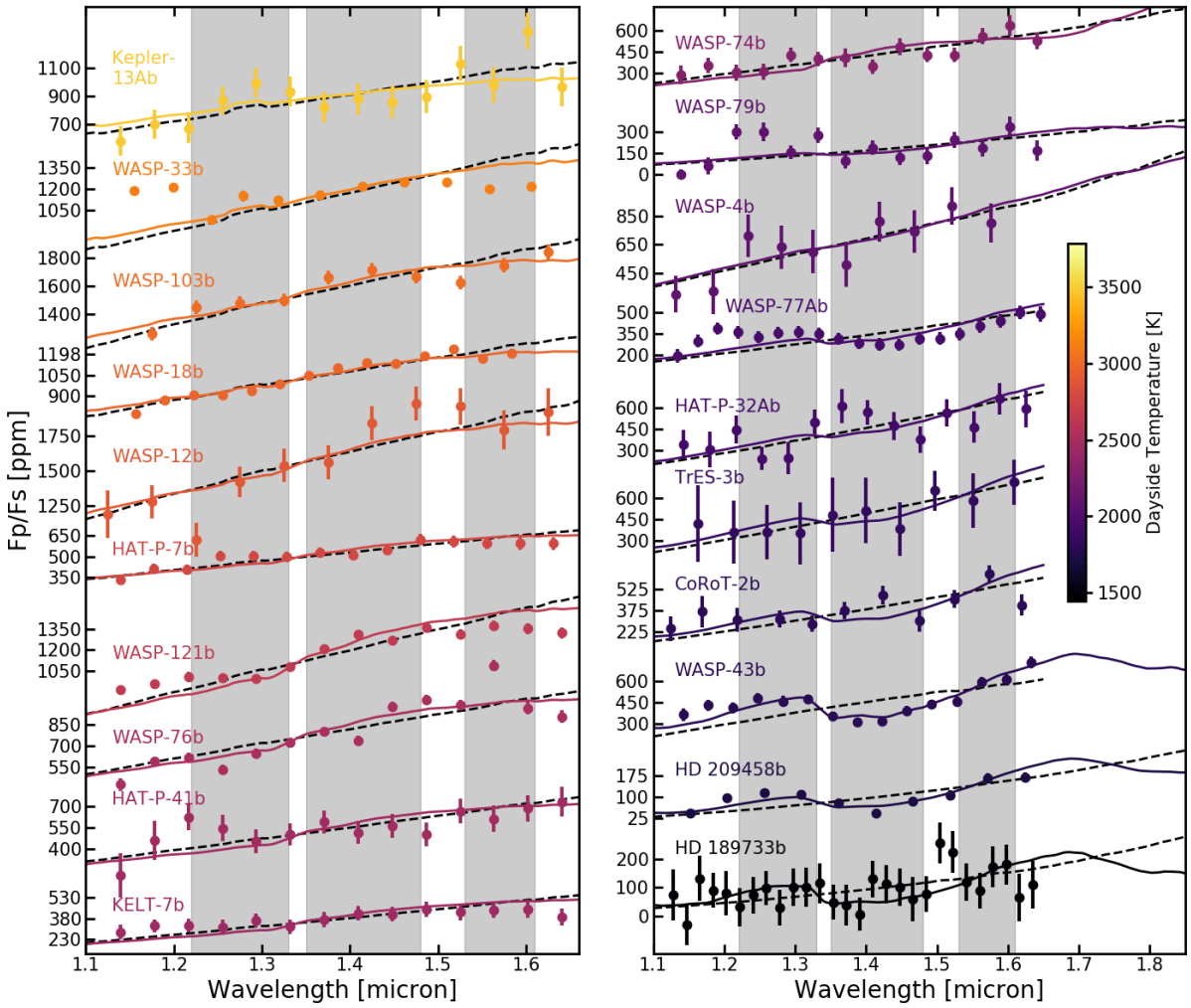

Figure 4.3: Secondary eclipse spectra for all 20 hot Jupiters considered in this study. Data sets are colored by dayside temperature, which is measured as described in the Methods and shown by the colorbar. Solid lines indicate interpolations from our solar composition fiducial model grid (see Section 4.2), while dashed lines indicate best-fit blackbodies. Shaded regions indicate the "out-of-band" and "in-band" regions used to calculate the water feature strength (S_{H_2O}) for each observed secondary eclipse spectrum. Note that for several data sets, the error bars are smaller than the point size.

show minimal water opacity. The temperature of this blackbody is referred to throughout this paper as the observed dayside temperature ($T_{\rm day}$) in this bandpass. Similar to previous studies [260], we found a linear relationship between this observed dayside temperature and the planetary irradiation temperature given by

$$T_{day} = 0.807^{+0.008}_{-0.004} T_{irr} + 71^{+25}_{-8}, \tag{4.7}$$

where $T_{irr} = T_{eff}\sqrt{R_*/a}$ is the irradiation temperature, R_* is the stellar radius, and a is the semi-major axis.

The water feature strength is then defined as

$$S_{H_2O} = \log_{10}\left(\frac{F_{B,in}}{F_{obs,in}}\right), \tag{4.8}$$

where $F_{B,in}$ and $F_{obs,in}$ are the flux of the fitted blackbody and the observed data, respectively, in the "in-band" region shown in Figure 4.4. The "in-band" wavelength region extends from $1.35 - 1.48$ μm and captures the center of the primary water band observed in the *HST*/WFC3 bandpass. The shaded regions in Figure 4.3 show the extent of the "out-of-band" and "in-band" regions. From this definition, S_{H_2O} will have a positive value when a water feature is observed in absorption, a negative value when a feature is observed in emission, and a value of zero if a blackbody is observed. We note that we use S_{H_2O} here instead of the traditional infrared J- and H-bands because the J- and H-bands exclude the strongest part of the water band at ≈ 1.4 μm. Therefore, the S_{H_2O} index we define gives us greater sensitivity to weak water features that may only produce significant deviation from a blackbody at the center of this absorption band.

Figures 4.5, 4.6 and 4.7 show the observed *HST* water feature strengths for the sample of 20 hot Jupiter emission spectra compared to those of the hot Jupiter models. Table 4.6 lists the value of S_{H_2O} for each planet. Figure 4.5 shows that the observed *HST*/WFC3 feature strengths generally fall within the region of parameter space spanned by the models,

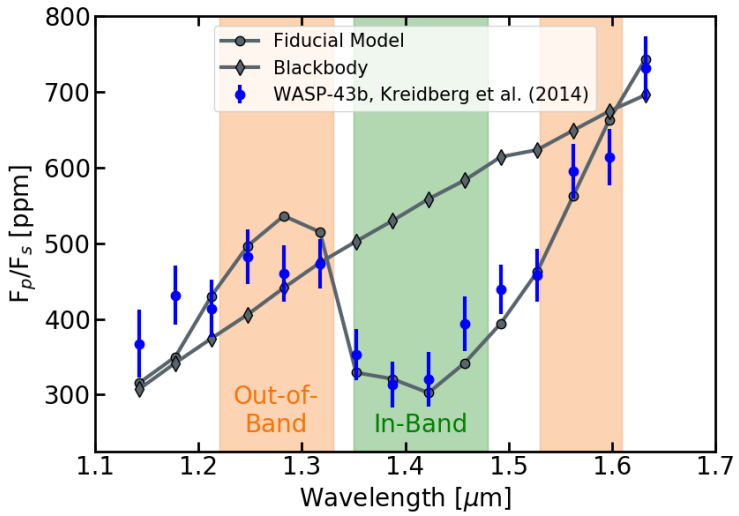

Figure 4.4: Construction of the *HST* water feature strength metric to compare observed spectra to models. Blue points show *HST*/WFC3 observations of WASP-43b [160]. The orange and green shaded regions indicate the spectral extent of the "out-of-band" and "in-band" flux, which are defined based on where the models in Figure 4.2 show water features. The gray line with circular points shows the best-fit model interpolated from those in Figure 4.2. The gray line with diamond-shaped points shows a blackbody fit to the out-of-band flux region.

with almost all of the planets fully within the predicted spread of the models. The models considered here assume elemental abundance ratios that fall within the range of commonly expected outcomes from planet formation models [213, 3, 187, 49]. We find that varying parameters in these simple models can explain the observed hot Jupiter population without having to appeal to less likely outcomes of planet formation [e.g., C/O$>$ 1 213, 3, 49] or exotic chemistry.

While the observations are generally within the parameter space spanned by the hot Jupiter models, Figure 4.5 shows that the brown dwarf models generally show very distinct spectra from the hot Jupiter models. In particular, the brown dwarf models consistently show negative values of S_{H_2O} indicating absorption features across the full range of temperatures modeled. This is because the atmospheric thermal inversions which produce emission features can only appear in atmospheres primarily heated from above [e.g., 125]. We find that the data are discrepant from all of the brown dwarf models at $\geq 10\sigma$ significance.

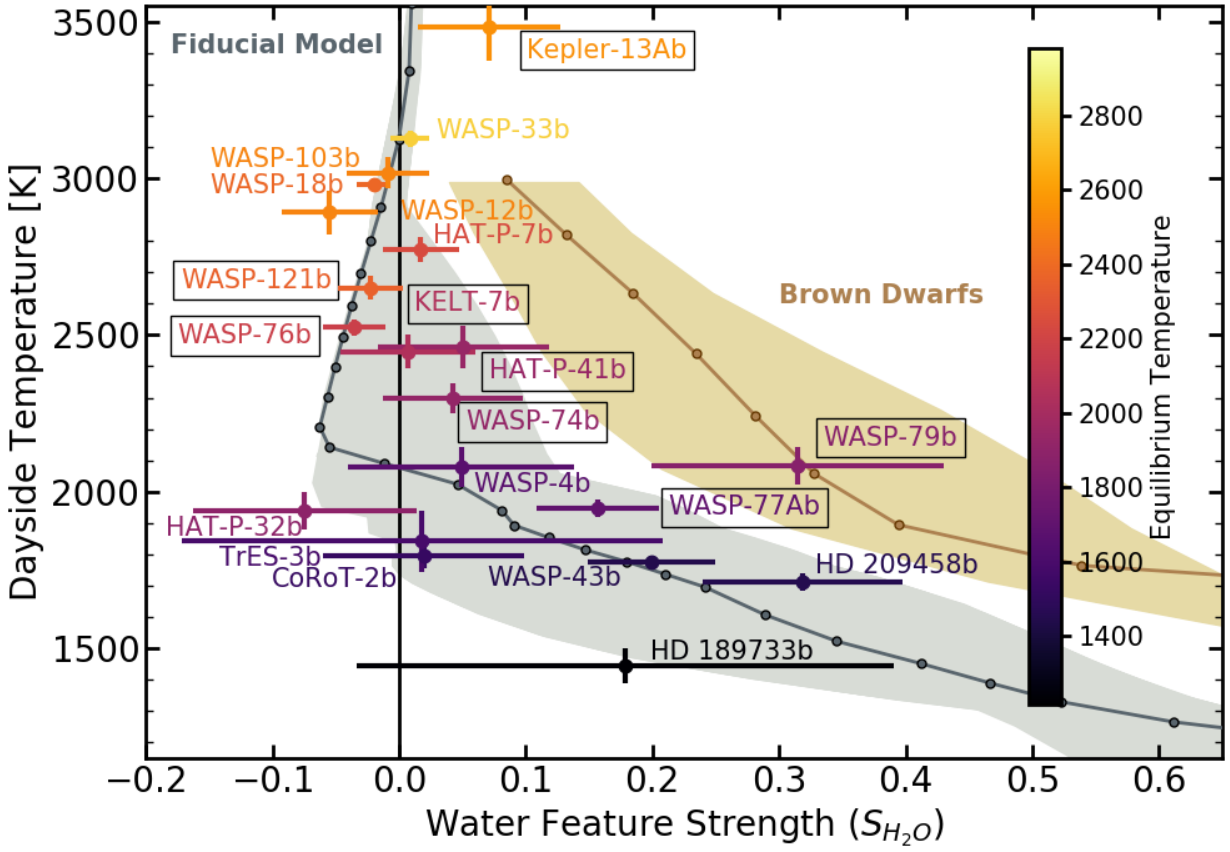

Figure 4.5: *HST* water feature strength diagram comparing observed secondary eclipse spectra to the model predictions in Figure 4.2. The y-axis shows the temperature of a blackbody fit to the "out-of-band" regions defined in Figure 4.4, which is the observed dayside temperature $T_{\rm day}$. The x-axis shows the strength of the observed feature in the water band at 1.4 μm compared to this blackbody, as defined by Equation 4.8. Featureless, blackbody-like spectra have $S_{H_2O} = 0$ and absorption/emission features have positive/negative values of S_{H_2O}, respectively. The gray line and points show the fiducial hot Jupiter models pictured in Figure 4.2. The light gray shaded region shows the full range of hot Jupiter model predictions assuming different values for the stellar effective temperature; the temperature where TiO opacity becomes important; and the planet gravity, C/O ratio, metallicity, and internal heat. Similarly, the brown line and points show the fiducial brown dwarf models, and the tan shaded region shows the full range of brown dwarf models assuming different values for the planet gravity and metallicity. Colored points with 1σ error bars show all planets with observed *HST*/WFC3 spectra, and boxes around planet names indicate new data reductions in this publication. The color scale indicates the planetary equilibrium temperature. The error bars include uncertainties in the stellar effective temperature.

Planet	T_{day} [K]	S_{H_2O}
CoRoT-2b	1796 ± 42	0.019 ± 0.079
HAT-P-7b	2772 ± 39	0.017 ± 0.030
HAT-P-32Ab	1939 ± 59	-0.074 ± 0.089
HAT-P-41b	2461 ± 66	0.051 ± 0.068
HD 189733b	1446 ± 57	0.178 ± 0.212
HD 209458b	1711 ± 28	0.319 ± 0.079
KELT-7b	2447 ± 54	0.007 ± 0.053
Kepler-13Ab	3484 ± 107	0.071 ± 0.056
TrES-3b	1842 ± 97	0.018 ± 0.190
WASP-4b	2079 ± 62	0.049 ± 0.089
WASP-12b	2890 ± 70	-0.055 ± 0.038
WASP-18b	2979 ± 20	-0.020 ± 0.013
WASP-33b	3126 ± 26	0.009 ± 0.015
WASP-43b	1775 ± 23	0.200 ± 0.050
WASP-74b	2298 ± 48	0.042 ± 0.055
WASP-76b	2523 ± 27	-0.035 ± 0.025
WASP-77Ab	1946 ± 28	0.157 ± 0.049
WASP-79b	2083 ± 58	0.315 ± 0.115
WASP-103b	3018 ± 50	-0.009 ± 0.033
WASP-121b	2651 ± 39	-0.023 ± 0.025

Table 4.6: Computed dayside temperatures (T_{day}) and water feature strengths (S_{H_2O}) for each planet following Equation 4.8. The errors include uncertainties in the stellar effective temperature.

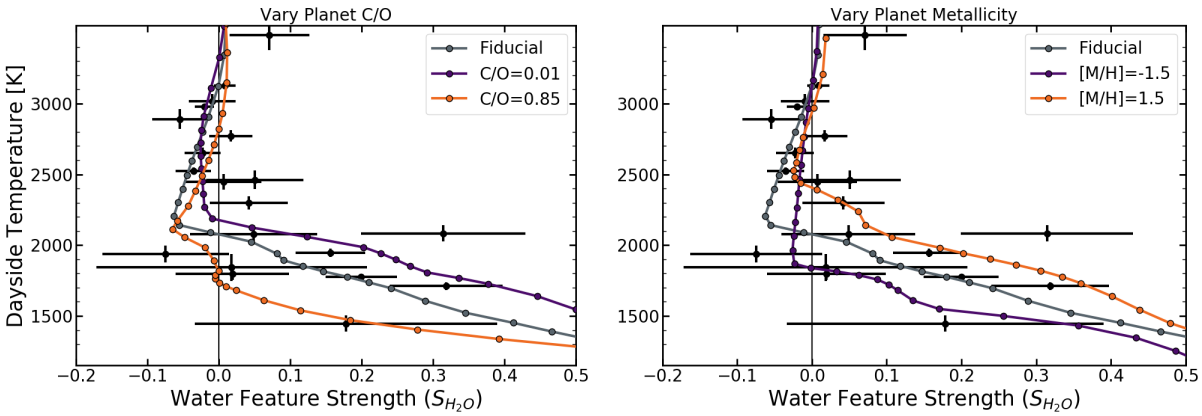

Figure 4.6: Diagrams illustrating the change in *HST* water feature strength from models with different parameters. All diagrams show the observed data as black points with 1σ error bars, while the lines show tracks for models with varying C/O ratio (left), and metallicity (right). In each case all other parameters are held fixed at the fiducial model values. The error bars include uncertainties in the stellar effective temperature. We found that changing the parameters shown in Figure 4.7 could not explain the observed scatter in water feature strengths, but changing the atmospheric C/O ratio and metallicity can explain the diversity of observed secondary eclipse spectra

Although the observed population of hot Jupiter emission spectra generally matches the trends in our hot Jupiter model predictions, we find that no single model track is the best fit for all 20 of the observations. When taking each model track individually, the data are discrepant from each track at $\geq 2\sigma$ significance. Figure 4.8 shows the best-fit model for each individual data set, and Table 4.7 lists the reduced chi-squared values for these best-fit models. We find that the model grid is generally able to produce good fits to the data, with the best fits to all but two data sets having reduced chi-squared values below 2.6. However, different data sets are best fit by models with different parameters, which suggests that one or more parameters may be varying between planets.

To determine which parameters can most easily explain the scatter in the observed data, we examined the water feature strength variation we could achieve through changing each of our model parameters individually. Figures 4.6 and 4.7 shows water strengths for each individual model we examined. We found that the stellar effective temperature, planet gravity, and extent of internal heating had relatively small impacts on the predicted wa-

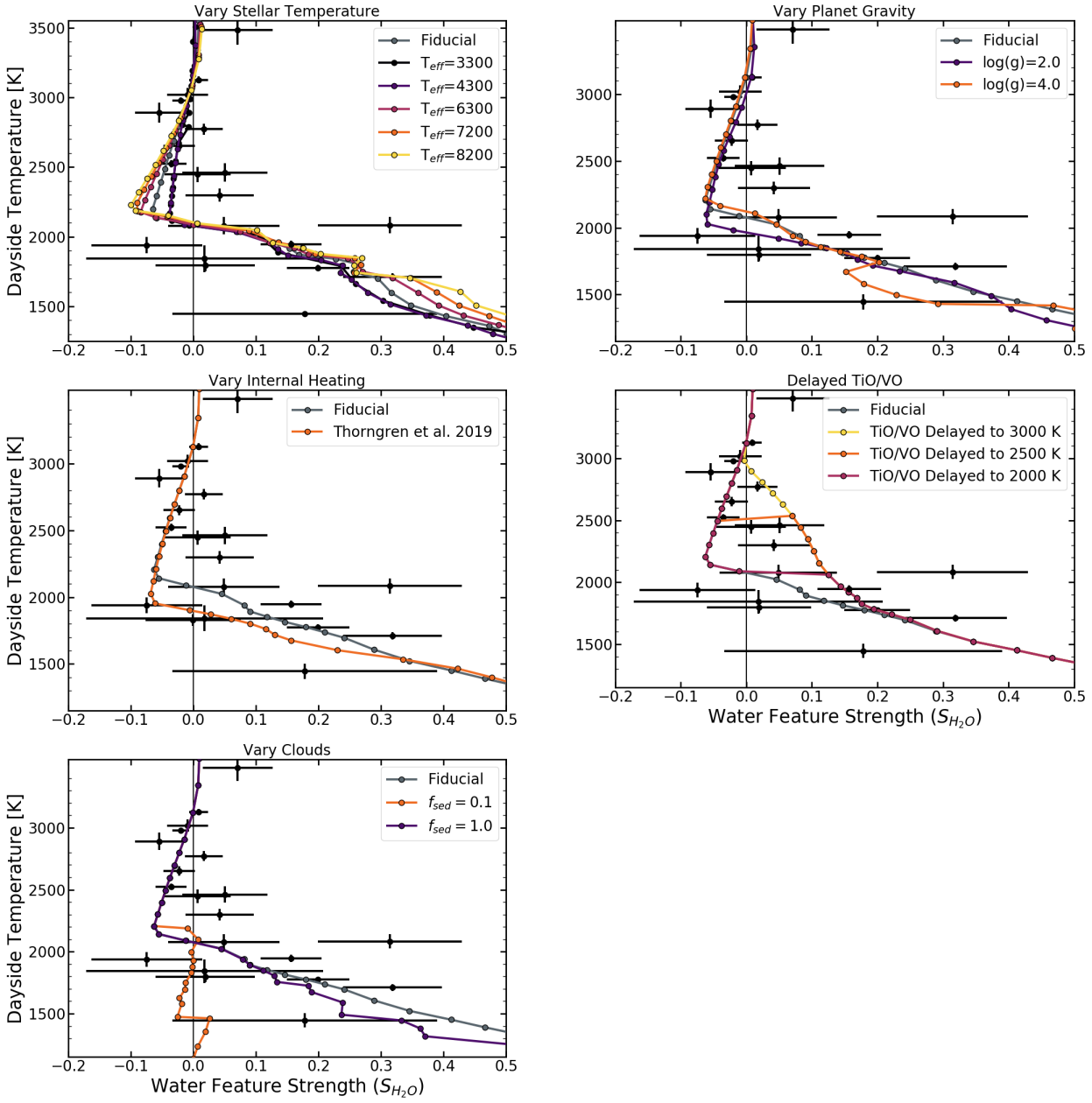

Figure 4.7: Same as Figure 4.6, but showing models with varying stellar temperature (top left), gravity (top right), internal heating (middle left), temperature to which TiO/VO opacity were ignored (middle right), and cloud opacity (bottom). We found that changing the stellar temperature, planetary gravity, and internal heating in our models had little impact on the derived water feature strengths, and changing the TiO/VO only had an impact at intermediate temperatures. Adding clouds to the model effectively weakened the water feature strengths and made the emission spectra more blackbody-like below dayside temperatures of about 2000 K. However, clouds had no effect on S_{H_2O} at $T_{day} \geq 2000$ K because the planets' daysides are too hot for any condensation to occur.

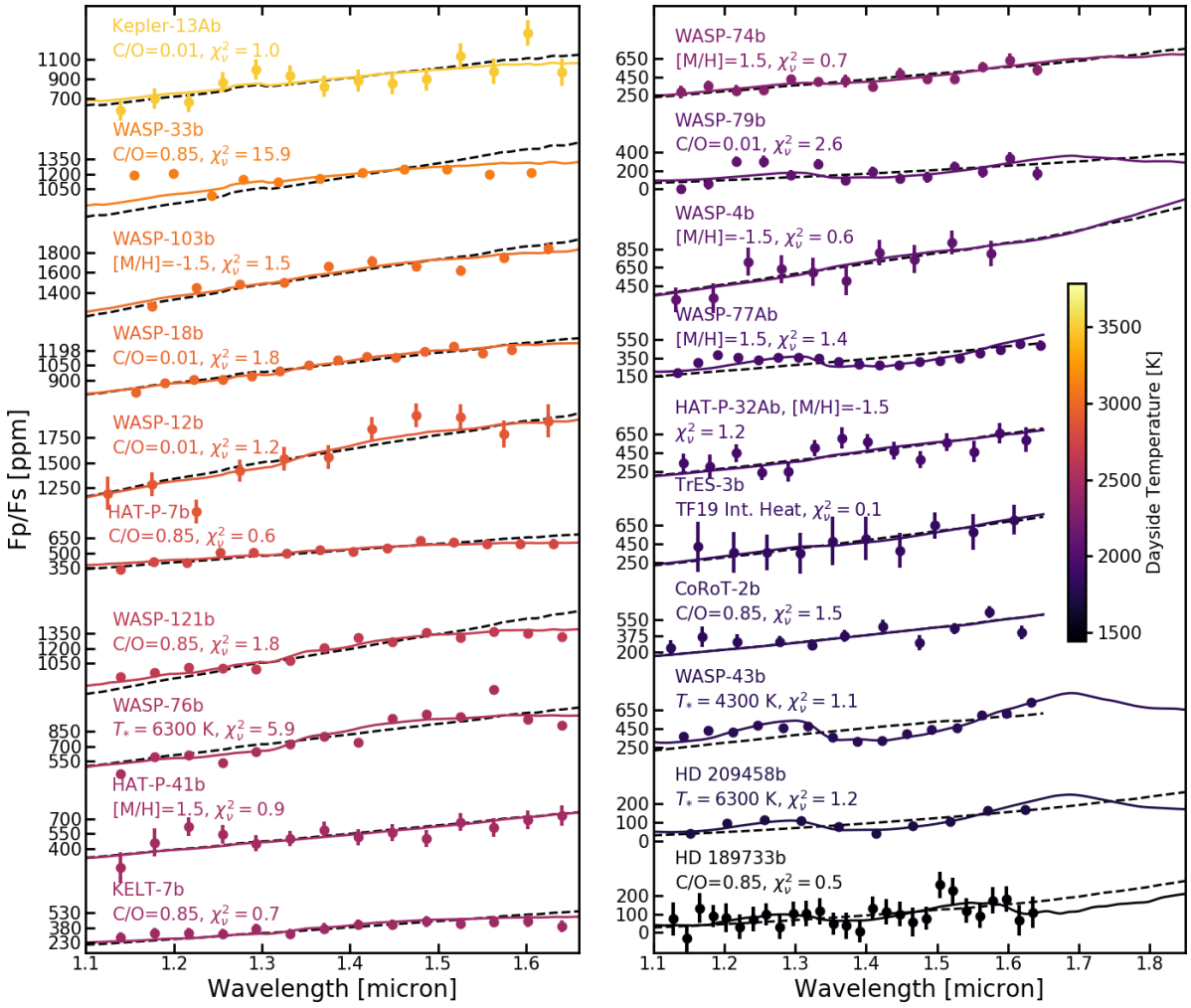

Figure 4.8: Same as Figure 4.3, but showing best-fit models from the model grid instead of models from only the fiducial grid. Text below each planet name lists the model which provided the best fit for that data set and the reduced chi-squared value for that model.

Planet	Best-Fit Model	χ^2_ν
CoRoT-2b	C/O = 0.85	1.5
HAT-P-7b	C/O = 0.85	0.6
HAT-P-32Ab	[M/H] = −1.5	1.2
HAT-P-41b	[M/H] = 1.5	0.9
HD 189733b	C/O = 0.85	0.5
HD 209458b	$T_* = 6300$ K	1.2
KELT-7b	C/O = 0.85	0.7
Kepler-13Ab	C/O = 0.01	1.0
TrES-3b	Thorngren et al. [295] Internal Heating	0.1
WASP-4b	[M/H] = −1.5	0.6
WASP-12b	C/O = 0.01	1.2
WASP-18b	C/O = 0.01	1.8
WASP-33b	C/O = 0.85	15.9
WASP-43b	$T_* = 4300$ K	1.1
WASP-74b	[M/H] = 1.5	0.7
WASP-76b	$T_* = 6300$ K	5.9
WASP-77Ab	[M/H] = 1.5	1.4
WASP-79b	C/O = 0.01	2.6
WASP-103b	[M/H] = −1.5	1.5
WASP-121b	C/O = 0.85	1.8

Table 4.7: Best-fit models for each data set and reduced chi-squared values (χ^2_ν) for those models. In general the models produce good fits, with the best fits to all but two data sets having $\chi^2_\nu \leq 2.6$. However, different data sets are best fit by models with different values for the atmospheric metallicity and C/O ratio, which suggests their atmospheres may have diverse compositions.

ter feature strengths throughout the range of temperatures of the hot Jupiter population. Adding clouds acts to weaken the water feature strengths below a dayside temperature of about 2000 K, with a smaller f_{sed} leading to more effective weakening. While clouds may provide a potential explanation for the weak water feature strength of HD 189733b, the lowest-temperature hot Jupiter in our population study, we find that including clouds can not generally explain the scatter we see in water feature strengths and has no impact on the feature strengths above $T_{day} = 2000$ K. Our results agree with those from general circulation models, which also show that clouds have little to no impact at temperatures above ≈ 2000 K [251, 232]. Additionally, the models with TiO/VO opacity removed at different temperatures could only account for some of the scatter at intermediate temperatures and could not explain scatter at the highest or lowest temperatures, where we have observed the most precise secondary eclipse spectra. However, changing the atmospheric metallicity and C/O ratio had a significant impact on the predicted *HST*/WFC3 water feature strengths. We found the observed scatter could be explained if the planets have atmospheric metallicites between $0.03 - 30\times$ solar and C/O ratios between 0.01-0.85 ($0.02 - 1.5\times$ solar). With the current data we are unable to compare each planet's specific atmospheric composition to this prediction, as even the most detailed *HST* secondary eclipse observations only constrain the metallicity to within 0.5 dex and often cannot constrain the C/O ratio, or can only place an upper limit [e.g., 6, 197, 211]. However, such variation is expected from planet formation models [213, 3] and has been suggested by a handful of transmission spectra studies [e.g., 49, 270]. The scatter we observed in emission spectra lends further support to the concept of compositional diversity among hot Jupiters.

4.4 Discussion and Future Work

We performed a population study of all 20 hot Jupiters which have been observed in secondary eclipse with *HST*/WFC3+G141 between $1.1 - 1.7$ μm. We found that the data were generally consistent with predictions from 1D radiative-convective-thermochemical equilib-

rium models of hot Jupiter atmospheres, but were discrepant from brown dwarf models at $\geq 10\sigma$ significance. Additionally, we found the amount of scatter in observed water feature strengths suggests there may be modest differences in metallicity and C/O ratio between planets.

Our hypothesis that hot Jupiters show compositional diversity can be tested through high-precision observations that cover more of the key O- and C-bearing molecules than are included in existing data sets (e.g, H_2O, CO, CO_2, and CH_4). Such observations will be possible with *JWST* [103] and stabilized, high-resolution spectrographs on large ground-based telescopes that have broad wavelength coverage [274]. Simultaneous detection of multiple molecules would lead to more precise constraints on metallicities, carbon-to-oxygen abundance ratios, and additional elemental ratios including nitrogen [31]. Beyond testing our hypothesis, more precise compositional constraints on exoplanet atmospheres would inform our understanding of the formation and evolution processes that have produced the diverse planetary systems revealed over the last 25 years.

Part II

Atmospheric Escape from Highly Irradiated Exoplanets

CHAPTER 5

DETECTION OF HELIUM IN THE ATMOSPHERE OF THE EXO-NEPTUNE HAT-P-11B

Close-in exoplanets are expected to experience atmospheric escape that is driven by the absorption of the copious high energy radiation they receive from their host stars [168, 170]. Such photoevaporation likely sculpts the observed population of close-in exoplanets, dividing small planets into two categories - those with radii smaller than $1.5R_{\oplus}$, which are likely rocky cores stripped of any primordial light-element atmospheres, and those with radii larger than $2R_{\oplus}$, which retain some hydrogen and helium in their atmospheres [177, 225, 226, 91, 308].

The theories describing the recently discovered planet radius gap can be refined through observations of escaping atmospheres, which will lead to a better understanding of the physics of photoevaporation. Atmospheric escape has been detected through observations of hydrogen absorption in the Lyman α line for two hot Jupiters [HD 209458b and HD 189733b; 313, 314, 171] and two hot Neptunes [GJ 436b and GJ 3470b; 66, 29]. However, interstellar absorption limits these observations to nearby planets with gas escaping at high velocities.

Another possible signature of an escaping atmosphere that is less affected by interstellar absorption is the helium triplet at 10,833 Å [note this is the wavelength of the feature in vacuum; 264, 223]. This feature was recently detected for the first time by Spake et al. [276] using *HST* observations of WASP-107b. Here we present similar *HST* observations for the hot Neptune HAT-P-11b [9][1]. The original motivation for our program was to precisely determine the atmospheric water abundance of the planet and further constrain

1. This chapter is based on Mansfield et al. [198], which was coauthored by Jacob L. Bean, Antonija Oklopčić, Laura Kreidberg, Jean-Michel Désert, Eliza M.-R. Kempton, Michael R. Line, Jonathan J. Fortney, Gregory W. Henry, Matthias Mallonn, Kevin B. Stevenson, Diana Dragomir, Romain Allart, and Vincent Bourrier. M. Mansfield reduced and analyzed the data presented in this chapter and led the data-model comparison. J. L. Bean is PI of the *HST* program GO-14793 which obtained the observations of HAT-P-11b. A. Oklopčić created the helium escape models described in Section 5.2.2. G. W. Henry and M. Mallonn observed and reduced the ground-based photometry described in Section 5.1.2. R. Allart and V. Bourrier observed the CARMENES spectrum of HAT-P-11b which is compared to our data in Figure 5.9. All other authors are co-Is on *HST* program GO-14793.

the exoplanet mass-metallicity relation [e.g., 160]. However, as was true for the Spake et al. [276] observations, these data also presented the serendipitous opportunity to search for the previously-theorized but unexploited-until-recently He triplet. Our analysis of these data was further inspired by the presentation of R. Allart at the Exoplanets II conference in July 2018 showing a detection of the He feature in HAT-P-11b using ground-based data from CARMENES [4].

Our observations of HAT-P-11b have yielded the second detection of helium escaping from a planet using *HST*, and a new detection of photoevaporation from a Neptune-sized exoplanet, and so help to constrain the nature of photoevaporation for planets smaller than Jupiter. Furthermore, HAT-P-11b now becomes the first exoplanet with the detection of the same signature of photoevaporation from both ground- and space-based facilities. In Section 5.1 we describe our observations and data reduction process. In Section 5.2 we compare our observations to models of photoevaporation, and we summarize our findings in Section 5.3.

5.1 Observations and Data Reduction

5.1.1 HST Data

We observed five transits of HAT-P-11b between 14 September and 26 December 2016 using the *HST*/WFC3 IR detector as part of program GO-14793. We used the G102 grism to measure the transmission spectrum of HAT-P-11b between 0.8−1.15 μm. Each visit consisted of four consecutive *HST* orbits in which HAT-P-11 was visible for approximately 56 minutes per orbit. At the beginning of each orbit, we took a direct image of the target with the F126N narrow-band filter for wavelength calibration.

The observations were taken in the spatial scan mode with the 256 × 256 subarray using the SPARS10, NSAMP=12 readout pattern, resulting in an exposure time of 81.089 s. We used a scan rate of 0.25 arcsec/s, which produced spectra extending approximately 180 pixels

in the spatial direction and with peak pixel counts of about 45,000 electrons per pixel. We used bi-directional scans, which yielded 25 exposures per orbit and a duty cycle of 74%.

We reduced the *HST* data using the data reduction pipeline described in Kreidberg et al. [161], with the addition of an extra step to subtract light from a background star that overlapped with the spectrum of HAT-P-11. The spectrum of the background star was measured in one visit in which it was separated from HAT-P-11, and then subtracted out of each image, accounting for the fact that its position along both the dispersion and spatial axes changed between visits. This subtraction did not substantially change the final shape of the spectrum.

Following standard procedure for *HST* transit observations, we discard the first orbit of each visit. We also discard the first exposure from each orbit to improve the quality of the fit. Additionally, three points in the third visit and four points in the fourth visit were removed because they showed higher relative fluxes consistent with starspot crossings, as can be seen in Figure 5.1.

We used the WFC3 G102 wavelength calibration outlined in Kuntschner et al. [164] to determine the wavelength of each pixel in our spectra from the direct image positions. However, we found that the calibrated data appeared to be shifted in wavelength space compared to the expected grism throughput. Both the red and blue edges of the spectrum were shifted by the same amount, but the shift was different for each visit, varying between 6 and 18 Å. This is likely due to the fact that *HST* must move slightly after taking the direct image in order to correctly position the spatial scan so it fits on the detector. The positioning of the spectral images relative to the direct image has an uncertainty of roughly 12 Å [62]. We shifted the wavelengths to the correct values using a least-squares fit to the drop-offs at both the red and blue edges of the throughput, as demonstrated in Figure 5.2.

We made a broadband spectrum by binning the observations into 16-pixel channels, resulting in 12 light curves with resolution $R \approx 40$. To search for the narrow helium feature, we summed the region of the spectrum between 10,590 Å and 11,150 Å into 22 overlapping

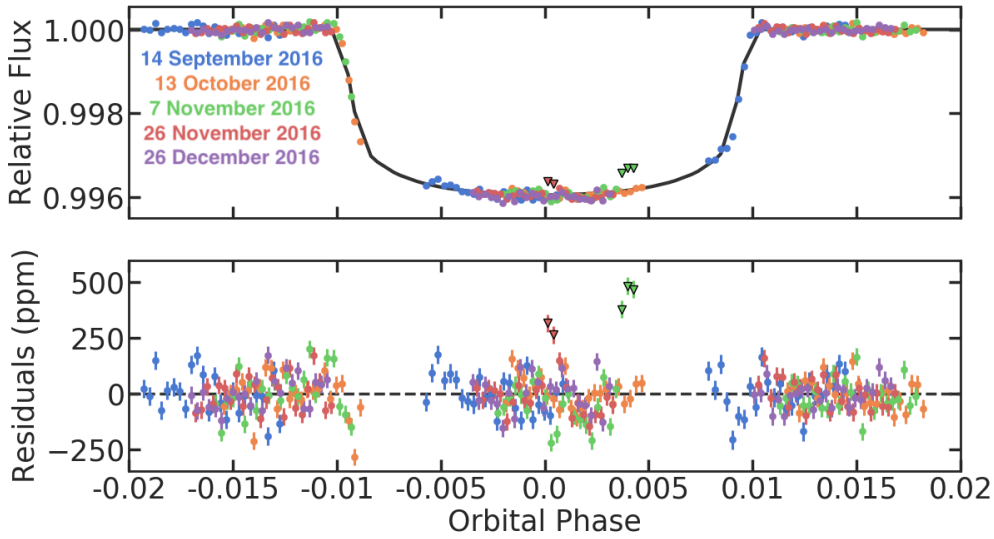

Figure 5.1: Best fit broadband white light curve (top) and residuals to the fit (bottom). The two sets of triangular points outlined in black, which have residuals greater than 250 ppm, are the starspot crossings that were removed before the data analysis. The fit had $\chi^2_\nu = 4.67$ and an average residual of 75 ppm.

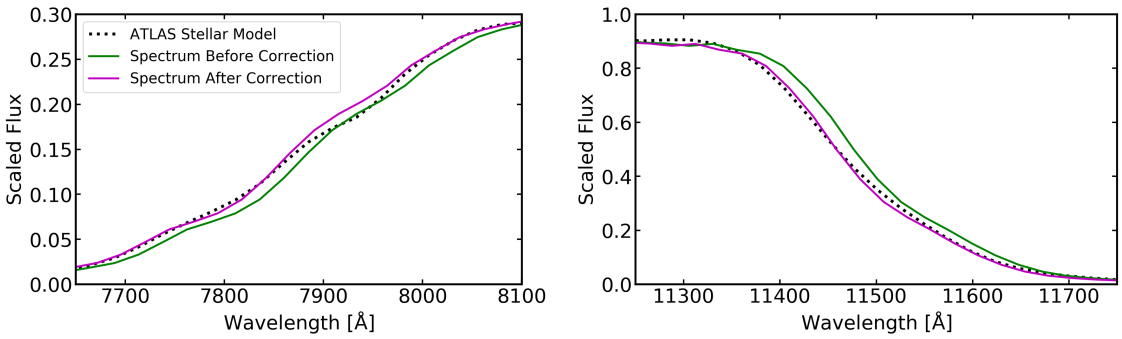

Figure 5.2: Comparison between an ATLAS stellar model for HAT-P-11b combined with the G102 throughput (black dashed line) and the observed spectrum. The green line is the observed spectrum using the wavelength calibration outlined by Kuntschner et al. [164] and assuming the distance between the direct image and the spectrum is exactly known, and the magenta line is the spectrum after adjusting the wavelength calibration. The plots show the blue (left) and red (right) edges of the spectrum, which were used to determine the wavelength shift.

bins that were 2 pixels wide (≈ 49 Å, for comparison a resolution element is ≈ 67 Å). Each bin was shifted by one pixel from the previous bin. We also summed over the entire $0.85-1.13$ μm wavelength range to make a white light curve.

We fit the white light curve with the model described in Kreidberg et al. [161], which includes a transit model [158] and a systematics model based on Berta et al. [24]. The orbital period and eccentricity were fixed to $P = 4.8878024$ days and $e = 0.265$, respectively [126]. We placed Gaussian priors on a/R_s and i with mean and standard deviations of 17.125 ± 0.060 and 89.549 ± 0.114, respectively [85]. We fixed limb darkening coefficients to theoretical quadratic limb darkening models predicted from ATLAS models [70, 42]. Including the instrument systematics, the fit to the white light curve contained a total of 24 free parameters (a normalization constant, visit-long linear slope, scaling factor to correct for an offset between scan directions, and the planet-to-star radius ratio varied between visits).

We estimated the parameters with a Markov Chain Monte Carlo (MCMC) fit using the `emcee` package for Python [82]. Figure 5.1 shows the best-fit broadband white light curve. The best-fit broadband white light curve had $\chi^2_\nu = 4.67$ and residuals of 75 ppm, which is typical for WFC3 observations of transiting planets orbiting bright host stars. The white light transit depth was 3371 ± 15 ppm.

We fit the spectroscopic light curves using the divide-white technique of Stevenson et al. [280] and Kreidberg et al. [161]. For the narrowband spectroscopic light curves surrounding the helium feature, we used a region spanning 10,590 – 11,150 Å to determine the white light curve systematics. The narrowband white light curve had $\chi^2_\nu = 3.27$ and residuals of 138 ppm. We fixed a/R_s and i to the prior mean values and the mid-transit times were fixed to the best-fit values from the white light curve fit. Before fitting each spectroscopic light curve, we rescaled the uncertainties by a constant factor such that each light curve had $\chi^2_\nu = 1$ to give more conservative error estimates.

Figure 5.3 shows the individual transit depths for each visit for both the broadband white light curve and the narrow band containing the helium feature. In both cases, the

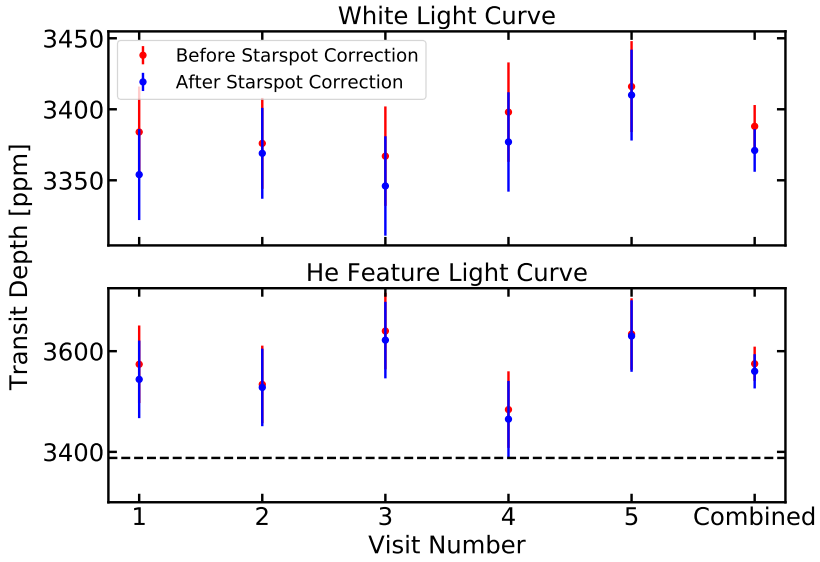

Figure 5.3: Individual white light curve transit depths (top) and transit depths in the narrow band containing the helium feature (bottom) for each visit. The final point shows the combined measurement from all five visits. For comparison, the dashed line in the lower plot shows the broadband white light transit depth from combining all five visits. Red and blue points show values before and after the starspot correction, respectively. For both the white light curve and the helium feature, the transit depths across all five visits were within 2σ of each other.

individual transit depths are all within 2σ of each other. Figure 5.4 shows the broadband spectrum, Figure 5.5 shows the narrowband spectrum, and Table 5.1 lists the transit depth in each channel. The derived transmission spectrum is largely featureless with the exception of a deeper transit in the narrowband spectroscopic channel corresponding to the unresolved infrared He triplet, which deviates from the surrounding continuum at the 4σ confidence level.

5.1.2 Ground-based Photometry

We obtained ground-based photometric monitoring from two sources to correct the transmission spectrum for changes in stellar activity. We obtained multi-color photometric monitoring with the 1.2 m robotic STELLA telescope using its wide-field imager WiFSIP [284]. Data were taken from June – October 2016 and March – July 2017 in Johnson B and V in nightly

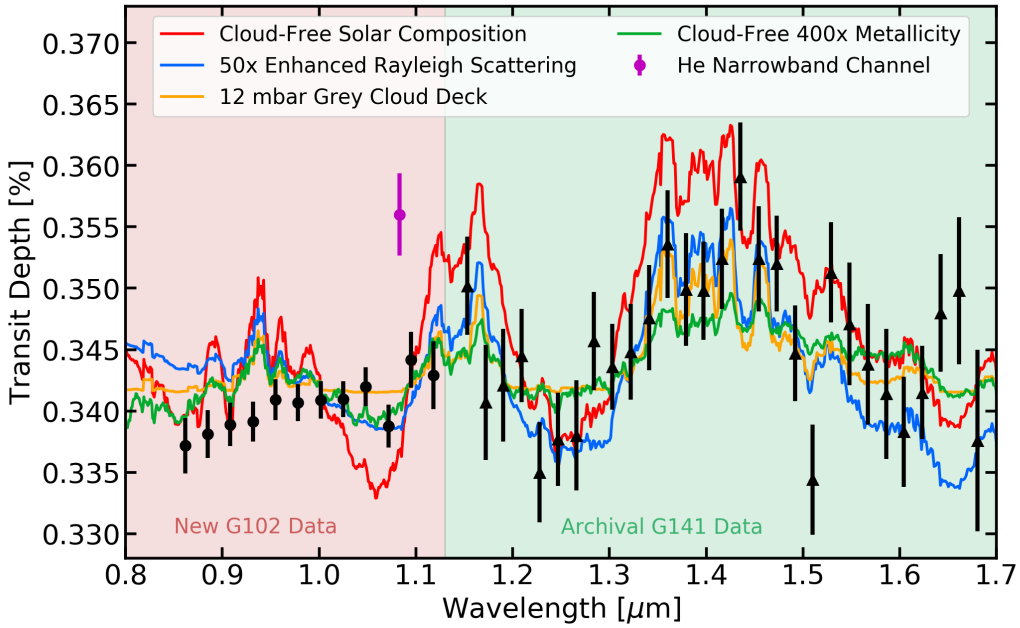

Figure 5.4: Spectrum of HAT-P-11b (black points with 1σ error bars) compared to a variety of models (lines) with different cloud parameterizations, which are described in Section 5.2.1. Circular points are our G102 data (in bins ≈ 233 Å wide), and triangular points are G141 data from Fraine et al. [85]. The magenta point shows the transit depth in the 49-Å wide channel containing the helium feature at 10,833 Å. The grey cloud deck model fits best, but does not match the upward slope seen between $0.8 - 1.1$ μm.

Table 5.1: Broadband (left) and narrowband (right) transmission spectra of HAT-P-11b.

Wavelength (Å)	Transit Depth (ppm)	Wavelength (Å)	Transit Depth (ppm)
$8500 - 8733$	3371 ± 23	$10614 - 10663$	3399 ± 32
$8733 - 8967$	3381 ± 19	$10663 - 10712$	3370 ± 30
$8967 - 9200$	3389 ± 18	$10712 - 10760$	3390 ± 32
$9200 - 9433$	3391 ± 16	$10760 - 10809$	3398 ± 35
$9433 - 9667$	3409 ± 17	$10809 - 10858$	3560 ± 34
$9667 - 9900$	3406 ± 15	$10858 - 10907$	3448 ± 39
$9900 - 10133$	3409 ± 15	$10907 - 10955$	3406 ± 39
$10133 - 10367$	3410 ± 15	$10955 - 11004$	3414 ± 39
$10367 - 10600$	3420 ± 16	$11004 - 11053$	3440 ± 48
$10600 - 10833$	3388 ± 17	$11053 - 11101$	3409 ± 46
$10833 - 11067$	3442 ± 23	$11101 - 11150$	3398 ± 45
$11067 - 11300$	3429 ± 28		

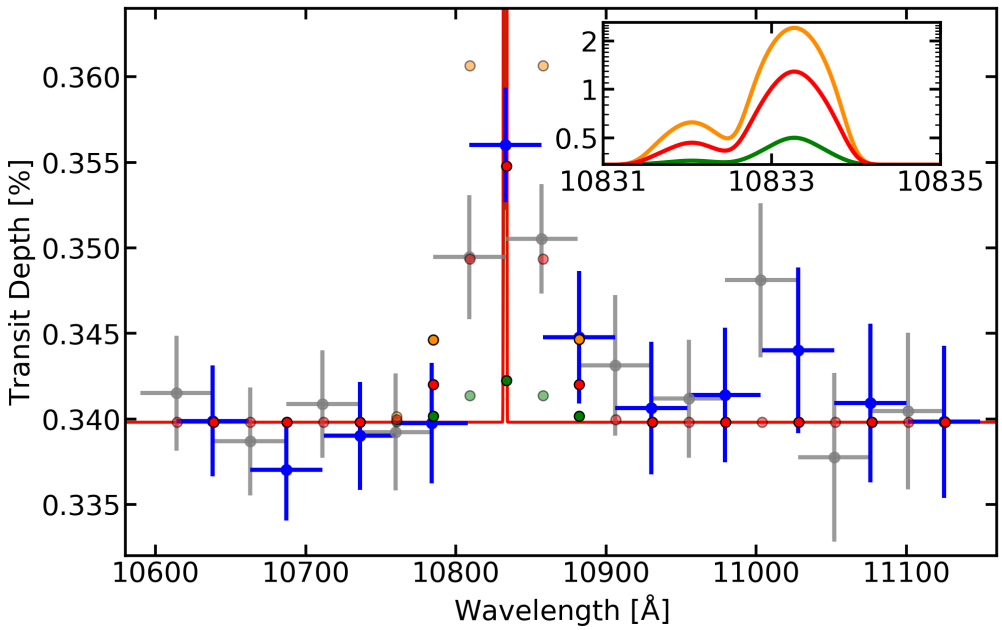

Figure 5.5: Narrowband spectrum of HAT-P-11b (blue and grey points with 1σ error bars) compared to three 1D models of hydrodynamic escape. The red line shows a model with $T = 7,000$ K and a mass loss rate of 2.5×10^{10} g s^{-1}, which provides an excellent match to the data. For comparison, the green and orange lines show models with $T = 7,000$ K and mass loss rates of 6.3×10^{9} g s^{-1} and 5.0×10^{10} g s^{-1}, respectively. These models are inconsistent with the the data at $\geq 3\sigma$ confidence. Blue points show non-overlapping bins. Red, green, and orange points outlined in black show the models convolved with the G102 instrument resolution [164] and binned to the sampling of the data. The inset shows the models at high resolution.

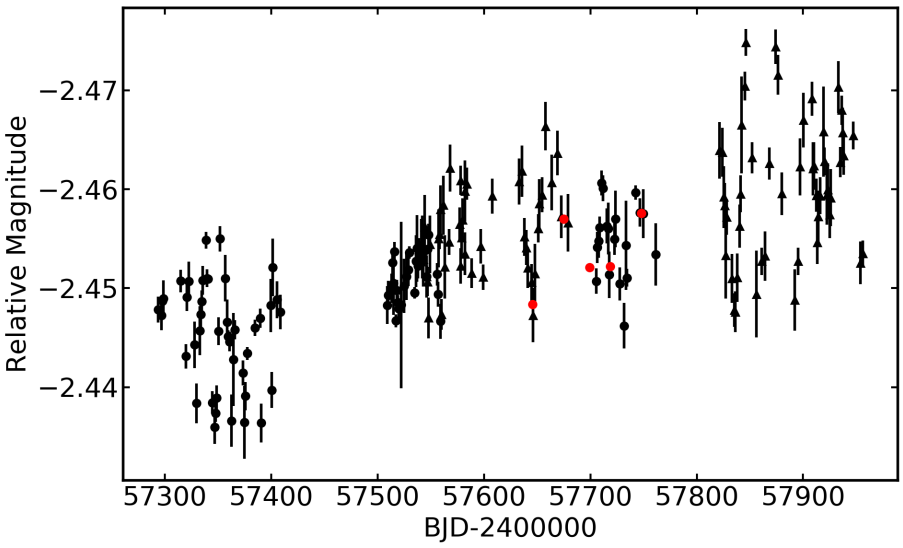

Figure 5.6: Ground-based photometry (black points) taken during the epoch of our *HST* observations. Circular and triangular points show photometry taken with the Tennessee State University C14 AIT [116] and the STELLA telescope [284], respectively. The red points show the interpolated values at the times of our observations.

blocks of four exposures per filter, which were averaged during data reduction. The data reduction followed the procedure of Mallonn et al. [193]. We also monitored the photometric variability using the Tennessee State University Celestron 14 inch (C14) automated imaging telescope (AIT), which is located at Fairborn Observatory [116]. These observations consisted of 89 nights between 27 September 2015 and 7 January 2017. Figure 5.6 shows these ground-based photometric observations.

We interpolated between these photometric observations to estimate the starspot covering fraction at the time of each *HST* observation. We used the relative amplitude of two occulted starspots in the white light curve to determine the temperature difference between the starspots and the star, which we found to be approximately 150 K. We assumed that the starspots were circular and that the entire starspot was occulted by the planet each time. We

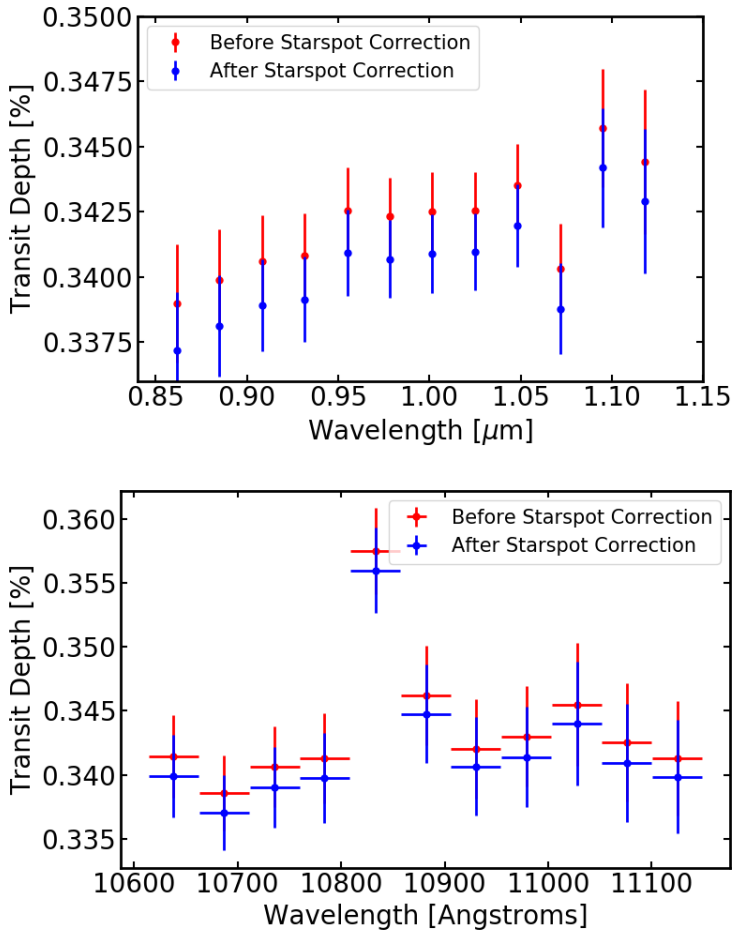

Figure 5.7: Effect of the correction for unocculted starspots on the broadband (top) and narrowband (bottom) spectra. The primary effect is to shift the entire spectrum up by about 20 ppm, but in the broadband spectrum the correction also shifts the blue end of the spectrum up by slightly more than the red end of the spectrum.

applied a wavelength-dependent correction to the R_p/R_s values measured from the WFC3 data to account for variations in starspot coverage between visits, assuming that both the spotted and unspotted parts of the star emitted as blackbodies and assuming that the mean photometric magnitude occurred when the spot covering fraction was 3%, which is the mean spot coverage for HAT-P-11b [215]. Figure 5.7 shows the effect of this starspot correction on both the broadband and the narrowband spectrum of HAT-P-11b.

We followed the method of Spake et al. [276] to check whether the He absorption feature we observed could be caused by stellar activity. They found that the He triplet equivalent width for a K4-type star like HAT-P-11 should be no larger than ≈ 0.4 Å, according to

both theoretical calculations and observations of K-dwarf stars. For our 49 Å-wide bins, this corresponds to a change in the transit depth of 30 ppm. The helium feature we observe has a depth of 162 ± 36 ppm, which is more than 3.5σ larger than the expected depth due to stellar activity. Our argument that the He feature can not be due to stellar activity alone is strengthened by the fact that our observations occurred near a minimum in HAT-P-11's activity cycle [217].

5.2 Analysis

5.2.1 Broadband Spectrum

We computed transmission spectra models to compare with the WFC3+G141 data from Fraine et al. [85] and our new broadband G102 data using the `Exo-Transmit` code [143]. We tested models with a cloud-free, solar composition; enhanced metallicity; a grey cloud deck; and enhanced Rayleigh scattering. Figure 5.4 shows these different cloud parameterizations compared to the spectrum of HAT-P-11b. The best-fitting model had grey clouds at 12 mbar and $\chi^2_\nu = 1.38$. The models with a cloud-free solar composition, 50× enhanced Rayleigh scattering, and 400× enhanced metallicity had $\chi^2_\nu = 4.22$, 2.49, and 1.53, respectively. However, none of the models we tested produced a particularly good fit to both the archival G141 data and our new G102 data, as none of them produced the upward slope seen between $0.8 - 1.1$ μm while simultaneously matching the water feature seen around $1.4\,\mu$m. One possible explanation for the upward slope we observe is the influence of unocculted, bright regions on the star [240]. A more detailed study of the broadband transmission spectrum is presented in Chachan et al. [43]. We turn our attention below to a detailed study of the narrowband spectrum around the He triplet feature.

5.2.2 Narrowband Helium Spectrum

We compared the helium absorption feature detected in our *HST* data to a grid of models of hydrodynamic escape computed using the methods of Oklopčić & Hirata [223]. Spherically-symmetric model atmospheres were constructed from 1D density and velocity profiles based on the isothermal Parker wind model [229, 167]. The atmospheres were assumed to be composed of hydrogen and helium atoms in 9:1 number ratio. Hydrogen and helium atomic level populations were computed taking into account photoionization, recombination, and collisional transitions. To calculate the photoionization rates, we constructed a spectrum appropriate for HAT-P-11 (a K4 star) by averaging the observed spectra of K2 and K6 stars, obtained from the MUSCLES survey [86]. With the planet mass, radius, and atmospheric composition fixed, and the mean molecular weight of the atmosphere evaluated iteratively (taking into account the free electrons produced by hydrogen photoionization), the remaining free parameters in the model are temperature and mass loss rate.

We model the atmosphere of HAT-P-11b as being in the hydrodynamic escape regime because the planet has a low gravitational potential [254] and the Jeans parameter at the exobase [$R > 10\,R_p$; 253] is $\lambda < 1.3$. Salz et al. [253] also predict that the exobase should be above both the sonic point and the Roche radius for HAT-P-11b. Additionally, the Jeans escape rate is generally expected to be substantially lower than the hydrodynamic escape rate for a planet like HAT-P-11b with an unstable thermosphere [297].

We computed models for a range of thermospheric temperatures between T = 3,000 – 12,000 K and total mass loss rates between $\dot{M} = 4.0 \times 10^8$ – 2.5×10^{11} g s^{-1}. We convolved each high-resolution model with a Gaussian function with the resolution of WFC3+G102, which is $R \approx 155$ at 10,400 Å [164], before binning the models to the sampling of our observations. We then determined the χ^2 of each model compared to the data using the three non-overlapping bins surrounding the helium feature that show a deviation from the baseline absorption level.

Figure 5.8 shows a contour plot of the fit quality for comparing the grid models to the

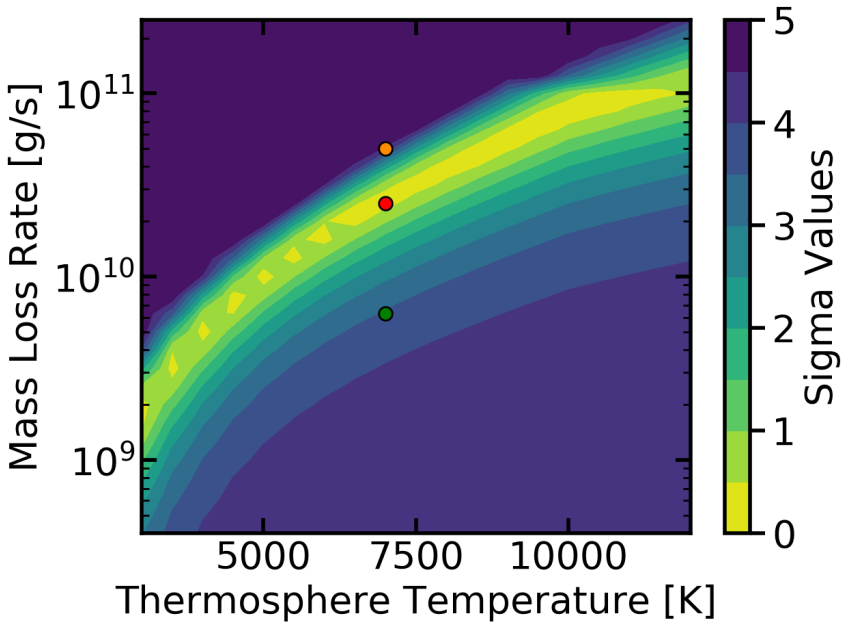

Figure 5.8: Contour plot showing the statistical significance of the deviation from a good fit for the comparison of the 1D grid model to our observations, as a function of the thermospheric temperature and mass loss rate. The red, green, and orange points outlined in black show the location in parameter space of the three models plotted in Figure 5.5.

data cast in terms of the statistical significance of the deviation from a good fit. The banana-shaped contour of good fit quality indicates that the thermospheric temperature and the mass loss rate can be traded against each other to give an acceptable fit to the data for a wide range of values in each parameter. According to the mass continuity equation $\dot{M} = 4\pi r\rho(r)v(r)$, the gas density required to produce the observed absorption signal can be achieved for different combinations of the mass loss rate and the gas radial velocity. For an isothermal Parker wind, the velocity is directly related to the gas temperature, thus giving rise to the mass loss rate - temperature degeneracy. This degeneracy can be reduced somewhat by resolving the shape of the absorption line. Even with the degeneracy between the temperature and the mass loss rate, a large portion of the parameter space can be excluded at high confidence despite the low-resolution of the *HST* data due to the sensitivity of the He triplet to the gas density. Figure 5.5 compares two example models from the excluded region of parameter space to the data, demonstrating the poor fit quality of such models.

The excess absorption in the He triplet that we detect suggests that HAT-P-11b's thermosphere extends to altitudes of at least $2\,\mathrm{R}_p$. Salz et al. [253] performed simulations of hydrodynamic escape from hot gas planets using a coupled photoionization and plasma simulation code with a general hydrodynamics code. For HAT-P-11b, Salz et al. [253] predict a temperature of $T \approx 7,000$ K at $2\,R_p$ and an overall escape rate of $\dot{M} = 2 \times 10^{10}\ \mathrm{g\,s^{-1}}$. Despite the caveats given by Salz et al. [253] for their model (uncertainty in the stellar wind strength, magnetic effects, the effect of metals in the atmosphere, and the correction factor to account for dayside-only heating), Figure 5.5 shows how their prediction falls within their estimated error of the region of good fit quality mapped in Figure 5.8.

We also compared our result to the data underlying the recent detection of the helium infrared triplet in HAT-P-11b using the CARMENES spectrograph [4]. Figure 5.9 shows the CARMENES spectrally resolved data convolved to the much lower resolution of our *HST* data. Our data sets agree well on the size of the helium absorption feature. The confirmation of the ground-based data with our space-based observations, which are free from the influence of telluric lines and transparency variations, adds significant confidence to the detection of this subtle feature.

5.3 Discussion

We find an overall mass loss rate of $0.04 - 2.3\%$ of the total mass of HAT-P-11b per billion years, assuming a 9:1 number ratio of hydrogen and helium in the atmosphere. Additionally, Salz et al. [253] predict a mass loss of $\approx 0.8\%$ over the first 100 Myr after planet formation, when the young star would have caused a much higher escape rate. A total mass loss of 1% would change the radius of HAT-P-11b by 0.4%, or 108 km [263]. As is expected for a Neptune-sized gas giant, this amount of photoevaporation will have a negligible effect on the composition of HAT-P-11b over its lifetime.

Although the mass loss from HAT-P-11b is negligible, smaller sub-Neptunes can be significantly impacted by photoevaporation over their lifetimes. Close-in planets smaller than

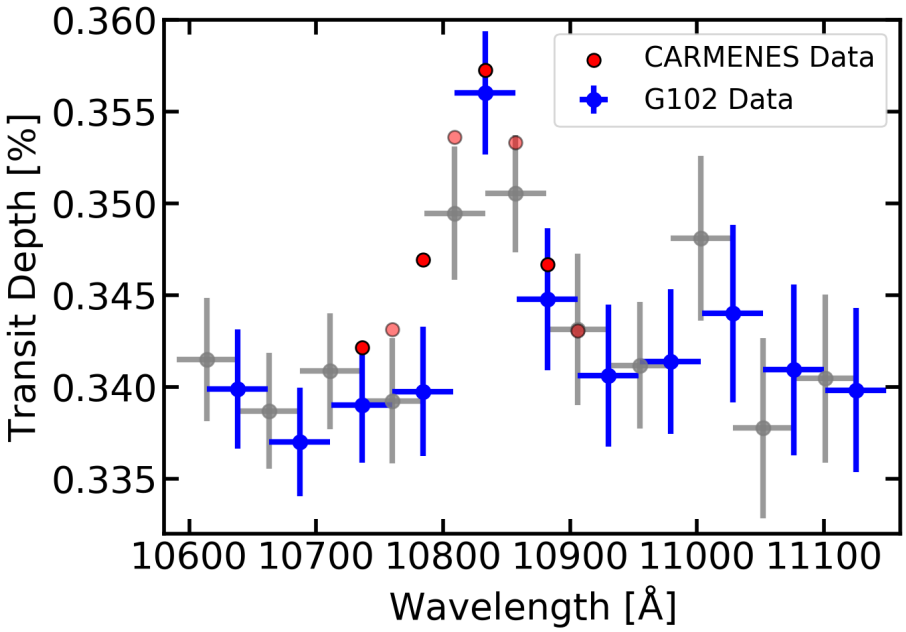

Figure 5.9: Narrowband G102 spectrum (blue and grey points) compared to recent observations of HAT-P-11b with the CARMENES spectrograph [4], convolved to the resolution of our data. The two data sets show excellent agreement in the size of the helium feature at 10,833 Å.

$1.5R_{\oplus}$ may even have their entire primary atmospheres stripped away [177, 225, 226, 91, 308]. Observations of the helium triplet at 10,833 Å provide us with a new way to characterize atmospheric loss from a wider range of planets, which will help to refine models of photoevaporation. Future observations of smaller planets at this wavelength will also help us better constrain the exact nature of super-Earth/sub-Neptune planets and how their atmospheres have evolved over time.

Part III

Data Analysis Methods for Future *JWST* Observations

CHAPTER 6

EIGENSPECTRA: A FRAMEWORK FOR IDENTIFYING SPECTRA FROM 3D ECLIPSE MAPPING

Planets are intrinsically 3D objects, but 1D models are often used to approximate planetary atmospheres[1]. While 1D (vertical-only) models provide computationally inexpensive estimates of the vertical structure and radiative transfer in a single atmospheric column, temperature-pressure profiles can vary substantially for different locations around the planet. Inferring properties of 3D atmospheres with 1D models can correspondingly give biased abundance estimates [79, 35], since these models only approximate the arithmetic mean profile of what can be obtained by General Circulation Models [GCMs; 26]. On the other hand, GCMs have the ability to model atmospheric structures and dynamics fully three-dimensionally, but are much more demanding computationally, making them infeasible for inference and only able to best constrain the physics where robust data sets are available.

Despite the necessity of 3D approaches to accurately model atmospheres, our current data from exoplanet atmospheres are almost entirely limited to 1D or 2D observations. For example, while phase curves are valuable in probing planetary brightness, they can reveal only longitudinal structure as the planet orbits its host star [e.g. 147], with vertical information also accessible if a phase curve is spectroscopic [282]. In order to recover information about all three spatial dimensions, we must combine different data sets in ways that further exploit either the geometry of the system or the spectral imprints of the atmospheric structure.

Secondary eclipses of transiting planets offer valuable opportunities to observe and understand the multidimensional nature of exoplanets [e.g. 321, 246]. As a planet goes behind

1. This chapter is based on Mansfield et al. [199], which was coauthored by Everett Schlawin, Jacob Lustig-Yaeger, Arthur D. Adams, Emily Rauscher, Jacob Arcangeli, Y. Katherina Feng, Prashansa Gupta, Dylan Keating, Kevin B. Stevenson, and Thomas G. Beatty. M. Mansfield led the creation of the Eigenmapping method described in this chapter. E. Schlawin, J. Lustig-Yaeger, A. D. Adams, and E. Rauscher assisted in creating the Eigenmapping method. All other authors contributed to the conception of the Eigenmapping method and early stages of code development.

its star, the stellar limb scans across the dayside hemisphere of the planet, permitting a 2D reconstruction of the planetary photosphere by probing the latitudinal structure. Combining these data with spectral information can add the third dimension, since in principle different wavelengths may probe different altitudes in the planet's atmosphere [albeit not necessarily through a simple correspondence, 58].

The first (and only) published eclipse map of a planet was for the hot Jupiter HD 189733b with the *Spitzer Space Telescope* [53, 190]. This map revealed a localized hot spot which was shifted eastward from the sub-stellar point, as predicted by GCMs [268] and found from the phase curve [147]. The *Spitzer* eclipse map, however, only probed the 2D structure at a single photospheric level because it used broadband photometry. It will be possible to construct spectroscopic secondary eclipse maps with the *James Webb Space Telescope* (*JWST*), which will allow investigations of changing atmospheric properties with altitude as well as with latitude and longitude. *JWST* will provide unprecedented measurements of exoplanet atmospheres due to its large aperture and wavelength range for time series ($\sim 0.6\,\mu$m to $\sim 11\,\mu$m) [e.g. 20, 103, 11]. This could enable high precision eclipse mapping of virtually every bright hot Jupiter observed by *JWST*. Under the Zhang & Showman [332] analytic parameterization of atmospheric dynamics, for example, a single eclipse light curve of HD 189733b with NIRCam's F322W2 grism mode will localize the hot spot longitude to $\sim \pm 3.5^\circ$ in longitude [259].

One of the challenges in mapping exoplanets is determining how to combine these pieces of spatial information in a way that extracts the maximum possible information on the physical state of the planet. Eclipse mapping does not provide a perfect proxy for each spatial dimension; one must account carefully for the inherent degeneracies and uncertainties when reconstructing a global brightness map. One approach is to assume a functional form of the variations in either temperature or flux in longitude and latitude, one that for example captures the angular dependence of the instellation and associated thermal energy budget [130]. From there one can calculate the associated molecular abundances and pressure-

temperature profiles.

Another approach is to forgo any explicit parametrizations about the flux, and instead quantify the available information content from observations by constructing an orthogonal basis of light curves. Spherical harmonics represent an orthogonal basis for 2D representations of maps on a planet photosphere. However, the observations used to make an eclipse map are brightness as a function of time, and spherical harmonics are not orthogonal in this parameter space. Rauscher et al. [247] addressed this issue by developing an orthogonal basis of eclipse light curves, which they term "eigencurves," to best represent the information available from both phase variations and secondary eclipses at a single wavelength. They constructed these eigencurves from linear combinations of spherical harmonic maps. This approach avoids making a priori assumptions about the structure of brightness variations across the planet's photosphere while also providing the ability to directly assess the effects of orbital uncertainties on the retrieval.

In order to extend this framework into the third dimension of multi-wavelength observations we present a method using K-means clustering to identify "eigenspectra,"[2] which are a set of spectra that together represent most of the variance in spectral properties observed over the dayside of the planet. The identification of these eigenspectra allows atmospheric retrievals to be performed on spectra with the smallest possible error bars, while ensuring that regions of the dayside with vastly different atmospheric properties do not get grouped into a single retrieval. We describe our method of identifying eigenspectra in Section 6.1, using three hypothetical *JWST* eclipse maps. We present the results of these hypothetical observations in Section 6.2 and discuss the limitations of the eigenspectra method. We summarize our method and discuss its utility in mapping real planets in Section 6.3.

2. We acknowledge that the spectra are not orthogonal and therefore not formally "eigenvectors," however we use this term colloquially in reference to the "eigencurves" used in our algorithm.

6.1 Methodology

To investigate the potential to perform 3D eclipse mapping with JWST, we first generate synthetic observations of an exoplanet observed in secondary eclipse at multiple wavelengths, and then attempt to recover our original planet map components and their respective emergent spectra. We describe our approach for generating synthetic eclipse light curves in Section 6.1.1, followed by a description of our newly developed model for fitting these multi-dimensional data in Section 6.1.2. The Python code developed for this paper is all publicly available on GitHub[3].

6.1.1 Construction of Planet Maps and Eclipse Light Curves

We demonstrate our method of identifying eigenspectra using three hypothetical maps constructed using the HEALpix projection [102] for which we try to recover the input parameters with our methodology. The model planet-star system for all three maps is based on HD 189733b properties determined by Stassun et al. [278]. Figure 6.1 shows the first map, which we refer to as the "Simplified Hotspot" map, and the spectra used to construct it. The Simplified Hotspot map consists of one higher-flux spectrum painted within a circular region surrounding the substellar point, and a second lower-flux spectrum painted onto the rest of the planet. This mimics a potential, albeit simplified, eclipse map that could result from observation of a hot, synchronously rotating planet such as those that *JWST* will observe. The hotspot has an angular diameter of 50°.

The spectra for the Simplified Hotspot are generated using the radiative transfer model described in detail by Line et al. [174]. We deliberately choose atmospheric parameters that create two distinct spectra. The spectrum assigned to the area inside the hotspot only has methane (CH_4) as a molecular opacity source at a mixing ratio of 10^{-2} ppm. Outside of the hotspot, we input water (H_2O) as a sole molecular opacity source with a mixing ratio of

3. `eigenspectra` code is available on GitHub at https://github.com/multidworlds/eigenspectra

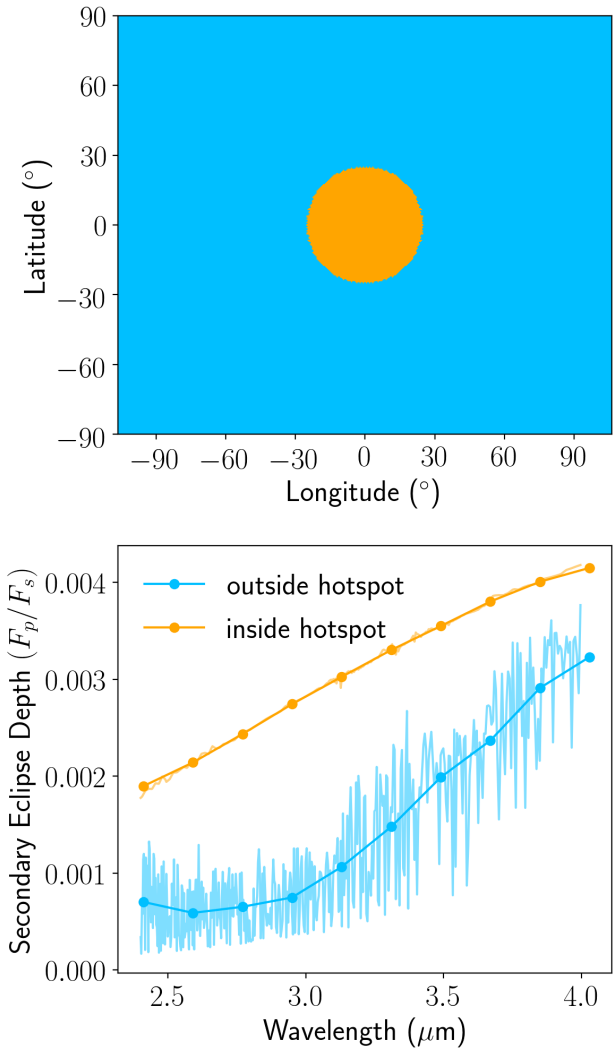

Figure 6.1: Input map (upper panel) and spectra (lower panel) for the Simplified Hotspot map. Colors indicate regions of the map where different spectra are painted on. Thin lines indicate unbinned spectra, and thick lines with points show spectra binned to the 10 wavelength bins used in our analysis. The map is centered on the substellar point and has a longitudinal and latitudinal extent set by the portion of the planet that is visible during our simulated secondary eclipse observing window.

10^3 ppm. We implement the same pressure-temperature profile parameterization to create both spectra: $\log \gamma_1 = -1$, $\log \gamma_2 = -1$, $\log \kappa_{\rm IR} = -1$, $\alpha = 0.5$, $\beta = 1$. We refer the reader to Line et al. [174] for a thorough description of these terms. Briefly, the profile follows one upwelling channel of thermal emission and two downwelling streams of visible radiation. The terms γ_1 and γ_2 correspond to the ratio of the Planck mean opacities of each visible stream to the thermal stream while α divides the flux between the two downwelling visible streams. The parameter β describes the irradiation temperature based on stellar properties. The values we have chosen ensure that there is no thermal inversion in the profile.

The second map we construct is based on the idea that a realistic planet will likely not have two fully separable regions with different spectra, but rather will show a continuum of spectra between regions. Therefore, we construct the "Continuum Hotspot" map shown in Figure 6.2, which has ten nested regions surrounding the substellar point. Each region has an angular width of 9° and is painted with a spectrum with a different water abundance and temperature profile, such that the spectra form a gradient of water abundance and temperature moving outward from the substellar point. We vary H_2O mixing ratio incrementally from 10^{-5} ppm to 10^4 ppm and pair each input abundance with a temperature parameter selected from a range of $\beta = 0.6$ and $\beta = 1.0$. Line et al. [174] define β to encapsulate albedo, emissivity, and day-night redistribution, which determines the irradiation experienced by the planet from the host star; lower values correspond to cooler temperatures. We design the hemisphere such that the central hot spot is high in temperature and saturated with water; as we move to areas further from the hot spot, both the temperature and water abundance decrease. This gradient is not necessarily meant to represent what we think would occur on the dayside of a realistic planet, but is instead intended as a toy model to test the ability of our method to resolve gradual changes in temperature and chemistry across the hemisphere.

The third map (Figure 6.3), which we refer to as the "Asymmetric Hotspot" map, tests the ability of our spherical harmonic-based mapping method to constrain an asymmetric map with a shifted hot spot. It is similar to the Simplified Hotspot map in that it uses

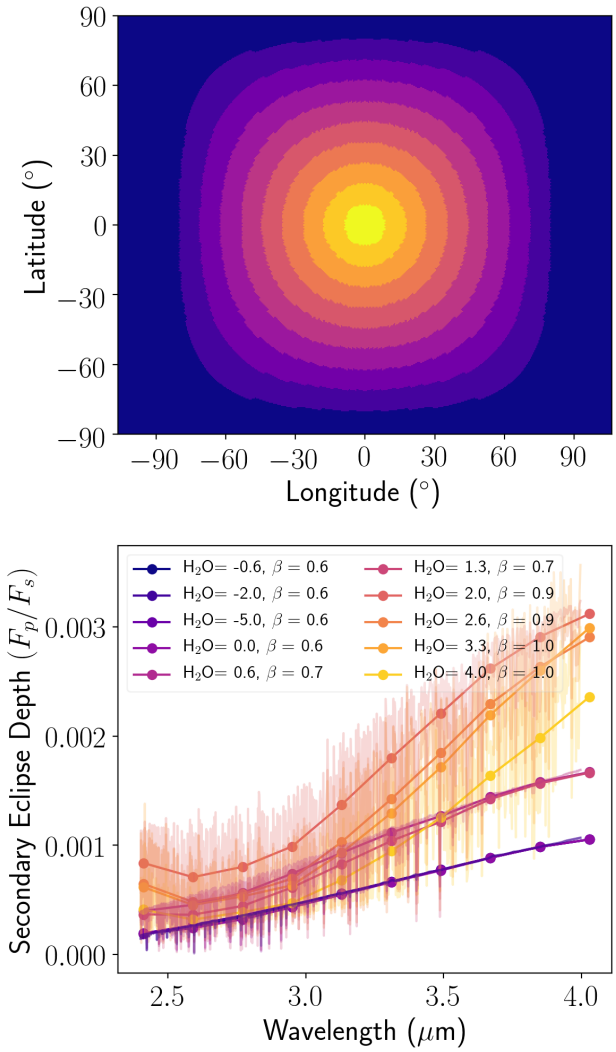

Figure 6.2: Input map (upper panel) and spectra (lower panel) for the Continuum Hotspot map. Colors indicate regions of the map where different spectra are painted on. Thin lines indicate unbinned spectra, and thick lines with points show spectra binned to the 10 wavelength bins used in our analysis. The map is centered on the substellar point and has concentric annular rings along which the fraction of incident flux that is absorbed (β) and log of the H_2O mixing ratio (in ppm) decrease radially from the substellar point.

two easily-separable spectra, but the hotspot is offset from the substellar point, centered at $+45^\circ$ latitude and -30° longitude, and has an angular diameter of 60°. For this test case, the two spectral components are designed to be easily separable and therefore differ in continuum flux, wavelength of their single spectral feature, and relative depth of that feature below the continuum. We specifically design the spectra in this map to have unrealistic shapes so we can separate out our ability to resolve structure across spatial dimensions on the map from our ability to resolve similarly-shaped spectra.

While we construct planet maps that cover the entire planet, we only consider observations during secondary eclipse and so can only constrain the planet's map on the dayside and the small fraction of the nightside we observe just before and after eclipse. However, the method we describe here could be used for full phase curve observations to produce a map covering the whole planet, although outside of secondary eclipse the observations would only be sensitive to variations with longitude, not latitude.

We use the analytic occultation code `starry`[4] [181] to model secondary eclipse light curves. We bin the high-resolution spectra at each HEALpix pixel to a lower resolution wavelength grid between 2.40 μm and 4.0 μm with a fixed $\Delta\lambda = 0.18$ μm, applicable to wavelength-binned data from the *JWST*/NIRCam instrument using the F322W2 filter [104]. For each low-resolution wavelength interval, we expand the HEALpix map in spherical harmonics up to degree $l = 18$, and define a `starry.Secondary` planet object with this wavelength-dependent map. We note that the transformation from HEALpix to spherical harmonics introduces a small amount of error into both the map and the spectra, but this amount is well below the precision of our simulated observations. Finally, we use `starry` to compute analytic secondary eclipse light curves at each wavelength. This results in 10 light curves, which are each normalized to the out-of-eclipse continuum flux at the respective wavelength. A vertical shift is applied so the bottom of the eclipse is defined to be zero planetary flux (but still 100% stellar flux).

4. We used `starry` version 0.3.0, now available at https://github.com/rodluger/starry/tree/v0.3.0.

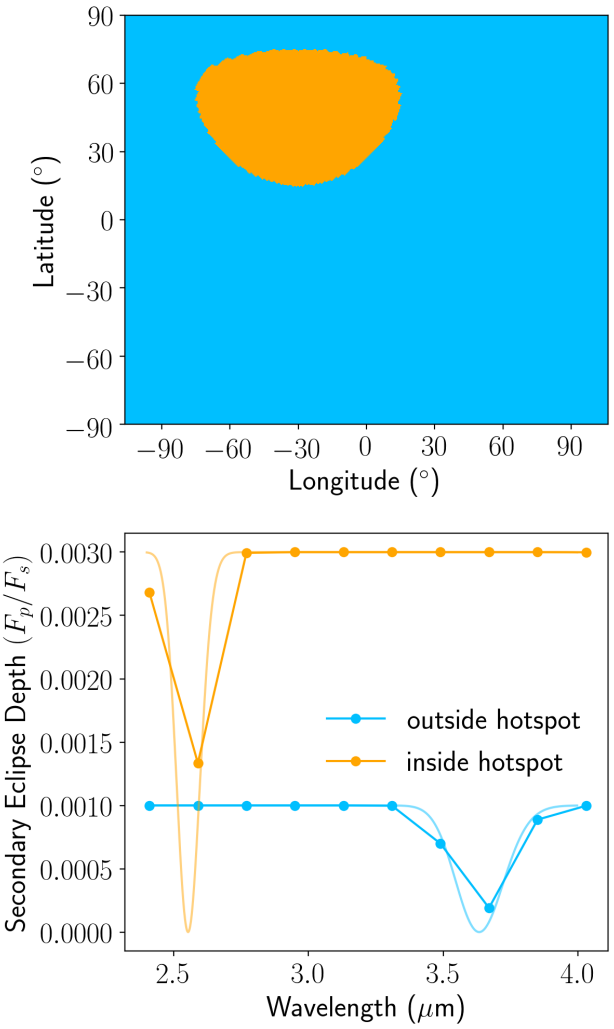

Figure 6.3: Input map (upper panel) and spectra (lower panel) for the Asymmetric Hotspot map. Colors indicate regions of the map where different spectra are painted on. Thin lines indicate unbinned spectra, and thick lines with points show spectra binned to the 10 wavelength bins used in our analysis. The map is centered on the substellar point and has a hotspot centered 45° north and 30° west of the substellar point, and spanning 60° in angular diameter.

We simulate a *JWST* time series observation corresponding to the `starry` light curves. As in Schlawin et al. [259], we use the `pynrc`[5] NIRCam observation simulator to calculate the signal to noise of the spectrum. The signal to noise per integration is used to create a time series for each wavelength. When creating the simulated time series, we add error bars based on the NIRCam observation simulation but do not actually add random noise to the time series.

6.1.2 Extracting the Eigenspectra from Simulated Observations

Figure 6.4 shows an overview of the process we use to extract the eigenspectra. We create a set of light curves from spherical harmonics using the `spiderman` package [180]. We use `spiderman` for this step and `starry` in Section 6.1.1 because of existing legacy code and because using two separate codes for injection and recovery makes the process less circular. We include spherical harmonics up to $l = 2$ because using this many harmonics provides 8 linearly independent eigencurves. This number is many more than can be constrained by eclipse observations at the precision of our simulated measurements [247], so including spherical harmonics up to $l = 2$ will ensure that the number of independent eigencurves is not the limiting factor in our ability to reconstruct eclipse maps. Including higher-order spherical harmonics decreases the efficiency of our code, so we use the smallest number of spherical harmonics possible without limiting the number of usable eigencurves. However, we include in our code the capability to fit for higher-order spherical harmonics if higher-precision data require it. We follow the methods of Rauscher et al. [247] and use principal component analysis (PCA) to construct orthogonal light curves from linear combinations of the spherical harmonics. Using these orthogonal "eigencurves" instead of directly fitting for spherical harmonic coefficients reduces the correlations between parameters, and the PCA produces a list of eigencurves ranked by their relative potential contribution to the observed light curve. For each wavelength that we fit for, we select the number of eigencurves to use

5. https://pynrc.readthedocs.io/en/latest/

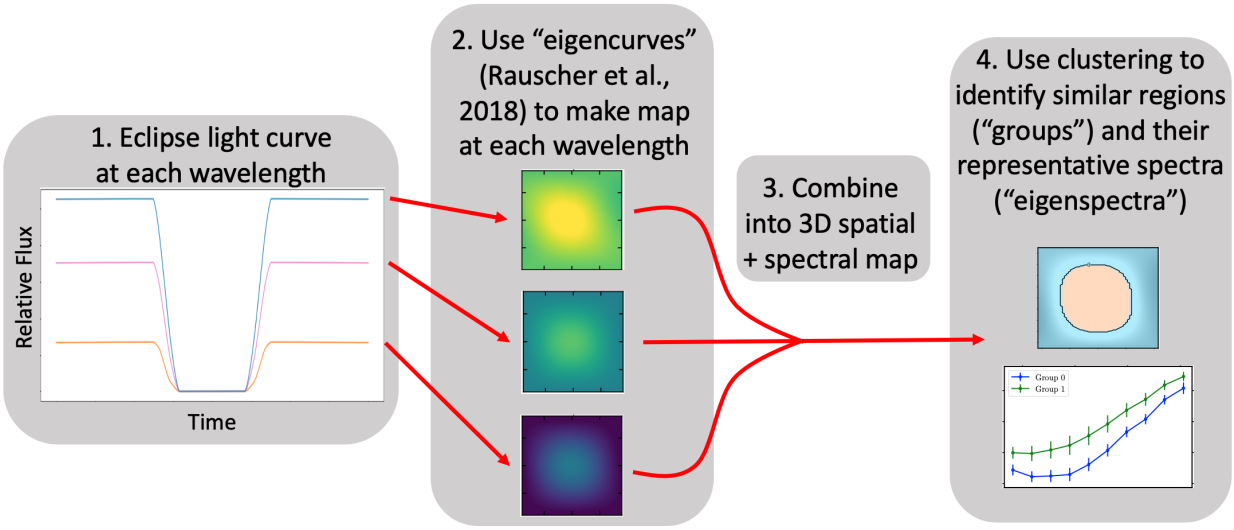

Figure 6.4: Overview of the process we use to extract eigenspectra from the eclipse light curves. We apply the method of Rauscher et al. [247] and use eigencurves to construct a map separately at each wavelength. We then combine these single-wavelength maps into a 3D spatial + spectral map. We use K-means clustering to identify similar regions on this 3D map ("groups") and their representative spectra ("eigenspectra").

at that wavelength by determining the largest number of eigencurves before any of them show significant cross-correlation with each other (see Section 6.2.2 for a discussion of how correlated eigencurves result in a less accurate map). Figure 6.5 shows simulated observations for a single wavelength of the Simplified Hotspot model and the resulting fit.

We estimate the contributions of each eigencurve with a Markov Chain Monte Carlo (MCMC) fit using the `emcee` package [82]. We use 100 walkers and a chain of 3000 steps with a 300-step burn-in. We test for convergence by computing the autocorrelation time for each free parameter and ensuring that the number of samples is at least 50 times larger than the autocorrelation time. We construct an extracted planet map by calculating the contributions of each eigencurve to each coefficient of the spherical harmonics for the map. The MCMC routine returns several hundred realizations of each set of fit components, so we quantify the propagated uncertainty in the flux maps by calculating the mean and variance in the flux at each point across all realizations.

We use K-means clustering to identify regions of the retrieved brightness map with similar

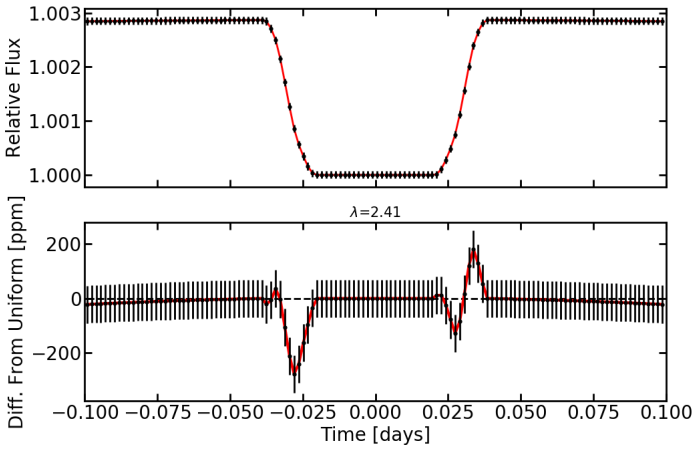

Figure 6.5: Top: Example light curve showing simulated data (black points) at $\lambda = 2.41$ μm for the Simplified Hotspot model. Red line shows the fit using the eigencurve method of Rauscher et al. [247]. Bottom: Difference in flux from a uniform sphere for our eigencurve fit (red line) and simulated data (black points).

spectra. K-means clustering is an algorithm that groups a number of observations n, which can be vectors, into K clusters [234]. We use K-means clustering rather than PCA because K-means provides the capability to cluster in multidimensional space, so we can identify regions that are spectrally similar. PCA could be used to pick out orthogonal spectral features that have the largest variance across the map but not group the spectra into similar categories. A further advantage with K-means is that its output can be more easily turned into a map because it assigns each spectrum to a single group, whereas PCA would output what percentages of each spectrum come from each principal component. We also note that the changes in spectral features due to a cloud or chemical difference may not necessarily be orthogonal.

We select 100 random samples from the MCMC chain to perform clustering on. For each sample, we divide the extracted planet map into $n = 10^4$ sectors (100 divisions each in latitude and longitude). We input the spectra from each section of each sample's map into the clustering algorithm. We treat the spectrum at each point as a multi-dimensional vector, and group the set of spectra into K groups and 10 spectral bins. This allows us to

identify regions on the retrieved map with similar spectra. From this, we take the mean of all the spectra in each group as the representative spectrum, or "eigenspectrum", of that group. The errors on each group's "eigenspectrum" are the standard deviation of all of the spectra from all of the maps which were identified as belonging to that group. We note that correctly propagating errors through a non-deterministic method such as K-means clustering is not straightforward, so we leave a more detailed study of the correct error propagation for future work. As we show in Section 6.2, the method we use in this paper is sufficient to identify large-scale spatial and spectral features in our simulated observations.

6.2 Mapping Results and Discussion

Figures 6.6, 6.7, and 6.8 show the output flux maps and groupings our pipeline produces for the Simplified Hotspot, Continuum Hotspot, and Asymmetric Hotspot maps, respectively. Figures 6.9, 6.10, and 6.11 show the corresponding eigenspectra retrieved from these maps compared to the input spectra. In Section 6.2.1 we use the Simplified Hotspot map to discuss how our pipeline performs in an idealized case. We use the Continuum Hotspot model to test the limits of our pipeline's ability to retrieve spectral information as quantified by the number of significant eigencurves (Section 6.2.2) and groups (Section 6.2.3). Finally, in Section 6.2.4, we use the Asymmetric Hotspot map to test how well our pipeline can represent flux distributions that aren't symmetric about the substellar point.

6.2.1 The Simplified Hotspot Map

The Simplified Hotspot map was originally created using two distinct spectra, so to test the ability of our methods to recover these spectra we use K-means clustering to create two groups with different eigenspectra. Figure 6.6 shows two ways to visualize the eigenspectra groupings on the Simplified Hotspot model. This figure shows the areas of the map grouped into the two eigenspectra, the calculated fluxes, and the uncertainties in the fluxes at a

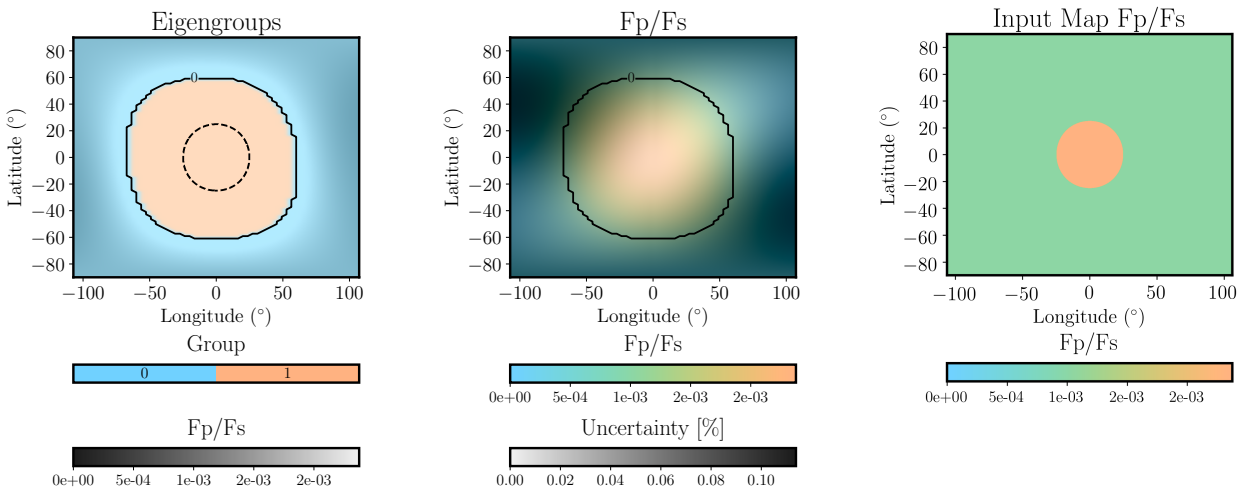

Figure 6.6: Retrieved spectral group maps for the Simplified Hotspot model. The solid contours delineate separations by best-fit groups in each plot. *Left:* The hue represents the best-fit group from the K-means clustering algorithm, and the brightness represents the mean intensity ratio (F_p/F_s) in the observed wavelength range. Note that here and in Figures 6.7 and 6.8 we use F_p to refer to the intensity of the planet at that point multiplied by the planet's solid angle, so that the ratio F_p/F_s is unitless. The dashed contour indicates the extent of the hotspot in the original input model. *Middle:* The hue represents the mean F_p/F_s, and the brightness represents the uncertainty in the eclipse depth. *Right:* The mean F_p/F_s from the input map, on the same color scale as the output map in the middle panel.

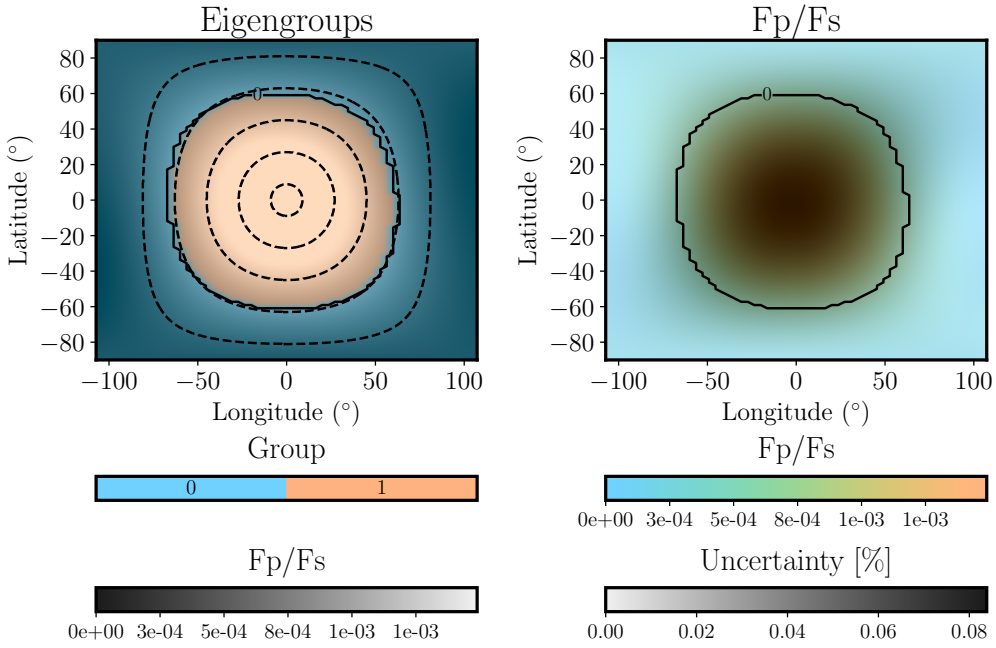

Figure 6.7: Same as first two panels of Figure 6.6, but for the Continuum Hotspot model. For clarity, the dashed lines show the boundary of every other ring in the original input model.

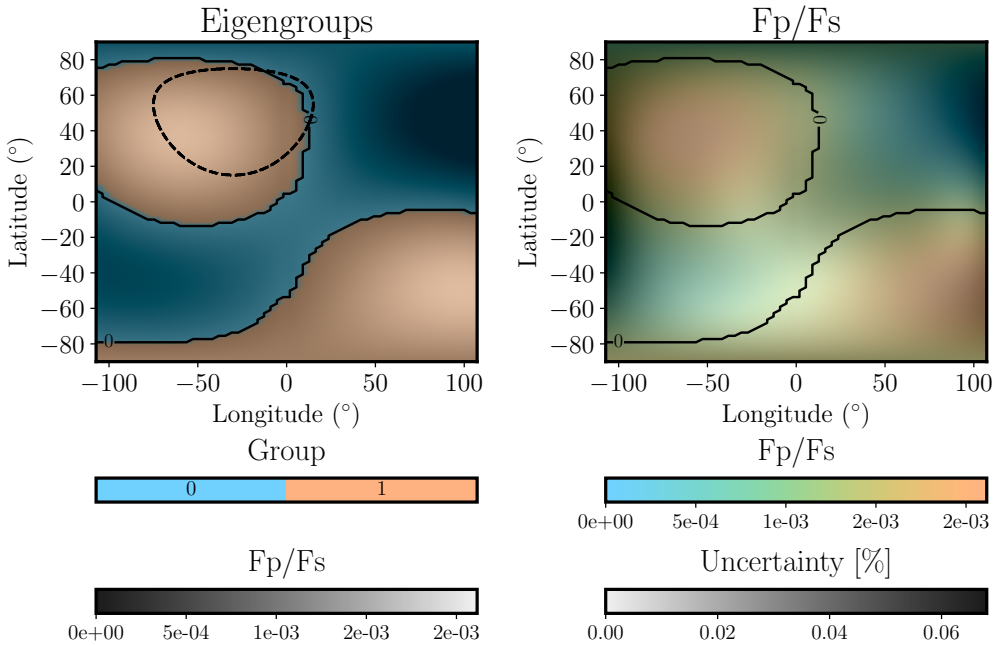

Figure 6.8: Same as first two panels of Figure 6.6, but for the Asymmetric Hotspot model.

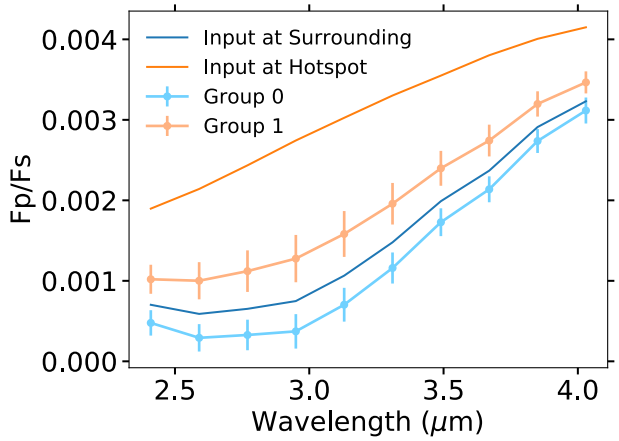

Figure 6.9: Results of K-means clustering to recover two groups from the Simplified Hotspot map. The orange and blue lines without error bars show the original input spectra from Figure 6.1, while the lines with error bars show output spectra for the regions of the map assigned to Group 0 (surrounding the hotspot) and Group 1 (inside the hotspot). The K-means clustering method identifies a larger hotspot than the input map, which results in some mixing of the input spectra, but generally correctly identifies the spectral shapes.

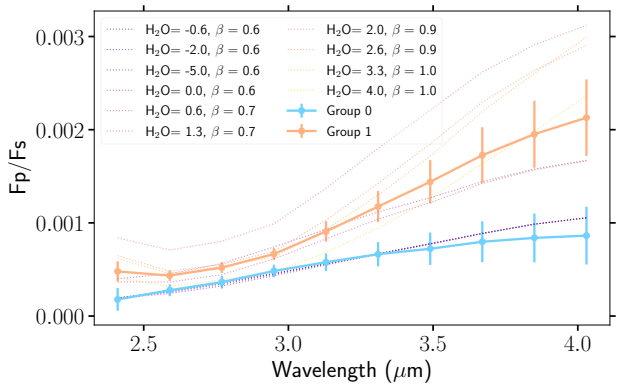

Figure 6.10: Results of K-means clustering to recover two groups from the Continuum Hotspot map, which has ten distinct input spectral groups. The dotted lines without error bars show the original input spectra from Figure 6.2, while the lines with error bars show output spectra for the regions of the map assigned to Group 0 (surrounding the hotspot) and Group 1 (inside the hotspot). The K-means clustering method delineates the groups at a radial distance intermediate between the center and boundary of the input continuum hotspot.

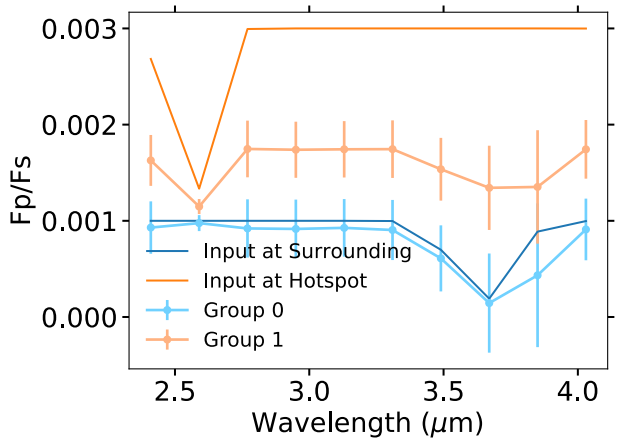

Figure 6.11: Results of K-means clustering to recover two groups from the Asymmetric Hotspot map. The orange and blue lines without error bars show the original input spectra from Figure 6.3, while the lines with error bars show output spectra for the regions of the map assigned to Group 0 (surrounding the hotspot) and Group 1 (inside the hotspot). The K-means clustering method identifies a secondary hotspot, which results in some mixing of the input spectra, but generally correctly identifies the spectral shapes.

wavelength of 2.43 μm. The rightmost plot in this Figure shows the original input map on the same flux scale as the output flux map for comparison. Figure 6.6 shows that the K-means clustering generally identified the structure of our input map correctly, although comparison to Figure 6.1 shows that the hotspot output by the K-means clustering is more spatially extended than the input hotspot. Our maps are constructed using the eigencurves method of Rauscher et al. [247], which can not reproduce sudden discontinuities in flux across the map, so our inability to identify the exact extent of the hotspot is likely because the eigencurves can not perfectly represent the sharp edge between the two groups. We construct this map using only the first four eigencurves because adding more eigencurves would result in larger error bars (see Section 6.2.2). This means our map is limited to large-scale flux differences and would not be able to show small-scale changes [247], which may be another reason for the broadening of the hotspot in our output map compared to the input map. Our inability to identify small-scale flux changes when representing the map with just a few eigencurves explains why the output map shows a high precision even in regions where the output map flux is many sigma away from the input map flux (for example, at around 30° away from the substellar point, where the input map shows a low flux outside the hotspot but the output map precisely identifies a high-flux hotspot region). Each realization of our output map from the MCMC correctly identifies that there is a substellar hotspot, but the angular size of this hotspot is restricted by the small number of eigencurves we use. Therefore, our output map shows a small uncertainty in this region because each realization of the map shows a very similar flux distribution there, despite the fact that this flux distribution does not match the "true" input distribution. We discuss in Section 6.2.2 why we restrict ourselves to this small number of eigencurves in this paper and methods for incorporating information from larger numbers of eigencurves, which could potentially identify smaller-scale features.

This slight mixing of the areas on the edges of the two input groups can also be seen in Figure 6.9, which shows the eigenspectra for the two groups identified by the K-means clustering compared to the input spectra for the hotspot and surrounding area. The K-means

clustering correctly identifies a higher-flux central region and a lower-flux surrounding region. However, the clustering algorithm includes some of the surrounding area in the hotspot, which dilutes it and leads to a lower-flux spectrum for the output Group 1. Despite this dilution, our method correctly identifies the general shape of the input map and spectra.

6.2.2 How Many Eigencurves Should Be Used?

We tested modeling the Continuum Hotspot map with different numbers of eigencurves to determine a best practice for selecting how many eigencurves to include when analyzing a set of data. Rauscher et al. [247] discuss how adding more eigencurves to a fit eventually results in maps that are more uncertain than those with fewer eigencurves. We find a similar result using the Continuum Hotspot map. We test modeling this map with up to five eigencurves and find that four eigencurves provide a good fit to the synthetic data, while at all wavelengths using five eigencurves introduces degeneracies that make the results more uncertain and increases the variance in the fits.

We demonstrate this degeneracy in Figures 6.12, 6.13, and 6.14. Figure 6.12 shows the cross-correlation coefficients at a wavelength of 2.41 μm for models using four (top panel) and five (bottom panel) eigencurves. When four eigencurves are used, the only terms showing high correlation coefficients > 0.8 are the first two terms, which as described in Rauscher et al. [247] are not expected to be orthogonal. However, with five eigencurves the other coefficients begin to show significant cross-correlation. The coefficients are designed to be orthogonal, so this correlation is a sign of using too many coefficients.

Rauscher et al. [247] also found that using more eigencurves than can be well constrained by the data resulted in larger uncertainties on the derived temperature as a function of longitude. Figure 6.13 shows that we find the same result for our test. This figure shows brightness temperature as a function of longitude for 1000 random samples from the MCMC fits using four vs. five eigencurves. With five eigencurves, the samples show a wider spread in derived temperatures. Additionally, when using five eigencurves, there are some samples

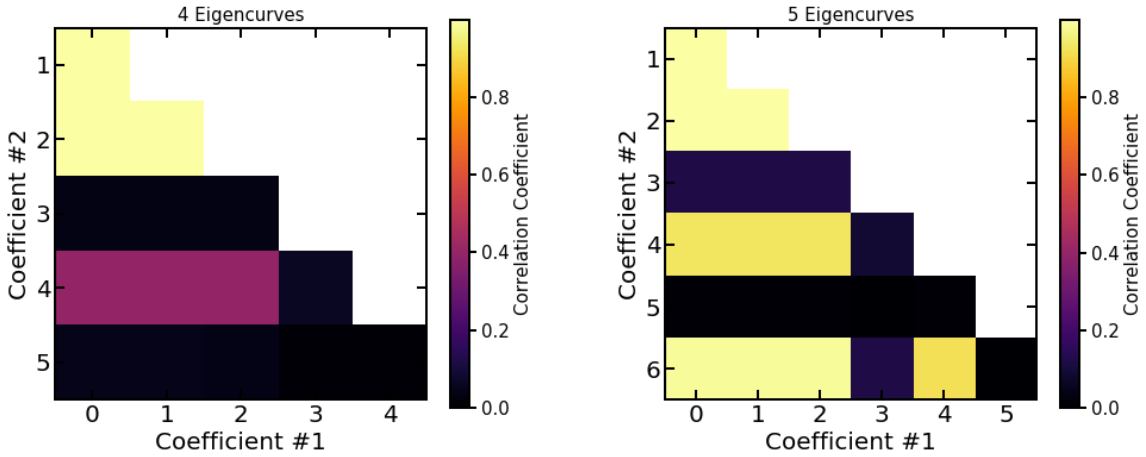

Figure 6.12: Diagrams showing cross-correlation coefficients between the eigencurves at a wavelength of 2.41 μm for models of the Continuum Hotspot using four and five eigencurves (left and right plots, respectively). For the case with four eigencurves, the only coefficients that are strongly correlated with any of the others are the first two coefficients, which represent the uniform-planet-brightness coefficient and a correction to the stellar flux. As described in Rauscher et al. [247], these two coefficients are not orthogonal by design the way the rest of the eigencurve coefficients are, so they are expected to show some correlation with the other coefficients. However, with five eigencurves there are several other eigencurve coefficients which are significantly correlated with each other. This indicates that the model produces a degenerate solution when more eigencurves are included than the amount that can be well-constrained at the noise level of the data [247].

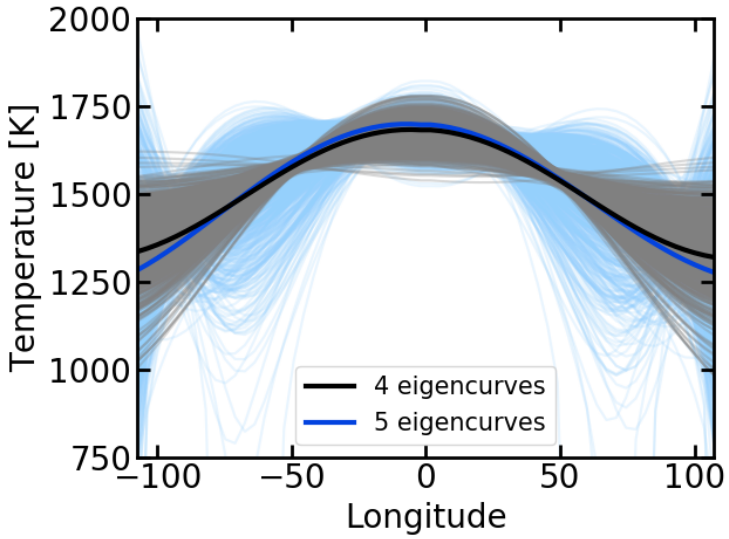

Figure 6.13: Brightness temperature along the equator as a function of longitude (in degrees) for the Continuum Hotspot Map, modeled using four (black) and five (blue) eigencurves. The thick line shows the best-fit solution, while the thin lines show 1000 random samples from the MCMC chain for each fit. Both models converge on similar best-fit solutions. However, the model using four eigencurves, which can be well constrained at the noise level of the data, shows a smaller spread in the derived temperatures. The model using five eigencurves shows a larger spread in the derived temperatures, including some MCMC samples where the temperature drops to unphysical negative values at some longitudes, because this model contains more eigencurves than can be well constrained by the data and is instead driven by the uninformative prior on the fifth eigencurve [247].

where the temperature drops to unphysical negative values at some longitudes. This increase in the variance of the temperature with a larger number of eigencurves is due to the way in which each eigencurve coefficient is influenced by the information contained in the simulated observations vs. the prior on that coefficient. As described by Rauscher et al. [247], the first few eigencurves contain the most information from the data. In this case, the first four eigencurves have posteriors that are primarily driven by the data. However, the posterior of the fifth eigencurve is primarily driven by its prior and not the data. We use uninformative, uniform priors for the eigencurves, so when we add an eigencurve with a posterior driven by this uniform prior to our fit, it results in a much larger uncertainty in the fit.

This increased uncertainty from using too many eigencurves can also be seen in Figure 6.14, which compares the output eigenspectra when using four vs. five eigencurves.

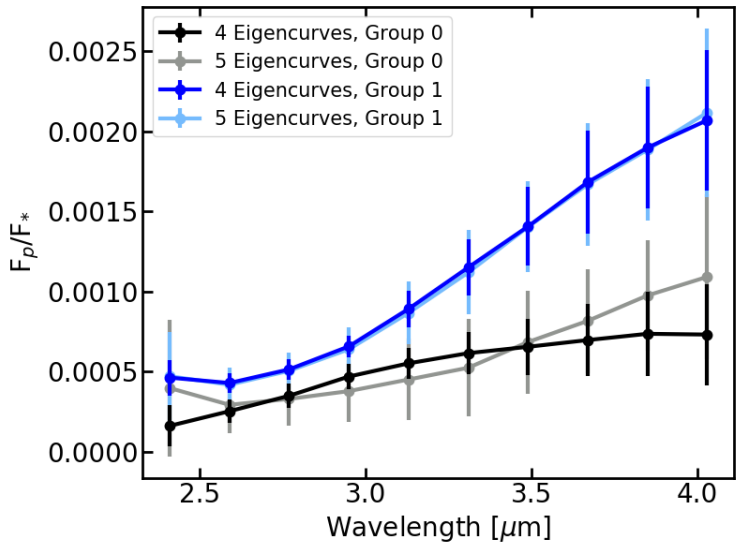

Figure 6.14: Eigenspectra for the Continuum Hotspot model when using four (dark blue and black points) vs. five (light blue and grey points) eigencurves. A model using five eigencurves results in spectra with larger error bars because some of the eigencurves are correlated, which leads to increased uncertainty in the planet map.

Even when the map is grouped into two regions in both cases, using four eigencurves results in both eigenspectra being better constrained and having smaller error bars than using five eigencurves.

When selecting the number of eigencurves to use to model a data set, we recommend using the method of Rauscher et al. [247] and using the largest number of eigencurves for which none of them are significantly correlated with each other. We also found that adding additional eigencurves beyond this point resulted in an increase in the Bayesian Information Criterion (BIC), so this fitting criterion can be used to identify how many eigencurves to use.

One way to include more eigencurves in the fit would be to use more informative priors on the eigencurves. In this case, the priors could be selected based on expectations from a GCM or other model. While this could in principle permit a map that shows smaller-scale structures than our maps which use only the first four eigencurves, we choose to limit ourselves to considering fits with smaller numbers of eigencurves because we aim to determine how much information could be extracted from the data without incorporating any prior

information from preexisting models. Additionally, while incorporating more restrictive priors could allow the use of more eigencurves without resulting in nonphysical solutions with negative temperatures, observing negative fluxes is informative because it shows that the solutions fall in a nonphysical region of parameter space.

6.2.3 How Many Groups Should Be Used?

We also used the Continuum Hotspot model to determine how many groups should be used when mapping. While the model contains 10 groups, the size of the error bars in the simulated observations determines how effectively these groups can be distinguished from each other. Figure 6.15 compares the planet maps when clustering the map into two or three groups. We performed the K-means clustering on 100 realizations of the map from the MCMC chain. The maps shown in Figure 6.15 display the mean group number at each point. The histograms show, for specific points on the maps, the grouping of that point over all of the MCMC samples which were run through the clustering algorithm.

We find that, for the Continuum Hotspot map, grouping the map into two groups results in clearly-defined groups, and at each step in the MCMC chain the group division occurs at almost the same position on the map. When using three groups, the mean map shows the shell structure contained in the original input map. However, the histograms show much more variation in the grouping of each individual point along the MCMC chain. With two groups almost all of the map pixels are consistently grouped into the same group, but with three groups the grouping varies significantly. This suggests that our data are only precise enough to constrain two distinct groups. We show the eigenspectra for the two-group case in Figure 6.10.

When selecting the number of groups to use in the K-means clustering, we recommend using the largest number of groups such that most of the map pixels are still precisely constrained to be within a single group across the MCMC chain.

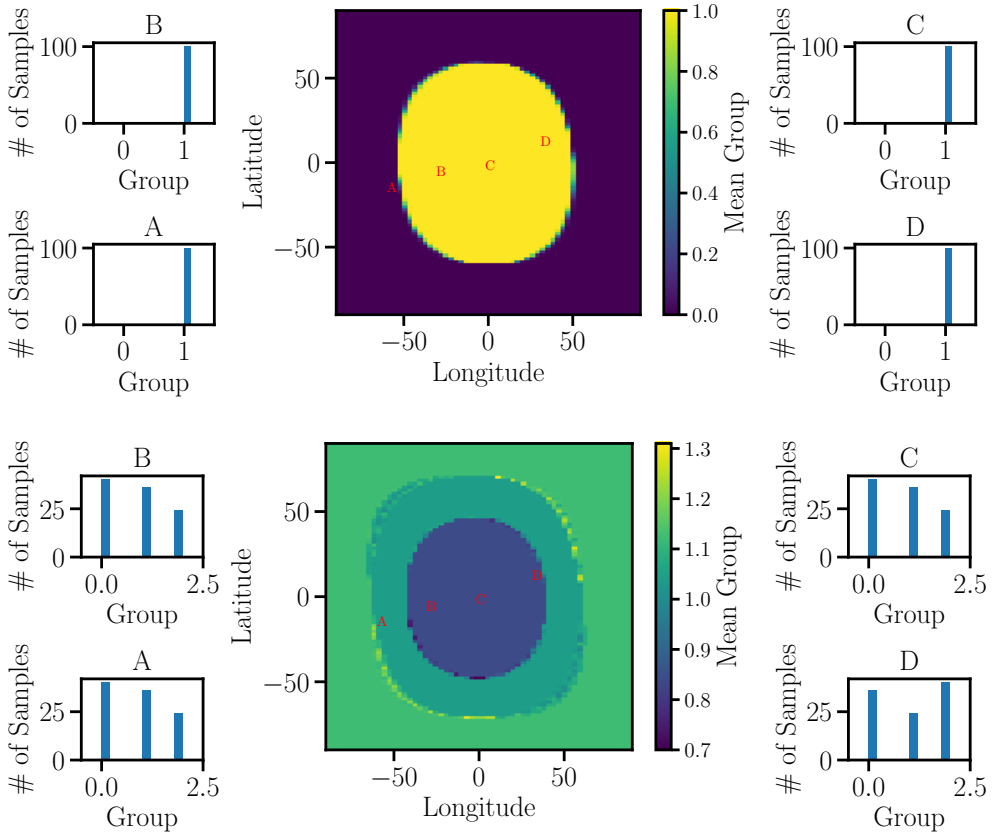

Figure 6.15: Group assignments for the Continuum Hotspot model for two groups (top) and three groups (bottom). Maps show the mean group assignment across 100 realizations from the MCMC chain, and histograms show the full distribution of groupings across those 100 realizations for the four points indicated by red letters on each map. When two groups are used, almost all points in the map are consistently placed in the same group across all 100 realizations. However, with three groups there is much more variation in the grouping, which indicates that our simulated data are only precise enough to constrain two groups.

6.2.4 Limits of Mapping Asymmetric Planets

The maps which have been discussed up to this point all show some form of a hotspot centered on the substellar point. However, close-in exoplanets may show hotspots offset from the substellar point [e.g. 147, 190], so we used the Asymmetric Hotspot map to examine how well a spherical harmonic-based model can represent structure on a map that is asymmetric about the substellar point. The eigenmapping method correctly identifies the location of the offset hotspot, as shown in Figure 6.8. However, one disadvantage of using the eigencurves method to model a planet map is they tend to produce structure that is somehow symmetric about the substellar point, because the first few eigencurves only give information on large-scale gradients that are all symmetric about the substellar point [247]. This is demonstrated in Figure 6.16, which shows maps corresponding to each individual eigencurve. The fourth map has a bright spot in the upper left quadrant of the dayside, similar to our Asymmetric Hotspot model, but also has a bright spot in the lower left quadrant. Combining this eigencurve with other eigencurves can mute the bright spot in the lower left quadrant slightly, but as shown in Figure 6.8 the final map still shows a secondary hotspot in the lower left quadrant. Our clustering groups this secondary hotspot with the primary one, which causes mixing of the input spectra in the output eigenspectra (Figure 6.11). Our method therefore seems to work best for maps which are symmetric about the substellar point or for determing large-scale flux gradients across the dayside, and small-scale structure within the maps should not be over-interpreted. However, our method is still useful for creating maps that only depend on a non-parametric model and are independent of any GCMs or other circulation models. More restrictive priors on the eigencurve coefficients could allow a fit with more eigencurves, which could in turn allow more accurate models of asymmetric flux distributions for the reasons discussed in Section 6.2.2. However, for this paper we choose to examine what can be observed without incorporating prior information from GCMs.

Our results from the Asymmetric Hotspot model also reveal that our mapping method is more sensitive to planets where the flux gradient between the hottest and coldest points

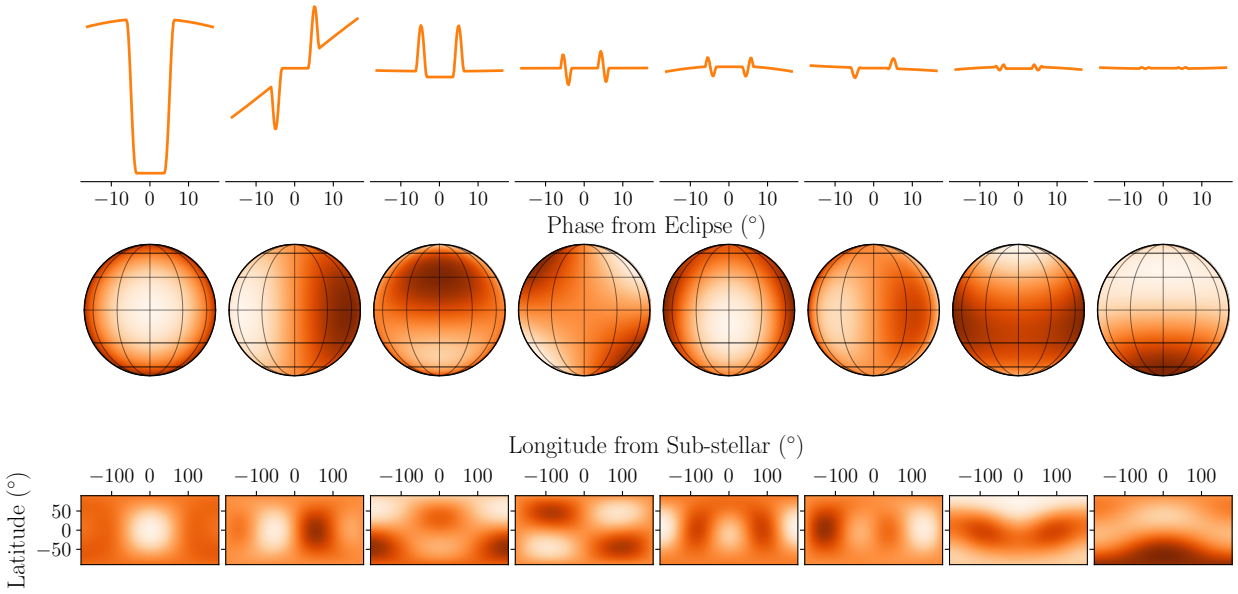

Figure 6.16: Eigencurves and eigenmaps for the Asymmetric Hotspot Map. The top row shows the eigencurves, or the relative flux contribution as a function of phase from eclipse. The middle and bottom rows show two different projections of maps corresponding to each individual eigencurve. The final map was constructed from between 4-7 eigencurves depending on the wavelength, and the number of eigencurves at each wavelength was chosen following the procedure in Section 6.2.2.

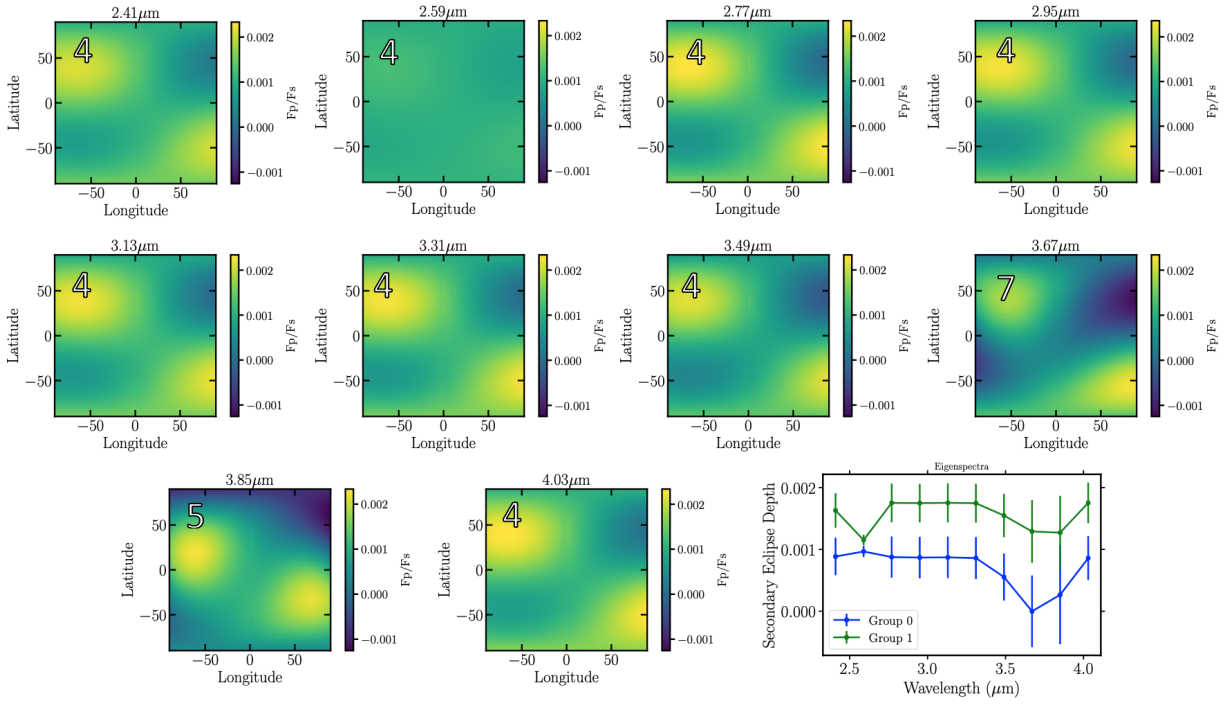

Figure 6.17: Final output maps from the eigencurve fitting routine for each individual wavelength for the Asymmetric Hotspot map. Note that the brightness scale in these maps shows the same mean intensity ratio as in Figures 6.6, 6.7, and 6.8. Numbers in the corner of each map show the number of eigencurves which was preferred at that wavelength. Bottom right plot shows the eigenspectra for the offset hotspot map. Generally the eigencurve fitting routine prefers more eigencurves at wavelengths where the difference between the eigenspectra is larger (e.g., 3.67 μm) and less eigencurves at wavelengths where the difference between the eigenspectra is smaller (e.g., 2.59 μm).

on the dayside is larger. Figure 6.17 displays the median maps output at each individual wavelength, along with the final eigenspectra. Large numbers on each plot indicate the number of eigencurves that were favored at that wavelength based on the procedure described in Section 6.2.2. We found that wavelengths where there is a larger contrast between the two input spectra allowed for a larger number of eigencurves to be fit, which in turn leads to a more detailed map.

6.3 Conclusion

We have developed a framework to group the dayside emission spectra of exoplanets observed in secondary eclipse into unique spectral components ("eigenspectra") emerging from different locations on the planetary disk. Our approach extends the method of 2D eclipse mapping into the wavelength dimension, opening the door to spatially-resolved studies of exoplanet atmospheric vertical structure and composition. To make such inference computationally tractable, our method identifies and groups spatial map components with intrinsically similar spectra, thereby reducing the dimensionality of any subsequent atmospheric retrieval.

Here we outline the main steps in our method. First, we use the `spiderman` package to fit a planet map to a light curve [180]. We base our fit on spherical harmonic maps and use the method of Rauscher et al. [247] to construct orthogonal eigencurves from these spherical harmonic maps. Once we have constructed this map, we use K-means clustering to select regions of the map with similar spectra, and from each of these regions extract an "eigenspectrum", which is the mean spectrum of that region. These eigenspectra could then be analyzed with an atmospheric retrieval code to assess the chemistry and thermal structure of the planet.

We demonstrated how this method can be used to analyze multi-wavelength eclipse light curves of hot Jupiters using *JWST*. To provide accurate and robust mapping results with our method, the following best practices should be used:

- As was found in Rauscher et al. [247], the number of eigencurves used to construct a map at any given wavelength should be the largest number for which the coefficients to the eigencurves do not show any significant correlation. The number of eigencurves in a fit could be increased by using informative priors based on GCMs for the eigencurve coefficients.

- The number of unique spectra in the final map can be found by iterating the K-means algorithm until the recovered spectra are not overlapping and are separated into clearly

defined regions of the map.

We additionally identify the following limitations of our method:

- Structures that are strongly asymmetric about the substellar point are hard to fit well with eigencurves unless additional information from circulation models is incorporated into the fit.

- Using a finite number of eigencurves limits the spatial resolution of our map, so sharp gradients or discontinuities may be blurred. Our method should be able to recover that there *are* large changes in conditions, but will not do a good job of resolving the *spatial scale* of the change.

Our technique is readily able to identify that a planet has regions with distinct spectral features. However, it may not resolve the exact scale of features on planets with sharp spatial discontinuities in atmospheric structure or properties (e.g., aerosols, H_2O dissociation) or planets with multiple gradients simultaneously impacting the flux distribution unless they have particularly distinct regions. A general recommendation for using this method is that particular attention is given to which pieces of spectral-spatial information are or are not accessible in the observations. In particular, rather than presenting a derived map as the true "image" of the planet, the component parts that were used in the fit must also be shown, so that it is clear what was the potentially recoverable information.

However, hot Jupiters, which are the class of planet most amenable to eclipse mapping, are predicted to show large hemispheric gradients, which is the type of spatial pattern that the eigenspectra method could most easily map. Additionally, our method avoids assuming that the flux pattern across the planet follows expectations from any one physical model, making it a useful tool for first investigations of large-scale structure in a planet map regardless of the exact spatial-spectral patterns. More complex, physical models such as GCMs could be used to investigate the planet in more detail after the eigenspectra method was used to

search for key large-scale patterns. The eigenspectra method could also be used to determine which features predicted by GCMs would be measureable via eclipse mapping.

With a large aperture and spectroscopic thermal infrared capability, *JWST* promises precision data products capable of advancing the legacy of *Spitzer*. In this paper, we have taken the first of many necessary steps towards a data-driven perspective on the 3D nature of exoplanet atmospheres.

CHAPTER 7

IDENTIFYING ATMOSPHERES ON ROCKY EXOPLANETS THROUGH INFERRED HIGH ALBEDO

The *Transiting Exoplanet Survey Satellite* (*TESS*) has already discovered many small, likely rocky exoplanets around K and M dwarfs [e.g., 310, 63, 107, 157, 183, 50, 322, 71, 304][1]. In the near future, the *James Webb Space Telescope* (*JWST*) will provide the capability for atmospheric characterization of such small planets. However, it is currently unknown whether small planets around M dwarfs can retain atmospheres. The high X-ray and ultraviolet flux ("XUV" flux) of M dwarfs may completely strip the atmospheres off small, close-in planets. This process is thought to sculpt the observed population of close-in exoplanets, dividing small planets into two categories - those with radii smaller than $\approx 1.5R_{\oplus}$, which are likely rocky cores stripped of any primordial light-element atmospheres, and those with radii larger than $\approx 2R_{\oplus}$, which retain some hydrogen and helium in their atmospheres [177, 225, 248, 226, 90, 308, but see Ginzburg et al. 100 for an alternate explanation]. However, small-radius planets with periods of order 10 days can nevertheless have secondary atmospheres if the volatiles are outgassed from their interiors late in the system's history relative to the early period of high UV flux [296], are delivered by late bombardments of comets or asteroids, have high molecular weight [60], or are effective infrared coolants [135].

One possible way to test for the presence of an atmosphere on a small planet is to look for a smaller phase curve amplitude than expected for bare rock, which for planets that are synchronously rotating would indicate the presence of an atmosphere redistributing heat to the planet's nightside [262]. However, this method requires a large investment of telescope

1. This chapter is based on Mansfield et al. [196], which was coauthored by Edwin S. Kite, Renyu Hu, Daniel D. B. Koll, Matej Malik, Jacob L. Bean, and Eliza M.-R. Kempton. M. Mansfield led the modeling of small planet albedos presented in this chapter. E. S. Kite contributed to the conception of the small planet albedo study. R. Hu created the rocky surface reflectance spectra shown in Figure 7.3. D. D. B. Koll and M. Malik wrote complementary papers on detecting the presence of atmospheres on terrestrial planets through heat redistribution to the nightside [152] and 1D [191] and 3D [150] terrestrial planet atmosphere modeling. All other authors contributed to the development of the terrestrial planet atmosphere detection methods described in this chapter and in Koll et al. [152].

time to observe at least a half orbit, if not a full orbit, of the planet. The atmosphere could also be detected through observing features in a transmission spectrum, but clouds or hazes may obscure any features even if the planet has an atmosphere [e.g., 161]. Emission spectroscopy can reveal atmospheric features without being limited by the presence of clouds or hazes, but it also requires a significant investment of telescope times to detect spectroscopic features, especially for cooler planets [214]. In a companion paper we present a fourth method, which is to look for heat redistribution through its effect on the broadband secondary eclipse depth [152]. If the planet's atmosphere is transporting heat from the dayside to the nightside, then the secondary eclipse depth will be much shallower than expected for a bare rock.

We present another approach for detecting the presence of an atmosphere. For a synchronously rotating rocky exoplanet orbiting a cool host star, observations of the thermal emission constrain the planet's dayside temperature, which can be used to infer its albedo at visible wavelengths by equating the incoming solar radiation to the planet's outgoing radiation. This method has been used previously to infer the albedos of giant exoplanets [47]. If possible exoplanet surface compositions have relatively low albedos, a high measured albedo would indicate the presence of an atmosphere, as illustrated in Figure 7.1.

This method of atmospheric detection is complementary to the methods described above, because it provides a way to detect thin atmospheres that do not transport enough heat to impact the planet's thermal phase curve or secondary eclipse depth but have high-albedo clouds. Solar system bodies with atmospheres thinner than 1 bar (e.g. Mars) are still able to host significant high-albedo cloud layers with optical depths of order unity, so it is possible that some exoplanet atmospheres will be similar [273, 45, 108]. Additionally, the top of the H_2SO_4 cloud deck on Venus is at a pressure level of $\approx$ 1 bar [72], suggesting that a thin atmosphere with a Venus-like composition could also host high-albedo clouds.

In Section 7.1.1 we calculate the range of planet substellar temperatures at which a high-albedo detection points unambiguously to the presence of an atmosphere. We describe our

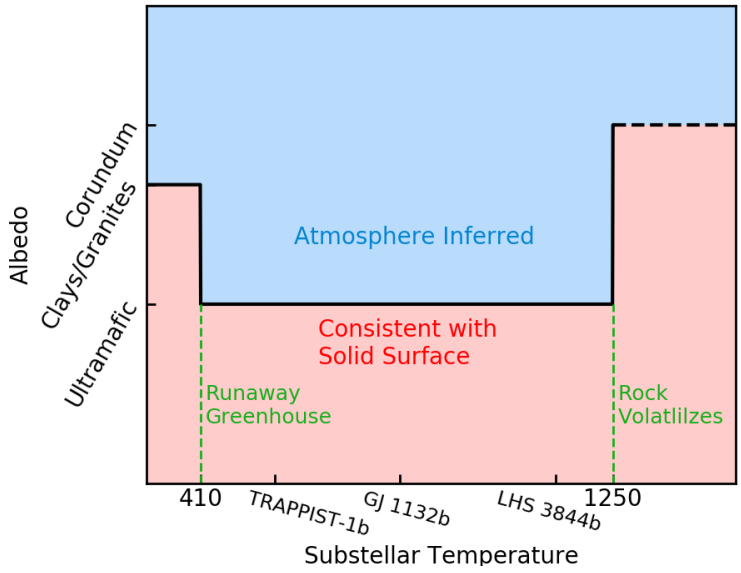

Figure 7.1: Cartoon demonstrating how measurements of the albedo can determine whether a planet hosts an atmosphere. As we describe in Section 7.1.1, high-albedo, water-rich materials such as clays and granites can form at temperatures below 410 K where planets are not guaranteed to have entered a runaway greenhouse. At temperatures above 1250 K, the rock partially volatilizes. This process may lead to the formation of a high-albedo corundum surface. Between these two extremes, the highest albedo surface that is likely to form is ultramafic, as described in Sections 7.2.1 and 7.3.1. The blue region indicates where an atmosphere would be inferred. Labels on the x-axis indicate the substellar temperatures of the three planets we consider in detail in this paper, assuming zero albedo and no heat redistribution.

method of calculating planet albedos from thermal infrared observations in Section 7.1.2. In Section 7.2 we discuss the albedos we derive for each of the planet surface compositions we consider, and the characteristics of cloud layers that would be implied by an atmospheric detection with this method. We discuss the surface compositions we expect to exist on these hot rocky planets in Section 7.3.1, and list processes that could act to darken or brighten the planet surface in Section 7.3.2. We compare our atmospheric detection method to other methods in Section 7.3.3 and conclude in Section 7.4.

7.1 Methods

7.1.1 Planet Substellar Temperature Range

The range of planetary temperatures we consider for this observational technique is limited to zero-albedo substellar temperatures between 410−1250 K by two theoretical calculations. We assume no heat redistribution, so the substellar temperature T_{sub} is related to the equilibrium temperature T_{eq} by the equation $T_{eq} = T_{sub}\left(\frac{1}{4}\right)^{1/4}$. The range of substellar temperatures $T_{sub} = 410 - 1250$ K corresponds to equilibrium temperatures of $300 - 880$ K.

The lower temperature limit is set by the runaway greenhouse limit at zero-age main-sequence luminosity. At temperatures lower than the greenhouse limit the planet's surface could include high-albedo salt flats or water-rich materials such as clays or granites, which would complicate the interpretation of a high-albedo detection. We base our estimate of the runaway greenhouse threshold on the calculations of Kopparapu et al. [156]. However, Yang et al. [328] found that clouds on the substellar hemisphere could prevent a planet around an M dwarf from entering a runaway greenhouse state until stellar fluxes twice as large as those reported by Kopparapu et al. [156]. Therefore, we double the stellar fluxes of the Kopparapu et al. [156] runaway greenhouse limit to conservatively account for clouds and other factors that may similarly delay the runaway greenhouse [328, 327, 149]. For all three planets we consider in this study, this method provides a lower substellar temperature

limit of $T_{sub} = 410$ K. The conservative runaway greenhouse limit given by this calculation depends on the specific stellar and planetary parameters, but for M dwarfs it will be at stellar fluxes of $\approx 2300-2500$ W/m^2.

The upper temperature limit is set by the rate at which rock can be partially devolatilized. At high enough temperatures, all components of the rock at the substellar point except corundum will vaporize, leaving behind a high-albedo calcium- and aluminum-rich surface made of materials such as Al_2O_3 [144]. This high-albedo surface would again prevent distinction of a high-albedo atmosphere from a lower-albedo surface, so we limit our study to lower temperatures.

To derive the temperature at which rock devolatilization would impact the overall albedo, we use the MAGMA model of gas-melt chemical equilibrium to calculate the rate at which rock could be devolatilized, assuming a starting composition equal to that of the Earth's continental crust [77, 258, 144]. Continental crust devolatilizes faster than other possible starting rock compositions because it has a higher vapor pressure, so this choice of starting composition gives a conservative (i.e., low) estimate of the temperature at which devolatilization becomes significant. The MAGMA model outputs the pressure P of the rock vapor over the surface, which we convert to a flux F of rock from the dayside hemisphere to the nightside hemisphere using the equation

$$F = \frac{c_s P}{g}, \tag{7.1}$$

where c_s is the sound speed and g is the gravitational acceleration. Here we assume that the wind speed of the rock vapor is equal to the sound speed. Models of tenuous vapor atmospheres, both for super-Earth exoplanets and for Jupiter's moon Io, indicate the presence of supersonic winds over a broad region of parameter space, with winds across the terminator typically 2-3 times the sound speed [129, 40].

We then convert this flux of material over the terminator to a rate R of vaporization

from the dayside hemisphere using the equation

$$R = \left(\frac{F}{\rho}\right)\left(\frac{2\pi R_p}{2\pi R_p^2}\right) = \frac{F}{R_p \rho}, \tag{7.2}$$

where R_p is the planet radius and ρ is the density of the rock.

Figure 7.2 shows the rate of devolatilization as a function of temperature. We compare this rate to the rate of meteoritic gardening, which determines how quickly fresh, low-albedo material could be mixed from below the rock surface [208]. We assume that impact gardening mixes regolith to a depth of order 1 m/Gyr based on analogy to the Solar System [319, 76], but our calculations are insensitive to the exact impact gardening rate to within an order of magnitude because the rock vapor pressure increases very rapidly with increasing substellar temperature (Figure 7.2). The rate of devolatilization will be slower than meteoritic gardening for substellar temperatures $\leq$ 1250 K. We find that this is approximately the temperature at the Roche lobe radius for an Earth-density planet orbiting a mid M dwarf, so all close-in planets around M dwarfs will be cool enough to avoid partial devolatilization.

7.1.2 Observed Planetary Fluxes and Albedos

We investigate a variety of potential rock compositions with different albedo properties. We consider the eight compositions outlined in Hu et al. [124]: basaltic, clay, feldspathic, Fe-oxidized (50% nanophase hematite, 50% basalt), granitoid, ice-rich (50% ice and 50% basalt), metal-rich (FeS_2), and ultramafic. Hu et al. [124] created reflectance spectra for three of these surfaces using laboratory measurements of rock powders, and for the other five surfaces used radiative-transfer modeling based on laboratory samples of component minerals. These model spectra assume relatively fine-grained rocks. Fine grains generally have higher albedos than coarse grains, so the albedos taken from Hu et al. [124] represent conservative upper limits of the albedos of these eight compositions.

Figure 7.3 shows the albedos of these surfaces as a function of wavelength [124]. The

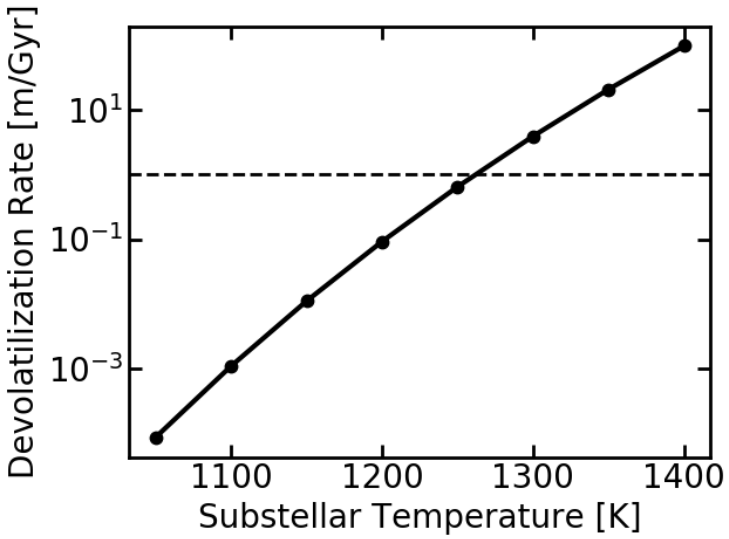

Figure 7.2: Devolatilization rate as a function of temperature. The horizontal dashed line shows an order-of-magnitude estimate of the inner Solar System rate of meteoritic gardening, which stirs fresh material to the surface. Values below this line indicate temperatures at which the rock composition is little-affected by devolatilization. The devolatilization rate is calculated using MAGMA [77, 258], for continental crust composition. Other plausible rocky planet crust compositions would have even lower devolatilization rate.

fundamental basis for the overall shapes of these spectra is that many rock-forming minerals have strong spectral slopes in the 0.4-5 μm range. We discuss the plausibility of these surfaces forming on terrestrial planets with $T_{sub} = 410$-1250 K in Section 7.3.1.

For each rock composition, we determine the temperature of a hypothetical planet with a surface of that composition by setting its outgoing flux equal to the absorbed flux it receives from its star. The absorbed flux from the star as a function of wavelength, $F_\star(\lambda)$, is given by

$$F_\star(\lambda) = [F_\lambda(1 - \alpha_\lambda)] \left(\frac{R_\star^2}{a^2}\right), \tag{7.3}$$

where $R_\star$ is the stellar radius, a is the distance from the planet to the star, α_λ is the planet's albedo as a function of wavelength, and F_λ is the spectral flux density in W m^{-3} from a PHOENIX model for the star [128]. The flux emitted by the planet is approximated by

$$F_p(\lambda) = \pi B_\lambda(T_{day})(1 - \alpha_\lambda), \tag{7.4}$$

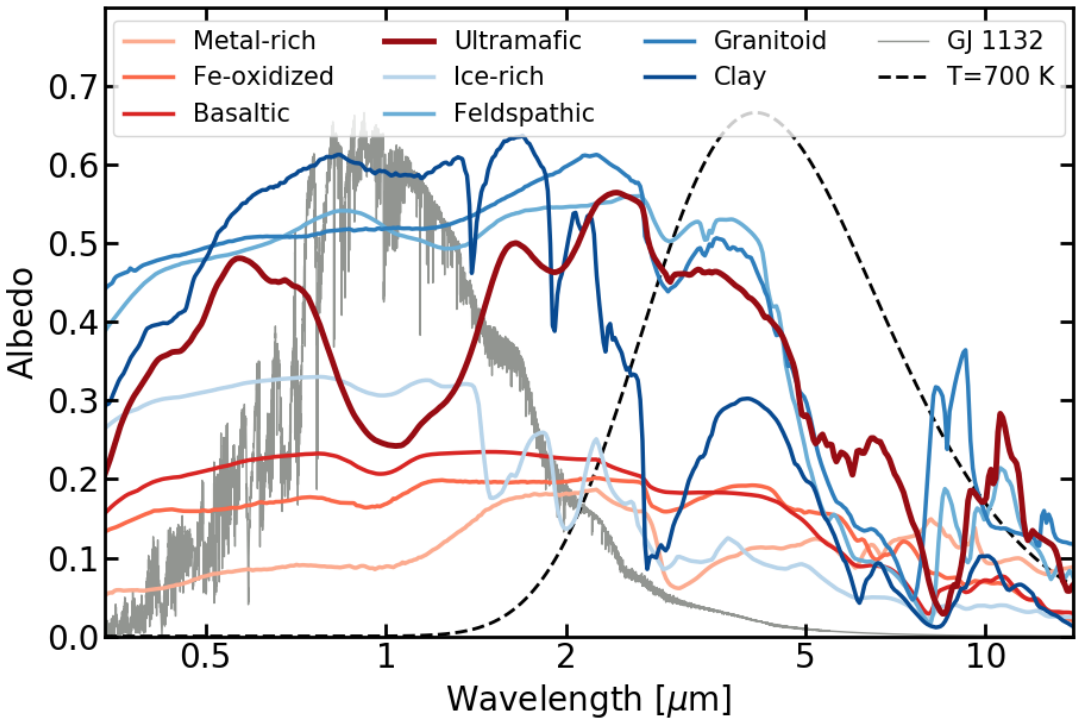

Figure 7.3: Albedo as a function of wavelength for the eight types of planetary surfaces we consider in detail in this paper, taken from Hu et al. [124]. The solid grey line shows a PHOENIX model for the stellar spectrum of GJ 1132 [128], and the dashed black line shows a blackbody at $T = 700$ K, which is the approximate temperature of the dayside of GJ 1132b. Red tinted lines indicate surface compositions that are more plausible for planets in $T = 410$-1250 K orbits, while blue tinted lines are compositions that are not likely to occur at these temperatures. The thick, dark red line indicates the reflectance spectrum of ultramafic rock, which is discussed in more detail throughout the paper because it has the highest albedo of the plausible surfaces, and so it is the limiting case for atmosphere identification using the method proposed in this paper.

where $B_\lambda(T)$ is the flux emitted by a blackbody and T_{day} is the planet dayside brightness temperature, which is related to the substellar temperature T_{sub} through the equation $T_{day} = \left(\frac{2}{3}\right)^{1/4} T_{sub}$. The factor of $\frac{2}{3}$ assumes zero heat redistribution and a bare rock surface [110].[2] We also assume here that the planet is in 1:1 spin:orbit resonance, because we are considering hot worlds in close-in orbits around K and M dwarfs. Additionally, approximating the entire dayside as a single blackbody implicitly assumes that the dayside surface is completely covered by one rock type. We integrate these two equations over wavelength and iterate until they are equal to determine the planetary temperature.

For each of these planet surfaces, we sum the light reflected and emitted by the planet to get a planet spectrum as a function of wavelength. We use PandExo to simulate observations of these planets with *JWST* [11]. We simulate sets of five secondary eclipse observations using the Mid-Infrared Instrument's Low-Resolution Spectroscopy (MIRI LRS) slitless mode to observe between 5 and 12 μm. We integrate over this entire wavelength range to produce one broadband planetary flux measurement.

We calculate the planetary brightness temperature that would be inferred from these observations by inverting the equation

$$\frac{F_p}{F_\star} = \left(\frac{R_p}{R_\star}\right)^2 \int_{\lambda=5\ \mu\mathrm{m}}^{12\ \mu\mathrm{m}} \left(\frac{B_\lambda(T_{day,obs})}{B_\lambda(T_\star)}\right) d\lambda, \tag{7.5}$$

where $\frac{F_p}{F_\star}$ is the observed broadband planet-to-star flux ratio and $T_{day,obs}$ is the planet dayside brightness temperature inferred from the observations. Note that this equation assumes that the planet's emissivity ($\epsilon_\lambda = 1 - \alpha_\lambda$) is unity. We make this assumption when interpreting our observed planet flux because the planet's emissivity cannot be known a priori. We approximate the star's flux as a blackbody for this calculation because the PHOENIX model spectra only extend to a wavelength of 5 μm. We then convert this temperature into an

2. Even a magma ocean would not redistribute much heat if heated only by the star, and confined to the dayside [144].

inferred planetary albedo using the equation

$$T_{day,obs} = T_\star \sqrt{\frac{R_\star}{a}} \left[\frac{2}{3}(1 - \alpha_{obs})\right]^{1/4}, \tag{7.6}$$

where α_{obs} is the albedo inferred from the observations. This equation again assumes unit emissivity.

We calculate the inferred albedo for each of the eight planet surfaces for three planets: the canonical high signal-to-noise planet GJ 1132b [25]; TRAPPIST-1 b, which orbits a very small star and so is a relatively high-signal transiting planet with an equilibrium temperature near the lower end of our temperature range [99]; and the newly-discovered *TESS* planet LHS 3844b, which is representative of the type of planets the *TESS* mission will continue to discover [310]. These three planets together span almost the entire temperature range from 410-1250 K. Table 7.1 list the details of each planet we consider.

7.2 Results

We find that all plausible surface compositions for planets in $T_{sub} = 410 - 1250$ K orbits have low albedos, and that even very thin atmospheres can host enough clouds to raise the albedo above that for a bare surface. Our main results depend on the relationship between the actual planet Bond albedo and the albedo inferred from observations at mid-infrared wavelengths, which we describe in detail in Section 7.2.1. We find that the albedo inferred from such observations is lower than the actual Bond albedo for all the surfaces we consider. In Section 7.2.2 we calculate the properties of clouds that have high enough albedos to be distinguishable from bare rock surfaces.

7.2.1 Comparison of Inferred and Actual Planetary Albedos

A key complication in relating an inferred albedo to the presence of an atmosphere is the difference between the inferred planet albedo and its actual Bond albedo. A realistic surface

Table 7.1: Stellar and planetary parameters for the three systems we consider.

Parameter	Value
TRAPPIST-1b	
Star radius	0.121 $R_\odot$
Star effective temperature	2511 K
Star K magnitude	10.296
Planet radius	1.12 $R_\oplus$
Planet orbital period	1.51 d
Planet dayside temperature[a]	508 K
GJ 1132b	
Star radius	0.207 $R_\odot$
Star effective temperature	3270 K
Star K magnitude	8.322
Planet radius	1.16 $R_\oplus$
Planet orbital period	1.63 d
Planet dayside temperature[a]	737 K
LHS 3844b	
Star radius	0.189 $R_\odot$
Star effective temperature	3036 K
Star K magnitude	9.145
Planet radius	1.32 $R_\oplus$
Planet orbital period	0.46 d
Planet dayside temperature[a]	1024 K

[a]Assumes no heat redistribution and zero albedo.

with a non-constant albedo at the wavelengths where it emits radiation will have an albedo inferred from observations of planetary radiation that differs from its true Bond albedo (the actual percentage of starlight at shorter wavelengths that is reflected off the planet's surface). This is related to Kirchhoff's law of thermal radiation: a planet with an albedo that changes as a function of wavelength will emit relatively more or less light at certain wavelengths compared to a blackbody with a constant emissivity at all wavelengths.

Figure 7.4 demonstrates why inferred albedo differs from Bond albedo for a simple example where the albedo is a step function given by

$$\alpha_\lambda = \begin{cases} 0.5, & \lambda < 4\mu\text{m} \\ 0.1, & \lambda > 4\mu\text{m} \end{cases}. \tag{7.7}$$

The lower panel of this figure shows the actual Bond albedo compared to the albedo inferred from observations with *JWST*/MIRI for a set of planets at different temperatures spanning the range we consider. For all of the planets, the step function means that the MIRI bandpass (5-12 μm) is at a lower albedo (and thus higher emissivity) than shorter wavelengths. Therefore, in order to satisfy energy balance, the planet must emit relatively more of its flux at the long wavelengths where the emissivity is higher than if it were emitting as a blackbody with a constant emissivity. This means the planet will appear to be at a higher temperature in the MIRI bandpass, and so the inferred albedo will be lower than the actual Bond albedo. For planets at higher temperatures, this effect is even stronger because more of the planet's emission is at low-emissivity short wavelengths. As a result, in order to satisfy energy balance, the relative amount emitted at longer wavelengths is even higher compared to a constant-emissivity blackbody.

Figure 7.5 shows a comparison of the insolation flux-weighted albedos of the eight planetary surfaces at shorter wavelengths (0.1-3.5 μm, the range in which all three of the M dwarf stars we consider emit $> 90\%$ of their flux) to their inferred albedos from broadband mid-infrared observations with *JWST*/MIRI. The error bars represent 1σ observational un-

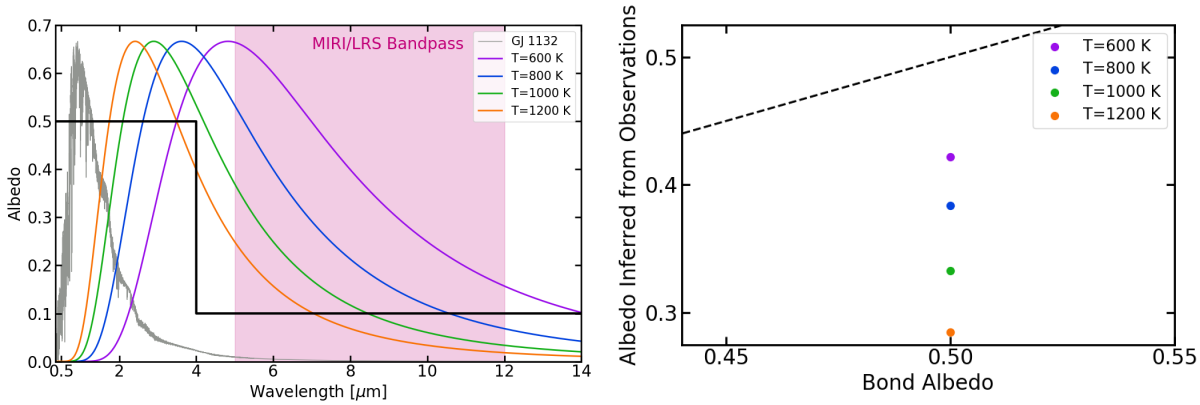

Figure 7.4: A simplified example showing how the inferred albedo can be different from the Bond albedo for a planet where the albedo changes as a function of wavelength. The left plot shows the simple step function albedo (black line) overplotting the stellar spectrum for GJ 1132 and example planet blackbodies at four different temperatures ranging from $T = 600$ K to $T = 1200$ K. The magenta shaded region indicates the MIRI/LRS bandpass. The right plot shows the albedo inferred from *JWST*/MIRI observations of each planet. The dashed line indicates where the inferred albedo equals the Bond albedo.

certainties for a set of five stacked secondary eclipses. In all cases the inferred albedo is lower than the actual Bond albedo because the spectra generally have higher albedos at shorter wavelengths and lower albedos at longer wavelengths.

The surfaces can be grouped into two rough categories based on the shapes of their spectra (Figure 7.3). First, feldspathic, granitoid, ultramafic, and clay generally show a high albedo at short wavelengths, then an abrupt transition around 2-5 μm to low albedo at longer wavelengths (Figure 7.3). All of these surfaces also have a lower emissivity at 3-5 μm (the peak of the flux for a planet at the temperature of GJ 1132b if that planet emitted as a blackbody) than at 5-12 μm (the MIRI bandpass). This means they will emit a larger percentage of their flux in the MIRI bandpass, leading to a higher inferred temperature and a lower inferred albedo. The larger the increase from the 3-5 μm emissivity to the 5-12 μm emissivity, the lower the inferred albedo will be relative to the Bond albedo. Feldspathic surfaces have the largest difference in its emissivity in these two wavelength ranges, followed by clay, then granitoid, then ultramafic. Therefore, in this set of four surfaces, the feldspathic surface shows the largest deviation from the 1:1 line in Figure 7.5, and the ultramafic shows

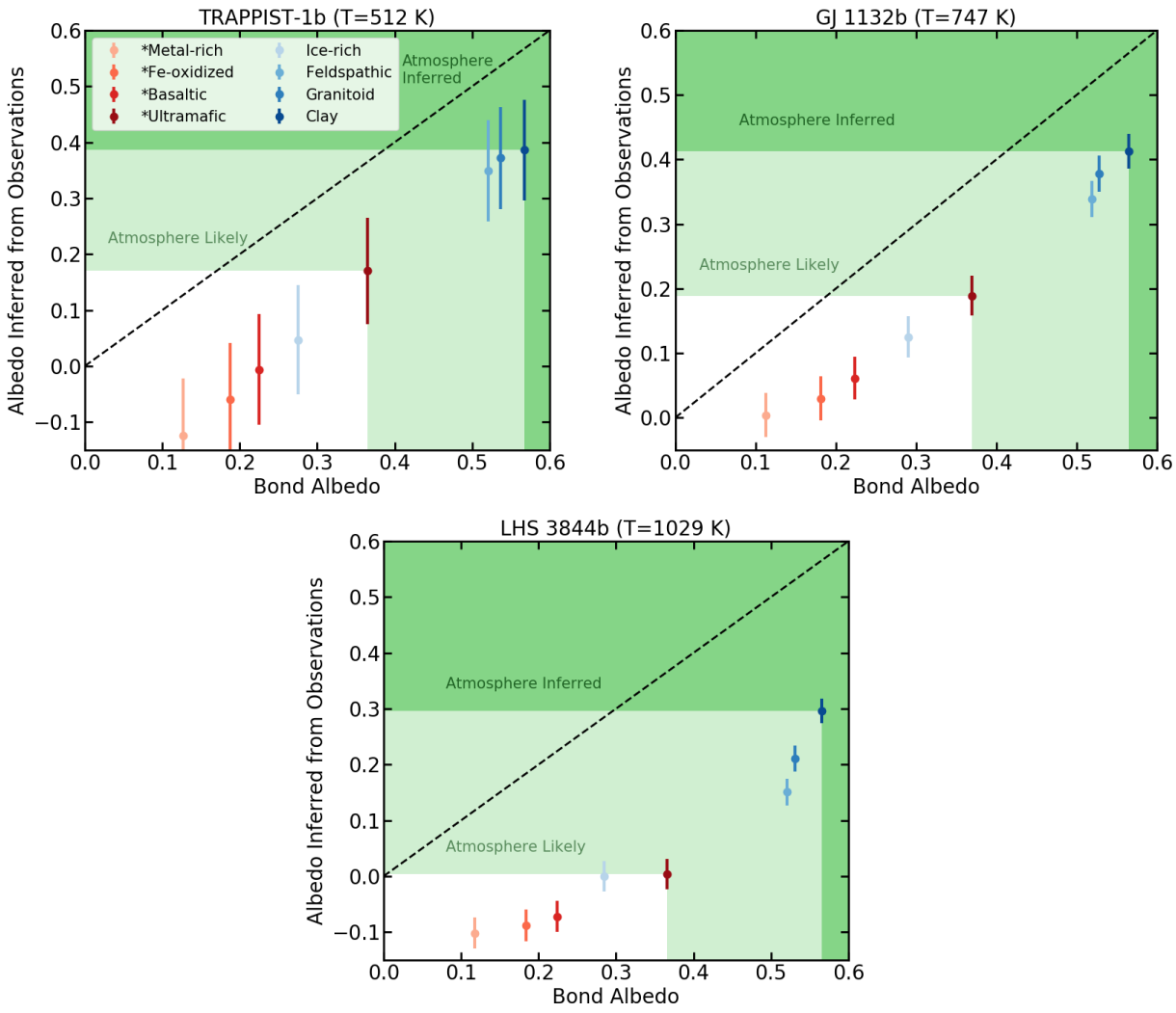

Figure 7.5: Insolation flux-weighted albedo of the eight possible planetary surfaces in the wavelength range from 0.1-3.5 μm compared to the albedo inferred from longer-wavelength observations with *JWST*/MIRI for TRAPPIST-1 b (upper left panel), GJ 1132b (upper right panel), and LHS 3844b (lower panel). Temperatures quoted in the plot titles assume $\alpha = 0$ and no heat redistribution. The error bars indicate 1σ observational uncertainty for five stacked secondary eclipse observations. The black dashed line shows where the Bond albedo equals the inferred albedo. In all cases, the inferred albedo is lower than the actual albedo. Note that in some cases the inferred albedo appears to be negative. This is due to the assumption of unit emissivity when calculating the albedo. The light and dark green shaded regions indicate where the albedo is high enough that an atmosphere is likely and where one is needed to explain the observation, respectively.

the smallest deviation.

The second category consists of ice-rich, basaltic, Fe-oxidized, and metal-rich surfaces. All of these surfaces can be approximated as a more gradual slope to lower albedos at longer wavelengths, without the sharp transition of the first four surfaces (Figure 7.3). Ice-rich is on the edge between the two categories, but its sharp drop-off is smaller and at shorter wavelengths. The metal-rich surface has an albedo that is close to constant, so its inferred albedo should be close to its Bond albedo and it should fall closest to the 1:1 line in Figure 7.5. The other three surfaces all have slightly higher emissivity at the MIRI wavelengths, so they should again all be slightly farther from the 1:1 line. Among those three surfaces, the Fe-oxidized surface has the smallest difference between its visible and MIRI emissivity, followed by ice-rich, then basaltic. So in this group of three surfaces, Fe-oxidized is closest to the 1:1 line and basaltic is farthest.

The stars GJ 1132 and LHS 3844 have nearly the same PHOENIX spectra because their effective temperatures only differ by 200 K. The Bond albedos for these two planets differ by < 0.01. Therefore, the primary difference between GJ 1132b and LHS 3844b is that LHS 3844b is much warmer than GJ 1132b (zero-albedo, zero-redistribution $T_{day} = 1024$ K for LHS 3844b as opposed to 737 K for GJ 1132b), so that LHS 3844b emits its flux at slightly shorter wavelengths. The overall effect is that a smaller percentage of the planet's blackbody curve is in the high emissivity regions at longer wavelengths, so the warmer planet will emit relatively more at these wavelengths and the inferred albedos will appear even lower than for the case of GJ 1132b. For all of the surfaces except clay, the surface albedos at the peak of GJ 1132b's blackbody flux and that of LHS 3844b are within 0.04 of each other, so those surfaces all uniformly have lower inferred albedos. For the clay surface, the peak flux of LHS 3844b happens to be emitting in a region where the albedo is almost 0.2 lower than the surrounding parts of the spectrum. This means the peak flux for the clay surface is at a higher emissivity, so relatively less flux needs to be emitted at the MIRI wavelengths. Therefore the clay surface has a higher inferred albedo relative to the other surfaces compared

to what it had for GJ 1132b.

The star TRAPPIST-1 is 700 K cooler than GJ 1132, but the difference in inferred albedos for TRAPPIST-1 b and GJ 1132b is again primarily due to the different planet temperatures (and not due to the difference in stellar effective temperature). TRAPPIST-1 b has a temperature of ≈ 470 K, which is cool enough that the peak of its flux is emitted in the MIRI bandpass. Therefore, the difference between the inferred albedo and the true Bond albedo simply depends on the difference between the emissivity at short wavelengths, where the starlight is absorbed, and at long wavelengths, where the planet emits its flux. A surface with a larger difference between its emissivity at wavelengths < 3.5 μm and its emissivity at $5 - 12$ μm will have a larger difference between its inferred and Bond albedos. Within the first category of surfaces, feldspathic has the largest difference between its short-wavelength and long-wavelength emissivities, followed by granitoid, ultramafic, and clay. Therefore, among these four surfaces, feldspathic has the largest difference between its inferred and Bond albedos. Similarly, the basaltic and metal-rich surfaces have the largest and smallest difference in emissivities among the second category of surfaces, so they have the largest and smallest difference between inferred and Bond albedos, respectively.

Our method of differentiating a bare rock surface from an atmosphere relies on the fact that bare surfaces have generally low albedos, so any high-albedo detection would have to come from an atmosphere. Our calculations indicate that observations of a bare rock surface would lead to inferring a lower albedo than that of the real surface. Additionally, despite the offset between Bond albedo and inferred albedo, low Bond albedo surfaces always lead to lower inferred albedos, and high Bond albedo surfaces always lead to higher inferred albedos. This means that the detection of a low secondary eclipse depth corresponding to a high inferred albedo above about 0.4 would unambiguously indicate an atmosphere. As discussed in Section 7.3.2, this conclusion is robust to considering processes that could darken or brighten the surface, which were not considered in Hu et al. [124].

7.2.2 Distinguishing Planetary Surfaces from High-Albedo Clouds

Given that an inferred high albedo can indicate the presence of an atmosphere, what can be said about that atmosphere? Although Rayleigh scattering alone can in principle cause an albedo > 0.5, in practice a more likely cause of high albedo is clouds. For example, Venus's high albedo of 0.7 is due to clouds.

We calculated the albedos of clouds with a variety of properties to determine what types of atmospheres could be distinguished from bare rock surfaces on the basis of albedo alone. We constructed a grid of atmospheres with cloud column masses between $10^{-10} - 10^{1}$ g/cm^2 and non-absorbing cloud particles with radii between $10^{-1} - 10^{1.7}$ μm. From these parameters we calculated the optical depth (τ) using the equation

$$\tau = \frac{3Qm_{col}}{4\rho_p r_p}, \tag{7.8}$$

where Q is the scattering efficiency, m_{col} is the cloud column mass, and ρ_p and r_p are the particle density and radius, respectively [236]. We then calculated the albedo (α) using the equation

$$\alpha = \alpha_a + \frac{(1-\alpha_a^{'})(1-\alpha_a)\alpha_g}{1-\alpha_a^{'}\alpha_g}, \tag{7.9}$$

where

$$\alpha_a^{'} = \frac{(1-g)\tau}{1+(1-g)\tau}, \tag{7.10}$$

$$\alpha_a = \frac{\frac{-1}{2}\beta + (1-\hat{g})\tau}{1+(1-\hat{g})\tau}, \tag{7.11}$$

and $\beta = 1 - \mathrm{e}^{-\tau}$ [236]. In these equations, $\hat{g}$ is the asymmetry factor and α_g is the albedo of the rock surface. Mbarek & Kempton [203] calculated equilibrium chemistry cloud compositions for secondary atmospheres at T = 410-1250 K, and several of these possible compositions (including K_2SO_4, KCl, and Na_2SO_4) have indices of refraction $n_R \approx 1.5$ and $n_I \approx 0$ [239, 172]. Therefore, we used values of Q and $\hat{g}$ for particles with indices of refraction

$n_R = 1.5$ and $n_I \approx 0$ (values range from $0.2 < Q < 4$ and $0.2 < \hat{g} < 0.8$).

Figure 7.6 shows a contour plot of potential albedos for GJ 1132b, assuming an ultramafic rock surface. The area above the black line is the region of parameter space where the total planet albedo is more than 2σ higher than the inferred albedo of the bare rock surface. A detection of an albedo higher than this value would suggest the presence of an atmosphere on this planet. For this surface, an atmosphere with a cloud column mass greater than 8×10^{-5}–3×10^{-2} g/cm^2 ($\tau > 0.8 - 5$) would have a higher albedo. The red, magenta, and orange stars on Figure 7.6 indicate typical cloud parameters for Earth [318], Venus [8], and Mars [45], respectively. While clouds made of larger, Earth-sized particles would be harder to detect using our method, smaller-particle hazes such as those found in Venus's upper atmosphere would be detectable at lower cloud column masses. Previous work has found that it would take ≈ 10 or more transits to detect an atmosphere on an exoplanet with Venus-like hazes using transmission spectroscopy [184]. Our method provides a way to detect such hazy atmospheres more efficiently.

Most of the surface types exhibit a similar behavior, with column masses greater than $4 \times 10^{-5} - 5 \times 10^{-2}$ g/cm^2 ($\tau > 0.5 - 7$) having high enough albedos to suggest an atmosphere. The minimum pressure required to support such high-albedo cloud layers is significantly smaller than the ≈ 1 bar required to transport heat. For example, Mars has regionally-extensive high-albedo clouds made of both H_2O and CO_2 ice in a 6 mbar atmosphere [273, 108]. These clouds can be optically thick, especially near surface ice deposits.

Our calculation implicitly assumes that a large portion of the dayside is covered in clouds so that the disk-integrated dayside albedo is large. This is a reasonable assumption for the close-in terrestrial exoplanets we consider, because 3D global climate simulations of synchronously rotating planets exhibit upwelling and cloud cover over much of the dayside, with downwelling and clear skies confined to the nightside [328].

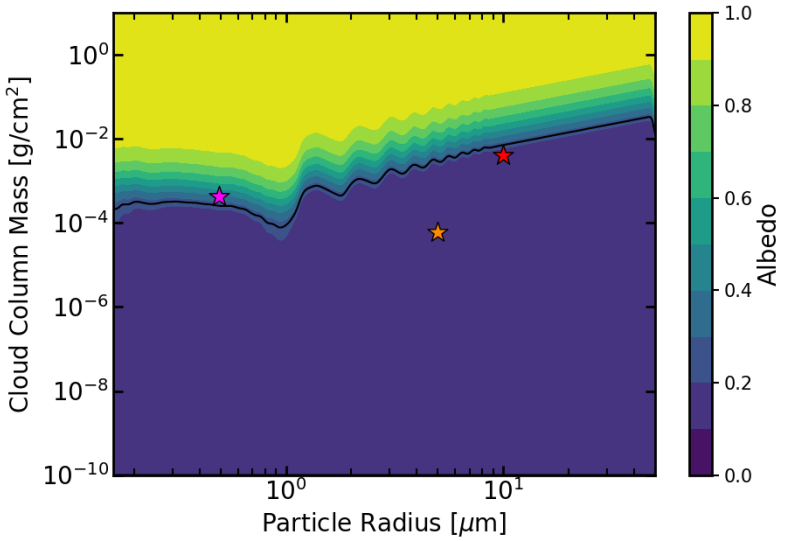

Figure 7.6: Contour plot of total planet albedo as a function of cloud particle radius and cloud column mass. The area above the black line is the region of parameter space where the albedo is more than 2σ greater than the inferred bare rock albedo of an ultramafic rock surface on GJ 1132b. The red, magenta, and orange stars indicate typical cloud parameters for Earth [318], Venus [8], and Mars [45], respectively.

7.3 Discussion

7.3.1 Which Surface Compositions Are Expected to Exist?

A high surface albedo can produce a low secondary eclipse depth, so using the secondary eclipse depth to screen for the presence of atmospheres will only work if there is a prior constraint on the distribution of possible surface albedos. We have two primary sources of information on the albedos of terrestrial planets: observations of rocky objects in the Solar System and laboratory spectra of geologically plausible surfaces.

Surfaces Observed in the Solar System

Table 7.2 lists the albedos of several Solar System bodies. The rocky bodies in the Solar System generally have low albedos [185]. E-type asteroids[3] are an interesting exception to

3. E-types are common between Mars and the inner edge of the main asteroid belt (Hungaria region). E-types are plausibly leftovers from the formation of Earth and Mars.

Body	Bond Albedo
Mercury	0.07
Moon	0.11
Mars	0.25
4 Vesta	0.18
1 Ceres	0.03
Io	0.6
44 Nysa	0.33

Table 7.2: Bond albedos of solar system bodies [185, 288].

the general trend of dark solar system rocks, with albedos > 0.3. One of the brightest E-type asteroids, 44 Nysa, is listed in Table 7.2 for comparison [288]. E-types are likely the source of enstatite chondrite meteorites. If this mapping between meteorite type and asteroid type is correct, then the cause of the high asteroidal albedo is that the rocks record very reducing conditions - so any iron gets reduced to Fe, and there is very little Fe^{2+} in the silicate (Fe and other transition metals being a big cause of the dark color of the most-common silicate rocks). This matters because the reducing conditions are analogous to those expected for evaporated cores (which will be discussed further in Section 7.3.2) if enough hydrogen was originally present to overwhelm buffering by Fe-oxides. Although it is unclear what an evaporated core will look like because we have never imaged one, this redox similarity leads us to speculate that E-types may be the best solar system analog to the surface composition of evaporated cores.

The near-infrared reflectance spectrum of enstatite is shown in Figure 7.7. At the wavelengths where M dwarfs emit most of their light, enstatite has an albedo between 0.3-0.4 that is similar in shape and magnitude to that of ultramafic rock. Therefore, observations of an enstatite surface would likely lead to a similar inferred albedo as that of an ultramafic surface. Our method of calculating inferred albedo would still allow detection of a high-albedo atmosphere on a planet with an enstatite surface.

Although sulfur species (mainly SO_2) are responsible for the high albedo of Io, SO_2 would not be condensed as a solid on the surface of the hot planets we consider here and sulfur

would be liquid (for $T > 427$K) and quite dark [218].

The solar system contains only one world in a $T > 410$ K orbit – the $\sim$0.06 $M_\oplus$ world Mercury. In principle exoplanet albedo measurements could be used to supplement solar system data, to build up an empirical prior on rocky planet surface albedo. However, so far direct measurements of rocky-exoplanet albedos are limited [252, 265, 266, 132]. Moreover, even to use the Solar System data for exoplanets in hotter orbits we need to think about how the albedo would (or would not) be affected by processes at work on a hotter orbit. Therefore, our primary focus in this work is on laboratory spectra of hypothetical planet surface compositions, as well as processes that would make those compositions more or less likely.

Laboratory Spectra of Hypothetical Surfaces

We calculate albedos for eight possible surfaces in this paper, but not all of these surfaces are likely to form at the high temperatures we consider. Many planetary surface types require water to form. For example, it is roughly true that "[n]o water, no granites - no oceans, no continents" [36]. Forming granites on Earth involves water. Water is difficult to accrete, and difficult to retain, in a $T_{sub} = 410$-1250 K orbit. As long as water is abundant at the surface, a runaway greenhouse climate is expected, and this will favor H escape to space [109]. If the water is retained somehow, then the planet will have a H_2O vapor atmosphere.

Several other high-albedo surface types also require water to form [207]. Clays need water to form, either as structural water or for the leaching weathering reactions that produce anhydrous phyllosilicates such as kaolinite. Salt flats such as those found in White Sands, New Mexico and Salar de Ayuni, Bolivia also require water to form. Although pure quartz sand (SiO_2) on Earth can be found in deserts, it again is a signature of water - desert sand is a breakdown product of high-Si crust, often weathered and physically concentrated by processes involving liquid water. Small amounts of high-Si rock can be made without water by partial re-melting of basalt, but this is unlikely to cover the entire planetary surface.

Feldspathic (plagioclase-feldspar-dominated) flotation crust can form on dry worlds. While feldspathic flotation crusts are a possibility for dry Moon-sized worlds, they are less likely for larger exoplanets [67]. The only feldspathic crust we know is the Lunar highlands. The standard story of origin for the Lunar highlands crust involves formation of plagioclase as a liquidus phase in a cooling magma ocean [68]. However, plagioclase will not crystallize from a mafic or ultramafic melt at pressure much above 1 GPa, so for a large Earth-sized planet it will only form during the last dregs of magma-ocean crystallization. Moreover the only feldspathic flotation crust we know of, the Moon, is not as high albedo as the plagioclase-feldspar laboratory spectra might suggest because of processes such as space weathering (see Section 7.3.2).

Several of the other planetary surface types we consider, including basalt and ultramafic rock, can form without water. Planetary crusts are primarily composed of basalt, a dark rock type with 45-53 wt% SiO_2. Basalt is very common in the Solar System because it is the expected product of low-percentage ($\sim$10%) partial melting of "average rock"[4] [10, 291]. Basalt has a relatively low albedo.

Relative to basalt, ultramafic rocks have a higher albedo and are a potential false positive for atmosphere detection using the secondary-eclipse-depth technique in all orbits, including those with $T_{sub} = 410-1250$ K. Ultramafic rocks (which have <45 wt% SiO_2) are the result of high-percentage [>30%; 106] partial melting of "average rock". Such high-percentage partial melts are expected for worlds with high mantle temperatures, including strongly tidally heated worlds and young worlds with strong radiogenic heating [145]. Geologic terrains from the first 2 Gyr of Earth history often contain ultramafic rocks (specifically komatiites) because they correspond to a time when Earth's mantle was hotter than it is today, and so

4. We assume that Solar System mantle rock compositions – which upon melting, yield basalt – are representative of rock elsewhere in the Universe. White dwarf data are consistent with Earth-like Mg/Si ratios [136] and stellar Mg/Si ratios show little scatter in the solar neighborhood [19]. However, we are not aware of any work to study how Mg/Si variability propagates into the percentage of partial melting nor the mineralogy of the resulting lavas. Therefore, this assumption is unverified, but could be modeled in the future using existing datasets [307, 119].

partial melt fractions were higher [117]. Although ultramafic rocks can be dark in outcrop, the dominant minerals in ultramafic rocks – pyroxene and olivine – have high reflectance in the visible [124]. The possibility of ultramafic surfaces on Earth-sized exoplanets is the limiting case for using albedo to detect atmospheres on worlds in $T_{sub} = 410 - 1250$ K orbits, as illustrated in Figure 7.1. It is hard to make more reflective surfaces for these worlds, so higher albedos imply an atmosphere. Other surface types shown in Figure 7.3, including Fe-oxidized, basaltic, and metal-rich, have lower albedos, and so they are not worrisome for the purposes of screening for atmospheres using secondary eclipse depth.

7.3.2 Factors That Could Affect Surface Albedo

There are several processes that could act to make the observed surfaces darker or brighter. We discuss these possibilities below.

Darkening Processes

Solar system worlds can be darkened by minor contaminants, which are not considered in the spectra shown in Figure 7.3. For example, Mercury's surface is very dark, likely due to minor graphite [131]. E-type asteroids are also likely darkened by minor contaminants. Even though they are among the highest albedo rocky objects in the Solar System ($\alpha \geq 0.3$), the bulk mineralogy of enstatite chondrites suggests that E-type asteroids should have even higher albedos. Grain size and texture effects can also impact how much a surface is darkened [38]. Darkening effects would strengthen the conclusion that a high-albedo detection is due to an atmosphere, because the surface would be expected to be even darker.

Space weathering also darkens surfaces [33, 59]. The space weathering effect on bare-rock exoplanets would depend on the balance of the resurfacing rate (by small craters, lava flows, e.t.c.) and the rate of weathering by micrometeorites and the solar wind (deflected by the planetary magnetic field). On rocky exoplanets, a very small residual atmosphere would be sufficient to prevent space weathering, even if that atmosphere was too thin to be detectable

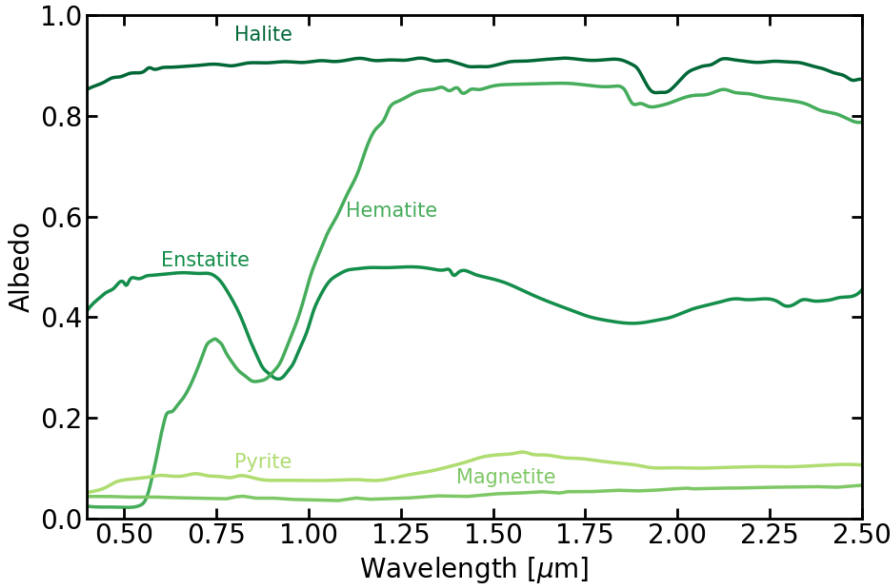

Figure 7.7: Near infrared reflectance spectra of minerals that might hypothetically form planet surfaces, but are not observed to be the primary material on the surface of any large Solar System bodies [105]. We do not consider these surfaces to be likely for worlds in $T_{sub} = 420 - 1250$ K orbits, for the reasons given in Section 7.3.2.

in transit. If rocky exoplanets have plate tectonics, then continued volcanism would reset the darkening caused by space weathering [309, 81].

Brightening Processes

In spite of the reasoning above, what could nevertheless give a surface a high albedo in a $T = 410-1250$ K orbit? The below possibilities are described in order of how concerning they are for our proposed screening tool, and their reflectance spectra are shown in Figure 7.7.

(1) *Shiny evaporated cores:* The silicate cores of low-density sub-Neptunes have T $\gtrsim$ 3000 K [123, 311, 27], and may have non-negligible partial pressures of "rock" in the H_2-rich envelope, especially during the first ∼1% of the planet's lifetime [78, 32]. If an H_2-rich envelope of 0.1-1 wt% of planet mass originally exists, but is subsequently stripped away, it will form a Super-Earth that is an "evaporated core" [224]. During this evaporation process, volatile and low-molecular-weight "rock" species will join the gas outflow [127]. The core-envelope

interface will cool because the H_2-induced warming goes down. The equilibrium vapor pressures of "rock" in the envelope will also go down, and so less-volatile species will condense at the core-envelope interface and be stirred back into the liquid silicate. When the core-envelope interface cools below ∼1673 K the liquid-silicate stirring will stop and anything still dissolved in the envelope will form onion-shell layers at the surface as it condenses. It is conceivable that the outer shell layers would have high albedo. Na is the best candidate among the major rock-forming elements for a species that is volatile enough to have a non-negligible saturation vapor pressure at ∼1673 K but has a high enough molecular weight and is refractory enough that it need not escape with the hydrogen [258]. However, creating a Na-metal surface through this scenario may require fine-tuning for an XUV flux intense and prolonged enough to shed all of the H_2 but weak enough that the other gases are not entrained away with the H_2.

(2) *Reflective metals/sulfides:* Metals volatilized during an H_2O-rich or CO_2-rich atmosphere phase could add a reflective coat to the surface. This has been proposed for the highlands of Venus [e.g., 257]. However, Figure 7.7 shows that pyrite, the most common sulfide among Earth minerals, has a relatively low albedo, and so would be distinguishable from an atmosphere using our method.

(3) *Iron oxides:* If the planet orbits an M-star, there could be significant oxidation due to the photodissociation of H_2O and the escape of hydrogen. In this case, we could observe a surface covered in iron oxides, some of which are very reflective in the near infrared. Such surfaces could have even greater Fe-oxide abundances than the case considered by Hu et al. [124] (50% nanophase hematite, 50% basalt) and shown in Fig. 7.3 (referred to as "Fe-oxidized"). Figure 7.7 shows two examples of common iron oxides, hematite and magnetite, which span the range of reflectance spectra of iron oxides. While hematite has a high albedo at wavelengths longer than ≈ 1.25 μm, its albedo is relatively low at shorter wavelengths where the stars we consider emit the majority of their light.

(4) *Pure iron:* If all of the rock has been removed we could observe a bare iron surface. A

completely iron surface is unlikely according to models of collisional mantle stripping [202], but this could be tested by using radial velocity measurements to constrain the planet's mass.

(5) *Salt flats:* The early escape of a steam atmosphere might lead to a surface covered in high-albedo salt flats. Figure 7.7 shows that the salt halite has a high albedo. However, volcanism on the planet would likely lead to these primordial salt flats being buried by low-albedo lava.

In addition to these possibilities, there are a wide variety of possible surface minerals [e.g., 46] that are not included in the surface types investigated by Hu et al. [124]. However, we struggle to come up with plausible scenarios that would result in the bulk of a planetary surface made up of other minerals not considered here, so for this paper we focus on the well-characterized surfaces that are known to exist on planetary bodies in the Solar System.

7.3.3 Relationship to Other Methods of Atmospheric Detection

Our method of using albedo to test for the presence of an atmosphere is complementary to that of Koll et al. [152], who consider the possibility of detecting an atmosphere through measurements of reduced dayside thermal emission or heat redistribution. Figure 7.8 shows the relationship between these two methods of atmospheric detection. Colored contours on this plot indicate dayside effective temperatures for LHS 3844b for a variety of atmospheric pressures and surface albedos, while triangles indicate the albedos of surfaces we consider in this paper. Koll et al. [152] present a method to detect an atmosphere that is thick enough to change the dayside temperature by greater than or equal to a certain amount (above/to the right of a given temperature contour in Figure 7.8), while our method allows detection of an atmosphere with an albedo higher than that of the most reflective plausible surface (above the dashed horizontal line in Figure 7.8).

While Koll et al. [152] find that an atmosphere thicker than about 1 bar will transport enough heat that its secondary eclipse depth will deviate from that of a bare rock, there

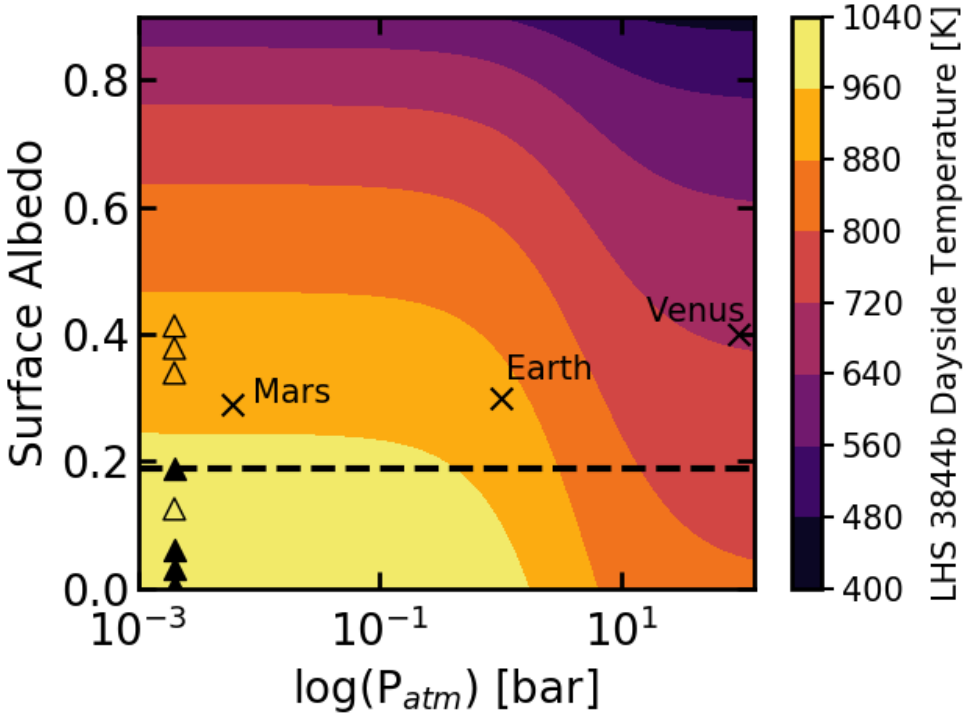

Figure 7.8: Figure showing the relationship between the atmospheric detection method of Koll et al. [152] and the method we present in this paper. Colored contours indicate planet dayside temperatures for LHS 3844b for a variety of atmospheric pressures and surface albedos, calculated following Koll et al. [152]. Black × marks show the location of the rocky Solar System planets on this plot. Filled triangles indicate the albedos of geologically plausible surfaces (e.g., basaltic or ultramafic) and empty triangles indicate the albedos of surfaces that are geologically implausible for $T_{sub} = 410 - 1250$ K worlds (e.g., granitoid or ice-rich). The method of Koll et al. [152] would have the necessary sensitivity to detect an atmosphere which changes the dayside temperature by greater than or equal to a certain amount (above/to the right of a given temperature contour). Our method allows for detection of an atmosphere at any pressure with an albedo higher than that of the most reflective plausible surface (above the dashed line).

are several ways to create a thinner atmosphere that has a high albedo. Any planet with plentiful surface condensables can make optically thick clouds at pressures well below those needed to shift heat between hemispheres. For example, Mars has a surface pressure of 6 mbar, but has CO_2 clouds, H_2O clouds, and dust storms, all of which can be optically thick at both visible and infrared wavelengths [273, 45, 108]. The top of the upper H_2SO_4 cloud deck on Venus is at a pressure level of $\approx$ 30 mbar [8]. Triton's clouds have an optical depth >0.1, and it is plausible that under a slightly different insolation Triton could make optically thick high-albedo clouds. Finally, sulfur hazes derived from volcanic sulfur can also be very reflective [92].

7.4 Conclusions

We present a method to distinguish a hot rocky exoplanet without an atmosphere from one that retains an atmosphere through measuring the planet's Bond albedo. This method is complementary to other proposed methods of atmosphere detection, including through transit or eclipse spectroscopy, reduced phase curve amplitude, or reduced secondary eclipse depth [262, 214, 152]. Our method allows the detection of an atmosphere that is too thin to transport enough heat to impact the secondary eclipse depth but is thick enough to support high-albedo clouds.

We find that this method can be used effectively for planets with substellar temperatures of T_{sub} =410-1250 K. At lower temperatures, high-albedo surfaces associated with water can exist and may complicate the interpretation of a high-albedo detection. At higher temperatures, partial devolatilization of the rock may produce a high-albedo patch at the substellar point.

We investigate the properties of eight plausible surface compositions [124]. We determine that an ultramafic surface is the highest-albedo ($\alpha \approx 0.19$) surface that would be likely to exist in a T = 410-1250 K orbit. For this surface (and the other surfaces investigated), cloud layers with optical depths of $\tau > 0.5 - 7$ will have high enough albedos to be distinguished

from a bare rock surface.

CHAPTER 8

CONCLUSION

In this thesis, I have used a wide variety of observations of highly irradiated exoplanets to advance our understanding of planetary formation, chemistry, and physics. In Part I, I presented observations of the hottest known exoplanets, ultra-hot Jupiters. These planets' atmospheres experience unique, high-temperature chemistry, including the dominance of H^- as an opacity source and strong molecular dissociation. Molecular dissociation can have a large, observable impact on their thermal structures, as demonstrated by the high amount of heat transport observed in the atmosphere of KELT-9b [200]. Additionally, molecular dissociation and H^- opacity provide an explanation for the many observations of featureless secondary eclipse spectra of ultra-hot Jupiters [6, 163, 197, 233].

Despite the broad-reaching impacts of molecular dissociation and H^- opacity, the population of hot Jupiters still show a wide diversity of secondary eclipse spectra. In Chapter 4, we examined trends in water feature strengths across a population of 20 hot Jupiters in order to quantify this diversity. We found that current models accounting for high-temperature effects such as molecular dissociation are generally able to match the observed spectra. However, the observed scatter in water feature strengths suggests that the planets' atmospheres may show modest differences in metallicity and C/O ratio.

Highly irradiated planets are also prone to intense atmospheric escape, which can shape their atmospheric compositions [e.g., 91]. In Part II, I presented a measurement of helium escape in the atmosphere of the exo-Neptune HAT-P-11b. We found that the mass loss rate is low enough that the bulk composition of HAT-P-11b has likely not changed significantly over its lifetime, which matches expectations from population statistics and photoevaporation models [e.g., 226].

While these studies of ultra-hot Jupiters have revealed some information about their compositions and thermal structures, there are still many unanswered questions. For example, the exact abundances of metals such as carbon and oxygen in their atmospheres are

unknown. While Chapter 4 suggested that ultra-hot Jupiters may have diverse compositions, the exact metallicities of these planets are generally only constrained to within 0.5-1.0 dex [e.g., 6, 197, 211]. Additionally, most of the current metallicity constraints are based solely on *HST* observations of water, and therefore only represent extrapolations from the observed oxygen abundances. Theory predicts that exoplanet atmospheres should show variation in the relative abundances of metals such as C, O, and N [e.g., 213, 3, 187], and Chapter 4 demonstrates that current *HST* observations also favor variations in the C/O ratio. Therefore, extrapolations of the total atmospheric metallicity will be much less accurate if they depend on observation of only a single species, such as water.

New, more advanced telescopes will expand our capability to observe exoplanet atmospheres. In the near future, the launch of *JWST* in October 2021 will revolutionize our ability to measure the atmospheric compositions and thermal structures of exoplanets. *JWST*'s broad wavelength coverage, spanning from $0.6 - 28$ μm, means we will be able to resolve spectral features of molecules such as CO, CH_4, and CO_2 in addition to water. These additional detections will lead to more precise measurements of the atmospheric metallicity and C/O ratio of hot Jupiters. Observations of several hot Jupiters are already planned to take place within the first year of *JWST*'s launch [e.g., 15], and these observations will elucidate the trends we observed in Chapter 4.

JWST will also provide the first opportunity to study the daysides of hot Jupiters in three dimensions simultaneously through spectroscopic eclipse mapping. The Eigenmapping method developed in Chapter 6 provides a framework for interpreting these observations. This unique capability will allow us to probe thermal and compositional gradients across hot Jupiter daysides.

The launch of *JWST* will also allow for the first detailed characterizations of terrestrial planet atmospheres. One of the first-order questions *JWST* will be able to address is whether small planets orbiting M dwarfs are able to retain atmospheres over long timescales. In Chapter 7, I presented a method for detecting atmospheres on terrestrial exoplanets us-

ing the albedo inferred from *JWST* secondary eclipse photometry. Once the planets with atmospheres are identified, *JWST* may have the precision to investigate the atmospheric compositions of some high-signal-to-noise terrestrial exoplanets [e.g., 214]. The presence of an atmosphere is a key prerequisite for the development of surface life, so *JWST* will enable the first steps toward determining the habitability of terrestrial exoplanets.

Recently, ground-based telescopes have been recognized as another avenue toward exoplanet atmospheric characterization. High-resolution observations on stabilized ground-based spectrographs can also place tight constraints on hot Jupiter metallicities and C/O ratios, especially when combined with space-based, low-resolution observations [e.g., 31]. Ground-based observations have also observed the signatures of helium escape in several exoplanets [e.g., 4, 220, 255, 228].

While this thesis focuses on the atmospheric characterization of highly irradiated planets, one of the main goals of future exoplanet observation will be the characterization of cooler planets more analogous to those in our own solar system, in particular of potentially habitable planets. Future ground-based and space-based observatories such as the *Habitable Exoplanet Observatory* [*HabEx*, 95], the *Large UV/Optical/Infrared Surveyor* [*LUVOIR*, 294], the European Extremely Large Telescope [ELT, 241] the Giant Magellan Telescope [GMT, 75], and the Thirty Meter Telescope (TMT, Skidmore et al. 272 but see also Kahanamoku et al. 137) will enable atmospheric characterization at even higher levels of precision. These more precise observations will make it feasible to extend spectroscopic studies of highly irradiated exoplanets down to lower temperatures, which will give us a more complete understanding of the full diversity of known exoplanets.

REFERENCES

[1] Ackerman, A. S., & Marley, M. S. 2001, ApJ, 556, 872

[2] Adcroft, A., Hill, C., Campin, J., Marshall, J., & Heimbach, P. 2004, Monthly Weather Review, 132, 2845

[3] Ali-Dib, M. 2017, MNRAS, 467, 2845

[4] Allart, R., Bourrier, V., Lovis, C., et al. 2018, Science, 362, 1384

[5] Amundsen, D. S., Mayne, N. J., Baraffe, I., et al. 2016, A&A, 595, A36

[6] Arcangeli, J., Désert, J.-M., Line, M. R., et al. 2018, ApJL, 855, L30

[7] Armstrong, D. J., de Mooij, E., Barstow, J., et al. 2016, Nature Astronomy, 1, 0004

[8] Arney, G., & Kane, S. 2018, arXiv e-prints, arXiv:1804.05889

[9] Bakos, G. Á., Torres, G., Pál, A., et al. 2010, ApJ, 710, 1724

[10] Basaltic Volcanism Study Project. 1981, Basaltic Volcanism on the Terrestrial Planets (Pergamon Press, Inc)

[11] Batalha, N. E., Mandell, A., Pontoppidan, K., et al. 2017, PASP, 129, 064501

[12] Baxter, C., Désert, J.-M., Parmentier, V., et al. 2020, A&A, 639, A36

[13] Bean, J. 2013, Follow The Water: The Ultimate WFC3 Exoplanet Atmosphere Survey, HST Proposal 13467

[14] Bean, J. L., Desert, J.-M., Dragomir, D., et al. 2016, Remastering the classics: A thermal inversion for the hot Jupiter archetype HAT-P-7b?, HST Proposal 14792

[15] Bean, J. L., Stevenson, K. B., Batalha, N. M., et al. 2018, PASP, 130, 114402

[16] Beatty, T. G., Madhusudhan, N., Tsiaras, A., et al. 2017, AJ, 154, 158

[17] Beatty, T. G., Marley, M. S., Gaudi, B. S., et al. 2019, AJ, 158, 166

[18] Beatty, T. G., Collins, K. A., Fortney, J., et al. 2014, ApJ, 783, 112

[19] Bedell, M., Bean, J. L., Meléndez, J., et al. 2018, ApJ, 865, 68

[20] Beichman, C., Benneke, B., Knutson, H., et al. 2014, PASP, 126, 1134

[21] Bell, K. L., & Berrington, K. A. 1987, Journal of Physics B: Atomic & Molecular Physics, 20, 1

[22] Bell, T. J., & Cowan, N. B. 2018, ApJL, 857, L20

[23] Benneke, B. 2015, ArXiv e-prints, arXiv:1504.07655

[24] Berta, Z. K., Charbonneau, D., Désert, J.-M., et al. 2012, ApJ, 747, 35

[25] Berta-Thompson, Z. K., Irwin, J., Charbonneau, D., et al. 2015, Nature, 527, 204

[26] Blecic, J., Dobbs-Dixon, I., & Greene, T. 2017, ApJ, 848, 127

[27] Bodenheimer, P., Stevenson, D. J., Lissauer, J. J., & D'Angelo, G. 2018, ApJ, 868, 138

[28] Borucki, W. J. 2017, Proceedings of the American Philosophical Society, 161, 38

[29] Bourrier, V., Lecavelier des Etangs, A., Ehrenreich, D., et al. 2018, A&A, 620, A147

[30] Brogi, M., Line, M., Bean, J., Désert, J.-M., & Schwarz, H. 2017, ApJL, 839, L2

[31] Brogi, M., & Line, M. R. 2019, AJ, 157, 114

[32] Brouwers, M. G., Vazan, A., & Ormel, C. W. 2018, A&A, 611, A65

[33] Brunetto, R., Loeffler, M. J., & Nesvorný, D. 2015, in Asteroids IV, ed. P. Michel, F. E. DeMeo, & W. F. Bottke (University of Arizona Press)

[34] Burrows, A., Sudarsky, D., & Hubeny, I. 2006, ApJ, 650, 1140

[35] Caldas, A., Leconte, J., Selsis, F., et al. 2019, A&A, 623, A161

[36] Campbell, I. H., & Taylor, S. R. 1983, GRL, 10, 1061

[37] Campo, C. J., Harrington, J., Hardy, R. A., et al. 2011, ApJ, 727, 125

[38] Carli, C., De Angelis, S., Tosi, F., et al. 2015, in Lunar and Planetary Science Conference, Lunar and Planetary Science Conference, 1800

[39] Carter, J. A., & Winn, J. N. 2009, ApJ, 704, 51

[40] Castan, T., & Menou, K. 2011, ApJL, 743, L36

[41] Castelli, F., & Kurucz, R. L. 2003, in Modelling of Stellar Atmospheres, ed. N. Piskunov, W. W. Weiss, & D. F. Gray, Vol. 210, A20

[42] Castelli, F., & Kurucz, R. L. 2004, ArXiv Astrophysics e-prints, astro-ph/0405087

[43] Chachan, Y., Knutson, H. A., Gao, P., et al. 2019, AJ, 158, 244

[44] Christiansen, J. L., Ballard, S., Charbonneau, D., et al. 2010, ApJ, 710, 97

[45] Clancy, R. T., Montmessin, F., Benson, J., et al. 2017, Mars Clouds, ed. R. M. Haberle, R. T. Clancy, F. Forget, M. D. Smith, & R. W. Zurek, 42–75

[46] Clark, R. N., Swayze, G. A., Wise, R., et al. 2007, USGS Digital Spectral Library 06, Tech. Rep. 231, U.S. Geological Survey

[47] Cowan, N. B., & Agol, E. 2011, ApJ, 729, 54

[48] Cowan, N. B., Chayes, V., Bouffard, É., Meynig, M., & Haggard, H. M. 2017, MNRAS, 467, 747

[49] Cridland, A. J., van Dishoeck, E. F., Alessi, M., & Pudritz, R. E. 2019, A&A, 632, A63

[50] Crossfield, I. J. M., Waalkes, W., Newton, E. R., et al. 2019, ApJL, 883, L16

[51] Crouzet, N., McCullough, P. R., Deming, D., & Madhusudhan, N. 2014, ApJ, 795, 166

[52] Cubillos, P., Harrington, J., Madhusudhan, N., et al. 2013, ApJ, 768, 42

[53] de Wit, J., Gillon, M., Demory, B.-O., & Seager, S. 2012, A&A, 548, A128

[54] Delrez, L., Santerne, A., Almenara, J. M., et al. 2016, MNRAS, 458, 4025

[55] Deming, D. 2010, The Atmospheric Structure of Giant Hot Exoplanets, HST Proposal 12181

[56] —. 2011, Near-IR Spectroscopy of the Hottest Known Exoplanet, WASP-33b, HST Proposal 12495

[57] Diamond-Lowe, H., Stevenson, K. B., Bean, J. L., Line, M. R., & Fortney, J. J. 2014, ApJ, 796, 66

[58] Dobbs-Dixon, I., & Cowan, N. B. 2017, ApJL, 851, L26

[59] Domingue, D. L., Chapman, C. R., Killen, R. M., et al. 2014, Space Sci. Rev., 181, 121

[60] Dorn, C., & Heng, K. 2018, ApJ, 853, 64

[61] Dransfield, G., & Triaud, A. H. M. J. 2020, MNRAS, 499, 505

[62] Dressel, L. 2018, Wide Field Camera 3 Instrument Handbook, Version 10.0 (Baltimore: STScI)

[63] Dumusque, X., Turner, O., Dorn, C., et al. 2019, A&A, 627, A43

[64] Eastman, J., Siverd, R., & Gaudi, B. S. 2010, PASP, 122, 935

[65] Edwards, B., Changeat, Q., Baeyens, R., et al. 2020, AJ, 160, 8

[66] Ehrenreich, D., Bourrier, V., Wheatley, P. J., et al. 2015, Nature, 522, 459

[67] Elkins-Tanton, L. T. 2012, Annual Review of Earth and Planetary Sciences, 40, 113

[68] Elkins-Tanton, L. T., Burgess, S., & Yin, Q.-Z. 2011, Earth and Planetary Science Letters, 304, 326

[69] Espinoza, N., Fortney, J. J., Miguel, Y., Thorngren, D., & Murray-Clay, R. 2017, ApJL, 838, L9

[70] Espinoza, N., & Jordan, A. 2015, Monthly Notices of the Royal Astronomical Society, 450, 1879

[71] Espinoza, N., Brahm, R., Henning, T., et al. 2020, MNRAS, 491, 2982

[72] Esposito, L. W., Knollenberg, R. G., Marov, M. I., Toon, O. B., & Turco, R. P. 1983, in Venus, ed. D. M. Hunten, L. Colin, T. M. Donahue, & V. I. Moroz, 484–564

[73] Evans, T. 2017, A global map of thermal inversions for an ultra-hot planet, HST Proposal 15134

[74] Faedi, F., Barros, S. C. C., Anderson, D. R., et al. 2011, A&A, 531, A40

[75] Fanson, J., Bernstein, R., Angeli, G., et al. 2020, in Society of Photo-Optical Instrumentation Engineers (SPIE) Conference Series, Vol. 11445, Society of Photo-Optical Instrumentation Engineers (SPIE) Conference Series, 114451F

[76] Fassett, C., Needham, D. H., Watters, W. A., & Hundal, C. 2017, AGU Fall Meeting Abstracts

[77] Fegley, B., & Cameron, A. G. W. 1987, Earth and Planetary Science Letters, 82, 207

[78] Fegley, Jr., B., Jacobson, N. S., Williams, K. B., et al. 2016, ApJ, 824, 103

[79] Feng, Y. K., Line, M. R., Fortney, J. J., et al. 2016, ApJ, 829, 52

[80] Fletcher, L. N., Orton, G. S., Teanby, N. A., Irwin, P. G. J., & Bjoraker, G. L. 2009, Icarus, 199, 351

[81] Foley, B. J., Bercovici, D., & Landuyt, W. 2012, Earth and Planetary Science Letters, 331, 281

[82] Foreman-Mackey, D., Hogg, D. W., Lang, D., & Goodman, J. 2013, Publications of the Astronomical Society of the Pacific, 125

[83] Fortney, J. J., Lodders, K., Marley, M. S., & Freedman, R. S. 2008, ApJ, 678, 1419

[84] Fortney, J. J., Mordasini, C., Nettelmann, N., et al. 2013, ApJ, 775, 80

[85] Fraine, J., Deming, D., Benneke, B., et al. 2014, Nature, 513, 526

[86] France, K., Loyd, R. O. P., Youngblood, A., et al. 2016, ApJ, 820, 89

[87] Freedman, R. S., Lustig-Yaeger, J., Fortney, J. J., et al. 2014, ApJS, 214, 25

[88] Fromang, S., Leconte, J., & Heng, K. 2016, Astronomy and Astrophysics, 591, A144

[89] Fu, G., Deming, D., Lothringer, J., et al. 2020, arXiv e-prints, arXiv:2005.02568

[90] Fulton, B. J., & Petigura, E. A. 2018, AJ, 156, 264

[91] Fulton, B. J., Petigura, E. A., Howard, A. W., et al. 2017, AJ, 154, 109

[92] Gao, P., Marley, M. S., Zahnle, K., Robinson, T. D., & Lewis, N. K. 2017, AJ, 153, 139

[93] Garhart, E., Deming, D., Mandell, A., et al. 2020, AJ, 159, 137

[94] Gaudi, B. S., Stassun, K. G., Collins, K. A., et al. 2017, Nature, 546, 514

[95] Gaudi, B. S., Seager, S., Mennesson, B., et al. 2020, arXiv e-prints, arXiv:2001.06683

[96] Gharib-Nezhad, E., & Line, M. R. 2019, ApJ, 872, 27

[97] Gillon, M., Triaud, A. H. M. J., Fortney, J. J., et al. 2012, A&A, 542, A4

[98] Gillon, M., Anderson, D. R., Collier-Cameron, A., et al. 2014, A&A, 562, L3

[99] Gillon, M., Triaud, A. H. M. J., Demory, B.-O., et al. 2017, Nature, 542, 456

[100] Ginzburg, S., Schlichting, H. E., & Sari, R. 2018, MNRAS, 476, 759

[101] Gordon, S., & Mcbride, B. J. 1994, Computer program for calculation of complex chemical equilibrium compositions and applications. Part 1: Analysis, Tech. Rep. 19950013764, NASA Lewis Research Center

[102] Górski, K. M., Hivon, E., Banday, A. J., et al. 2005, ApJ, 622, 759

[103] Greene, T. P., Line, M. R., Montero, C., et al. 2016, ApJ, 817, 17

[104] Greene, T. P., Kelly, D. M., Stansberry, J., et al. 2017, Journal of Astronomical Telescopes, Instruments, and Systems, 3, 035001

[105] Grove, C. I., Hook, S. J., & II, E. D. P. 1992, Laboratory Reflectance Spectra of 160 Minerals, 0.4 to 2.5 Micrometers, Tech. rep., Jet Propulsion Laboratory

[106] Grove, T. L., & Parman, S. W. 2004, Earth and Planetary Science Letters, 219, 173

[107] Günther, M. N., Pozuelos, F. J., Dittmann, J. A., et al. 2019, Nature Astronomy, 3, 1099

[108] Haberle, R. M., Clancy, R. T., Forget, F., Smith, M. D., & Zurek, R. W. 2017, The atmosphere and climate of Mars (Cambridge University Press), doi:10.1017/9781139060172

[109] Hamano, K., Abe, Y., & Genda, H. 2013, Nature, 497, 607

[110] Hansen, B. M. S. 2008, ApJS, 179, 484

[111] Hartman, J. D., Bakos, G. Á., Kipping, D. M., et al. 2011, ApJ, 728, 138

[112] Haynes, K., Mandell, A. M., Madhusudhan, N., Deming, D., & Knutson, H. 2015, ApJ, 806, 146

[113] Hebb, L., Collier-Cameron, A., Loeillet, B., et al. 2009, ApJ, 693, 1920

[114] Hellier, C., Anderson, D. R., Collier Cameron, A., et al. 2011, A&A, 535, L7

[115] Heng, K., Frierson, D. M. W., & Phillipps, P. J. 2011, MNRAS, 418, 2669

[116] Henry, G. W. 1999, PASP, 111, 845

[117] Herzberg, C., Condie, K., & Korenaga, J. 2010, Earth and Planetary Science Letters, 292, 79

[118] Hindle, A., Bushby, P., & Rogers, T. 2019, The Astrophysical Journal Letters, 872, L27

[119] Hinkel, N. R., & Unterborn, C. T. 2018, ApJ, 853, 83

[120] Hoeijmakers, H. J., Ehrenreich, D., Heng, K., et al. 2018, Nature, 560, 453

[121] Hoeijmakers, H. J., Ehrenreich, D., Kitzmann, D., et al. 2019, A&A, 627, A165

[122] Horne, K. 1986, PASP, 98, 609

[123] Howe, A. R., & Burrows, A. 2015, ApJ, 808, 150

[124] Hu, R., Ehlmann, B. L., & Seager, S. 2012, ApJ, 752, 7

[125] Hubeny, I., Burrows, A., & Sudarsky, D. 2003, ApJ, 594, 1011

[126] Huber, K. F., Czesla, S., & Schmitt, J. H. M. M. 2017, Astronomy and Astrophysics, 597

[127] Hunten, D. M., Pepin, R. O., & Walker, J. C. G. 1987, Icarus, 69, 532

[128] Husser, T.-O., Wende-von Berg, S., Dreizler, S., et al. 2013, A&A, 553, A6

[129] Ingersoll, A. P., Summers, M. E., & Schlipf, S. G. 1985, Icarus, 64, 375

[130] Irwin, P. G. J., Parmentier, V., Taylor, J., et al. 2020, MNRAS, 493, 106

[131] Izenberg, N. R., Klima, R. L., Murchie, S. L., et al. 2014, Icarus, 228, 364

[132] Jansen, T., & Kipping, D. 2018, MNRAS, 478, 3025

[133] John, T. L. 1988, A&A, 193, 189

[134] Johnson, M. C., Cochran, W. D., Addison, B. C., Tinney, C. G., & Wright, D. J. 2017, AJ, 154, 137

[135] Johnstone, C. P., Güdel, M., Lammer, H., & Kislyakova, K. G. 2018, A&A, 617, A107

[136] Jura, M., & Young, E. D. 2014, Annual Review of Earth and Planetary Sciences, 42, 45

[137] Kahanamoku, S., 'Anolani Alegado, R., Kagawa-Viviani, A., et al. 2020, arXiv e-prints, arXiv:2001.00970

[138] Kammer, J. A., Knutson, H. A., Line, M. R., et al. 2015, ApJ, 810, 118

[139] Karkoschka, E., & Tomasko, M. G. 2011, Icarus, 211, 780

[140] Kataria, T., Showman, A. P., Fortney, J. J., et al. 2015, ApJ, 801, 86

[141] Keating, D., & Cowan, N. B. 2017, ApJL, 849, L5

[142] Keating, D., Cowan, N. B., & Dang, L. 2019, Nature Astronomy, 3, 1092

[143] Kempton, E. M.-R., Lupu, R., Owusu-Asare, A., Slough, P., & Cale, B. 2017, PASP, 129, 044402

[144] Kite, E. S., Fegley, Jr., B., Schaefer, L., & Gaidos, E. 2016, ApJ, 828, 80

[145] Kite, E. S., Manga, M., & Gaidos, E. 2009, ApJ, 700, 1732

[146] Kitzmann, D., Heng, K., Rimmer, P. B., et al. 2018, ApJ, 863, 183

[147] Knutson, H. A., Charbonneau, D., Allen, L. E., et al. 2007, Nature, 447, 183

[148] Knutson, H. A., Lewis, N., Fortney, J. J., et al. 2012, ApJ, 754, 22

[149] Kodama, T., Nitta, A., Genda, H., et al. 2018, Journal of Geophysical Research (Planets), 123, 559

[150] Koll, D. D. B. 2019, arXiv e-prints, arXiv:1907.13145

[151] Koll, D. D. B., & Komacek, T. D. 2018, ApJ, 853, 133

[152] Koll, D. D. B., Malik, M., Mansfield, M., et al. 2019, ApJ, 886, 140

[153] Komacek, T., Showman, A., & Tan, X. 2017, The Astrophysical Journal, 835, 198

[154] Komacek, T. D., & Showman, A. P. 2016, ApJ, 821, 16

[155] Komacek, T. D., & Tan, X. 2018, Research Notes of the American Astronomical Society, 2, 36

[156] Kopparapu, R. K., Ramirez, R., Kasting, J. F., et al. 2013, ApJ, 765, 131

[157] Kostov, V. B., Schlieder, J. E., Barclay, T., et al. 2019, AJ, 158, 32

[158] Kreidberg, L. 2015, PASP, 127, 1161

[159] Kreidberg, L., Bean, J., Stevenson, K., et al. 2014, Exploring the Frontier of Exoplanet Atmosphere Dynamics with NASA's Great Observatories, Spitzer Proposal

[160] Kreidberg, L., Bean, J. L., Désert, J.-M., et al. 2014, ApJL, 793, L27

[161] —. 2014, Nature, 505, 69

[162] Kreidberg, L., Line, M. R., Bean, J. L., et al. 2015, ApJ, 814, 66

[163] Kreidberg, L., Line, M. R., Parmentier, V., et al. 2018, AJ, 156, 17

[164] Kuntschner, H., Bushouse, H., Kümmel, M., & Walsh, J. R. 2009, WFC3 SMOV proposal 11552: Calibration of the G102 grism, Tech. Rep. WFC3-2009-18

[165] Kurucz, R., & Bell, B. 1995, Atomic Line Data (R.L. Kurucz and B. Bell) Kurucz CD-ROM No. 23. Cambridge, 23

[166] Lacis, A. A., & Oinas, V. 1991, JGR, 96, 9027

[167] Lamers, H. J. G. L. M., & Cassinelli, J. P. 1999, Introduction to Stellar Winds, 452

[168] Lammer, H., Selsis, F., Ribas, I., et al. 2003, ApJL, 598, L121

[169] Lanotte, A. A., Gillon, M., Demory, B. O., et al. 2014, A&A, 572, A73

[170] Lecavelier des Etangs, A., Vidal-Madjar, A., McConnell, J. C., & Hébrard, G. 2004, A&A, 418, L1

[171] Lecavelier Des Etangs, A., Ehrenreich, D., Vidal-Madjar, A., et al. 2010, A&A, 514, A72

[172] Lide, D. R., ed. 2005, CRC Handbook of Chemistry and Physics (Boca Raton, FL: CRC Press)

[173] Line, M. R., Knutson, H., Wolf, A. S., & Yung, Y. L. 2014, ApJ, 783, 70

[174] Line, M. R., Wolf, A. S., Zhang, X., et al. 2013, ApJ, 775, 137

[175] Line, M. R., Stevenson, K. B., Bean, J., et al. 2016, AJ, 152, 203

[176] Lodders, K., Palme, H., & Gail, H.-P. 2009, Landolt Börnstein, arXiv:0901.1149

[177] Lopez, E. D., & Fortney, J. J. 2013, ApJ, 776, 2

[178] Lothringer, J., Barman, T., & Koskinen, T. 2018, The Astrophysical Journal, 866, 27

[179] Lothringer, J. D., & Barman, T. 2019, ApJ, 876, 69

[180] Louden, T., & Kreidberg, L. 2018, MNRAS, 477, 2613

[181] Luger, R., Agol, E., Foreman-Mackey, D., et al. 2019, AJ, 157, 64

[182] Lupu, R. E., Zahnle, K., Marley, M. S., et al. 2014, ApJ, 784, 27

[183] Luque, R., Pallé, E., Kossakowski, D., et al. 2019, A&A, 628, A39

[184] Lustig-Yaeger, J., Meadows, V. S., & Lincowski, A. P. 2019, AJ, 158, 27

[185] Madden, J. H., & Kaltenegger, L. 2018, Astrobiology, 18, 1559

[186] Madhusudhan, N., Amin, M. A., & Kennedy, G. M. 2014, ApJL, 794, L12

[187] Madhusudhan, N., Bitsch, B., Johansen, A., & Eriksson, L. 2017, MNRAS, 469, 4102

[188] Madhusudhan, N., & Seager, S. 2010, ApJ, 725, 261

[189] Mai, C., & Line, M. R. 2019, ApJ, 883, 144

[190] Majeau, C., Agol, E., & Cowan, N. B. 2012, ApJL, 747, L20

[191] Malik, M., Kempton, E. M. R., Koll, D. D. B., et al. 2019, ApJ, 886, 142

[192] Malik, M., Kitzmann, D., Mendonça, J. M., et al. 2019, AJ, 157, 170

[193] Mallonn, M., Herrero, E., Juvan, I. G., et al. 2018, A&A, 614, A35

[194] Mandel, K., & Agol, E. 2002, ApJ, 580, L171

[195] Manjavacas, E., Apai, D., Zhou, Y., et al. 2019, AJ, 157, 101

[196] Mansfield, M., Kite, E. S., Hu, R., et al. 2019, ApJ, 886, 141

[197] Mansfield, M., Bean, J. L., Line, M. R., et al. 2018, AJ, 156, 10

[198] Mansfield, M., Bean, J. L., Oklopčić, A., et al. 2018, ApJL, 868, L34

[199] Mansfield, M., Schlawin, E., Lustig-Yaeger, J., et al. 2020, MNRAS, 499, 5151

[200] Mansfield, M., Bean, J. L., Stevenson, K. B., et al. 2020, ApJL, 888, L15

[201] Mansfield, M., Arcangeli, J., Bean, J. L., et al. 2020, Stuck in the Middle with WASP-77Ab: Defining Transitions in Hot Jupiter Atmospheres, HST Proposal 16168

[202] Marcus, R. A., Sasselov, D., Hernquist, L., & Stewart, S. T. 2010, ApJL, 712, L73

[203] Mbarek, R., & Kempton, E. M.-R. 2016, ApJ, 827, 121

[204] McCullough, P. 2012, Spanning the chasms: re-observing the transiting exoplanet HD 189733b, HST Proposal 12881

[205] McCullough, P., & MacKenty, J. 2012, Considerations for using Spatial Scans with WFC3, Space Telescope WFC Instrument Science Report 2012-08

[206] McKay, C. P., Pollack, J. B., & Courtin, R. 1989, Icarus, 80, 23

[207] McSween, H. Y., Moersch, J. E., Burr, D., et al. 2019, Planetary Geoscience (Cambridge University Press)

[208] Melosh, H. J. 2011, in Planetary Surface Processes (Cambridge University Press), 276–318

[209] Melville, G., Kedziora-Chudczer, L., & Bailey, J. 2020, MNRAS, 494, 4939

[210] Mendonça, J. M., Malik, M., Demory, B.-O., & Heng, K. 2018, AJ, 155, 150

[211] Mikal-Evans, T., Sing, D. K., Kataria, T., et al. 2020, MNRAS, 496, 1638

[212] Mollière, P., van Boekel, R., Dullemond, C., Henning, T., & Mordasini, C. 2015, ApJ, 813, 47

[213] Mordasini, C., van Boekel, R., Mollière, P., Henning, T., & Benneke, B. 2016, ApJ, 832, 41

[214] Morley, C. V., Kreidberg, L., Rustamkulov, Z., Robinson, T., & Fortney, J. J. 2017, ApJ, 850, 121

[215] Morris, B. M., Hebb, L., Davenport, J. R. A., Rohn, G., & Hawley, S. L. 2017, ApJ, 846, 99

[216] Morris, B. M., Mandell, A. M., & Deming, D. 2013, ApJL, 764, L22

[217] Morris, B. M., Hawley, S. L., Hebb, L., et al. 2017, ApJ, 848, 58

[218] Nelson, R. M., Pieri, D. C., Baloga, S. M., Nash, D. B., & Sagan, C. 1983, Icarus, 56, 409

[219] Nikolov, N., Sing, D. K., Goyal, J., et al. 2018, MNRAS, 474, 1705

[220] Nortmann, L., Pallé, E., Salz, M., et al. 2018, Science, 362, 1388

[221] Nugroho, S. K., Kawahara, H., Masuda, K., et al. 2017, AJ, 154, 221

[222] Öberg, K. I., Murray-Clay, R., & Bergin, E. A. 2011, ApJL, 743, L16

[223] Oklopčić, A., & Hirata, C. M. 2018, ApJL, 855, L11

[224] Owen, J. E. 2019, Annual Review of Earth and Planetary Sciences, 47

[225] Owen, J. E., & Wu, Y. 2013, ApJ, 775, 105

[226] —. 2017, ApJ, 847, 29

[227] Pál, A., Bakos, G. Á., Torres, G., et al. 2008, ApJ, 680, 1450

[228] Palle, E., Nortmann, L., Casasayas-Barris, N., et al. 2020, A&A, 638, A61

[229] Parker, E. N. 1958, ApJ, 128, 664

[230] Parmentier, V., & Crossfield, I. J. M. 2018, Exoplanet Phase Curves: Observations and Theory, ed. H. J. Deeg & J. A. Belmonte, 116

[231] Parmentier, V., Fortney, J. J., Showman, A. P., Morley, C., & Marley, M. S. 2016, ApJ, 828, 22

[232] Parmentier, V., Showman, A. P., & Fortney, J. J. 2021, MNRAS, 501, 78

[233] Parmentier, V., Line, M. R., Bean, J. L., et al. 2018, A&A, 617, A110

[234] Pedregosa, F., Varoquaux, G., Gramfort, A., et al. 2011, Journal of Machine Learning Research, 12, 2825

[235] Perna, R., Menou, K., & Rauscher, E. 2010, ApJ, 719, 1421

[236] Pierrehumbert, R. T. 2010, Principles of Planetary Climate (Cambridge University Press)

[237] Piskorz, D., Buzard, C., Line, M. R., et al. 2018, AJ, 156, 133

[238] Pluriel, W., Whiteford, N., Edwards, B., et al. 2020, AJ, 160, 112

[239] Querry, M. R. 1987, Optical Constants of Minerals and Other Materials From the Millimeter to the Ultraviolet, Tech. Rep. CRDEC-CR-88009, U.S. Army Armament Munitions Chemical Command, Aberdeen, MD

[240] Rackham, B. V., Apai, D., & Giampapa, M. S. 2018, ApJ, 853, 122

[241] Ramsay, S., Cirasuolo, M., Amico, P., et al. 2021, arXiv e-prints, arXiv:2103.11376

[242] Ranjan, S., Charbonneau, D., Désert, J.-M., et al. 2014, ApJ, 785, 148

[243] Rauscher, E., & Menou, K. 2010, ApJ, 714, 1334

[244] Rauscher, E., & Menou, K. 2012, The Astrophysical Journal, 750, 96

[245] —. 2013, The Astrophysical Journal, 764, 103

[246] Rauscher, E., Menou, K., Seager, S., et al. 2007, ApJ, 664, 1199

[247] Rauscher, E., Suri, V., & Cowan, N. B. 2018, AJ, 156, 235

[248] Rogers, L. A. 2015, ApJ, 801, 41

[249] Rogers, T., & Komacek, T. 2014, The Astrophysical Journal, 794, 132

[250] Rogers, T. M. 2017, Nature Astronomy, 1, 0131

[251] Roman, M. T., Kempton, E. M. R., Rauscher, E., et al. 2021, ApJ, 908, 101

[252] Rouan, D., Deeg, H. J., Demangeon, O., et al. 2011, ApJL, 741, L30

[253] Salz, M., Czesla, S., Schneider, P. C., & Schmitt, J. H. M. M. 2016, A&A, 586, A75

[254] Salz, M., Schneider, P. C., Czesla, S., & Schmitt, J. H. M. M. 2016, A&A, 585, L2

[255] Salz, M., Czesla, S., Schneider, P. C., et al. 2018, A&A, 620, A97

[256] Saumon, D., & Marley, M. S. 2008, ApJ, 689, 1327

[257] Schaefer, L., & Fegley, B. 2004, Icarus, 168, 215

[258] —. 2009, ApJL, 703, L113

[259] Schlawin, E., Greene, T. P., Line, M., Fortney, J. J., & Rieke, M. 2018, AJ, 156, 40

[260] Schwartz, J. C., & Cowan, N. B. 2015, MNRAS, 449, 4192

[261] Schwartz, J. C., Kashner, Z., Jovmir, D., & Cowan, N. B. 2017, ApJ, 850, 154

[262] Seager, S., & Deming, D. 2009, ApJ, 703, 1884

[263] Seager, S., Kuchner, M., Hier-Majumder, C. A., & Militzer, B. 2007, ApJ, 669, 1279

[264] Seager, S., & Sasselov, D. D. 2000, ApJ, 537, 916

[265] Sheets, H. A., & Deming, D. 2014, ApJ, 794, 133

[266] —. 2017, AJ, 154, 160

[267] Showman, A. P., Fortney, J. J., Lian, Y., et al. 2009, ApJ, 699, 564

[268] Showman, A. P., & Guillot, T. 2002, A&A, 385, 166

[269] Shporer, A. 2017, PASP, 129, 072001

[270] Sing, D. K., Fortney, J. J., Nikolov, N., et al. 2016, Nature, 529, 59

[271] Sing, D. K., Lopez-Morales, M., Ballester, G. E., et al. 2016, The Panchromatic Comparative Exoplanetary Treasury Program, HST Proposal 14767

[272] Skidmore, W., TMT International Science Development Teams, & Science Advisory Committee, T. 2015, Research in Astronomy and Astrophysics, 15, 1945

[273] Smith, M. D. 2008, Annual Review of Earth and Planetary Sciences, 36, 191

[274] Snellen, I. A. G., de Kok, R. J., de Mooij, E. J. W., & Albrecht, S. 2010, Nature, 465, 1049

[275] Southworth, J., Bohn, A. J., Kenworthy, M. A., Ginski, C., & Mancini, L. 2020, A&A, 635, A74

[276] Spake, J. J., Sing, D. K., Evans, T. M., et al. 2018, Nature, 557, 68

[277] Sromovsky, L. A., Fry, P. M., & Kim, J. H. 2011, Icarus, 215, 292

[278] Stassun, K. G., Collins, K. A., & Gaudi, B. S. 2017, AJ, 153, 136

[279] Stevenson, K. B., Bean, J. L., Madhusudhan, N., & Harrington, J. 2014, ApJ, 791, 36

[280] Stevenson, K. B., Bean, J. L., Seifahrt, A., et al. 2014, AJ, 147, 161

[281] Stevenson, K. B., Harrington, J., Fortney, J. J., et al. 2012, ApJ, 754, 136

[282] Stevenson, K. B., Désert, J.-M., Line, M. R., et al. 2014, Science, 346, 838

[283] Stevenson, K. B., Line, M. R., Bean, J. L., et al. 2017, AJ, 153, 68

[284] Strassmeier, K. G., Granzer, T., Weber, M., et al. 2004, Astronomische Nachrichten, 325, 527

[285] Sudarsky, D., Burrows, A., & Pinto, P. 2000, ApJ, 538, 885

[286] Swain, M. 2010, The effect of radiation forcing on an exoplanet atmosphere, HST Proposal 12230

[287] Swain, M., Deroo, P., Tinetti, G., et al. 2013, Icarus, 225, 432

[288] Takahashi, J., Itoh, Y., & Takahashi, S. 2011, PASJ, 63, 499

[289] Tan, X., & Komacek, T. D. 2019, ApJ, 886, 26

[290] Taylor, J., Parmentier, V., Line, M. R., et al. 2020, arXiv e-prints, arXiv:2009.12411

[291] Taylor, S. R., & McLennan, S. 2009, Planetary Crusts: Their Composition, Origin and Evolution (Cambridge University Press)

[292] Tennyson, J., Yurchenko, S. N., Al-Refaie, A. F., et al. 2020, JQSRT, 255, 107228

[293] ter Braak, C. J. F., & Vrugt, J. A. 2008, Statistics and Computing, 18, 435

[294] The LUVOIR Team. 2019, arXiv e-prints, arXiv:1912.06219

[295] Thorngren, D., Gao, P., & Fortney, J. J. 2019, ApJL, 884, L6

[296] Tian, F. 2009, ApJ, 703, 905

[297] Tian, F., Toon, O. B., Pavlov, A. A., & De Sterck, H. 2005, ApJ, 621, 1049

[298] Tinetti, G., Drossart, P., Eccleston, P., et al. 2016, in Proc. SPIE, Vol. 9904, Space Telescopes and Instrumentation 2016: Optical, Infrared, and Millimeter Wave, 99041X

[299] Toon, O. B., McKay, C. P., Ackerman, T. P., & Santhanam, K. 1989, JGR, 94, 16287

[300] Torres, G., Fischer, D. A., Sozzetti, A., et al. 2012, ApJ, 757, 161

[301] Torres, G., Winn, J. N., & Holman, M. J. 2008, ApJ, 677, 1324

[302] Triaud, A. H. M. J., Lanotte, A. A., Smalley, B., & Gillon, M. 2014, MNRAS, 444, 711

[303] Triaud, A. H. M. J., Collier Cameron, A., Queloz, D., et al. 2010, A&A, 524, A25

[304] Trifonov, T., Caballero, J. A., Morales, J. C., et al. 2021, Science, 371, 1038

[305] Tsiaras, A., Waldmann, I. P., Zingales, T., et al. 2018, AJ, 155, 156

[306] Turner, J. D., Pearson, K. A., Biddle, L. I., et al. 2016, MNRAS, 459, 789

[307] Unterborn, C. T., & Panero, W. R. 2017, ApJ, 845, 61

[308] Van Eylen, V., Agentoft, C., Lundkvist, M. S., et al. 2018, MNRAS, 479, 4786

[309] van Heck, H. J., & Tackley, P. J. 2011, Earth and Planetary Science Letters, 310, 252

[310] Vanderspek, R., Huang, C. X., Vanderburg, A., et al. 2019, ApJL, 871, L24

[311] Vazan, A., Ormel, C. W., Noack, L., & Dominik, C. 2018, ApJ, 869, 163

[312] Venturini, J., Alibert, Y., & Benz, W. 2016, A&A, 596, A90

[313] Vidal-Madjar, A., Lecavelier des Etangs, A., Désert, J.-M., et al. 2003, Nature, 422, 143

[314] Vidal-Madjar, A., Désert, J.-M., Lecavelier des Etangs, A., et al. 2004, ApJL, 604, L69

[315] Wakeford, H. R., Sing, D. K., Evans, T., Deming, D., & Mandell, A. 2016, ApJ, 819, 10

[316] Wakeford, H. R., Sing, D. K., Kataria, T., et al. 2017, Science, 356, 628

[317] Wakeford, H. R., Sing, D. K., Deming, D., et al. 2018, AJ, 155, 29

[318] Wallace, J. M., & Hobbs, P. V. 2006, Atmospheric Science: An Introductory Survey, 2nd edn. (Elsevier)

[319] Warner, N. H., Golombek, M. P., Sweeney, J., et al. 2017, Space Sci. Rev., 211, 147

[320] Wilkins, A. N., Deming, D., Madhusudhan, N., et al. 2014, ApJ, 783, 113

[321] Williams, P. K. G., Charbonneau, D., Cooper, C. S., Showman, A. P., & Fortney, J. J. 2006, ApJ, 649, 1020

[322] Winters, J. G., Medina, A. A., Irwin, J. M., et al. 2019, AJ, 158, 152

[323] Wong, I., Knutson, H. A., Kataria, T., et al. 2016, ApJ, 823, 122

[324] Wong, I., Shporer, A., Kitzmann, D., et al. 2020, AJ, 160, 88

[325] Wong, M. H., Mahaffy, P. R., Atreya, S. K., Niemann, H. B., & Owen, T. C. 2004, Icarus, 171, 153

[326] Yadav, R., & Thorngren, D. 2017, The Astrophysical Journal Letters, 849, L12

[327] Yang, J., Boué, G., Fabrycky, D. C., & Abbot, D. S. 2014, ApJL, 787, L2

[328] Yang, J., Cowan, N. B., & Abbot, D. S. 2013, ApJL, 771, L45

[329] Youdin, A., & Mitchell, J. 2010, The Astrophysical Journal, 721, 1113

[330] Zahnle, K., Marley, M. S., Morley, C. V., & Moses, J. I. 2016, ApJ, 824, 137

[331] Zhang, M., Knutson, H. A., Kataria, T., et al. 2018, AJ, 155, 83

[332] Zhang, X., & Showman, A. P. 2017, ApJ, 836, 73

[333] Zhao, M. 2013, Near-IR spectroscopy of the highly inflated, hottest known Jupiter KOI-13.01, HST Proposal 13308

[334] —. 2014, Near-IR spectroscopy of the newly discovered benchmark hot Jupiter WASP-103b, HST Proposal 13660

[335] Zhou, G., Bayliss, D. D. R., Kedziora-Chudczer, L., et al. 2015, MNRAS, 454, 3002

REFERENCES

[1] Ackerman, A. S., & Marley, M. S. 2001, ApJ, 556, 872

[2] Adcroft, A., Hill, C., Campin, J., Marshall, J., & Heimbach, P. 2004, Monthly Weather Review, 132, 2845

[3] Ali-Dib, M. 2017, MNRAS, 467, 2845

[4] Allart, R., Bourrier, V., Lovis, C., et al. 2018, Science, 362, 1384

[5] Amundsen, D. S., Mayne, N. J., Baraffe, I., et al. 2016, A&A, 595, A36

[6] Arcangeli, J., Désert, J.-M., Line, M. R., et al. 2018, ApJL, 855, L30

[7] Armstrong, D. J., de Mooij, E., Barstow, J., et al. 2016, Nature Astronomy, 1, 0004

[8] Arney, G., & Kane, S. 2018, arXiv e-prints, arXiv:1804.05889

[9] Bakos, G. Á., Torres, G., Pál, A., et al. 2010, ApJ, 710, 1724

[10] Basaltic Volcanism Study Project. 1981, Basaltic Volcanism on the Terrestrial Planets (Pergamon Press, Inc)

[11] Batalha, N. E., Mandell, A., Pontoppidan, K., et al. 2017, PASP, 129, 064501

[12] Baxter, C., Désert, J.-M., Parmentier, V., et al. 2020, A&A, 639, A36

[13] Bean, J. 2013, Follow The Water: The Ultimate WFC3 Exoplanet Atmosphere Survey, HST Proposal 13467

[14] Bean, J. L., Desert, J.-M., Dragomir, D., et al. 2016, Remastering the classics: A thermal inversion for the hot Jupiter archetype HAT-P-7b?, HST Proposal 14792

[15] Bean, J. L., Stevenson, K. B., Batalha, N. M., et al. 2018, PASP, 130, 114402

[16] Beatty, T. G., Madhusudhan, N., Tsiaras, A., et al. 2017, AJ, 154, 158

[17] Beatty, T. G., Marley, M. S., Gaudi, B. S., et al. 2019, AJ, 158, 166

[18] Beatty, T. G., Collins, K. A., Fortney, J., et al. 2014, ApJ, 783, 112

[19] Bedell, M., Bean, J. L., Meléndez, J., et al. 2018, ApJ, 865, 68

[20] Beichman, C., Benneke, B., Knutson, H., et al. 2014, PASP, 126, 1134

[21] Bell, K. L., & Berrington, K. A. 1987, Journal of Physics B: Atomic & Molecular Physics, 20, 1

[22] Bell, T. J., & Cowan, N. B. 2018, ApJL, 857, L20

[23] Benneke, B. 2015, ArXiv e-prints, arXiv:1504.07655

[24] Berta, Z. K., Charbonneau, D., Désert, J.-M., et al. 2012, ApJ, 747, 35

[25] Berta-Thompson, Z. K., Irwin, J., Charbonneau, D., et al. 2015, Nature, 527, 204

[26] Blecic, J., Dobbs-Dixon, I., & Greene, T. 2017, ApJ, 848, 127

[27] Bodenheimer, P., Stevenson, D. J., Lissauer, J. J., & D'Angelo, G. 2018, ApJ, 868, 138

[28] Borucki, W. J. 2017, Proceedings of the American Philosophical Society, 161, 38

[29] Bourrier, V., Lecavelier des Etangs, A., Ehrenreich, D., et al. 2018, A&A, 620, A147

[30] Brogi, M., Line, M., Bean, J., Désert, J.-M., & Schwarz, H. 2017, ApJL, 839, L2

[31] Brogi, M., & Line, M. R. 2019, AJ, 157, 114

[32] Brouwers, M. G., Vazan, A., & Ormel, C. W. 2018, A&A, 611, A65

[33] Brunetto, R., Loeffler, M. J., & Nesvorný, D. 2015, in Asteroids IV, ed. P. Michel, F. E. DeMeo, & W. F. Bottke (University of Arizona Press)

[34] Burrows, A., Sudarsky, D., & Hubeny, I. 2006, ApJ, 650, 1140

[35] Caldas, A., Leconte, J., Selsis, F., et al. 2019, A&A, 623, A161

[36] Campbell, I. H., & Taylor, S. R. 1983, GRL, 10, 1061

[37] Campo, C. J., Harrington, J., Hardy, R. A., et al. 2011, ApJ, 727, 125

[38] Carli, C., De Angelis, S., Tosi, F., et al. 2015, in Lunar and Planetary Science Conference, Lunar and Planetary Science Conference, 1800

[39] Carter, J. A., & Winn, J. N. 2009, ApJ, 704, 51

[40] Castan, T., & Menou, K. 2011, ApJL, 743, L36

[41] Castelli, F., & Kurucz, R. L. 2003, in Modelling of Stellar Atmospheres, ed. N. Piskunov, W. W. Weiss, & D. F. Gray, Vol. 210, A20

[42] Castelli, F., & Kurucz, R. L. 2004, ArXiv Astrophysics e-prints, astro-ph/0405087

[43] Chachan, Y., Knutson, H. A., Gao, P., et al. 2019, AJ, 158, 244

[44] Christiansen, J. L., Ballard, S., Charbonneau, D., et al. 2010, ApJ, 710, 97

[45] Clancy, R. T., Montmessin, F., Benson, J., et al. 2017, Mars Clouds, ed. R. M. Haberle, R. T. Clancy, F. Forget, M. D. Smith, & R. W. Zurek, 42–75

[46] Clark, R. N., Swayze, G. A., Wise, R., et al. 2007, USGS Digital Spectral Library 06, Tech. Rep. 231, U.S. Geological Survey

[47] Cowan, N. B., & Agol, E. 2011, ApJ, 729, 54

[48] Cowan, N. B., Chayes, V., Bouffard, É., Meynig, M., & Haggard, H. M. 2017, MNRAS, 467, 747

[49] Cridland, A. J., van Dishoeck, E. F., Alessi, M., & Pudritz, R. E. 2019, A&A, 632, A63

[50] Crossfield, I. J. M., Waalkes, W., Newton, E. R., et al. 2019, ApJL, 883, L16

[51] Crouzet, N., McCullough, P. R., Deming, D., & Madhusudhan, N. 2014, ApJ, 795, 166

[52] Cubillos, P., Harrington, J., Madhusudhan, N., et al. 2013, ApJ, 768, 42

[53] de Wit, J., Gillon, M., Demory, B.-O., & Seager, S. 2012, A&A, 548, A128

[54] Delrez, L., Santerne, A., Almenara, J. M., et al. 2016, MNRAS, 458, 4025

[55] Deming, D. 2010, The Atmospheric Structure of Giant Hot Exoplanets, HST Proposal 12181

[56] —. 2011, Near-IR Spectroscopy of the Hottest Known Exoplanet, WASP-33b, HST Proposal 12495

[57] Diamond-Lowe, H., Stevenson, K. B., Bean, J. L., Line, M. R., & Fortney, J. J. 2014, ApJ, 796, 66

[58] Dobbs-Dixon, I., & Cowan, N. B. 2017, ApJL, 851, L26

[59] Domingue, D. L., Chapman, C. R., Killen, R. M., et al. 2014, Space Sci. Rev., 181, 121

[60] Dorn, C., & Heng, K. 2018, ApJ, 853, 64

[61] Dransfield, G., & Triaud, A. H. M. J. 2020, MNRAS, 499, 505

[62] Dressel, L. 2018, Wide Field Camera 3 Instrument Handbook, Version 10.0 (Baltimore: STScI)

[63] Dumusque, X., Turner, O., Dorn, C., et al. 2019, A&A, 627, A43

[64] Eastman, J., Siverd, R., & Gaudi, B. S. 2010, PASP, 122, 935

[65] Edwards, B., Changeat, Q., Baeyens, R., et al. 2020, AJ, 160, 8

[66] Ehrenreich, D., Bourrier, V., Wheatley, P. J., et al. 2015, Nature, 522, 459

[67] Elkins-Tanton, L. T. 2012, Annual Review of Earth and Planetary Sciences, 40, 113

[68] Elkins-Tanton, L. T., Burgess, S., & Yin, Q.-Z. 2011, Earth and Planetary Science Letters, 304, 326

[69] Espinoza, N., Fortney, J. J., Miguel, Y., Thorngren, D., & Murray-Clay, R. 2017, ApJL, 838, L9

[70] Espinoza, N., & Jordan, A. 2015, Monthly Notices of the Royal Astronomical Society, 450, 1879

[71] Espinoza, N., Brahm, R., Henning, T., et al. 2020, MNRAS, 491, 2982

[72] Esposito, L. W., Knollenberg, R. G., Marov, M. I., Toon, O. B., & Turco, R. P. 1983, in Venus, ed. D. M. Hunten, L. Colin, T. M. Donahue, & V. I. Moroz, 484–564

[73] Evans, T. 2017, A global map of thermal inversions for an ultra-hot planet, HST Proposal 15134

[74] Faedi, F., Barros, S. C. C., Anderson, D. R., et al. 2011, A&A, 531, A40

[75] Fanson, J., Bernstein, R., Angeli, G., et al. 2020, in Society of Photo-Optical Instrumentation Engineers (SPIE) Conference Series, Vol. 11445, Society of Photo-Optical Instrumentation Engineers (SPIE) Conference Series, 114451F

[76] Fassett, C., Needham, D. H., Watters, W. A., & Hundal, C. 2017, AGU Fall Meeting Abstracts

[77] Fegley, B., & Cameron, A. G. W. 1987, Earth and Planetary Science Letters, 82, 207

[78] Fegley, Jr., B., Jacobson, N. S., Williams, K. B., et al. 2016, ApJ, 824, 103

[79] Feng, Y. K., Line, M. R., Fortney, J. J., et al. 2016, ApJ, 829, 52

[80] Fletcher, L. N., Orton, G. S., Teanby, N. A., Irwin, P. G. J., & Bjoraker, G. L. 2009, Icarus, 199, 351

[81] Foley, B. J., Bercovici, D., & Landuyt, W. 2012, Earth and Planetary Science Letters, 331, 281

[82] Foreman-Mackey, D., Hogg, D. W., Lang, D., & Goodman, J. 2013, Publications of the Astronomical Society of the Pacific, 125

[83] Fortney, J. J., Lodders, K., Marley, M. S., & Freedman, R. S. 2008, ApJ, 678, 1419

[84] Fortney, J. J., Mordasini, C., Nettelmann, N., et al. 2013, ApJ, 775, 80

[85] Fraine, J., Deming, D., Benneke, B., et al. 2014, Nature, 513, 526

[86] France, K., Loyd, R. O. P., Youngblood, A., et al. 2016, ApJ, 820, 89

[87] Freedman, R. S., Lustig-Yaeger, J., Fortney, J. J., et al. 2014, ApJS, 214, 25

[88] Fromang, S., Leconte, J., & Heng, K. 2016, Astronomy and Astrophysics, 591, A144

[89] Fu, G., Deming, D., Lothringer, J., et al. 2020, arXiv e-prints, arXiv:2005.02568

[90] Fulton, B. J., & Petigura, E. A. 2018, AJ, 156, 264

[91] Fulton, B. J., Petigura, E. A., Howard, A. W., et al. 2017, AJ, 154, 109

[92] Gao, P., Marley, M. S., Zahnle, K., Robinson, T. D., & Lewis, N. K. 2017, AJ, 153, 139

[93] Garhart, E., Deming, D., Mandell, A., et al. 2020, AJ, 159, 137

[94] Gaudi, B. S., Stassun, K. G., Collins, K. A., et al. 2017, Nature, 546, 514

[95] Gaudi, B. S., Seager, S., Mennesson, B., et al. 2020, arXiv e-prints, arXiv:2001.06683

[96] Gharib-Nezhad, E., & Line, M. R. 2019, ApJ, 872, 27

[97] Gillon, M., Triaud, A. H. M. J., Fortney, J. J., et al. 2012, A&A, 542, A4

[98] Gillon, M., Anderson, D. R., Collier-Cameron, A., et al. 2014, A&A, 562, L3

[99] Gillon, M., Triaud, A. H. M. J., Demory, B.-O., et al. 2017, Nature, 542, 456

[100] Ginzburg, S., Schlichting, H. E., & Sari, R. 2018, MNRAS, 476, 759

[101] Gordon, S., & Mcbride, B. J. 1994, Computer program for calculation of complex chemical equilibrium compositions and applications. Part 1: Analysis, Tech. Rep. 19950013764, NASA Lewis Research Center

[102] Górski, K. M., Hivon, E., Banday, A. J., et al. 2005, ApJ, 622, 759

[103] Greene, T. P., Line, M. R., Montero, C., et al. 2016, ApJ, 817, 17

[104] Greene, T. P., Kelly, D. M., Stansberry, J., et al. 2017, Journal of Astronomical Telescopes, Instruments, and Systems, 3, 035001

[105] Grove, C. I., Hook, S. J., & II, E. D. P. 1992, Laboratory Reflectance Spectra of 160 Minerals, 0.4 to 2.5 Micrometers, Tech. rep., Jet Propulsion Laboratory

[106] Grove, T. L., & Parman, S. W. 2004, Earth and Planetary Science Letters, 219, 173

[107] Günther, M. N., Pozuelos, F. J., Dittmann, J. A., et al. 2019, Nature Astronomy, 3, 1099

[108] Haberle, R. M., Clancy, R. T., Forget, F., Smith, M. D., & Zurek, R. W. 2017, The atmosphere and climate of Mars (Cambridge University Press), doi:10.1017/9781139060172

[109] Hamano, K., Abe, Y., & Genda, H. 2013, Nature, 497, 607

[110] Hansen, B. M. S. 2008, ApJS, 179, 484

[111] Hartman, J. D., Bakos, G. Á., Kipping, D. M., et al. 2011, ApJ, 728, 138

[112] Haynes, K., Mandell, A. M., Madhusudhan, N., Deming, D., & Knutson, H. 2015, ApJ, 806, 146

[113] Hebb, L., Collier-Cameron, A., Loeillet, B., et al. 2009, ApJ, 693, 1920

[114] Hellier, C., Anderson, D. R., Collier Cameron, A., et al. 2011, A&A, 535, L7

[115] Heng, K., Frierson, D. M. W., & Phillipps, P. J. 2011, MNRAS, 418, 2669

[116] Henry, G. W. 1999, PASP, 111, 845

[117] Herzberg, C., Condie, K., & Korenaga, J. 2010, Earth and Planetary Science Letters, 292, 79

[118] Hindle, A., Bushby, P., & Rogers, T. 2019, The Astrophysical Journal Letters, 872, L27

[119] Hinkel, N. R., & Unterborn, C. T. 2018, ApJ, 853, 83

[120] Hoeijmakers, H. J., Ehrenreich, D., Heng, K., et al. 2018, Nature, 560, 453

[121] Hoeijmakers, H. J., Ehrenreich, D., Kitzmann, D., et al. 2019, A&A, 627, A165

[122] Horne, K. 1986, PASP, 98, 609

[123] Howe, A. R., & Burrows, A. 2015, ApJ, 808, 150

[124] Hu, R., Ehlmann, B. L., & Seager, S. 2012, ApJ, 752, 7

[125] Hubeny, I., Burrows, A., & Sudarsky, D. 2003, ApJ, 594, 1011

[126] Huber, K. F., Czesla, S., & Schmitt, J. H. M. M. 2017, Astronomy and Astrophysics, 597

[127] Hunten, D. M., Pepin, R. O., & Walker, J. C. G. 1987, Icarus, 69, 532

[128] Husser, T.-O., Wende-von Berg, S., Dreizler, S., et al. 2013, A&A, 553, A6

[129] Ingersoll, A. P., Summers, M. E., & Schlipf, S. G. 1985, Icarus, 64, 375

[130] Irwin, P. G. J., Parmentier, V., Taylor, J., et al. 2020, MNRAS, 493, 106

[131] Izenberg, N. R., Klima, R. L., Murchie, S. L., et al. 2014, Icarus, 228, 364

[132] Jansen, T., & Kipping, D. 2018, MNRAS, 478, 3025

[133] John, T. L. 1988, A&A, 193, 189

[134] Johnson, M. C., Cochran, W. D., Addison, B. C., Tinney, C. G., & Wright, D. J. 2017, AJ, 154, 137

[135] Johnstone, C. P., Güdel, M., Lammer, H., & Kislyakova, K. G. 2018, A&A, 617, A107

[136] Jura, M., & Young, E. D. 2014, Annual Review of Earth and Planetary Sciences, 42, 45

[137] Kahanamoku, S., 'Anolani Alegado, R., Kagawa-Viviani, A., et al. 2020, arXiv e-prints, arXiv:2001.00970

[138] Kammer, J. A., Knutson, H. A., Line, M. R., et al. 2015, ApJ, 810, 118

[139] Karkoschka, E., & Tomasko, M. G. 2011, Icarus, 211, 780

[140] Kataria, T., Showman, A. P., Fortney, J. J., et al. 2015, ApJ, 801, 86

[141] Keating, D., & Cowan, N. B. 2017, ApJL, 849, L5

[142] Keating, D., Cowan, N. B., & Dang, L. 2019, Nature Astronomy, 3, 1092

[143] Kempton, E. M.-R., Lupu, R., Owusu-Asare, A., Slough, P., & Cale, B. 2017, PASP, 129, 044402

[144] Kite, E. S., Fegley, Jr., B., Schaefer, L., & Gaidos, E. 2016, ApJ, 828, 80

[145] Kite, E. S., Manga, M., & Gaidos, E. 2009, ApJ, 700, 1732

[146] Kitzmann, D., Heng, K., Rimmer, P. B., et al. 2018, ApJ, 863, 183

[147] Knutson, H. A., Charbonneau, D., Allen, L. E., et al. 2007, Nature, 447, 183

[148] Knutson, H. A., Lewis, N., Fortney, J. J., et al. 2012, ApJ, 754, 22

[149] Kodama, T., Nitta, A., Genda, H., et al. 2018, Journal of Geophysical Research (Planets), 123, 559

[150] Koll, D. D. B. 2019, arXiv e-prints, arXiv:1907.13145

[151] Koll, D. D. B., & Komacek, T. D. 2018, ApJ, 853, 133

[152] Koll, D. D. B., Malik, M., Mansfield, M., et al. 2019, ApJ, 886, 140

[153] Komacek, T., Showman, A., & Tan, X. 2017, The Astrophysical Journal, 835, 198

[154] Komacek, T. D., & Showman, A. P. 2016, ApJ, 821, 16

[155] Komacek, T. D., & Tan, X. 2018, Research Notes of the American Astronomical Society, 2, 36

[156] Kopparapu, R. K., Ramirez, R., Kasting, J. F., et al. 2013, ApJ, 765, 131

[157] Kostov, V. B., Schlieder, J. E., Barclay, T., et al. 2019, AJ, 158, 32

[158] Kreidberg, L. 2015, PASP, 127, 1161

[159] Kreidberg, L., Bean, J., Stevenson, K., et al. 2014, Exploring the Frontier of Exoplanet Atmosphere Dynamics with NASA's Great Observatories, Spitzer Proposal

[160] Kreidberg, L., Bean, J. L., Désert, J.-M., et al. 2014, ApJL, 793, L27

[161] —. 2014, Nature, 505, 69

[162] Kreidberg, L., Line, M. R., Bean, J. L., et al. 2015, ApJ, 814, 66

[163] Kreidberg, L., Line, M. R., Parmentier, V., et al. 2018, AJ, 156, 17

[164] Kuntschner, H., Bushouse, H., Kümmel, M., & Walsh, J. R. 2009, WFC3 SMOV proposal 11552: Calibration of the G102 grism, Tech. Rep. WFC3-2009-18

[165] Kurucz, R., & Bell, B. 1995, Atomic Line Data (R.L. Kurucz and B. Bell) Kurucz CD-ROM No. 23. Cambridge, 23

[166] Lacis, A. A., & Oinas, V. 1991, JGR, 96, 9027

[167] Lamers, H. J. G. L. M., & Cassinelli, J. P. 1999, Introduction to Stellar Winds, 452

[168] Lammer, H., Selsis, F., Ribas, I., et al. 2003, ApJL, 598, L121

[169] Lanotte, A. A., Gillon, M., Demory, B. O., et al. 2014, A&A, 572, A73

[170] Lecavelier des Etangs, A., Vidal-Madjar, A., McConnell, J. C., & Hébrard, G. 2004, A&A, 418, L1

[171] Lecavelier Des Etangs, A., Ehrenreich, D., Vidal-Madjar, A., et al. 2010, A&A, 514, A72

[172] Lide, D. R., ed. 2005, CRC Handbook of Chemistry and Physics (Boca Raton, FL: CRC Press)

[173] Line, M. R., Knutson, H., Wolf, A. S., & Yung, Y. L. 2014, ApJ, 783, 70

[174] Line, M. R., Wolf, A. S., Zhang, X., et al. 2013, ApJ, 775, 137

[175] Line, M. R., Stevenson, K. B., Bean, J., et al. 2016, AJ, 152, 203

[176] Lodders, K., Palme, H., & Gail, H.-P. 2009, Landolt Börnstein, arXiv:0901.1149

[177] Lopez, E. D., & Fortney, J. J. 2013, ApJ, 776, 2

[178] Lothringer, J., Barman, T., & Koskinen, T. 2018, The Astrophysical Journal, 866, 27

[179] Lothringer, J. D., & Barman, T. 2019, ApJ, 876, 69

[180] Louden, T., & Kreidberg, L. 2018, MNRAS, 477, 2613

[181] Luger, R., Agol, E., Foreman-Mackey, D., et al. 2019, AJ, 157, 64

[182] Lupu, R. E., Zahnle, K., Marley, M. S., et al. 2014, ApJ, 784, 27

[183] Luque, R., Pallé, E., Kossakowski, D., et al. 2019, A&A, 628, A39

[184] Lustig-Yaeger, J., Meadows, V. S., & Lincowski, A. P. 2019, AJ, 158, 27

[185] Madden, J. H., & Kaltenegger, L. 2018, Astrobiology, 18, 1559

[186] Madhusudhan, N., Amin, M. A., & Kennedy, G. M. 2014, ApJL, 794, L12

[187] Madhusudhan, N., Bitsch, B., Johansen, A., & Eriksson, L. 2017, MNRAS, 469, 4102

[188] Madhusudhan, N., & Seager, S. 2010, ApJ, 725, 261

[189] Mai, C., & Line, M. R. 2019, ApJ, 883, 144

[190] Majeau, C., Agol, E., & Cowan, N. B. 2012, ApJL, 747, L20

[191] Malik, M., Kempton, E. M. R., Koll, D. D. B., et al. 2019, ApJ, 886, 142

[192] Malik, M., Kitzmann, D., Mendonça, J. M., et al. 2019, AJ, 157, 170

[193] Mallonn, M., Herrero, E., Juvan, I. G., et al. 2018, A&A, 614, A35

[194] Mandel, K., & Agol, E. 2002, ApJ, 580, L171

[195] Manjavacas, E., Apai, D., Zhou, Y., et al. 2019, AJ, 157, 101

[196] Mansfield, M., Kite, E. S., Hu, R., et al. 2019, ApJ, 886, 141

[197] Mansfield, M., Bean, J. L., Line, M. R., et al. 2018, AJ, 156, 10

[198] Mansfield, M., Bean, J. L., Oklopčić, A., et al. 2018, ApJL, 868, L34

[199] Mansfield, M., Schlawin, E., Lustig-Yaeger, J., et al. 2020, MNRAS, 499, 5151

[200] Mansfield, M., Bean, J. L., Stevenson, K. B., et al. 2020, ApJL, 888, L15

[201] Mansfield, M., Arcangeli, J., Bean, J. L., et al. 2020, Stuck in the Middle with WASP-77Ab: Defining Transitions in Hot Jupiter Atmospheres, HST Proposal 16168

[202] Marcus, R. A., Sasselov, D., Hernquist, L., & Stewart, S. T. 2010, ApJL, 712, L73

[203] Mbarek, R., & Kempton, E. M.-R. 2016, ApJ, 827, 121

[204] McCullough, P. 2012, Spanning the chasms: re-observing the transiting exoplanet HD 189733b, HST Proposal 12881

[205] McCullough, P., & MacKenty, J. 2012, Considerations for using Spatial Scans with WFC3, Space Telescope WFC Instrument Science Report 2012-08

[206] McKay, C. P., Pollack, J. B., & Courtin, R. 1989, Icarus, 80, 23

[207] McSween, H. Y., Moersch, J. E., Burr, D., et al. 2019, Planetary Geoscience (Cambridge University Press)

[208] Melosh, H. J. 2011, in Planetary Surface Processes (Cambridge University Press), 276–318

[209] Melville, G., Kedziora-Chudczer, L., & Bailey, J. 2020, MNRAS, 494, 4939

[210] Mendonça, J. M., Malik, M., Demory, B.-O., & Heng, K. 2018, AJ, 155, 150

[211] Mikal-Evans, T., Sing, D. K., Kataria, T., et al. 2020, MNRAS, 496, 1638

[212] Mollière, P., van Boekel, R., Dullemond, C., Henning, T., & Mordasini, C. 2015, ApJ, 813, 47

[213] Mordasini, C., van Boekel, R., Mollière, P., Henning, T., & Benneke, B. 2016, ApJ, 832, 41

[214] Morley, C. V., Kreidberg, L., Rustamkulov, Z., Robinson, T., & Fortney, J. J. 2017, ApJ, 850, 121

[215] Morris, B. M., Hebb, L., Davenport, J. R. A., Rohn, G., & Hawley, S. L. 2017, ApJ, 846, 99

[216] Morris, B. M., Mandell, A. M., & Deming, D. 2013, ApJL, 764, L22

[217] Morris, B. M., Hawley, S. L., Hebb, L., et al. 2017, ApJ, 848, 58

[218] Nelson, R. M., Pieri, D. C., Baloga, S. M., Nash, D. B., & Sagan, C. 1983, Icarus, 56, 409

[219] Nikolov, N., Sing, D. K., Goyal, J., et al. 2018, MNRAS, 474, 1705

[220] Nortmann, L., Pallé, E., Salz, M., et al. 2018, Science, 362, 1388

[221] Nugroho, S. K., Kawahara, H., Masuda, K., et al. 2017, AJ, 154, 221

[222] Öberg, K. I., Murray-Clay, R., & Bergin, E. A. 2011, ApJL, 743, L16

[223] Oklopčić, A., & Hirata, C. M. 2018, ApJL, 855, L11

[224] Owen, J. E. 2019, Annual Review of Earth and Planetary Sciences, 47

[225] Owen, J. E., & Wu, Y. 2013, ApJ, 775, 105

[226] —. 2017, ApJ, 847, 29

[227] Pál, A., Bakos, G. Á., Torres, G., et al. 2008, ApJ, 680, 1450

[228] Palle, E., Nortmann, L., Casasayas-Barris, N., et al. 2020, A&A, 638, A61

[229] Parker, E. N. 1958, ApJ, 128, 664

[230] Parmentier, V., & Crossfield, I. J. M. 2018, Exoplanet Phase Curves: Observations and Theory, ed. H. J. Deeg & J. A. Belmonte, 116

[231] Parmentier, V., Fortney, J. J., Showman, A. P., Morley, C., & Marley, M. S. 2016, ApJ, 828, 22

[232] Parmentier, V., Showman, A. P., & Fortney, J. J. 2021, MNRAS, 501, 78

[233] Parmentier, V., Line, M. R., Bean, J. L., et al. 2018, A&A, 617, A110

[234] Pedregosa, F., Varoquaux, G., Gramfort, A., et al. 2011, Journal of Machine Learning Research, 12, 2825

[235] Perna, R., Menou, K., & Rauscher, E. 2010, ApJ, 719, 1421

[236] Pierrehumbert, R. T. 2010, Principles of Planetary Climate (Cambridge University Press)

[237] Piskorz, D., Buzard, C., Line, M. R., et al. 2018, AJ, 156, 133

[238] Pluriel, W., Whiteford, N., Edwards, B., et al. 2020, AJ, 160, 112

[239] Querry, M. R. 1987, Optical Constants of Minerals and Other Materials From the Millimeter to the Ultraviolet, Tech. Rep. CRDEC-CR-88009, U.S. Army Armament Munitions Chemical Command, Aberdeen, MD

[240] Rackham, B. V., Apai, D., & Giampapa, M. S. 2018, ApJ, 853, 122

[241] Ramsay, S., Cirasuolo, M., Amico, P., et al. 2021, arXiv e-prints, arXiv:2103.11376

[242] Ranjan, S., Charbonneau, D., Désert, J.-M., et al. 2014, ApJ, 785, 148

[243] Rauscher, E., & Menou, K. 2010, ApJ, 714, 1334

[244] Rauscher, E., & Menou, K. 2012, The Astrophysical Journal, 750, 96

[245] —. 2013, The Astrophysical Journal, 764, 103

[246] Rauscher, E., Menou, K., Seager, S., et al. 2007, ApJ, 664, 1199

[247] Rauscher, E., Suri, V., & Cowan, N. B. 2018, AJ, 156, 235

[248] Rogers, L. A. 2015, ApJ, 801, 41

[249] Rogers, T., & Komacek, T. 2014, The Astrophysical Journal, 794, 132

[250] Rogers, T. M. 2017, Nature Astronomy, 1, 0131

[251] Roman, M. T., Kempton, E. M. R., Rauscher, E., et al. 2021, ApJ, 908, 101

[252] Rouan, D., Deeg, H. J., Demangeon, O., et al. 2011, ApJL, 741, L30

[253] Salz, M., Czesla, S., Schneider, P. C., & Schmitt, J. H. M. M. 2016, A&A, 586, A75

[254] Salz, M., Schneider, P. C., Czesla, S., & Schmitt, J. H. M. M. 2016, A&A, 585, L2

[255] Salz, M., Czesla, S., Schneider, P. C., et al. 2018, A&A, 620, A97

[256] Saumon, D., & Marley, M. S. 2008, ApJ, 689, 1327

[257] Schaefer, L., & Fegley, B. 2004, Icarus, 168, 215

[258] —. 2009, ApJL, 703, L113

[259] Schlawin, E., Greene, T. P., Line, M., Fortney, J. J., & Rieke, M. 2018, AJ, 156, 40

[260] Schwartz, J. C., & Cowan, N. B. 2015, MNRAS, 449, 4192

[261] Schwartz, J. C., Kashner, Z., Jovmir, D., & Cowan, N. B. 2017, ApJ, 850, 154

[262] Seager, S., & Deming, D. 2009, ApJ, 703, 1884

[263] Seager, S., Kuchner, M., Hier-Majumder, C. A., & Militzer, B. 2007, ApJ, 669, 1279

[264] Seager, S., & Sasselov, D. D. 2000, ApJ, 537, 916

[265] Sheets, H. A., & Deming, D. 2014, ApJ, 794, 133

[266] —. 2017, AJ, 154, 160

[267] Showman, A. P., Fortney, J. J., Lian, Y., et al. 2009, ApJ, 699, 564

[268] Showman, A. P., & Guillot, T. 2002, A&A, 385, 166

[269] Shporer, A. 2017, PASP, 129, 072001

[270] Sing, D. K., Fortney, J. J., Nikolov, N., et al. 2016, Nature, 529, 59

[271] Sing, D. K., Lopez-Morales, M., Ballester, G. E., et al. 2016, The Panchromatic Comparative Exoplanetary Treasury Program, HST Proposal 14767

[272] Skidmore, W., TMT International Science Development Teams, & Science Advisory Committee, T. 2015, Research in Astronomy and Astrophysics, 15, 1945

[273] Smith, M. D. 2008, Annual Review of Earth and Planetary Sciences, 36, 191

[274] Snellen, I. A. G., de Kok, R. J., de Mooij, E. J. W., & Albrecht, S. 2010, Nature, 465, 1049

[275] Southworth, J., Bohn, A. J., Kenworthy, M. A., Ginski, C., & Mancini, L. 2020, A&A, 635, A74

[276] Spake, J. J., Sing, D. K., Evans, T. M., et al. 2018, Nature, 557, 68

[277] Sromovsky, L. A., Fry, P. M., & Kim, J. H. 2011, Icarus, 215, 292

[278] Stassun, K. G., Collins, K. A., & Gaudi, B. S. 2017, AJ, 153, 136

[279] Stevenson, K. B., Bean, J. L., Madhusudhan, N., & Harrington, J. 2014, ApJ, 791, 36

[280] Stevenson, K. B., Bean, J. L., Seifahrt, A., et al. 2014, AJ, 147, 161

[281] Stevenson, K. B., Harrington, J., Fortney, J. J., et al. 2012, ApJ, 754, 136

[282] Stevenson, K. B., Désert, J.-M., Line, M. R., et al. 2014, Science, 346, 838

[283] Stevenson, K. B., Line, M. R., Bean, J. L., et al. 2017, AJ, 153, 68

[284] Strassmeier, K. G., Granzer, T., Weber, M., et al. 2004, Astronomische Nachrichten, 325, 527

[285] Sudarsky, D., Burrows, A., & Pinto, P. 2000, ApJ, 538, 885

[286] Swain, M. 2010, The effect of radiation forcing on an exoplanet atmosphere, HST Proposal 12230

[287] Swain, M., Deroo, P., Tinetti, G., et al. 2013, Icarus, 225, 432

[288] Takahashi, J., Itoh, Y., & Takahashi, S. 2011, PASJ, 63, 499

[289] Tan, X., & Komacek, T. D. 2019, ApJ, 886, 26

[290] Taylor, J., Parmentier, V., Line, M. R., et al. 2020, arXiv e-prints, arXiv:2009.12411

[291] Taylor, S. R., & McLennan, S. 2009, Planetary Crusts: Their Composition, Origin and Evolution (Cambridge University Press)

[292] Tennyson, J., Yurchenko, S. N., Al-Refaie, A. F., et al. 2020, JQSRT, 255, 107228

[293] ter Braak, C. J. F., & Vrugt, J. A. 2008, Statistics and Computing, 18, 435

[294] The LUVOIR Team. 2019, arXiv e-prints, arXiv:1912.06219

[295] Thorngren, D., Gao, P., & Fortney, J. J. 2019, ApJL, 884, L6

[296] Tian, F. 2009, ApJ, 703, 905

[297] Tian, F., Toon, O. B., Pavlov, A. A., & De Sterck, H. 2005, ApJ, 621, 1049

[298] Tinetti, G., Drossart, P., Eccleston, P., et al. 2016, in Proc. SPIE, Vol. 9904, Space Telescopes and Instrumentation 2016: Optical, Infrared, and Millimeter Wave, 99041X

[299] Toon, O. B., McKay, C. P., Ackerman, T. P., & Santhanam, K. 1989, JGR, 94, 16287

[300] Torres, G., Fischer, D. A., Sozzetti, A., et al. 2012, ApJ, 757, 161

[301] Torres, G., Winn, J. N., & Holman, M. J. 2008, ApJ, 677, 1324

[302] Triaud, A. H. M. J., Lanotte, A. A., Smalley, B., & Gillon, M. 2014, MNRAS, 444, 711

[303] Triaud, A. H. M. J., Collier Cameron, A., Queloz, D., et al. 2010, A&A, 524, A25

[304] Trifonov, T., Caballero, J. A., Morales, J. C., et al. 2021, Science, 371, 1038

[305] Tsiaras, A., Waldmann, I. P., Zingales, T., et al. 2018, AJ, 155, 156

[306] Turner, J. D., Pearson, K. A., Biddle, L. I., et al. 2016, MNRAS, 459, 789

[307] Unterborn, C. T., & Panero, W. R. 2017, ApJ, 845, 61

[308] Van Eylen, V., Agentoft, C., Lundkvist, M. S., et al. 2018, MNRAS, 479, 4786

[309] van Heck, H. J., & Tackley, P. J. 2011, Earth and Planetary Science Letters, 310, 252

[310] Vanderspek, R., Huang, C. X., Vanderburg, A., et al. 2019, ApJL, 871, L24

[311] Vazan, A., Ormel, C. W., Noack, L., & Dominik, C. 2018, ApJ, 869, 163

[312] Venturini, J., Alibert, Y., & Benz, W. 2016, A&A, 596, A90

[313] Vidal-Madjar, A., Lecavelier des Etangs, A., Désert, J.-M., et al. 2003, Nature, 422, 143

[314] Vidal-Madjar, A., Désert, J.-M., Lecavelier des Etangs, A., et al. 2004, ApJL, 604, L69

[315] Wakeford, H. R., Sing, D. K., Evans, T., Deming, D., & Mandell, A. 2016, ApJ, 819, 10

[316] Wakeford, H. R., Sing, D. K., Kataria, T., et al. 2017, Science, 356, 628

[317] Wakeford, H. R., Sing, D. K., Deming, D., et al. 2018, AJ, 155, 29

[318] Wallace, J. M., & Hobbs, P. V. 2006, Atmospheric Science: An Introductory Survey, 2nd edn. (Elsevier)

[319] Warner, N. H., Golombek, M. P., Sweeney, J., et al. 2017, Space Sci. Rev., 211, 147

[320] Wilkins, A. N., Deming, D., Madhusudhan, N., et al. 2014, ApJ, 783, 113

[321] Williams, P. K. G., Charbonneau, D., Cooper, C. S., Showman, A. P., & Fortney, J. J. 2006, ApJ, 649, 1020

[322] Winters, J. G., Medina, A. A., Irwin, J. M., et al. 2019, AJ, 158, 152

[323] Wong, I., Knutson, H. A., Kataria, T., et al. 2016, ApJ, 823, 122

[324] Wong, I., Shporer, A., Kitzmann, D., et al. 2020, AJ, 160, 88

[325] Wong, M. H., Mahaffy, P. R., Atreya, S. K., Niemann, H. B., & Owen, T. C. 2004, Icarus, 171, 153

[326] Yadav, R., & Thorngren, D. 2017, The Astrophysical Journal Letters, 849, L12

[327] Yang, J., Boué, G., Fabrycky, D. C., & Abbot, D. S. 2014, ApJL, 787, L2

[328] Yang, J., Cowan, N. B., & Abbot, D. S. 2013, ApJL, 771, L45

[329] Youdin, A., & Mitchell, J. 2010, The Astrophysical Journal, 721, 1113

[330] Zahnle, K., Marley, M. S., Morley, C. V., & Moses, J. I. 2016, ApJ, 824, 137

[331] Zhang, M., Knutson, H. A., Kataria, T., et al. 2018, AJ, 155, 83

[332] Zhang, X., & Showman, A. P. 2017, ApJ, 836, 73

[333] Zhao, M. 2013, Near-IR spectroscopy of the highly inflated, hottest known Jupiter KOI-13.01, HST Proposal 13308

[334] —. 2014, Near-IR spectroscopy of the newly discovered benchmark hot Jupiter WASP-103b, HST Proposal 13660

[335] Zhou, G., Bayliss, D. D. R., Kedziora-Chudczer, L., et al. 2015, MNRAS, 454, 3002